공학박사학위논문

Theoretical and Empirical Approaches to Easy Band Gap Engineering of Graphene for a Variety of Applications

다양한 응용을 위한 그래핀 옥사이드의 쉬운
밴드갭 엔지니어링에 대한 이론 및 실제적 접근

2020년 8월

서울대학교 대학원
재료공학부
박 지 수

Abstract

Theoretical and Empirical Approaches to Easy Band Gap Engineering of Graphene for a Variety of Applications

Jisoo Park

Department of Materials Science and Engineering

The Graduate School

Seoul National University

Graphene has been taken attention because of its astounding properties than other transitional materials. Therefore, there have been tremendous studies on developing high performance devices using graphene in a variety of applications. However, many researchers failed to achieve devices with high performance because of negligence about the material properties of graphene that can be altered by the preparation process. Especially in the case of electronic applications, band gap, which considered as important property that decides electrical properties, can be altered by the physical and chemical characteristics of the graphene itself. Therefore, for the improved performance of graphene based devices, fine tuning of band gap is essential.

For the fine tuning of graphene's band gap, some of the researchers tried to find the materials parameters of graphene which decide the band gap itself, but failed to find the

clear relationship. In order to overcoming this huddle, unveiling of hidden parameters which control the band gap of graphene based on carbon atom is important. Therefore this research is focused on the establishment of the relationship between sp^2 carbon and graphene's band gap. In addition, through the empirical application of graphene which has fine-tuned band gap for representative applications.

Part I summarizes the background and necessity for fine tuning of graphene's band gap. The current research trends in the band gap engineering of graphene are reviewed. In order to overcome the gap between the theoretically predicted performance of graphene and the practical graphene based devices, the objectives and scopes of this study were established.

In Part II, basic fundamentals are studied to examine the theoretically predicted band gap of graphene. Based on the sp^2 carbon, key parameters that determine practical band gap according to the surface characteristics are derived. Key material parameters are derived by examining the theory of basic electronics, while the area of sp^2 carbon and boundary sp^2 carbon is introduced to predict the band gap of graphene from chemical route. And this relationship between sp^2 carbon and band gap is experimentally reviewed and extended to graphene embedded materials.

Part III focuses on the design and synthesis of the graphene with tailor fitted band gap according to the design guidelines presented in Part II. Chapter 4 attempt to overcome the lower the band gap of graphene by induced defect. In Chapter 4, edge selectively oxidation of graphene are used to overcome the induced defect on basal plane during reduction process of graphene oxide, resulting in improved electrical conductivity. In Chapter 5, the surface of the graphene oxide is modified to improve the absorption of target gas molecule and transfer of charge carrier by selectively reduction of epoxide group, thereby increasing the sensitivity of the sensing material. In Chapter 6, graphene is embedded in indium-gallium-zinc-oxide (IGZO) for the improvement of electrical transport of channel materials of thin film transistor. By using lower functionalized graphene oxide to minimize the pore generation during heat treatment of channel materials to effectively increase the charge transport of band gap tuned graphene / IGZO composite. As a result, the mobility of graphene embedded thin film transistor is

maximized resulting in much lowered roughness.

This study derives key material parameters that affect the band gap of graphene through theoretical considerations for variables related to the performance of graphene based devices. The graphene design guidelines presented in this study can provide insight to overcoming the gap between the theoretically predicted performance of graphene and practical device performance in addition to advancing the research into next generation graphene based materials.

Keywords: Graphene, Graphene Oxide, Band Gap, Material design, Tailor Fitted Synthesis
Student Number: 2014-21442

Contents

Part I Introduction

Chapter 1 General introduction to band gap engineering of graphene 2

1.1 General introduction of graphene 2

1.2 Theoretical approaches for band gap engineering of graphene 5

1.3 Experimental approaches for band gap engineering of graphene. 9

1.3.1 Graphene nanoribbon 9

1.3.2 Graphene quantum dot 13

1.3.3 Few-layer graphene 16

1.3.4 Heteroatom doped graphene 19

1.4 Probable issues. 22

1.4.1 Limitation of scale-up production of physically modified graphene. 22

1.4.2 Limited Range of generated band gap of resultant graphene after heteroatom doping. 27

1.5 Advantage of graphene oxide based graphene. 30

1.5.1 Easy preparation 30

1.5.2 Large tunable band gap range 34

1.6 Aim and scope of this research 37

1.6.1 Finding controllable parameters for band gap Engineering of graphene oxide based graphene 37

1.6.2 Finding effect of graphene oxide based graphene to graphene embedded materials 40

1.7 References 42

Part II Fine tuning of band gap of graphene fittable to various end uses.

Chapter 2 Development of easy experimental ways to tailor fitted band gap of graphene to various applications..... 51

2.1 Introduction 51
2.2 Effect of sp2 carbon on electron transfer of graphene 52
2.3 Effect of sp2 carbon and edge sp2 carbon to band gap of graphene : re-colligate calculation research 58
2.4 Band gap graphene embedded materials by band gap of graphene: combined with work function 60
2.5 Conclusion 66
2.6 References 67

Chapter 3 Development of easy experimental ways to tailor fitted band gap of graphene to various applications..... 70

3.1 Band gap tuning of graphene by oxidation 70
3.1.1 Introduction 70
3.1.2 Experimental 71
3.1.2.1 Materials 71
3.1.2.2 Preparation of graphene oxide 71
3.1.2.3 Preparation of edge selectively oxidized graphene 72
3.1.2.4 Preparation of GO with modified HCl washing process 73
3.1.2.4 Characterization 74
3.1.3 Results and discussion 75

3.1.4 Conclusion 87
3.2 Band gap tuning of graphene by oxidation 88
3.2.1 Introduction 88
3.2.2 Experimental 89
3.2.2.1 Materials 89
3.2.2.2 Preparation of reduced graphene oxide 89
3.2.2.3 Characterization 90
3.2.3 Results and discussion 91
3.2.4 Conclusion 103
3.3Band gap tuning of graphene by hybridization 104
3.3.1 Introduction 104
3.3.2 Experimental 105
3.2.2.1 Materials 105
3.2.2.2 Preparation of IGZO/reduced graphene oxide hybrid 105
3.2.2.3 Characterization 106
3.2.3 Results and discussion 107
3.3.4 Conclusion 115
3.4 Conclusion 116
3.5 References 117

Part III Performance of a few representative devices based on graphene with fine-tuned band gap

Chapter 4 Electrode performance of band gap tuned graphene 124

4.1 Introduction 124
4.2 Experimental 128
4.2.1 Materials 128
4.2.2 Syntheses of the EOG, FOG, and GO Samples 128
4.2.3 Liquid Phase Exfoliation of EOG and Graphite 130
4.2.4 Fabrication of LPEOG and GO Thin Film and Gold Chloride Doping 130
4.2.5 Characterization 131
4.3 Results and discussion 132
4.3.1 Synthesis of EOG 132
4.3.2 Liquid Phase Exfoliation of EOG 143
4.3.3 Application of LPEOG as a conductive ink 155
4.4 Conclusion 162
4.5 References 163

Chapter 5 Gas sensing performance of band gap tuned graphene 169

5.1 Introduction 169
5.2 Experimental 171
5.2.1 Materials 171
5.2.2 Syntheses of the GO, AGO, and HGO 171
5.2.3 Sensor fabrication 172
5.2.4 NO_2 sensor measurement 172
5.2.3 Characterization 174
5.2.3 Computational method 175
5.3 Results and discussion 176
5.3.1 Band gap engineering of graphene oxide to semiconductor 176
5.3.2 Performance of NO_2 gas sensor of band gap engineered GO 192
5.3.3 Theoretically consideration about the requirement of narrowing band gap of GO

for high gas sensing performance. 201
5.4 Conclusion 205
5.5 References 206

Chapter 6 Thin film transistor performance of IGZO with band gap tuned graphene 214

6.1 Introduction 214
6.2 Experimental 216
6.2.1 Materials 216
6.2.2 Preparation of graphene oxide/IGZO composite 216
6.2.3 Fabrication of thin film transistor 217
6.2.4 Characterization 217
6.3 Results and discussion 219
6.3.1 Band gap modification of IGZO/RGO and IGZO/RHGO by concentration of graphene 219
6.3.2 Effect of gas generation by reduction of graphene to carrier transport of resultant IGZO/RGO composite. 224
6.3.3 Effect of RGO arrangement to the performance of IGZO/RGO 230
6.4 Conclusion 239
6.5 References 240

Part IV Concluding remarks

Chapter 7 Concluding remarks 248

7.1 General guidelines for band gap engineering of graphene oxide based graphene 248
7.2 Further work 252
7.2.1 Band gap engineering of graphene with other foreign atoms. 252
7.2.2 Requirement of guidelines for band gap engineering of graphene in various surrounding materials. 254
7.3 References 258

List of Tables

Table 5.1 NO_2 sensing parameters, band gap, and negative adsorption energy (eV) of representative sensing materials for finding the linear relationship between [$Exp^2(-E_{ad}/k_BT)/E_g^3$)] and 1 / LOD.

List of Figures

Figure 1.1 Materials properties of graphene compared to other materials.
Figure 1.2 Sp^2 Bonding structure and electrical structure of graphene with Dirac cone.
Figure 1.3. Density of state of electron of 1D (upper) and 0D structure (under)
Figure 1.4. Model of periodic energy barrier of quantum physics (upper) and energy band structure calculated by Bloch equation. (under)
Figure 1.5 (a) (left) poly(*m*-phenylenevinylene-*co*-2,5-dioctoxy-*p*-phenylenevinylene) (PmPV) in 1,2-dichloroethane (DCE) with graphene nanoribbons (GNRs) stably suspended in the solution. (right) Schematic diagram of a graphene nanoribbon with adsorbed two units of a PmPV polymer chain. (b) AFM images of selected GNRs with widths in the sub-10 nm region. (scale bars 100 nm). (c) Bandgaps determined from experimental data (symbols) for various GNRs *versus* the ribbon width. (d) Single- or few-layer GNRs of different widths and heights. (scale bars 100 nm).
Figure 1.6 (a) Representation of the gradual unzipping of one wall of a carbon nanotube to form a nanoribbon. (b) AFM image of GNRs nanoribbons with generally single-layered. (c) Scanning electron microscopy (SEM) image of single-layer nanoribbon.
Figure 1.7. (a) STM topographic and (inset) topographic derivative images of a graphene quantum dot (GQD) with lateral dimensions of ≈7 nm exhibiting triangular lattice symmetry. A white hexagonal lattice is overlaid on the derivative image to highlight the orientation of the C lattice. Scale bar: 2 nm. (b) Sample of 0.08 monolayer (ML) C_{60}/Ru after being annealed at 725 K for 2 min. Inset: Magnified view of mushroom-shaped dots. (c) Magnified view of triangular (2.7 nm) GQDs.

Figure 1.8 Band gap of Triangular, parallelogram-shaped, and hexagonal GQD.
Figure 1.9 Schematic diagrams and band structures of (a) monolayer graphene, (b) bilayer graphene and (c) bilayer graphene in an external electric field.
Figure 1.10 (a) Experimental and (b) calculated gate-induced infrared absorption spectra at the charge neutrality point for different applied displacement fields *D*. (c) Experimentally determined gap values (red squares) compared with theoretical predictions based on self-consistent tight-binding (black trace), *ab initio* density functional theory (red trace) and unscreened tight-binding calculations (blue dashed trace).
Figure 1.11 (a) Schematic diagram of a 10 × 10 unit cell of graphene doped with $(BN)_{12}$. (b) Calculated bandgap of BN-doped graphene in a 2 × 2 unit cell plotted as a function of the BN dopant concentration.
Figure 1.12 Magnified π–π* regions of selected normalized C K-edge X-ray absorption near-edge structure (XANES) and K_α X-ray emission (XES) spectra of pristine graphene and BNG films (left side, XES; right side, XANES) with various concentrations of BN dopant.
Figure 1.13 Compartment of quality and price for mass production of various methodology for preparing graphene
Figure 1.14 (a) Schematics of the CVD growth of uniform bilayer graphene over a Cu–Ni alloy film deposited on a sapphire c-plane substrate. (b–d) Optical microscope images of graphene transferred on SiO_2/Si substrates grown under different CVD conditions. (e) Optical transmission spectra of bi-layered graphene (red curve, Ni-22%/Cu-78%) and mono-layered graphene (blue curve, pure Cu) transferred on quartz substrates. Inset shows the photograph of the samples on a SiO_2/Si substrate
Figure 1.15 AFM images of GNRs on mica and corresponding height profiles along the black lines.

Figure 1.16. (a) TEM image of the GQDs and (b) the HRTEM image of the GQDs; (c) a typical single GQD, the size and its lattice parameter are 3.39 and 0.214 nm, respectively; (d) HRTEM image of a typical single GQD, and its corresponding selected area FFT image (inset); (e) the diameter distribution of the GQDs, the red line is the Gaussian fitting curve; (f) AFM image of the GQDs; (g) the height distribution of the GQDs as shown in AFM image f; (h) the GQDs diameter dependent on heating time. The GQDs were prepared using 11.1 wt % glucose solution and 5 min (except for panel h) microwave heating at 595 W.
Figure 1.17 Simulated bonding of foreign atoms and real bonding of Oxygen atoms bonded to graphene using STM
Figure 1.18 (a) Typical AFM image of the reacted graphene (b) dependence of the B content on the ion reaction time measured by the secondary ion mass spectroscopy. (c) Experimental band gaps and corresponding calculation results of B-doped graphenes versus B content for various FETs. Inset: dependence of doping level (the position of the Fermi level from the Dirac point) on the content of substitutional B.
Figure 1.19 Preparation route of RGO from chemical exfoliation of graphite.
Figure 1.20 Oxidation mechanism of graphene by Hummers method.
Figure 1.21 Possible ink based process by concentration of GO ink.
Figure 1.22 Band gap of GO by different oxidation degree.
Figure 1.23 Band gap of RGO by different reduction degree by various reduction agent.
Figure 1.24 Colligated calculation and experimental result of band gap by differed ratio of oxygen atoms.
Figure 1.25 Energy diagram of ZnO/RGO suggested by former research.
Figure 2.1 (a) Linear relationship between sp^2 carbon and effective mass of electron and (b) Linear relationship between band gap and effective mass of

graphene calculated with the model of graphene which some domains exchanged to insulative boron nitride (upper)
Figure 2.2 Linear relationship between band gap and effective mass of (left) various semiconductive materials and graphene and (right) III-V nanowires.
Figure 2.3. (a), (e) ADF-STEM images, (b), (f) electric field strength maps, (c), (g) electric field vector maps, (d), (h)calculated electric field strength maps from simulated STEM images for the 16 segmented detectors, in the coordination of Si–C_3 and Si–C_4, respectively. The numbers in (a), (e) indicate the number of members in the ring. (Scale bars: 2 Å)
Figure 2.4. Replotted calculated band gap of graphene from previous studies replotted by multiple of [1-(ratio of sp^2 carbon)] and (I_D/I_G ratio).
Figure 2.5. (upper right) Band diagram of ZnO/graphene and (lower) graphene in molecular model of d_1, d_2 (upper left)
Figure 2.6 Band diagram of (a1) TiO_2/graphene of structure (a), (b1) TiO_2/ C dangled graphene of structure (b), and (c1) TiO_2/oxygen dangle graphene of structure (c)
Figure 2.7 Band diagram of graphene and work function alternation by type of dopant atom.
Figure 2.8. Replotted calculated work function of graphene from previous studies replotted by oxygen content
Figure 2.9. Suggested band diagram of rutile TiO_2/graphene from previous study that consider band gap and work function of embedded graphene.
Figure 3.1 Thermogravimetric analysis (TGA) results of GO with modified Hummers method.
Figure 3.2 Fourier transform infrared (FT-IR) results of GO with modified Hummers method.
Figure 3.3 Binding ratio of carbon atoms measured by X-ray photoelectron spectroscopy (XPS) results of GO with modified Hummers method.

Figure 3.4 Deconvoluted C1s peak measured by X-ray photoelectron spectroscopy (XPS) results of GO with modified Hummers method.
Figure 3.5 I_D/I_G ratio measured by Raman spectrum results of GO with modified Hummers method.
Figure 3.6 Raman spectra of GO with modified Hummers method.
Figure 3.7 Modified Tauc plot of GO with modified Hummers method from the absorbance measured by UV-vis spectra.
Figure 3.8 Thermogravimetric analysis (TGA) result of GO and HGO by differed heating ratio and those resultant Kissinger plot.
Figure 3.9 X-ray photoelectron spectroscopy (XPS) result of (left) HGO and 40 h annealed HGO and (right) GO and 16h annealed GO.
Figure 3.10 GO reduction mechanism by (left) hydriodic acid (HI) (middle) sodium hydroxide (NaOH) (right) Heat proposed in previous study.
Figure 3.11 Thermogravimetric analysis (TGA) results of RGO reduced by heat, HI, and NaOH
Figure 3.12 Fourier transform infrared (FT-IR) results of RGO reduced by heat, HI, and NaOH.
Figure 3.13 Binding ratio of carbon atoms measured by X-ray photoelectron spectroscopy (XPS) results of reduced by heat, HI, and NaOH.
Figure 3.14 Deconvoluted C1s peak measured by X-ray photoelectron spectroscopy (XPS) results of reduced by heat, HI, and NaOH.
Figure 3.15 I_D/I_G ratio measured by Raman spectrum results of reduced by heat, HI, and NaOH.
Figure 3.16 Raman spectra of reduced by heat, HI, and NaOH.
Figure 3.17 Modified Tauc plot of reduced by heat, HI, and NaOH from the absorbance measured by UV-vis spectra.
Figure 3.18 Linear plot of band gap of GO based graphene plotted by the multiple of (non sp^2 carbon ratio) and (I_D/I_G ratio).

Figure 3.19 Linear plot of work function of GO based graphene plotted by the oxygen content.
Figure 3.20 Band diagram of typical metal oxides proposed in previous studies.
Figure 3.21 (left) Deconvoluted C1s peak measured by X-ray photoelectron spectroscopy (XPS) results of RGO reduced at 450°C (right) Tauc plot of ZnO/RGO from the absorbance measured by UV-vis spectra.
Figure 3.22 (left) Deconvoluted C1s peak measured by X-ray photoelectron spectroscopy (XPS) results of RGO reduced at 180°C (right) Tauc plot of TiO_2/RGO from the absorbance measured by UV-vis spectra.
Figure 3.23 (left) Deconvoluted C1s peak measured by X-ray photoelectron spectroscopy (XPS) results (right) Secondary electron spectra measured by UPS RGO reduced at 500°C.
Figure 3.24 Modified Tauc plot of IGZO/RGO that weight percent of 0.05 wt.% ~ 0.4 wt.% from the absorbance measured by UV-vis spectra.
Figure 4.1 Experimental scheme for producing LPEOG suspension.
Figure. 4.2 (a) Solution of oxidant for step II oxidation and (b) step I oxidation.
Figure 4.3 Raman spectra of (a) graphite, (b) E7024, and (c) FOG, and 2D mapping images (x100) for (d) graphite, (e) E7024, and (f) FOG.
Figure. 4.4 Graphite, EOG and FOG's 2D mapping of I_D/I_G ratio
Figure. 4.5 Results of Raman spectroscopy and I_D/I_G ratio of graphite, EOG and FOG
Figure 4.6 X-ray diffraction peaks of (a) graphite, EOG and (b) FOG normalized with the peak of 26.2˚.
Figure 4.7 (a) Binding ratios and (b) C/O ratios examined by XPS. (c) FT-IR spectroscopy and (d) TGA data of graphite, EOG and FOG.
Figure 4.8 Results of Raman spectroscopy and I_D/I_G ratio of graphite, EOG and FOG

Figure. 4.9 EOG dispersions for various solvents and EOG, which was dispersed in NaOH 0.1M and settled for 9 months.
Figure 4.10 (a) Photograph and concentration of LPEOG suspension after dialysis. The inset shows images of LPEOG suspension 9 months after dispersion. (b) Zeta potentials of LPEOG and graphene oxide. (c) Bonding ratios and (d) C/O ratios obtained from the XPS results.
Figure 4.11 Concentrated LE7024 before and after drying. Concentration of concentrated LE7024 were measured by weighing.
Figure 4.12 Deconvoluted Cls peak of exfoliated graphite, and LPEOG and graphene oxide measured by XPS.
Figure 4.13 (a) Topography image and (b) profile of the LPEOG sheet, (c) ratio of single layered LPEOG sheets, and (d) average lateral size measured by AFM in aqueous solution
Figure. 4.14 Atomic Force Microscopy (AFM) topology image and profiles of the LPEOG sheets.
Figure 4.15 Lateral size distribution of the LPEOG sheets measured by AFM.
Figure 4.16 (a, d) Normal image, (b, e) high resolution image, and (c, f) SAED pattern of LE7024 and GO sheet.
Figure 4.17 Transmission electron microscopy (TEM) normal images, high resolution images of the edge, and selective area electron diffraction (SAED) peaks of LPEOG and GO sheets.
Figure 4.18 (a) Photograph of electric circuit drawn by LPEOG ink by brush printing on glass substrate, and (b) circuit test of rLE7024 film, which annealed at 500˚C. (c) Performance of $AuCl_3$ doped rLE7024 and rGO transparent conducting film measured by a 4-point probe and ultraviolet–visible spectroscopy, and (d) image of $AuCl_3$ doped rLE7024 based transparent conducting film.

Figure 4.19 Thickness of rLE7024, rGO film for the measurement of electrical conductivity which were annealed under temperature condition of 400˚C + 1100˚C and 500˚C.
Figure 4.20 (a) Binding ratios and C/O ratios, and (b) deconvoluted C1s peak measured by (XPS)of 1100 ˚C annealed rLE7024 and rGO.
Figure 4.21 (a) Optoelectrical performance of rLE7024 and rGO transparent conductive film (TCF) measured by a 4-point probe and ultraviolet–visible (UV-vis) spectroscopy, and (b) results of Raman spectroscopy and I_D/I_G ratio of RLE7024 and RGO.
Figure 4.21 Transmittance at visible light range of rLE024, rGO, $AuCl_3$ doped rLE024, and $AuCl_3$ doped rGO transparent conductive film.
Figure 5.1 Schematic view of partially reduction of GO for synthesis of HGO_5M by hydrolysis and hydration reaction by HCl.
Figure 5.2 (a) Normalized FTIR spectrum normalized upon the absorbance of the C=C double bond from the graphitic domain, (b) Bonding configuration, and (c) C/O atomic ratio measured by XPS.
Figure 5.3 XPS C1s spectra of GO, AGO, HGO_1M and HGO_5M sheet.
Figure 5.4. (a) Weihgt loss of GO, AGO, HGO_1M and HGO_5M from 100 ℃ ~ 500 ℃ measureed by TGA. (b) Negatice zeta potential of water dispered GO, AGO, HGO_1M and HGO_5M.
Figure 5.5 The TEM image of edge (x 25,000) and SAED pattern (inset) of GO, AGO, HGO_1M, and HGO_5M.
Figure 5.6 The (a) Raman and (b) XRD spectra of GO, AGO, HGO_1M, and HGO_5M
Figure 5.7 AFM topology image, profile of GO, AGO, HGO_1M and HGO_5M sheet.
Figure 5.8 (a) Dispersed GO, AGO, HGO_1M and HGO_5M after neutralized by DI water. (b) UV-vis absorbance spectra of GO, AGO, HGO_1M and

HGO_5M dispersed in water. (concentration: 0.2 mg/ml)
Figure 5.9 Modified Tauc plot of each GO, AGO, HGO_1M, and HGO_5M caculated from the UV-vis absorbance of **Figure 5.8**
Figure 5.10 I-V curve of GO, AGO, HGO_1M and HGO_5M thin film deposited on Au electrode patterned Si subsrate obtained by 2-point-probe method.
Figure 5.11 Thickness GO, AGO, HGO_1M and HGO_5M thin film obtained by AFM.
Figure 5.12 The band gap and eletctical conductivity of GO, AGO, HGO_1M, and HGO 5M changed by recovered of sp^2 structure of graphene.
Figure 5.13, Distribution of lateral size of GO, AGO, HGO_1M and HGO_5M sheet obtained from the dynamic light scattering (DLS) result.
Figure 5.14 (a) Scheme of fabricating the GO, AGO, HGO_1M, and HGO_5M gas sensors and (b) optical microscope image of the HGO_5M gas sensor (left: x 5, right: x 10).
Figure 5.15 Thickness of fabricated HGO thin film measured by AFM (3㎛ × 3㎛)
Figure 5.16 Response of GO, AGO, HGO_1M and HGO_5M gas sensor under 5ppm NO_2 injected once.
Figure 5.17 Response of HGO_5M sensor to NO_2 gas measured under room temperature.
Figure 5.18 (a) Response under 5ppm NO_2 gas, recovery under dry gas, and (b) response time of the GO, AGO, HGO_1M, and HGO_5M gas sensors calculated from the gas sensing curve. (c) Response of the HGO_5M gas sensor under NO_2 (5ppm), NH_3 (50ppm), CO (50ppm) and H_2(50ppm). (d), (e) Response of the HGO_5M sensor under injection NO_2 with different concentrations from 1ppm to 9ppm for calculating LOD. (f) Gas sensing curve

of HGO_5M sensor under repeated injection and subtraction of 5ppm NO_2 gas.
Figure 5.19 Response of HGO_5M sensor to 5 ppm NO_2 gas after 0 h and 24 h measurement normalized by the response after 0h.
Figure 5.20 Response of HGO_5M sensor to NO_2 gas measured under dry air and RH 50% condition normalized by the response under dry air with 5ppm NO_2 gas.
Figure 5.21 Base response of HGO_5M gas sensor under O_2 (21%) / N_2 (79%) dry air for the calculation of RMS noise.
Figure 5.22, Stable molecular structure of NO_2 on GO and HGO_5M used to calculation of adsorption energy with distance between NO_2 molecule to adsorbable functional group of HGO_5M and resultant adsorption energy calculated by Monte Carlo simulation.
Figure 5.23. The linear relationship between [$Exp^2(-E_{ad}/k_BT) / E_g^3$)] and 1/ LOD shows the influence of band gap and adsorption energy to NO_2 gas sensing performance of materials.
Figure 6.1 Deconvoluted XPS C1s peak of (left) GO and (right) HGO
Figure 6.2 Raman spectra of (left) GO and (right) HGO
Figure 6.3 Band gap of (left) RGO and (right) RHGO reduced at 500 °C calculated by modified Tauc plot from the absorbance of UV-vis spectra.
Figure 6.4 UPS secondary electron spectra of (left) RGO and (right) RHGO reduced at 500 °C calculated for the calculation of work function.
Figure 6.5 IGZO/GO solution that contains 0.1, 0.2, 0.4, and 0.8 wt.% of GO
Figure 6.6 Band gap of (left) IGZO/RGO and (right) IGZO/RHGO reduced at 500 °C that contains 0.1, 0.2, 0.4, and 0.8 wt.% of reduced graphene, calculated by modified Tauc plot from the absorbance of UV-vis spectra.
Figure 6.7 Scheme of gas generation during annealing of IGZO/GO.
Figure 6.8 FT-IR spectra from ATR mode of GO and HGO

Figure 6.9 Surface roughness of (left) IGZO/RGO and (right) IGZO/RHGO reduced at 500 °C calculated from AFM topology image.
Figure 6.10 Electrical resistivity of (left) IGZO/RGO and (right) IGZO/RHGO reduced at 500 °C.
Figure 6.11 (upper) Schematic view of fabricating IGZO/RGO and IGZO/RHGO based TFT device (lower) SEM image of the patterned Au on n^+Si / SiO_2 substrate (magnification : x1000)
Figure 6.12 (left) Source drain current of IGZO/RGO TFT with various concentration of RGO by altered gate voltage (right) carrier mobility of IGZO/RGO TFT
Figure 6.13 SEM image if IGZO/RGO on Si substrate with various concentration of RGO (magnification: x10000)
Figure 6.14 Source drain current of (left) IGZO/RHGO and (right) IGZO/RGO TFT with 0.2 wt.% concentration of graphene by altered gate voltage under source drain voltage of 0.1V and 10V
Figure 6.15 Zeta potential of GO and HGO dispersed in Ethanol.
Figure 6.16 Carrier mobility and on/off ratio of various graphene based TFT for the compartment of the performance of IGZO/RHGO TFT with other graphene based TFT.
Figure 7.1 Schematic view of the process of band gap engineering of GO based graphene and its composite for target application.
Figure 7.2 (upper) Expected application of GO based graphene and (lower) predicted band gap range of GO based graphene and its composite for each application.
Figure 7.3 Thermogravimetric analysis (TGA) result of GO and HGO by differed heating ratio and those resultant Kissinger plot.
Figure 7.4 (left) Band gap calculated by Tauc plot and (right) transistor performance of ink based IGTO channel after annealing process.

Figure 7.5 Improved carrier mobility of ZnO/GO transistor channel by elimination of depletion mode by adding gold doping of GO.
Figure 7.6 Improved carrier mobility of ZnO/graphene transistor channel by adding large sized graphene.

Part I.

Introduction

Chapter 1 General introduction to band gap engineering of graphene

1.1 General introduction of graphene

Graphene, composed of two dimensional network of sp^2 hybridized carbon network, showed astounding electrical, thermal, and mechanical properties than other traditional materials as shown in **Figure 1.1**. The excellent electronic properties of graphene, viz, the theoretical mobility of graphene of 200,000 cm^2/Vs, and resistivity of 6.4 μΩcm [1], and the two dimensional morphological features with high aspect ratio, are very attractive, particularly when considered as future electronic, thermal, and energy storage devices. However, in practice, such unprecedented advantage of graphene have not been realized regardless of graphene has been applied, i.e, either in nanocomposites or in graphene itself. [2] For example, graphene has been consider as an future channel materials for semiconductive devices, but cannot show high performance because of its zero band gap from electron structure of Dirac cone of **Figure 1.2** [3] . This gives us that band gap engineering is essential for the right application of graphene, but the parameters that determines graphene has not been clearly defined.

Figure 1.1 Materials properties of graphene compared to other materials. [1]

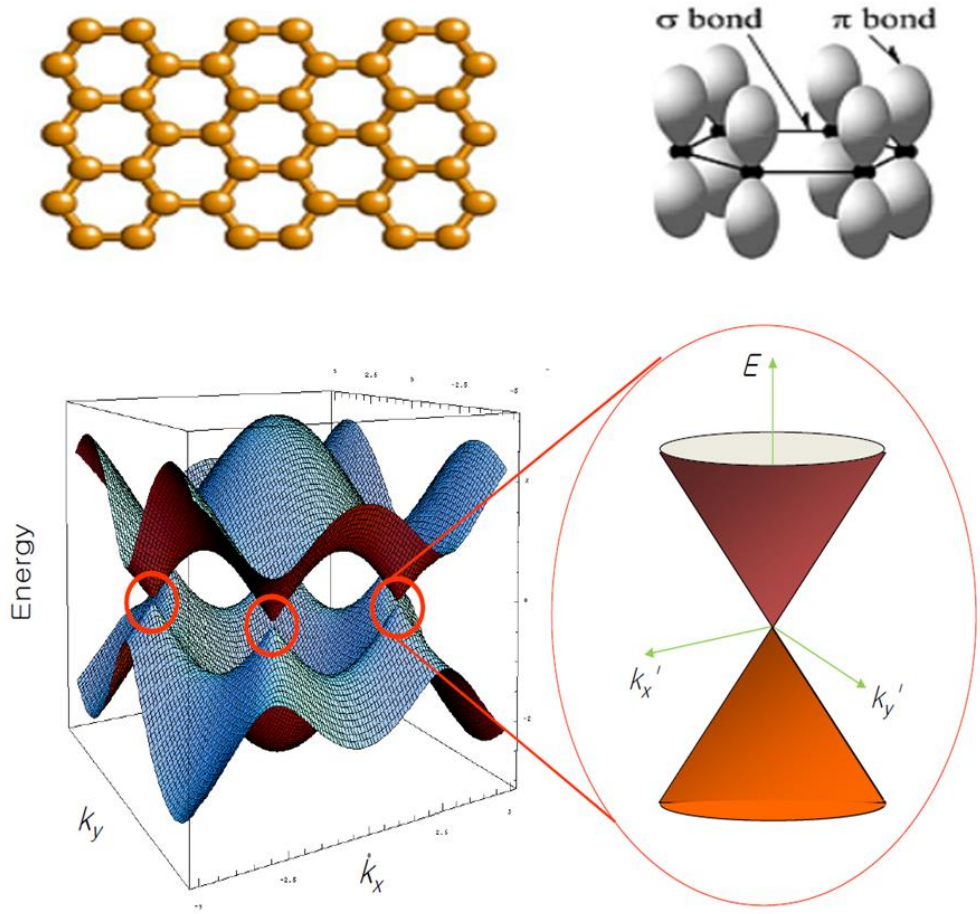

Figure 1.2. Sp^2 Bonding structure and electrical structure of graphene with Dirac cone. [3]

1.2 Theoretical approaches for band gap engineering of graphene

Band gap has zero band gap nature because of its sp^2 hybridized structure of carbon atoms, which can electron moves rapidly like free electron of zero effective mass. Therefore, in order to enlarge band gap of graphene, quantum mechanics in case of free electron should be studied.

In the case of free electron, band gap can be generated by quantum confinement effect, as known as in basic theory of quantum physics. As in the case if 1D nanowire and 0D quantum dot structure, density of state quantified as shown in **Figure 1.3** by the equation (1.1) and (1.2) followed below. Especially, effective mass of free electron is almost zero and density of state of 1D structure can be quantified as like 0D structure. [4]

$$\rho_{\text{energy}}(E) = \frac{1}{\pi}\sqrt{\frac{2m_{\text{eff}}}{\hbar^2}} \sum_{n_x,n_y} \frac{1}{\sqrt{E - E_{n_x,n_y}}} \Theta(E - E_{n_x,n_y}) \tag{1.1}$$

$$\rho_{\text{energy}} = 2 \sum_{n_x,n_y,n_z} \delta(E - E_{n_x,n_y,n_z}) \tag{1.2}$$

$\boldsymbol{\rho}$ means density of state, $\boldsymbol{m_{\text{eff}}}$ means effective mass of electron, $\boldsymbol{n}$ means periodic state number of electron. As shown in the quantification effect by structure of electron path shows that structure of graphene should be changed to 1D or 0D in order to enlarge band gap of itself.

Other ways of theoretical approaches to band gap generation gives energy barrier to electrical pathway. Using Bloch equation, Energy band diagram of finite energy barrier can be estimated from the basic quantum physics as shown in the equation (1.3) and (1.4) and shown as **Figure 1.4**. [5]

$$P\frac{\sin \alpha a}{\alpha a} + \cos \alpha a = coska \tag{1.3}$$

$$P = \frac{4\pi^2 maV_0 b}{h^2} \quad (k = \text{wave number}, \alpha = \frac{4\pi mE}{h}) \tag{1.4}$$

a means the distance between energy barrier, b means area of energy barrier, V_0 means the height of energy barrier, m means mass of electron. By the parameter of V_0 b, forbidden zone of electron is generated and the band gap is generated. This equation gives the way of enlarge band gap of graphene by induce barrier of electron transport.

Equation (1.1) from (1.4) indicates that the importance of change of physical and chemical modification of graphene should be accompanied when engineering of graphene. Without change of those surface characteristics of graphene, sp^2 bonded structure of graphene is preserved, makes changing electronic structure of Dirac cone to difficult work.

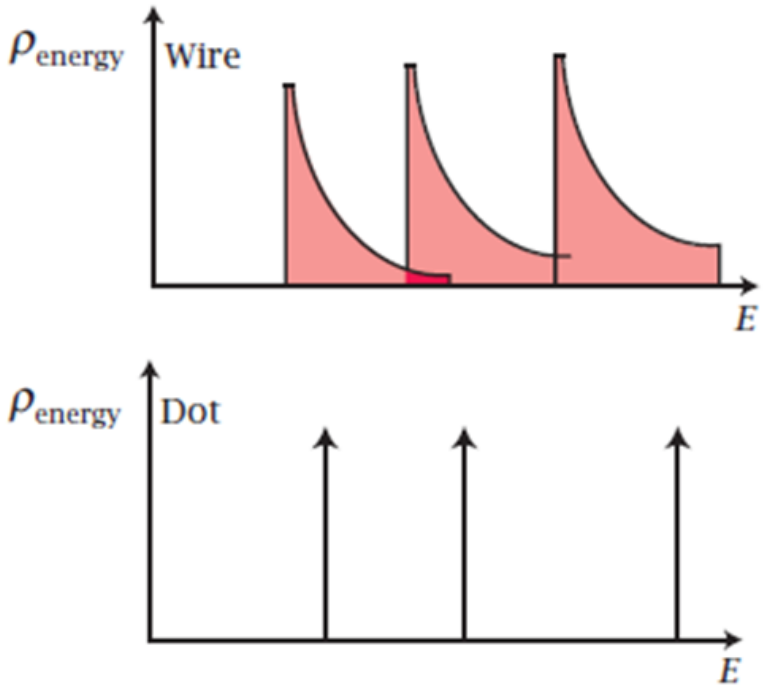

Figure 1.3. Density of state of electron of 1D (upper) and 0D structure (under) [4]

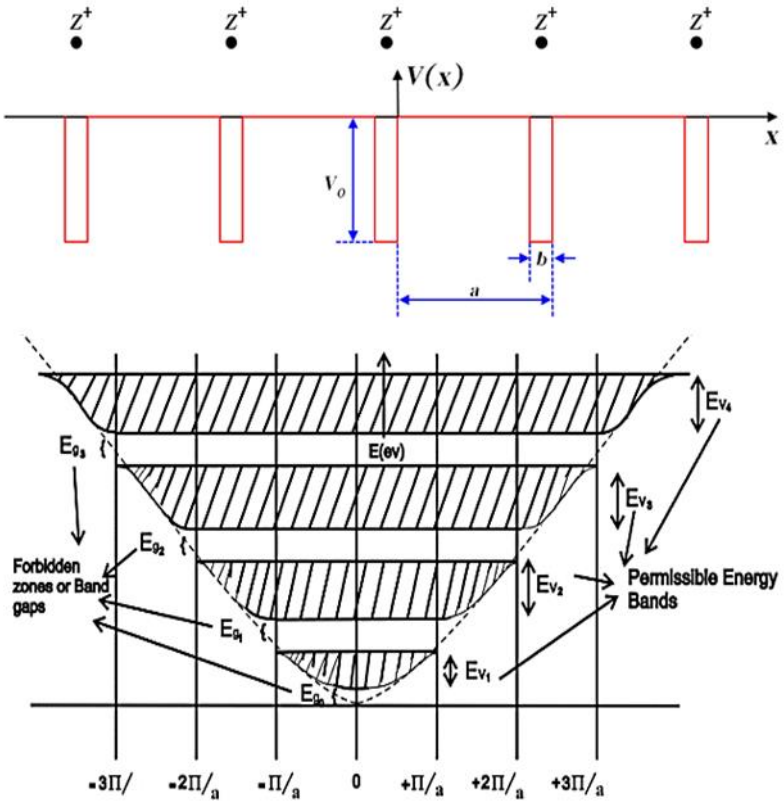

Figure 1.4. Model of periodic energy barrier of quantum physics (upper) and energy band structure calculated by Bloch equation. (under) [5]

1.3 Experimental approaches for band gap engineering of graphene.

1.3.1 Graphene nanoribbon

Graphene nanoribbon (GNR) with a width of a nanometer tested owing to their feasible synthesis methods. [6, 7] GNR can be synthesized either top-down starting from graphite, graphene or carbon nanotubes or bottom-up using molecular precursors.

Top-down fabrication processes can be realized by unzipping graphene or carbon nanotubes. X. L. Li et al developed chemical route for producing GNRs with a width of less than 10 nanometres, [8] which obtain single ribbons with various nanometer widths with dispersed state (**Figure 1.5**(a)) in solvents and showed well-defined zigzag or armchair edge structures. The bandgaps determined from experimental data for various GNRs are plotted *versus* the ribbon width in **Figure 1.5**(c). L. Y. Jiao et al developed another approach for obtaining GNRs by unzipping multiwalled carbon nanotubes by plasma etching at partly embedded in a polymer film. [9] The GNRs had smooth edges and a narrow width distribution (mostly 10–20 nm) (**Figure 1.5**(d). Moreover, D. V. Kosynkin et al established a simple solution-based oxidative process for lengthwise cutting and unravelling of carbon nanotube sidewalls, (**Figure 1.6**(a-c)) [10] which showed the presence of shortened single-atom layers.

In addition to top-down processes, GNRs can be chemically obtained by bottom-up by assembly of molecular precursors. A simple method for the production of atomically precise armchair GNRs uses the surface-assisted coupling of molecular precursors to linear polyphenylenes and their subsequent cyclodehydrogenation developed by J. M. Cai et al. [11] Chen et al. also developed a bottom-up synthesis by fusing segments made from two different molecular precursor to obtain GNR heterojunctions. [12] which shows the

possibility of bandgap engineering with the result of calculations of the electronic structure of 7–13 GNR heterojunctions..

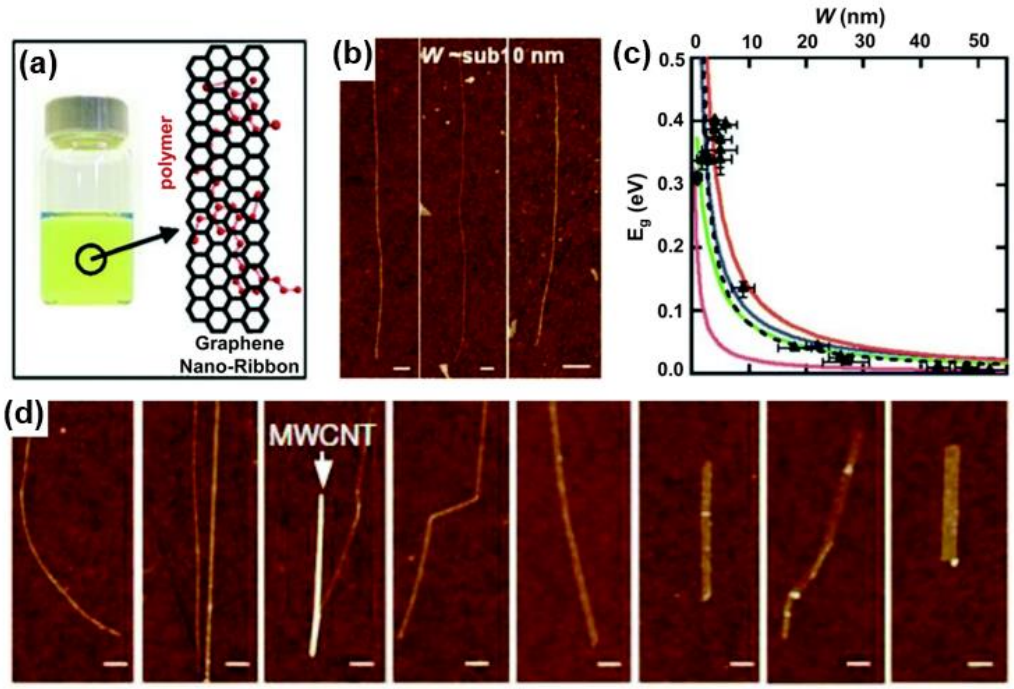

Figure 1.5 (a) (left) poly(*m*-phenylenevinylene-*co*-2,5-dioctoxy-*p*-phenylenevinylene) (PmPV) in 1,2-dichloroethane (DCE) with graphene nanoribbons (GNRs) stably suspended in the solution. (right) Schematic diagram of a graphene nanoribbon with adsorbed two units of a PmPV polymer chain. (b) AFM images of selected GNRs with widths in the sub-10 nm region. (scale bars 100 nm). (c) Bandgaps determined from experimental data (symbols) for various GNRs *versus* the ribbon width. [8] (d) Single- or few-layer GNRs of different widths and heights. (scale bars 100 nm). [9]

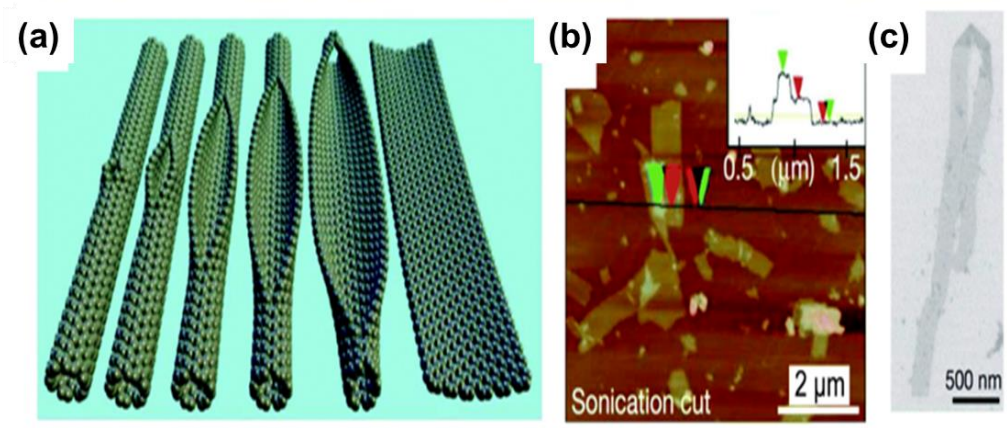

Figure 1.6 (a) Representation of the gradual unzipping of one wall of a carbon nanotube to form a nanoribbon. (b) AFM image of GNRs nanoribbons with generally single-layered. (c) Scanning electron microscopy (SEM) image of single-layer nanoribbon. [10]

1.3.2 Graphene quantum dot

By the confinement to 0D, GQDs are another form of graphene derivatives that has taken attention because of its unique optical and electronic properties. [13-16] Ritter *et al.* succeed to investigate the local electronic structure of GQDs with ultrahigh-vacuum STM and revealed that structure of the graphene edges significantly influences the electronic properties of nanometre-sized graphene (**Figure. 1.7**(a)) [13] They experimentally found the relationship between the bandgap (E_g) and size for GQDs and correlated the E_g measurements with the edge structure of the GQDs. The correlation between the electronic properties of GQDs and their atomic structure, as well as their lateral size, has been studied (**Figure. 1.7**(b)).[14] Triangular (**Figure. 1.7**(c)), parallelogram-shaped and hexagonal GODs with lateral dimensions of 5 nm and 10 nm were found to exhibit band gaps of 0.8 eV, 0.6 eV, 0.4 eV and 0.25 eV, respectively. The bandgap of GQDs increases by a decrement of their lateral size with the relationship E_g (eV) = 1.77 ± 0.12 eV nm/$L^{0.9\pm0.1}$, showed similar result to the trend of E_g (eV) = 1.68 eV nm/L predicted from quantum confinement. [17]

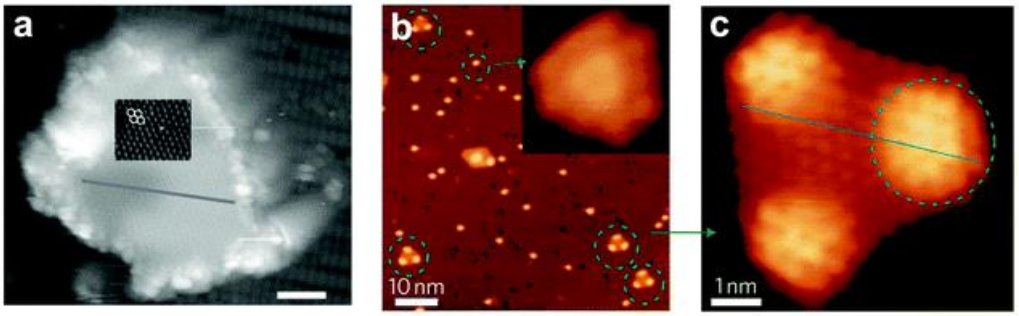

Figure 1.7. (a) STM topographic and (inset) topographic derivative images of a graphene quantum dot (GQD) with lateral dimensions of ≈7 nm exhibiting triangular lattice symmetry. A white hexagonal lattice is overlaid on the derivative image to highlight the orientation of the C lattice. Scale bar: 2 nm. [13]. (b) Sample of 0.08 monolayer (ML) C_{60}/Ru after being annealed at 725 K for 2 min. Inset: Magnified view of mushroom-shaped dots. (c) Magnified view of triangular (2.7 nm) GQDs. [14]

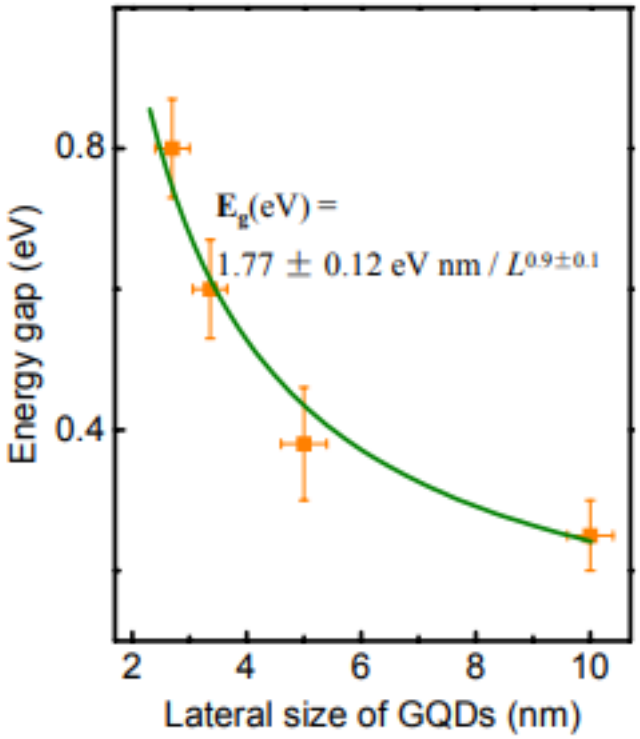

Figure 1.8 Band gap of Triangular, parallelogram-shaped, and hexagonal GQD. [14]

1.3.3 Few-layer graphene

When an external electric field is applied, bandgap arises in few-layer graphene (**Figure 1.9**(a–c)) and the stacking order showed an important role. [18-20] A potential topological phase transition and the emergence of valley- and spin-polarized edge states are also associated.

Castro *et al.* firstly showed field-induced bandgap in bilayer graphene. [18] The device was biased chemically, and then the voltage V_g was swept through the charge neutrality point (CNP).[21] Oostinga et.al. did low-temperature transport measurements in dual-gated monolayer and bilayer graphene and showed the displacement of biased electric field results in the increment of CNP peak resistance in bilayer graphene. [22]

Different stacking orders result in distinctive features. An experimentally resolvable field-induced bandgap has only been observed in Bernal-BLG and r-TLG,[18, 20] owing to the difference in electrostatic potential between the two sublattices in the first and second layers. [21]. This phenomena can be explained by 'chiral model' and this model can predict bandgap opening in *N*-layer ABC stacked graphene. [23] In spite of the monotonic increase in the bandgap saturation of the bandgap was reported in high displacement fields ($D \approx 3$ V nm^{-1}). [23, 24]

Avetisyan *et al.* summarized the dependence of bandgaps on the stacking order, layer number and bias potential in few-layer graphene using self-consistent tight-binding calculations. [25, 26] This results also shown in ABA and ABC stacked multilayer graphene (from $N = 3$ to $N = 20$) tested by Koshino *et al*. [27]

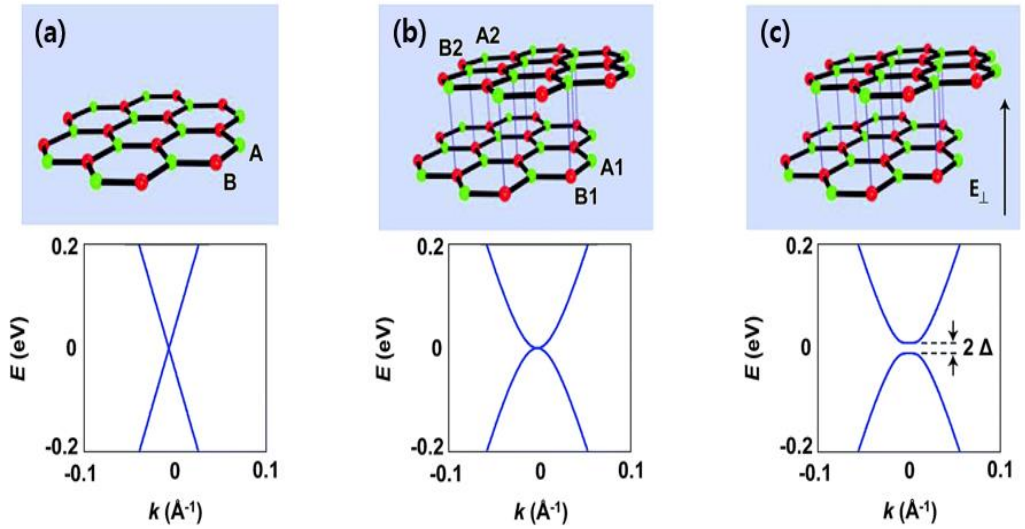

Figure 1.9 Schematic diagrams and band structures of (a) monolayer graphene, (b) bilayer graphene and (c) bilayer graphene in an external electric field. [22]

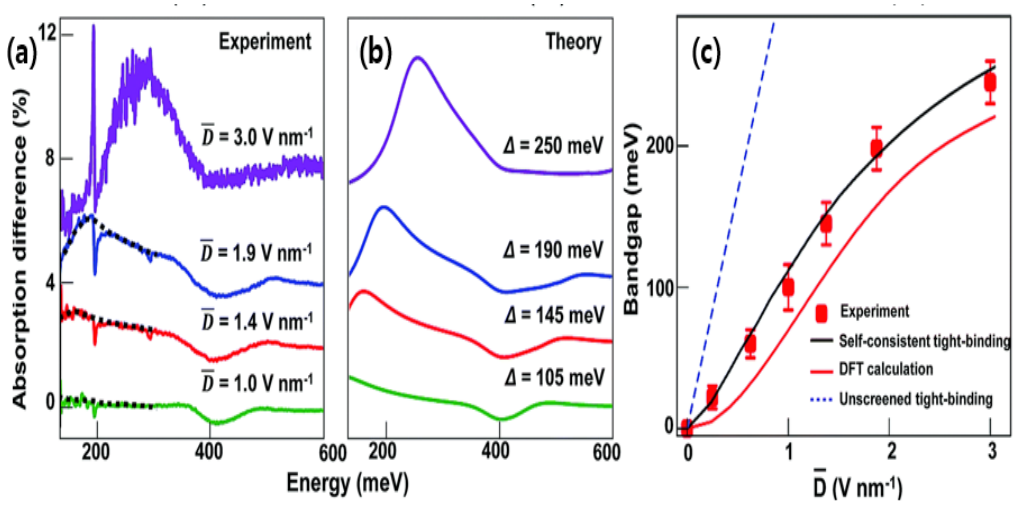

Figure 1.10 (a) Experimental and (b) calculated gate-induced infrared absorption spectra at the charge neutrality point for different applied displacement fields *D*. (c) Experimentally determined gap values (red squares) compared with theoretical predictions based on self-consistent tight-binding (black trace), *ab initio* density functional theory (red trace) and unscreened tight-binding calculations (blue dashed trace). [19]

1.3.4 Heteroatom doped graphene

Doping is an effective way for engineering the band gap of graphene and [28-32] lots of work has been carried out to study the electronic properties of Boron and Nitrogen doped graphene. [28-32] An efficient method for the large-scale preparation of N-doped graphene with *s*-triazine molecules was developed and bandgap of 300 meV induced by a graphitic nitrogen content of 0.4 atom% has been detected. [33] As well as B- or N-doped graphene, B/N-co-doped graphene (**Figure 1.11**(a)) also studied and [34] bandgaps in the doping configuration shown in **Figure 1.11**(a) exhibit a non-linear dependence on the concentration of BN domains. But linear relationship between the bandgap value and dopant concentration can be found with a small concavity. (**Figure 1.11**(b)) It was found that the size of the bandgap is mainly determined by the width of the carbon wall between neighbouring BN QDs. Ci et. al. developed way of preparing large-area atomic layers of h-BNC materials by a thermal catalytic CVD method [32] and showed bandgaps of 1.62 eV and 1.51 eV for samples with 65 atom% C and 84 atom% C. More recently, Chang et. al. prepared BN-doped graphene films with a bandgap of as large as 600 meV grown by a low-pressure CVD and the band gap increased monotonically with the BN concentration in a low-doped sample (**Figure 1.12**). [35] This bandgap opening in BN-doped graphene is attributed to breaking of the inherent equivalence of graphene sublattices.

In addition to B and/or N atoms (2p elements), other atomic dopants such as 3p elements (Si, Al, S, or P) and other elements (Ag) are also tried to doped to graphene. [36] P-doped graphene with a dopant content of 3 atom% showed the bandgap of 0.67 eV. Furthermore, when two carbon atoms are replaced by one 2p atom (B, N, or O) and one 3p atom (Al, Si, P or S), the bandgap computed at the Heyd–Scuseria–Ernzerhof level is smaller than monodoped graphene. [37]

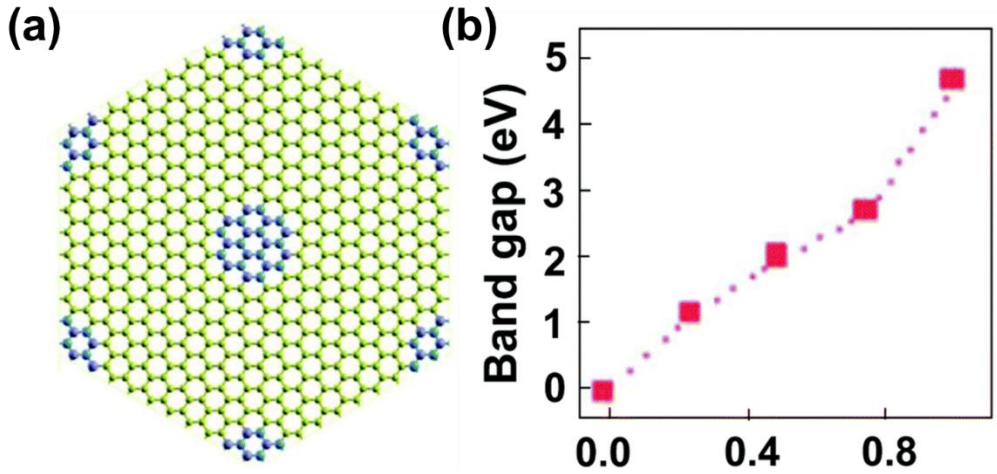

Figure 1.11 (a) Schematic diagram of a 10 × 10 unit cell of graphene doped with $(BN)_{12}$. (b) Calculated bandgap of BN-doped graphene in a 2 × 2 unit cell plotted as a function of the BN dopant concentration. [34]

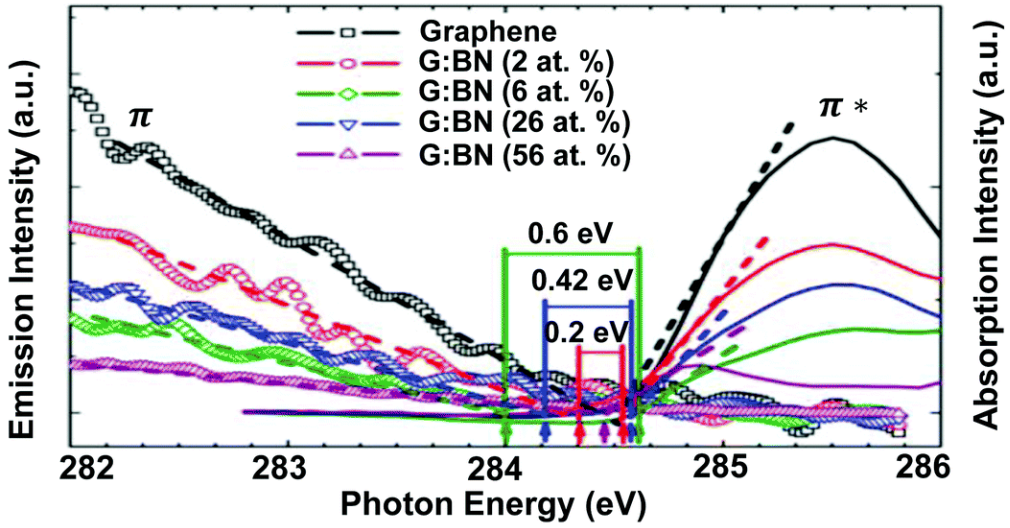

Figure 1.12 Magnified π–π* regions of selected normalized C K-edge X-ray absorption near-edge structure (XANES) and K_α X-ray emission (XES) spectra of pristine graphene and BNG films (left side, XES; right side, XANES) with various concentrations of BN dopant. [35]

1.4 Probable issues

1.4.1 Limitation of scale-up production of physically modified graphene.

Preparation of graphene derivatives with high band gap based on the physical modification succeed to enlarge band gap, however there are many limitations to use them in real application fields by many technical issues. One of the representative issue is limitation of scale up production.

Bi-layer graphene, which is produced by chemical vapor deposition (CVD) or Epitaxial, shows high price for mass production. [1] Plus, formation of uniformly layered graphene by those method are still remained as big huddle. Takesaki et. Al, developed method that preparing high ratio of bi-layer graphene (~93%), but 7% of graphene are exited as single and tri-layered state, and AB staked graphene and twisted structure are co-existed. [38] (**Figure 1.13** (a-e)) And this kind of graphene shows band gap under the high electrical field, usable area of it are limited.

In the case of graphene nanoribbons (GNRs), produced by unzipping by chemical route and self assembly, the low yield of production method are remained big huddle. [6] In addition, the regularity of size is not secured and GNRs with standardized band gap is difficult. Timothy et. al. developed large scale solution synthesis using self assembly, but the length and width is not standardized (**Figure 1.14** (a-c)). [39] Considering band gap of GNRs are decided by the aspect ratio, this is an huge limitation for applicate to GNR based devices.

Graphene quantum dots (GQDs) has similar limitations with GNRs because the preparation method is quite similar to GNRs.[15, 16] Therefore, problem of regularity of size is remained. Tang et. al. developed small sized GQDs with large band gap of 4.1eV, but it's size of range from 2.9 - 4 nm. In the case of GQDs, band gap is differed by small change of size, and this can be remained as issue for applications. [40] (**Figure 1.16 (**a-h**)**)

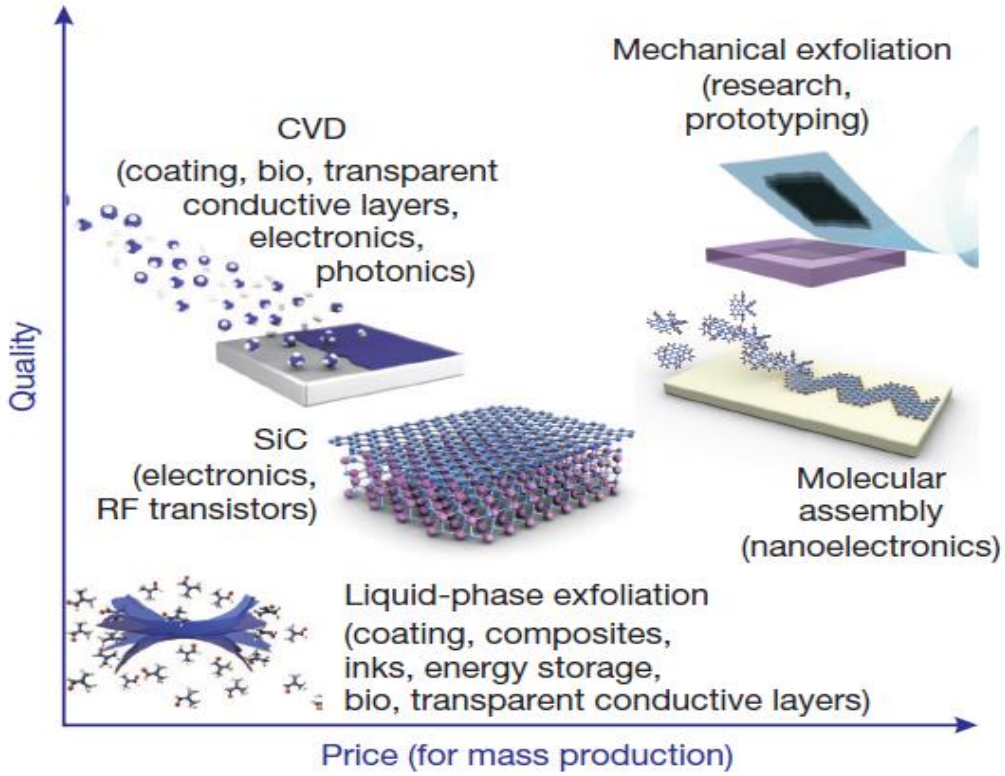

Figure 1.13 Compartment of quality and price for mass production of various methodology for preparing graphene. [2]

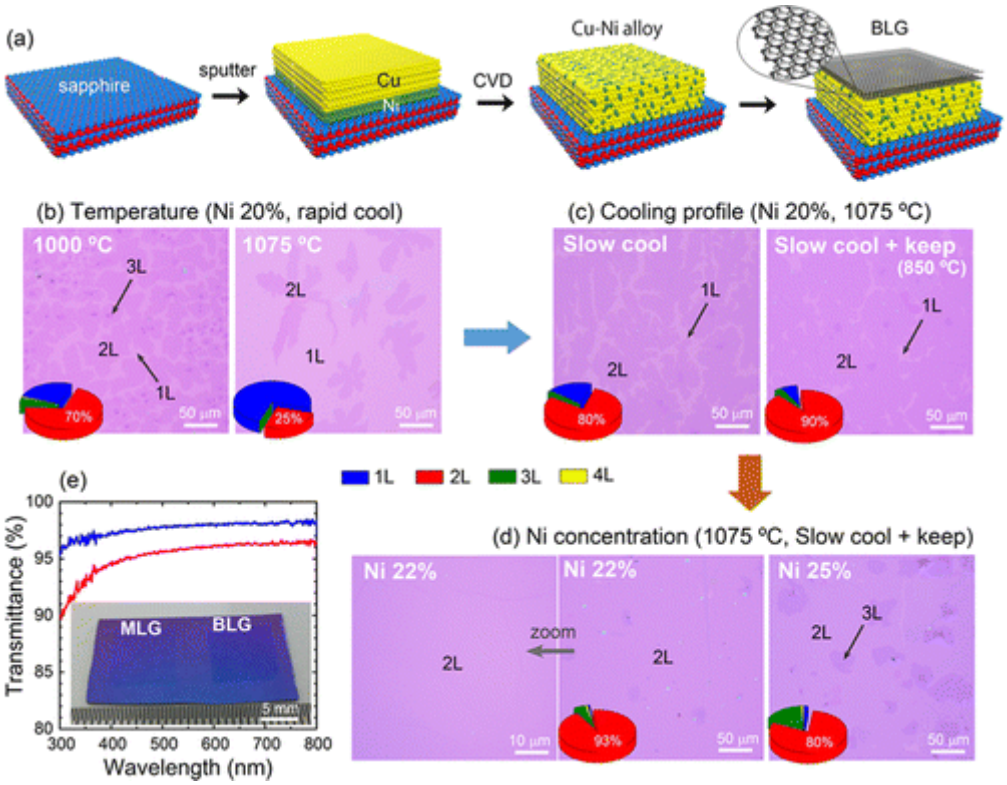

Figure 1.14 (a) Schematics of the CVD growth of uniform bilayer graphene over a Cu–Ni alloy film deposited on a sapphire c-plane substrate. (b–d) Optical microscope images of graphene transferred on SiO_2/Si substrates grown under different CVD conditions. (e) Optical transmission spectra of bi-layered graphene (red curve, Ni-22%/Cu-78%) and mono-layered graphene (blue curve, pure Cu) transferred on quartz substrates. Inset shows the photograph of the samples on a SiO_2/Si substrate [38]

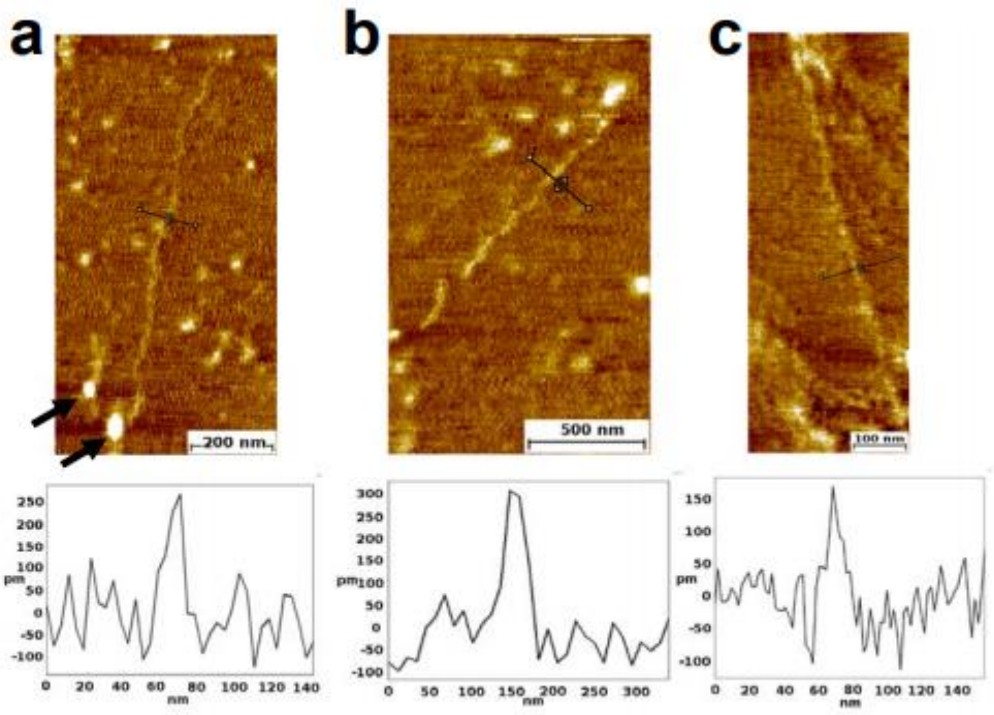

Figure 1.15 AFM images of GNRs on mica and corresponding height profiles along the black lines. [39]

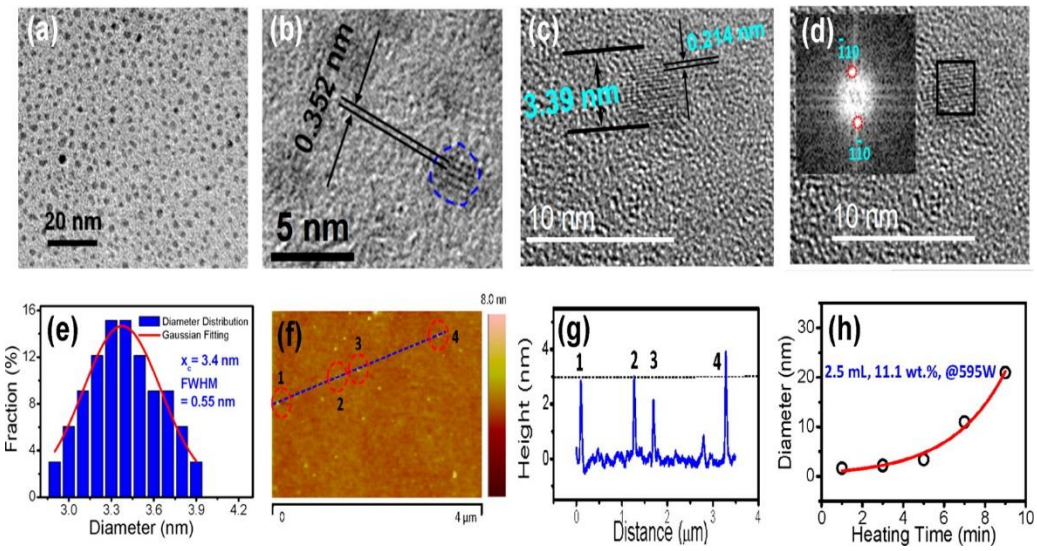

Figure 1.16. (a) TEM image of the GQDs and (b) the HRTEM image of the GQDs; (c) a typical single GQD, the size and its lattice parameter are 3.39 and 0.214 nm, respectively; (d) HRTEM image of a typical single GQD, and its corresponding selected area FFT image (inset); (e) the diameter distribution of the GQDs, the red line is the Gaussian fitting curve; (f) AFM image of the GQDs; (g) the height distribution of the GQDs as shown in AFM image f; (h) the GQDs diameter dependent on heating time. The GQDs were prepared using 11.1 wt % glucose solution and 5 min (except for panel h) microwave heating at 595 W. [40]

1.4.2 Limited Range of generated band gap of resultant graphene after heteroatom doping.

In case of heteroatom doped graphene, there are various preparation routes because of graphene from CVD, mechanical and chemical exfoliation, and bottom up synthesis. [15, 16] Heteroatoms can be chemically bonded to graphene by plasma, ball billing, and chemical reactions. However, except the case of graphene oxide, which is generated by chemical exfoliation of graphite by oxidation, any graphene failed to highly degree of doping over 20 at.% [15] and there are limitation of enlargement of band gap because heteroatoms prefers to bonded to defected carbon of graphene which has higher activation energy. (**Figure 1.17**) [41] Tang et al. tried to achieve highly boron doped graphene by plasma treatment for the use of transistor, but boron cannot be doped over 15 at.% in spite of treatment time over 20 minute and showed low on/off ratio of 10^2. (**Figure 1.18**) [42] This result implies that usage of graphene oxide based graphene is essential to get highly doped graphene.

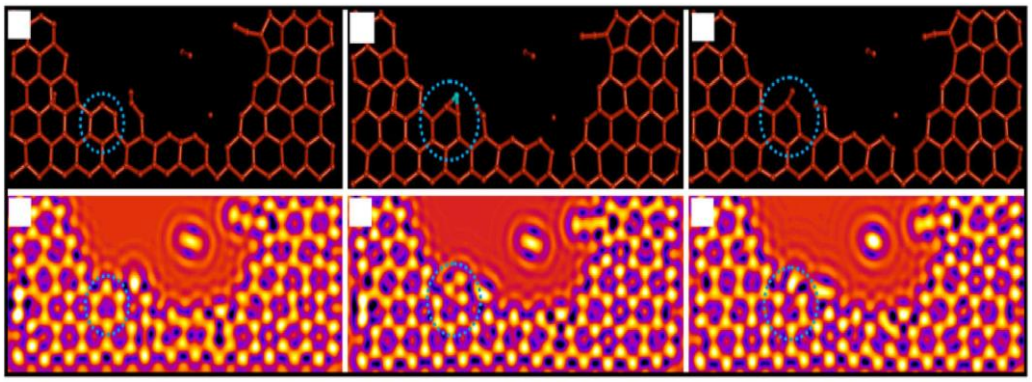

Figure 1.17 Simulated bonding of foreign atoms and real bonding of Oxygen atoms bonded to graphene using STM [41]

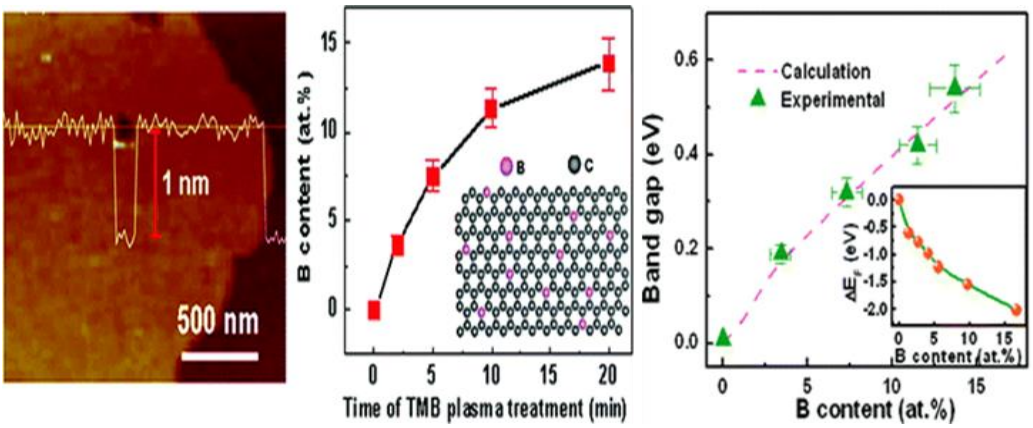

Figure 1.18 (a) Typical AFM image of the reacted graphene (b) dependence of the B content on the ion reaction time measured by the secondary ion mass spectroscopy. (c) Experimental band gaps and corresponding calculation results of B-doped graphenes versus B content for various FETs. Inset: dependence of doping level (the position of the Fermi level from the Dirac point) on the content of substitutional B. [42]

1.5 Advantage of graphene oxide based graphene

1.5.1 Easy preparation

Graphene oxide (GO) based graphene, named as reduced graphene oxide (RGO), are prepared from the chemical exfoliation of graphite by oxidation. After thermal, chemical, and electrochemical method, graphene oxide is reduced turns into RGO. (**Figure 1.19**) [43-45] This preparation route of graphene shows higher yield than any other preparation route because of simple oxidation and reduction method. [1, 45]

Method of chemical exfoliation of graphite is studied by Brodie, Staudenmaier, and Hummers. [44, 45] Especially method developed by Hummers (**Figure 1.20**) shows highest yield of production with easy method and mostly used. [43, 45] In addition, the resultant graphene oxide has high dispersiblity in water and it can use to solution based process for various applications.(**Figure 1.21**) [46]

Graphene oxide is easily reduced by heat, chemicals, microwaves, and electrochemical stimulus. [43, 44]The physical and chemical characteristics of resulting graphene vary considerably with the reduction conditions and methods [43, 47-51] Especially, oxygen functional groups attached to graphene layer can be controlled by reduction degree and it is easy to control band gap by dangled oxygen heteroatoms.

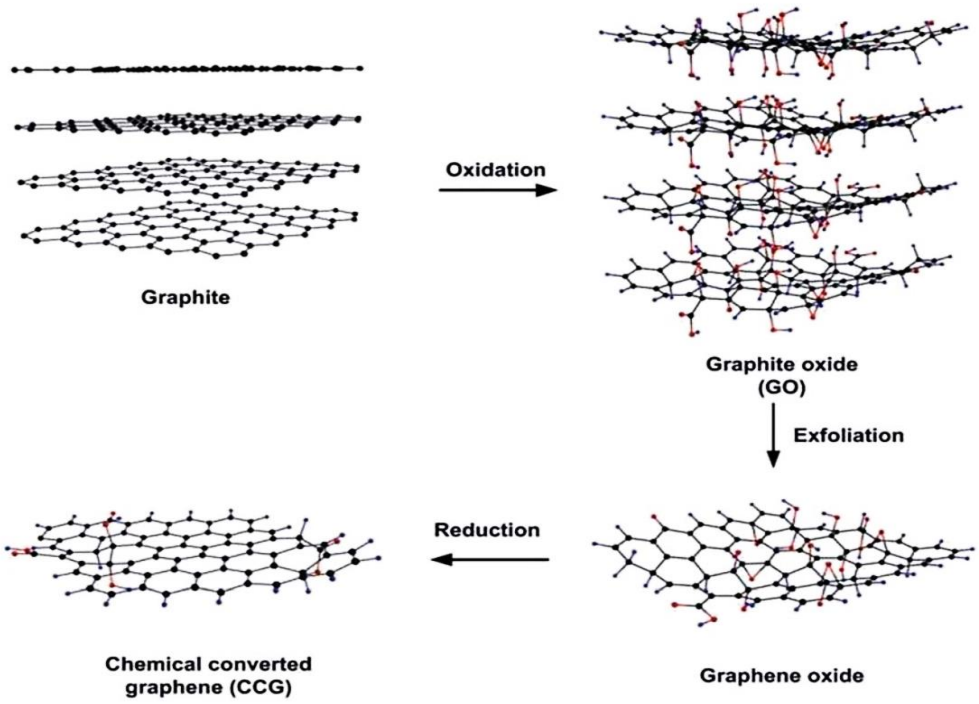

Figure 1.19 Preparation route of RGO from chemical exfoliation of graphite. [44]

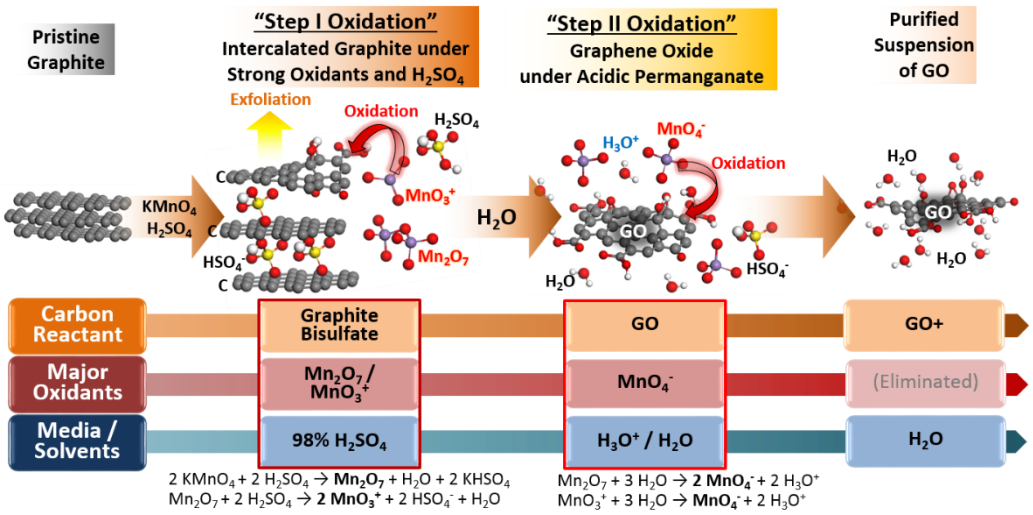

Figure 1.20 Oxidation mechanism of graphene by Hummers method. [45]

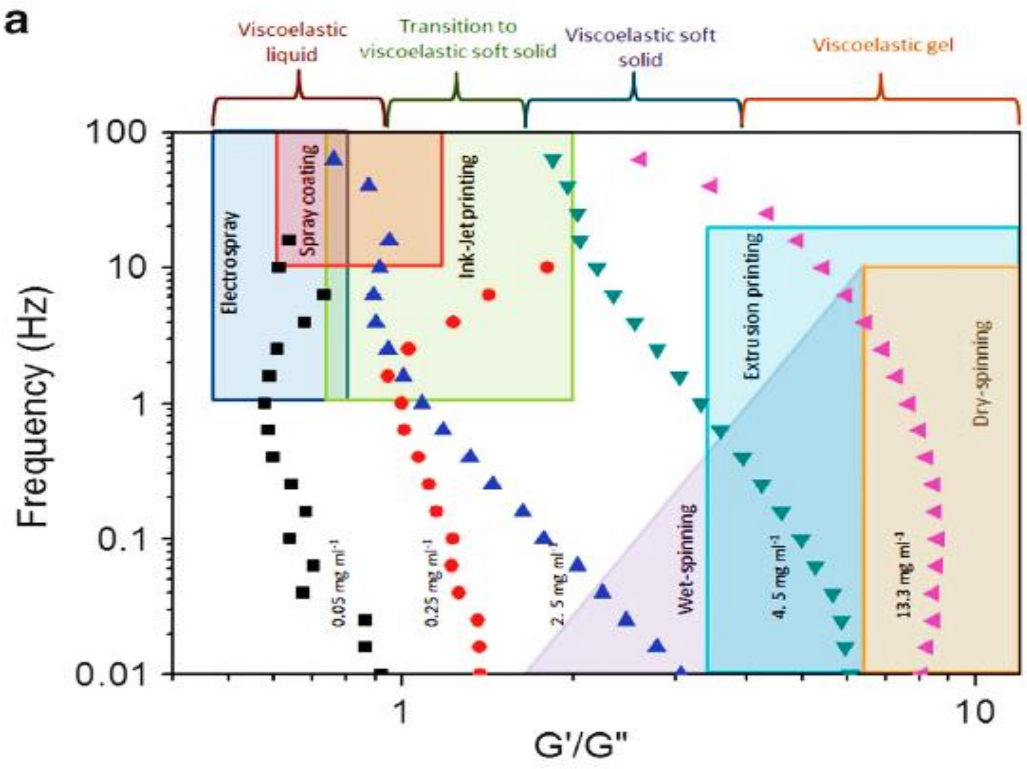

Figure 1.21 Possible ink based process by concentration of GO ink. [46]

1.5.2 Large tunable band gap range

By oxidation of graphene by chemical oxidation, various functional group is generated and dangled to graphene layer. Therefore, oxygen doping of graphene is generated. The amount of oxygen atom attached to graphene layer can be reached around 50 at.% and highly doped graphene can be generated. [44, 52] By the ease of highly doping, band gap of graphene enlarged to around 3.0eV, enables to large tunable band gap range by controlling oxidation degree. Yeh et. al. GO prepared by different oxidation time showed differed band gap by amount of oxygenated functional groups. [53] (**Figure 1.22**)

By reduction process, band gap also can be controlled by degree of reduction because amount of oxygenated functional group can be controlled by reduction process. Velasco-Soto et. al. tried to control reduction degree with various reduction agents and reduction time, and showed that band gap of RGO can be controlled by the reduction degree. [54] (**Figure 1.23**)

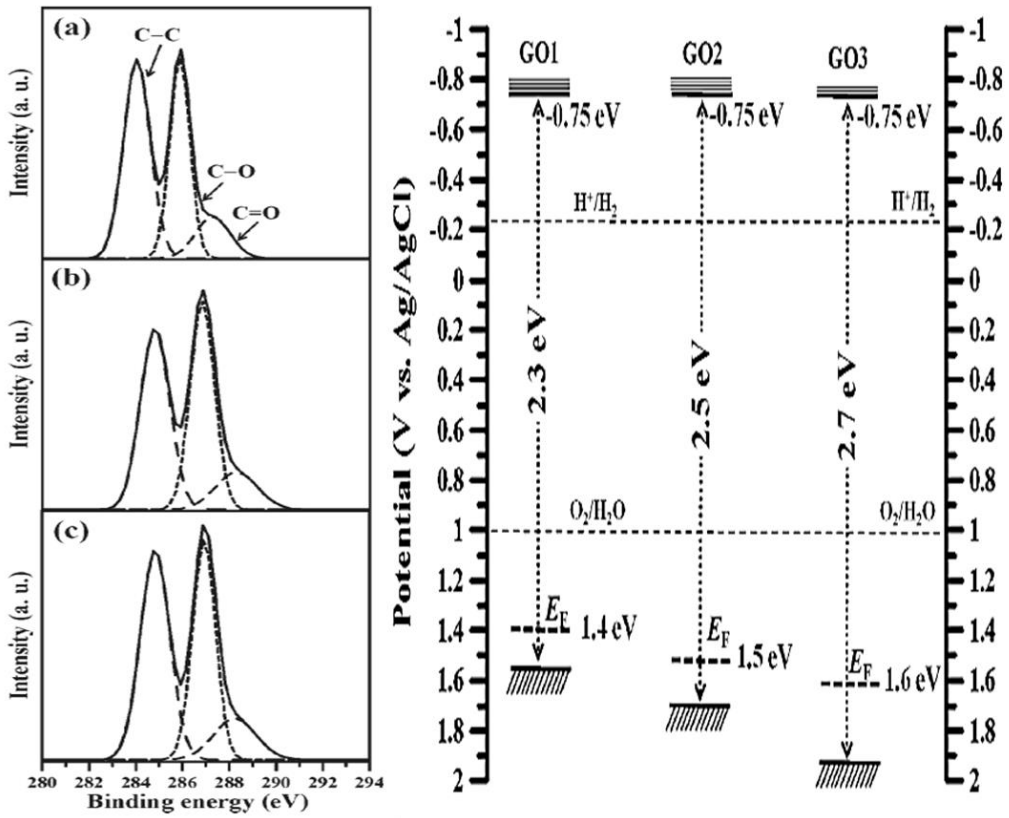

Figure 1.22 Band gap of GO by different oxidation degree. [53]

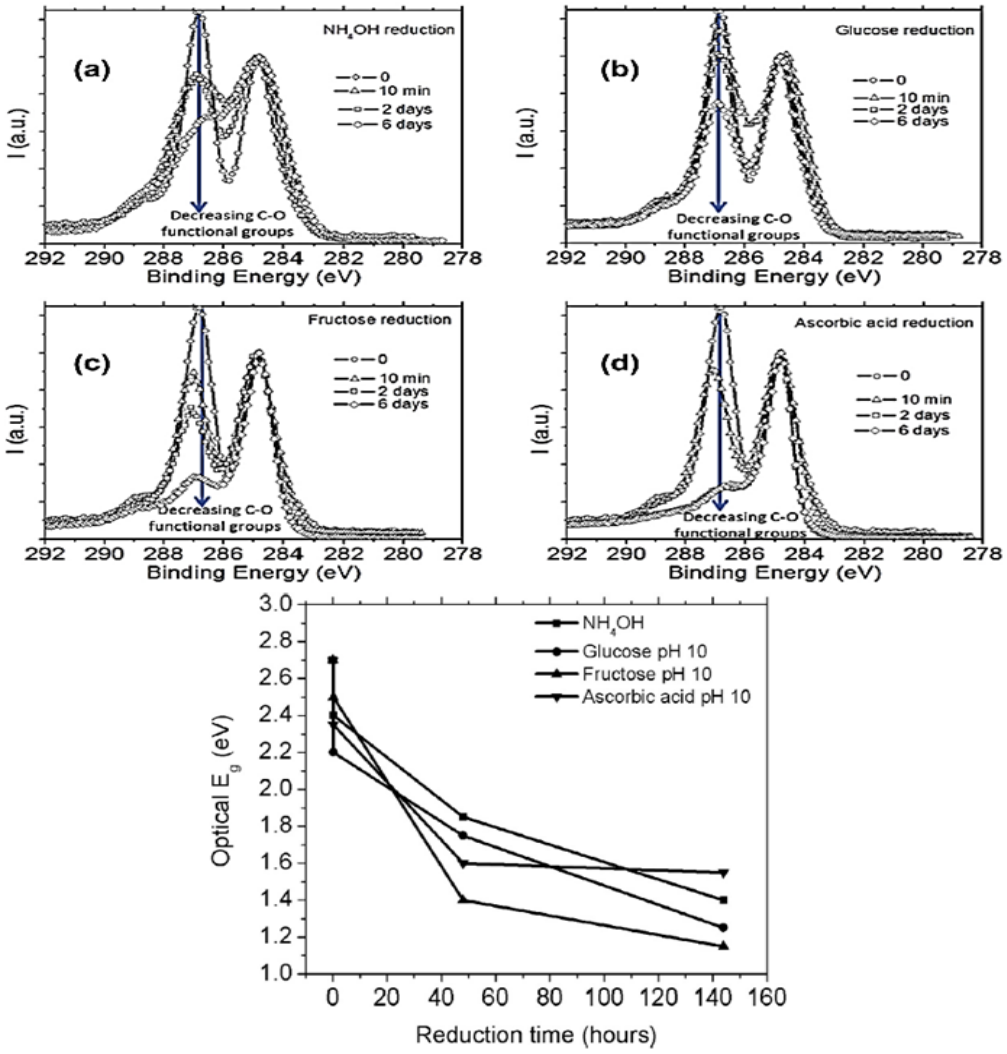

Figure 1.23 Band gap of RGO by different reduction degree by various reduction agent. [54]

1.6 Aim and scope of this research

1.6.1 Finding controllable parameters for band gap Engineering of graphene oxide based graphene

In case of RGO from GO, band gap enlargement by the amount of oxygenated functional groups has been widely studied because it showed the possibility of band gap engineering of graphene which can be directly used to application field because of its ease of preparation. Therefore, many researchers tried to simulate band gap of oxygenated graphene by theoretical calculation by controlling the amount of functional group. [55-62] Many experimental studies followed this point of view and tried to find the relationship between amount of oxygen dangled to graphene and band gap of graphene oxide based graphene. [53, 54, 60, 63-65] However, when colligate the result of theoretical and experimental result, the trend of enlargement of band gap by ration of oxygen atom is different as shown in **Figure 1.24**.

This indicates that the hidden parameters that control the band gap of graphene oxide based graphene and it should be found clearly for the fine band gap tuning. In this research, band gap enlargement of graphene is studied based on carbon, not oxygen, and tried to find the relationship between sp^2 carbon and band gap of RGO by colligate the calculation and experimental results in Chapter 2.

In addition, in chapter 4, band gap engineered graphene fitted to conductive range is tried to applicate in graphene based conductive ink. Band gap of RGO is decreased by the reduced amount of defect by the use of edge selectively oxidized graphene during minimize oxidation degree of basal plane by controlled preparation process of GO.

In chapter 5, we tried to use band gap engineered graphene to semiconductive range to nitrogen dioxide (NO_2) gas sensing. Considering epoxide group has low absorbability to NO_2 gas, we tried to decrease band gap of GO selectively reduce

of epoxide group with modified preparation method of GO in order to prepare NO_2 gas sensing materials with high sensitivity.

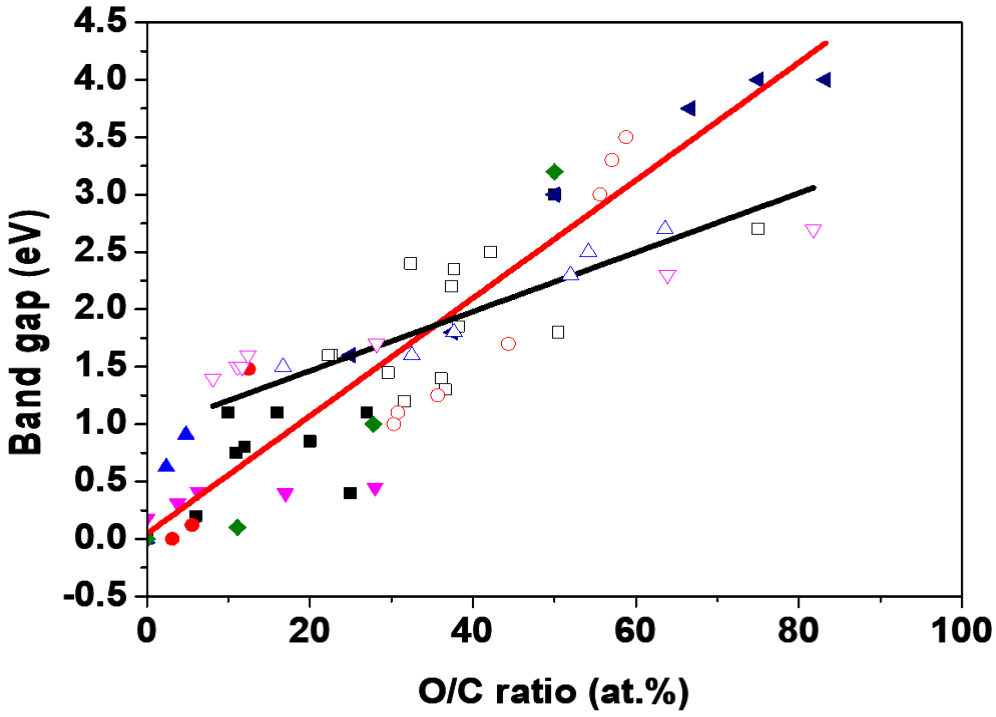

Figure 1.24 Colligated calculation and experimental result of band gap by differed ratio of oxygen atoms. [53-65]

1.6.2 Finding effect of graphene oxide based graphene to graphene embedded materials

GO showed high dispersity in various solvents, many researchers tried to produce composite with GO and other materials in order to enhance electrical transport in various application area after thermal reduction. [66-71] When other materials are embedding RGO showed different band gap compared to graphene is not exist. However, when calculating band gap of RGO embedded materials, the band gap of graphene does not considered as shown in **Figure 1.25** [72] and this disturbs the right estimation of RGO embedded materials. By the preparation method, band gap of RGO is differed and it should be considered when calculating band gap of RGO embedded materials. Therefore, we tried to estimate to RGO embedded materials in this research based on the engineered band gap by sp^2 carbon with colligated calculation and experiment data in Chapter 3.

Plus in Chapter 6, band gap engineered RGO embedded indium-gallium-zinc oxide (IGZO) by controlled the amount of RGO was tried to use to thin film transistor (TFT). During the heat treatment, IGZO / RGO composite can get pore by released gas by reduction of GO, and we tried to get low porous IGZO / RGO composite by using less oxidized GO and enhance the electrical transport if band gap engineered RGO embedded IGZO.

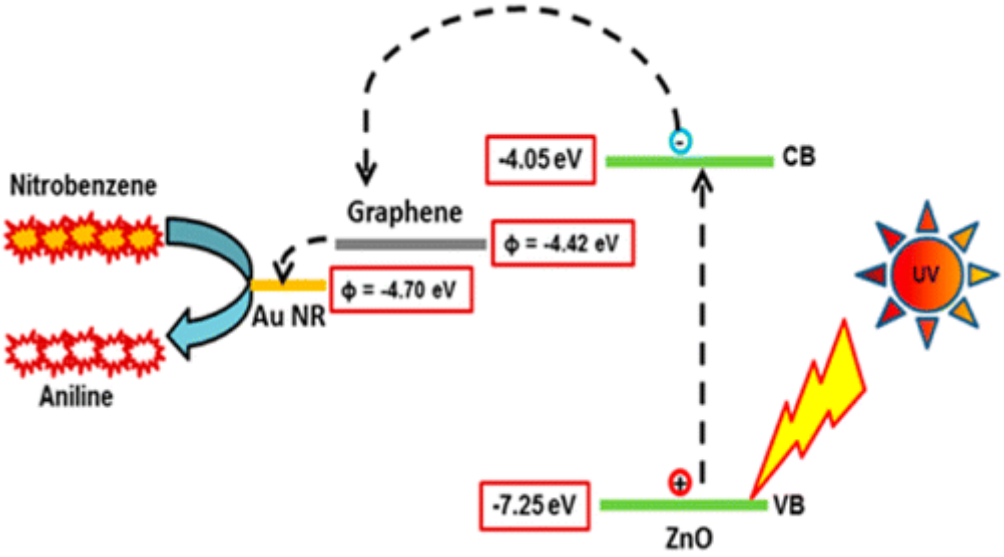

Figure 1.25 Energy diagram of ZnO/RGO suggested by former research. [72]

1.7 Reference

[1] K.S. Novoselov, V.I. Fal′ko, L. Colombo, P.R. Gellert, M.G. Schwab, K. Kim, A roadmap for graphene, Nature 490(7419) (2012) 192-200.

[2] A. Zurutuza, C. Marinelli, Challenges and opportunities in graphene commercialization, Nature Nanotechnology 9(10) (2014) 730-734.

[3] P.R. Wallace, The Band Theory of Graphite, Physical Review 71(9) (1947) 622-634.

[4] M. Kuno, Introductory nanoscience: Physical and chemical concepts, MRS Bulletin 37(2) (2012) 169-170.

[5] R.E. Hummel, Electronic Properties of Materials, Springer New York2011.

[6] J.M. Marmolejo-Tejada, J. Velasco-Medina, Review on graphene nanoribbon devices for logic applications, Microelectronics Journal 48 (2016) 18-38.

[7] S. Dutta, S.K. Pati, Novel properties of graphene nanoribbons: a review, Journal of Materials Chemistry 20(38) (2010) 8207-8223.

[8] X. Li, X. Wang, L. Zhang, S. Lee, H. Dai, Chemically Derived, Ultrasmooth Graphene Nanoribbon Semiconductors, 319(5867) (2008) 1229-1232.

[9] L. Jiao, L. Zhang, X. Wang, G. Diankov, H. Dai, Narrow graphene nanoribbons from carbon nanotubes, Nature 458(7240) (2009) 877-880.

[10] D.V. Kosynkin, A.L. Higginbotham, A. Sinitskii, J.R. Lomeda, A. Dimiev, B.K. Price, J.M. Tour, Longitudinal unzipping of carbon nanotubes to form graphene nanoribbons, Nature 458(7240) (2009) 872-876.

[11] J. Cai, P. Ruffieux, R. Jaafar, M. Bieri, T. Braun, S. Blankenburg, M. Muoth, A.P. Seitsonen, M. Saleh, X. Feng, K. Müllen, R. Fasel, Atomically precise bottom-up fabrication of graphene nanoribbons, Nature 466(7305) (2010) 470-473.

[12] Y.-C. Chen, T. Cao, C. Chen, Z. Pedramrazi, D. Haberer, D.G. de Oteyza, F.R. Fischer, S.G. Louie, M.F. Crommie, Molecular bandgap engineering of

bottom-up synthesized graphene nanoribbon heterojunctions, Nature Nanotechnology 10(2) (2015) 156-160.
[13] K.A. Ritter, J.W. Lyding, The influence of edge structure on the electronic properties of graphene quantum dots and nanoribbons, Nature Materials 8(3) (2009) 235-242.
[14] J. Lu, P.S.E. Yeo, C.K. Gan, P. Wu, K.P. Loh, Transforming C60 molecules into graphene quantum dots, Nature Nanotechnology 6(4) (2011) 247-252.
[15] H. Li, Z. Kang, Y. Liu, S.-T. Lee, Carbon nanodots: synthesis, properties and applications, Journal of Materials Chemistry 22(46) (2012) 24230-24253.
[16] P. Tian, L. Tang, K.S. Teng, S.P. Lau, Graphene quantum dots from chemistry to applications, Materials Today Chemistry 10 (2018) 221-258.
[17] C. Berger, Z. Song, X. Li, X. Wu, N. Brown, C. Naud, D. Mayou, T. Li, J. Hass, A.N. Marchenkov, E.H. Conrad, P.N. First, W.A. de Heer, Electronic Confinement and Coherence in Patterned Epitaxial Graphene, 312(5777) (2006) 1191-1196.
[18] E.V. Castro, K.S. Novoselov, S.V. Morozov, N.M.R. Peres, J.M.B.L. dos Santos, J. Nilsson, F. Guinea, A.K. Geim, A.H.C. Neto, Biased Bilayer Graphene: Semiconductor with a Gap Tunable by the Electric Field Effect, Physical Review Letters 99(21) (2007) 216802.
[19] Y. Zhang, T.-T. Tang, C. Girit, Z. Hao, M.C. Martin, A. Zettl, M.F. Crommie, Y.R. Shen, F. Wang, Direct observation of a widely tunable bandgap in bilayer graphene, Nature 459(7248) (2009) 820-823.
[20] C.H. Lui, Z. Li, K.F. Mak, E. Cappelluti, T.F. Heinz, Observation of an electrically tunable band gap in trilayer graphene, Nature Physics 7(12) (2011) 944-947.
[21] E. McCann, Asymmetry gap in the electronic band structure of bilayer graphene, Physical Review B 74(16) (2006) 161403.
[22] J.B. Oostinga, H.B. Heersche, X. Liu, A.F. Morpurgo, L.M.K. Vandersypen,

Gate-induced insulating state in bilayer graphene devices, Nature Materials 7(2) (2008) 151-157.
[23] F. Zhang, B. Sahu, H. Min, A.H. MacDonald, Band structure of ABC-stacked graphene trilayers, Physical Review B 82(3) (2010) 035409.
[24] K. Zou, F. Zhang, C. Clapp, A.H. MacDonald, J. Zhu, Transport Studies of Dual-Gated ABC and ABA Trilayer Graphene: Band Gap Opening and Band Structure Tuning in Very Large Perpendicular Electric Fields, Nano Letters 13(2) (2013) 369-373.
[25] A.A. Avetisyan, B. Partoens, F.M. Peeters, Electric-field control of the band gap and Fermi energy in graphene multilayers by top and back gates, Physical Review B 80(19) (2009) 195401.
[26] A.A. Avetisyan, B. Partoens, F.M. Peeters, Stacking order dependent electric field tuning of the band gap in graphene multilayers, Physical Review B 81(11) (2010) 115432.
[27] M. Koshino, Interlayer screening effect in graphene multilayers with ABA and ABC stacking, Physical Review B 81(12) (2010) 125304.
[28] A. Lherbier, X. Blase, Y.-M. Niquet, F. Triozon, S. Roche, Charge Transport in Chemically Doped 2D Graphene, Physical Review Letters 101(3) (2008) 036808.
[29] A.Y. Liu, R.M. Wentzcovitch, M.L. Cohen, Atomic arrangement and electronic structure of ${\mathrm{BC}}_{2}$N, Physical Review B 39(3) (1989) 1760-1765.
[30] Y. Miyamoto, A. Rubio, M.L. Cohen, S.G. Louie, Chiral tubules of hexagonal ${\mathrm{BC}}_{2}$N, Physical Review B 50(7) (1994) 4976-4979.
[31] X. Wang, X. Li, L. Zhang, Y. Yoon, P.K. Weber, H. Wang, J. Guo, H. Dai, N-Doping of Graphene Through Electrothermal Reactions with Ammonia, 324(5928) (2009) 768-771.

[32] L. Ci, L. Song, C. Jin, D. Jariwala, D. Wu, Y. Li, A. Srivastava, Z.F. Wang, K. Storr, L. Balicas, F. Liu, P.M. Ajayan, Atomic layers of hybridized boron nitride and graphene domains, Nature Materials 9(5) (2010) 430-435.
[33] D. Usachov, O. Vilkov, A. Grüneis, D. Haberer, A. Fedorov, V.K. Adamchuk, A.B. Preobrajenski, P. Dudin, A. Barinov, M. Oehzelt, C. Laubschat, D.V. Vyalikh, Nitrogen-Doped Graphene: Efficient Growth, Structure, and Electronic Properties, Nano Letters 11(12) (2011) 5401-5407.
[34] X. Fan, Z. Shen, A.Q. Liu, J.-L. Kuo, Band gap opening of graphene by doping small boron nitride domains, Nanoscale 4(6) (2012) 2157-2165.
[35] C.-K. Chang, S. Kataria, C.-C. Kuo, A. Ganguly, B.-Y. Wang, J.-Y. Hwang, K.-J. Huang, W.-H. Yang, S.-B. Wang, C.-H. Chuang, M. Chen, C.-I. Huang, W.-F. Pong, K.-J. Song, S.-J. Chang, J.-H. Guo, Y. Tai, M. Tsujimoto, S. Isoda, C.-W. Chen, L.-C. Chen, K.-H. Chen, Band Gap Engineering of Chemical Vapor Deposited Graphene by in Situ BN Doping, ACS Nano 7(2) (2013) 1333-1341.
[36] P.A. Denis, Band gap opening of monolayer and bilayer graphene doped with aluminium, silicon, phosphorus, and sulfur, Chemical Physics Letters 492(4) (2010) 251-257.
[37] P.A. Denis, C. Pereyra Huelmo, A.S. Martins, Band Gap Opening in Dual-Doped Monolayer Graphene, The Journal of Physical Chemistry C 120(13) (2016) 7103-7112.
[38] Y. Takesaki, K. Kawahara, H. Hibino, S. Okada, M. Tsuji, H. Ago, Highly Uniform Bilayer Graphene on Epitaxial Cu–Ni(111) Alloy, Chemistry of Materials 28(13) (2016) 4583-4592.
[39] T.H. Vo, M. Shekhirev, D.A. Kunkel, M.D. Morton, E. Berglund, L. Kong, P.M. Wilson, P.A. Dowben, A. Enders, A. Sinitskii, Large-scale solution synthesis of narrow graphene nanoribbons, Nature Communications 5(1) (2014) 3189.
[40] L. Tang, R. Ji, X. Cao, J. Lin, H. Jiang, X. Li, K.S. Teng, C.M. Luk, S. Zeng,

J. Hao, S.P. Lau, Deep Ultraviolet Photoluminescence of Water-Soluble Self-Passivated Graphene Quantum Dots, ACS Nano 6(6) (2012) 5102-5110.
[41] K. He, G.-D. Lee, A.W. Robertson, E. Yoon, J.H. Warner, Hydrogen-free graphene edges, Nature Communications 5(1) (2014) 3040.
[42] Y.-B. Tang, L.-C. Yin, Y. Yang, X.-H. Bo, Y.-L. Cao, H.-E. Wang, W.-J. Zhang, I. Bello, S.-T. Lee, H.-M. Cheng, C.-S. Lee, Tunable Band Gaps and p-Type Transport Properties of Boron-Doped Graphenes by Controllable Ion Doping Using Reactive Microwave Plasma, ACS Nano 6(3) (2012) 1970-1978.
[43] S. Pei, H.-M. Cheng, The reduction of graphene oxide, Carbon 50(9) (2012) 3210-3228.
[44] Y. Zhu, S. Murali, W. Cai, X. Li, J.W. Suk, J.R. Potts, R.S. Ruoff, Graphene and graphene oxide: synthesis, properties, and applications, Adv Mater 22(35) (2010) 3906-24.
[45] J. Park, Y.S. Cho, S.J. Sung, M. Byeon, S.J. Yang, C.R. Park, Characteristics tuning of graphene-oxide-based-graphene to various end-uses, Energy Storage Materials 14 (2018) 8-21.
[46] S. Gambhir, R. Jalili, D.L. Officer, G.G. Wallace, Chemically converted graphene: scalable chemistries to enable processing and fabrication, NPG Asia Materials 7(6) (2015) e186-e186.
[47] S. Mao, H. Pu, J. Chen, Graphene oxide and its reduction: modeling and experimental progress, RSC Advances 2(7) (2012) 2643-2662.
[48] S. Stankovich, Synthesis of graphene-based nanosheets via chemical reduction of exfoliated graphite oxide, Carbon 45 (2007) 1558-1565.
[49] W. Gao, L.B. Alemany, L. Ci, P.M. Ajayan, New insights into the structure and reduction of graphite oxide, Nat Chem 1(5) (2009) 403-408.
[50] S.J. Yang, J.H. Kang, H. Jung, T. Kim, C.R. Park, Preparation of a freestanding, macroporous reduced graphene oxide film as an efficient and recyclable sorbent for oils and organic solvents, Journal of Materials Chemistry

A 1(33) (2013) 9427.
[51] H. Jung, S.J. Yang, T. Kim, J.H. Kang, C.R. Park, Ultrafast room-temperature reduction of graphene oxide to graphene with excellent dispersibility by lithium naphthalenide, Carbon 63 (2013) 165-174.
[52] D.R. Dreyer, S. Park, C.W. Bielawski, R.S. Ruoff, The chemistry of graphene oxide, Chemical Society Reviews 39(1) (2010) 228-240.
[53] T.-F. Yeh, F.-F. Chan, C.-T. Hsieh, H. Teng, Graphite Oxide with Different Oxygenated Levels for Hydrogen and Oxygen Production from Water under Illumination: The Band Positions of Graphite Oxide, The Journal of Physical Chemistry C 115(45) (2011) 22587-22597.
[54] M.A. Velasco-Soto, S.A. Pérez-García, J. Alvarez-Quintana, Y. Cao, L. Nyborg, L. Licea-Jiménez, Selective band gap manipulation of graphene oxide by its reduction with mild reagents, Carbon 93 (2015) 967-973.
[55] F. Nasehnia, S. Mohammadpour Lima, M. Seifi, E. Mehran, First principles study on optical response of graphene oxides: From reduced graphene oxide to the fully oxidized surface, Computational Materials Science 114 (2016) 112-120.
[56] A. Nourbakhsh, M. Cantoro, A.V. Klekachev, G. Pourtois, J. Hofkens, M.H. van der Veen, M.M. Heyns, S. De Gendt, B.F. Sels, Single Layer vs Bilayer Graphene: A Comparative Study of the Effects of Oxygen Plasma Treatment on Their Electronic and Optical Properties, The Journal of Physical Chemistry C 115(33) (2011) 16619-16624.
[57] A. Nourbakhsh, M. Cantoro, T. Vosch, G. Pourtois, F. Clemente, M.H. van der Veen, J. Hofkens, M.M. Heyns, S. De Gendt, B.F. Sels, Bandgap opening in oxygen plasma-treated graphene, Nanotechnology 21(43) (2010) 435203.
[58] H. Huang, Z. Li, J. She, W. Wang, Oxygen density dependent band gap of reduced graphene oxide, 111(5) (2012) 054317.
[59] S.D. Dabhi, P.K. Jha, Tuning the electronic band gap of graphene by oxidation, 1665(1) (2015) 090013.

[60] L. Guo, R.-Q. Shao, Y.-L. Zhang, H.-B. Jiang, X.-B. Li, S.-Y. Xie, B.-B. Xu, Q.-D. Chen, J.-F. Song, H.-B. Sun, Bandgap Tailoring and Synchronous Microdevices Patterning of Graphene Oxides, The Journal of Physical Chemistry C 116(5) (2012) 3594-3599.
[61] R.J.W.E. Lahaye, H.K. Jeong, C.Y. Park, Y.H. Lee, Density functional theory study of graphite oxide for different oxidation levels, Physical Review B 79(12) (2009) 125435.
[62] M. Lundie, Ž. Šljivančanin, S. Tomić, Electronic and optical properties of reduced graphene oxide, Journal of Materials Chemistry C 3(29) (2015) 7632-7641.
[63] A. Mathkar, D. Tozier, P. Cox, P. Ong, C. Galande, K. Balakrishnan, A. Leela Mohana Reddy, P.M. Ajayan, Controlled, Stepwise Reduction and Band Gap Manipulation of Graphene Oxide, The Journal of Physical Chemistry Letters 3(8) (2012) 986-991.
[64] A.I. Aria, A.W. Gani, M. Gharib, Effect of dry oxidation on the energy gap and chemical composition of CVD graphene on nickel, Applied Surface Science 293 (2014) 1-11.
[65] Y. Shen, S. Yang, P. Zhou, Q. Sun, P. Wang, L. Wan, J. Li, L. Chen, X. Wang, S. Ding, D.W. Zhang, Evolution of the band-gap and optical properties of graphene oxide with controllable reduction level, Carbon 62 (2013) 157-164.
[66] M.S. Chang, T. Kim, J.H. Kang, J. Park, C.R. Park, The effect of surface characteristics of reduced graphene oxide on the performance of a pseudocapacitor, 2D Materials 2(1) (2015) 014007.
[67] Y. Yu, G. Li, S. Zhou, X. Chen, H.-W. Lee, W. Yang, Self–adaptive Si/reduced graphene oxide scrolls for high–performance Li–ion battery anodes, Carbon 120 (2017) 397-404.
[68] R. Zhou, Y. Zheng, D. Hulicova-Jurcakova, S.Z. Qiao, Enhanced electrochemical catalytic activity by copper oxide grown on nitrogen-doped

reduced graphene oxide, Journal of Materials Chemistry A 1(42) (2013) 13179-13185.
[69] V.V. Quang, N.V. Dung, N.S. Trong, N.D. Hoa, N.V. Duy, N.V. Hieu, Outstanding gas-sensing performance of graphene/SnO2 nanowire Schottky junctions, Applied Physics Letters 105(1) (2014) 013107.
[70] L. Li, S. He, M. Liu, C. Zhang, W. Chen, Three-Dimensional Mesoporous Graphene Aerogel-Supported SnO2 Nanocrystals for High-Performance NO2 Gas Sensing at Low Temperature, Analytical Chemistry 87(3) (2015) 1638-1645.
[71] X. Zhu, Y. Guo, H. Ren, C. Gao, Y. Zhou, Enhancing the NO2 gas sensing properties of rGO/SnO2 nanocomposite films by using microporous substrates, Sensors and Actuators B: Chemical 248 (2017) 560-570.
[72] P. Roy, A.P. Periasamy, C.-T. Liang, H.-T. Chang, Synthesis of Graphene-ZnO-Au Nanocomposites for Efficient Photocatalytic Reduction of Nitrobenzene, Environmental Science & Technology 47(12) (2013) 6688-6695.

Part II

Fine tuning of band gap of graphene fittable to various end uses.

Chapter 2 Development of easy experimental ways to tailor fitted band gap of graphene to various applications.

2.1 Introduction

There has been significant researches with regard to the application of graphene, especially GO based graphene including RGO. However, the theoretically predicted performance of GO based graphene has not yet to be realized in practical application field because of there are any effective way of control the band gap of itself.

Base on the point of equation (1.3), many researchers tried to predict the band gap of graphene and it gives the point of view based on the attached oxygen atom, [1-12] but the result of **Figure 1.24** shows that this point of view is not sufficient for precise prediction of band gap of GO based graphene. Indeed, derived from the equation from the modern physics in the case of existing energy barrier, we should think that what act as an energy barrier in GO based graphene.

To overcome the limitations shown in **Figure 1.24**, this study introduces a proper theoretical approaches which consider the sp^2 carbon as the electron pathway, and carbon atom which can electron can be scattered as an energy barrier of graphene. The goal is to find the rational relationship among the ratio of sp^2 carbon atoms, edge carbon atoms, and the band gap of GO based graphene and hopefully realize the theoretical performance of GO based graphene realized in the real application field.

2.2 Effect of sp^2 carbon on electron transfer of graphene

Many researchers tried to correlate amount of oxygen atoms and band gap of graphene. Although this point of view provide the simple way of band gap engineering of GO based graphene, but the resultant band gap by experimental study showed a different trend compared to calculation research as shown in **Figure 1.24**. Therefore, the requirement for finding hidden parameter of graphene that determine the band gap of itself.

In order to make right application of theory of modern physics to graphene, which shown in formula (1.3), electron pathway should be estimated to sp^2 carbon that electron is transferred in graphene. Therefore, energy barrier of electron transport has to set up to non-sp^2 carbon, the insulate region of GO based graphene. Effect of non-sp^2 carbon area of band gap of GO based graphene, effective mass should be considered because effective mass of graphene is generated when insulative area is generated on graphene as shown in **Figure 2.1**. [13] Especially, when effective mass of graphene showed linear relationship with the band gap itself, the relationship should be theoretically defined.

Applying Tight Binding model to the Dirac cone model of graphene, the energy dispersion of graphene near fermi energy can be expressed **Equation 2.1** as shown in below. [14]

$$E(\mathbf{k}) = E_0 \pm \frac{3}{2} t_0 r_0 |\mathbf{k} - \mathbf{k}_F| \qquad \text{----------(2.1)}$$

where E_0 is the on-site energy which is equal to the Fermi energy E_F, t_0 is the hopping parameter, and r_0 is the equilibrium bond length. After calculating effective mass by second derivation of equation (1), we can get the relationship between effective mass m^* and band gap of graphene as shown in **Equation 2.2** where $\hbar$ is the flank constant. [14]

$$m^* = \frac{2\hbar^2}{9t_0^2 r_0^2} E_g$$ ----------(2.2)

From this simple equation, it can be found that effective mass of graphene shows the linear relationship. In order to see this relationship in real, Zhang et. al tried to linear fit between band gap and effective mass in various semiconductive materials and succeed to define this linear relationship. (**Figure 2.2**) [15] Therefore, as shown in this research, it can be thought that the band gap of GO based Graphene can show the linear relationship with the ratio of non-sp^2 carbon.

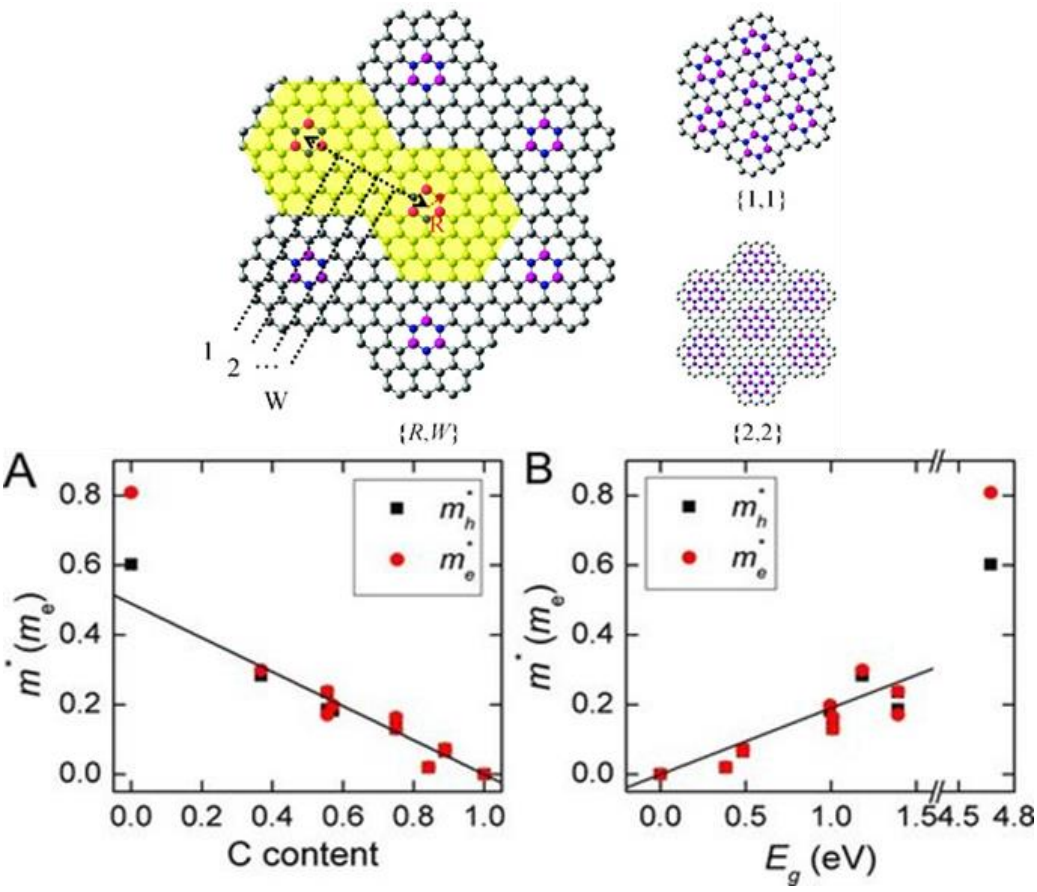

Figure 2.1 (a) Linear relationship between sp^2 carbon and effective mass of electron and (b) Linear relationship between band gap and effective mass of graphene calculated with the model of graphene which some domains exchanged to insulative boron nitride (upper) [13]

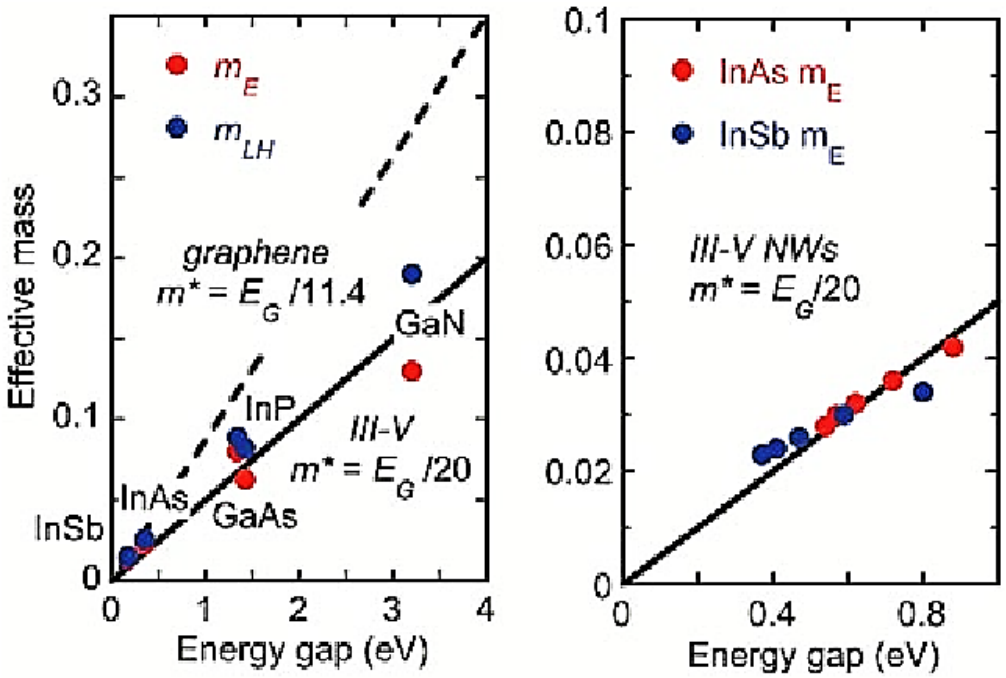

Figure 2.2 Linear relationship between band gap and effective mass of (left) various semiconductive materials and graphene and (right) III-V nanowires. [15]

Meanwhile, considering electron transport of graphene, effective mass is also can be generated by electron scattering as shown in **Equation 2.3** where μ is the drift mobility, q is the elementary charge, and τ is the average scattering time. [16]

$$\mu = \frac{q}{m^*}\bar{\tau} \quad \text{----------(2.3)}$$

Considering the mobility has inverse relationship between band gap, [14] and it can be estimated that band gap has inverse relationship by average scattering time as shown in **Equation 2.4**.

$$E_g \propto \frac{m^*}{q\tau} \propto m^* \times (scattering\ site) \quad \text{----------(2.4)}$$

Therefore, when estimate average scattering time is linearly decreased by the amount of site of electron scattering, such as edge carbon that is connected to heteroatom or vacancy as shown in **Figure 2.3**, [17] it can be though that band gap of graphene has linear relationship with the multiplies of effective mass and the site of electron scattering.

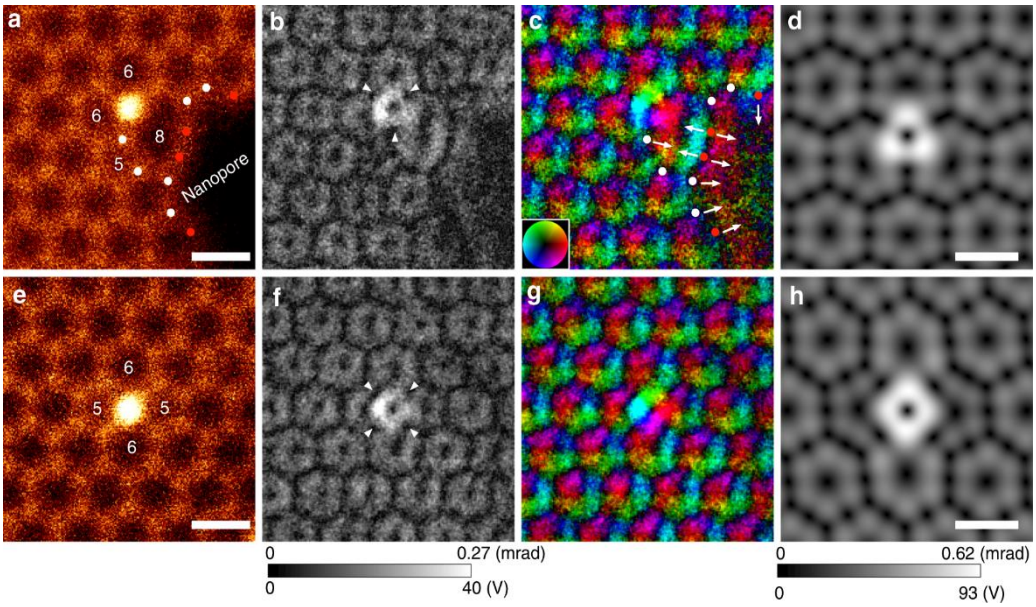

Figure 2.3. (a), (e) ADF-STEM images, (b), (f) electric field strength maps, (c), (g) electric field vector maps, (d), (h)calculated electric field strength maps from simulated STEM images for the 16 segmented detectors, in the coordination of Si–C_3 and Si–C_4, respectively. The numbers in (a), (e) indicate the number of members in the ring. (Scale bars: 2 Å) [17]

2.3 Effect of sp^2 carbon and edge sp^2 carbon to band gap of graphene : re-colligate calculation research

From the equation 4, band gap of graphene can be controlled by non sp^2 carbon and edge carbon connected to heteroatom of vacancy. Considering edge carbon can be detected by I_D/I_G ratio of Raman spectroscopy, [18] the controllable parameter can be set to [1-(ratio of sp^2 carbon)] and (I_D/I_G ratio). Based on this point of view, calculation researches which was plotted in **Figure 1.22**, [2-6, 8-10] the band gap is replotted by multiple of [1-(ratio of sp^2 carbon)] and (I_D/I_G ratio). After the linear plot as shown in **Figure 2.4**, the linear relationship of equation 4 can be seen clearly with the R-square of 0.96. This result indicates that there are high possibilities of which band gap of GO based graphene can be easily controlled by multiple of [1-(ratio of sp^2 carbon)] and (I_D/I_G ratio).

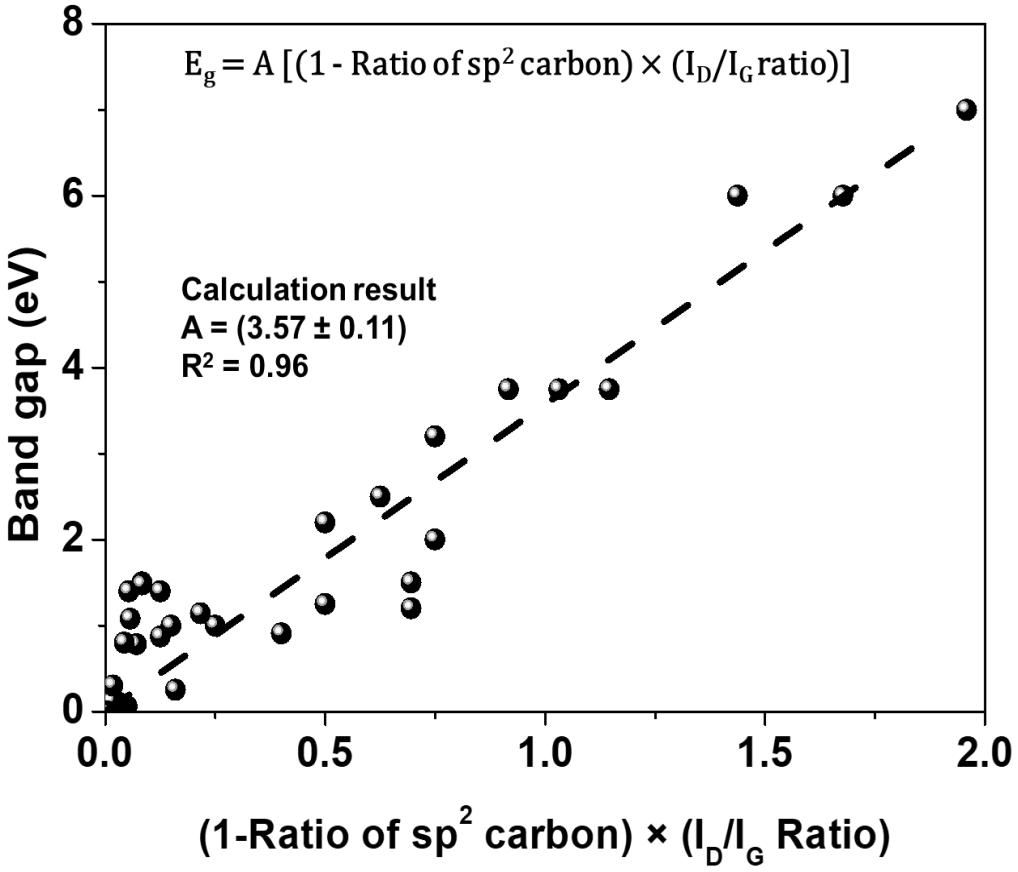

Figure 2.4. Replotted calculated band gap of graphene from previous studies [2-6, 8-10] replotted by multiple of [1-(ratio of sp^2 carbon)] and (I_D/I_G ratio).

2.4 Band gap graphene embedded materials by band gap of graphene: combined with work function

In fact, GO based graphene are used in composite and around 17% of researches about GO based graphene is about its use as a composited form. [19] Therefore, establishment band gap engineering way of GO based graphene composites for the variety of end uses. However, in application field, there are any considerations about the band gap of embedded graphene [20] and this remains as a huge huddle for realize materials properties of GO based graphene.

In order to calculate band gap of composite using GO based graphene, two main parameters should be considered, one is work function and another is band gap of graphene itself because electron transport is mainly occurred by graphene. [21] Band gap and work function of graphene is not shifted by the simple mixing with other materials as shown in other previous calculation researches as shown in **Figure 2.5** [22] and **Figure 2.6** [23], designing band diagram of GO based graphene composite can be a simple work.

Band gap of graphene can be calculated using the result of **Figure 2.4**, band diagram can be designed when the work function itself can be calculated. Therefore, it is important to finding controllable parameter which decide work function of graphene. In previous work, work function can be controlled by the induced charge as shown in the **Figure 2.7**, [24] and it can be controlled by the amount of heteroatoms. Therefore, in this point of view, plotting work function of graphene with the amount of oxygen atom of calculation researches [25, 26] showed high linearity with the r-square of 0.9. This result implies that work function of graphene can be easily modified by the oxidation degree and it should be applied to the estimation of band gap of GO based graphene composite materials as shown in **Figure 2.8**.

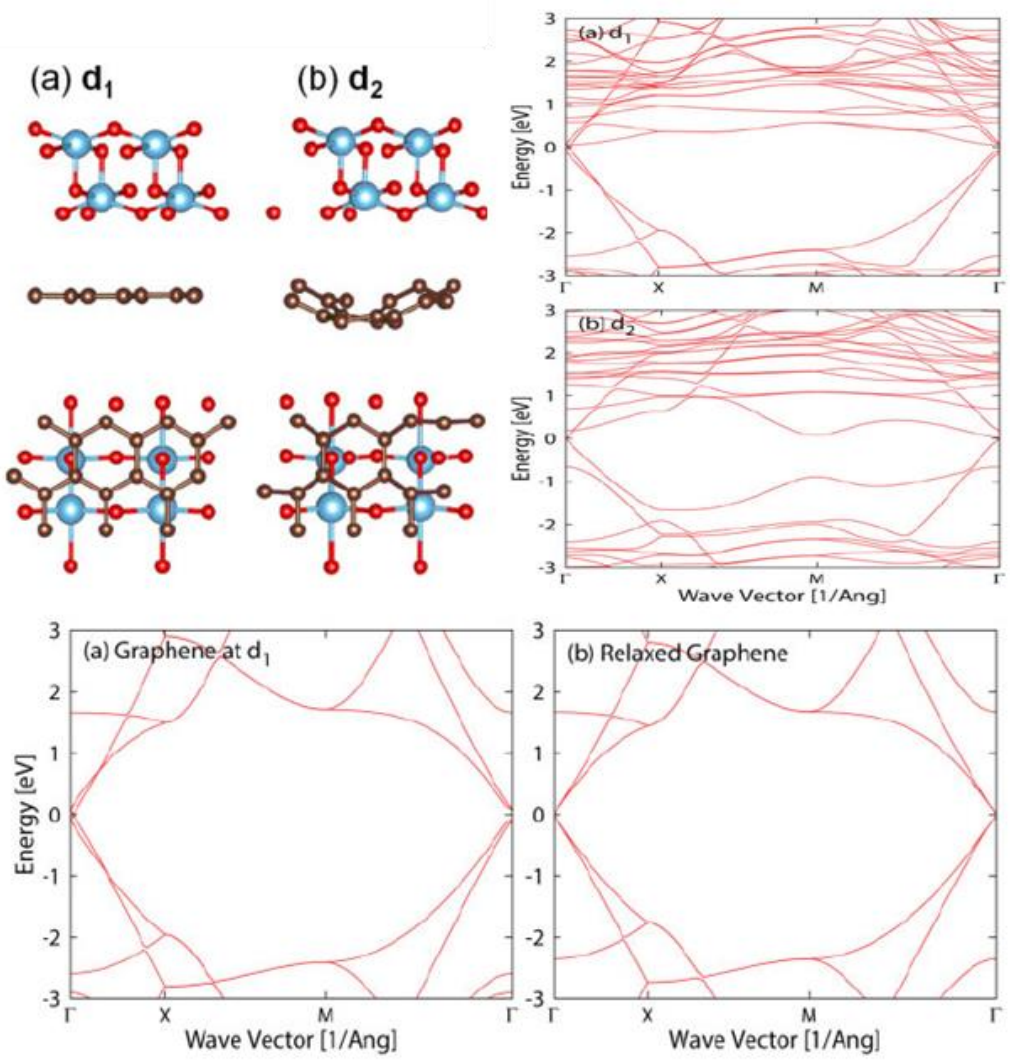

Figure 2.5. (upper right) Band diagram of ZnO/graphene and (lower) graphene in molecular model of d_1, d_2 (upper left) [22]

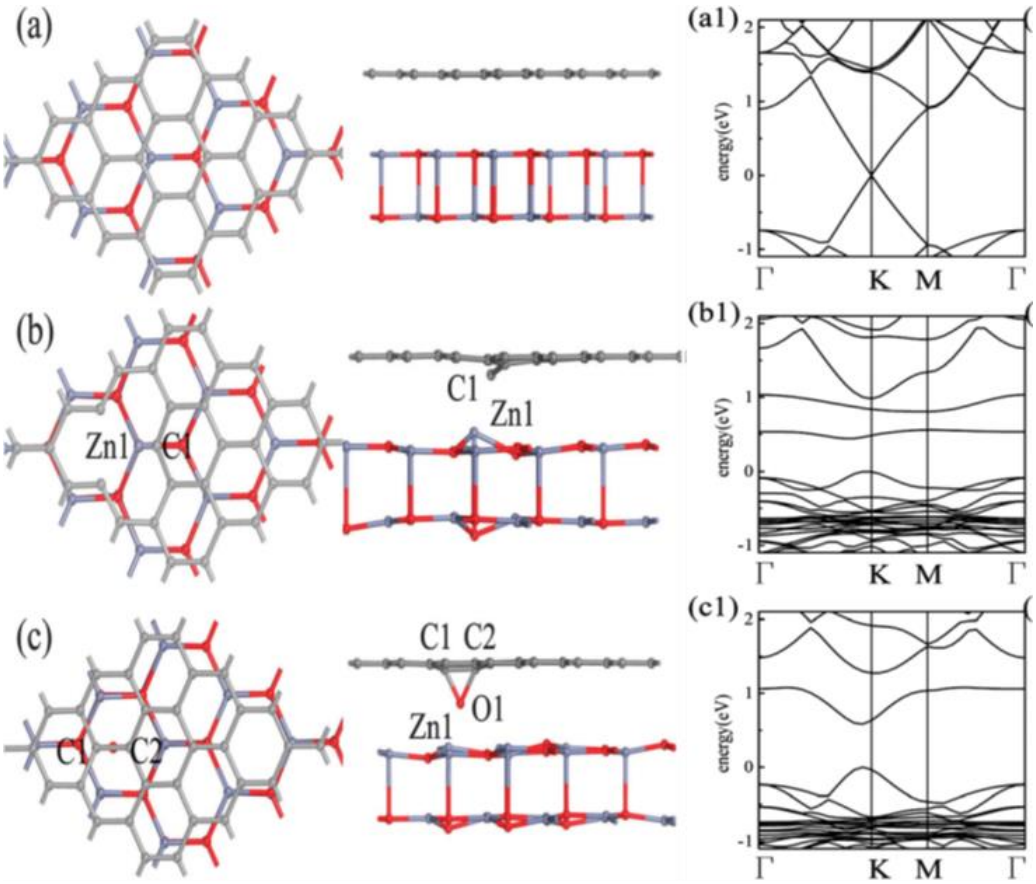

Figure 2.6 Band diagram of (a1) TiO_2/graphene of structure (a), (b1) TiO_2/ C dangled graphene of structure (b), and (c1) TiO_2/oxygen dangle graphene of structure (c) [23]

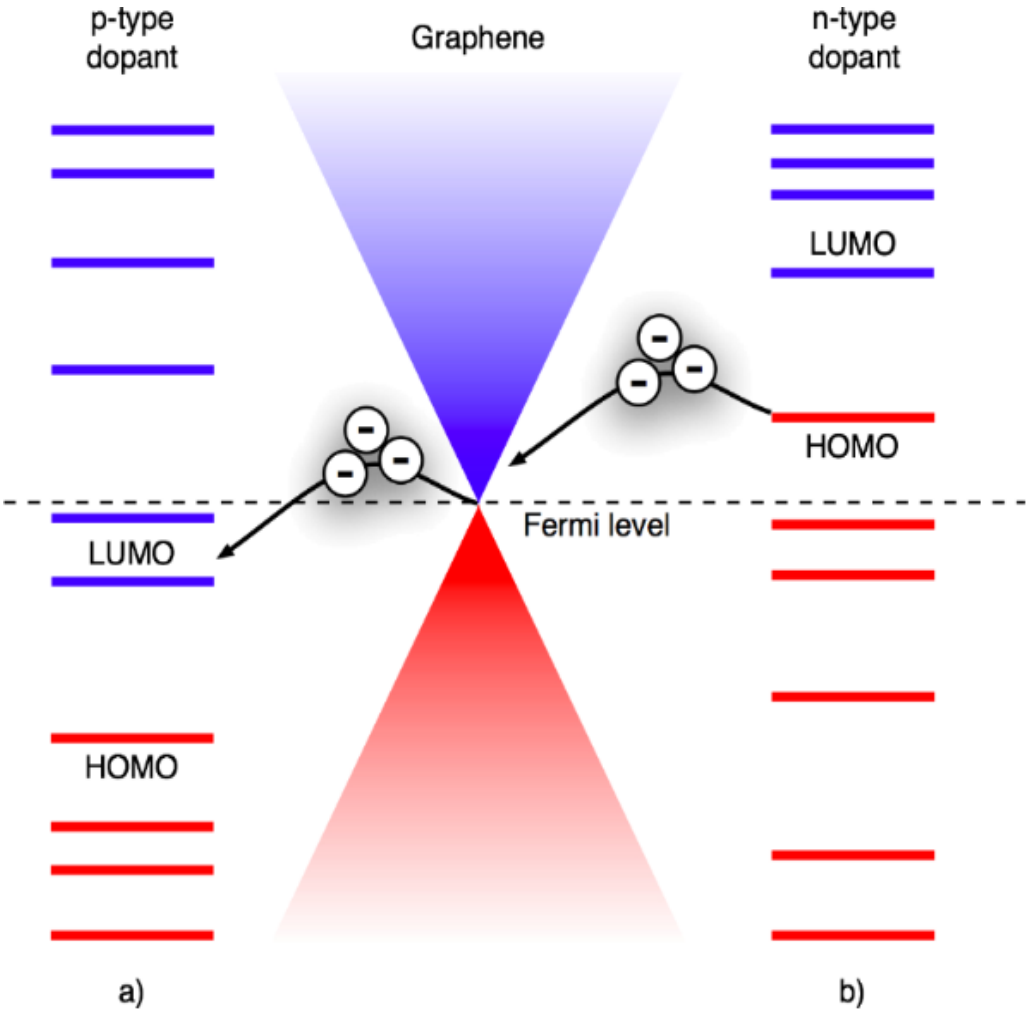

Figure 2.7 Band diagram of graphene and work function alternation by type of dopant atom. [24]

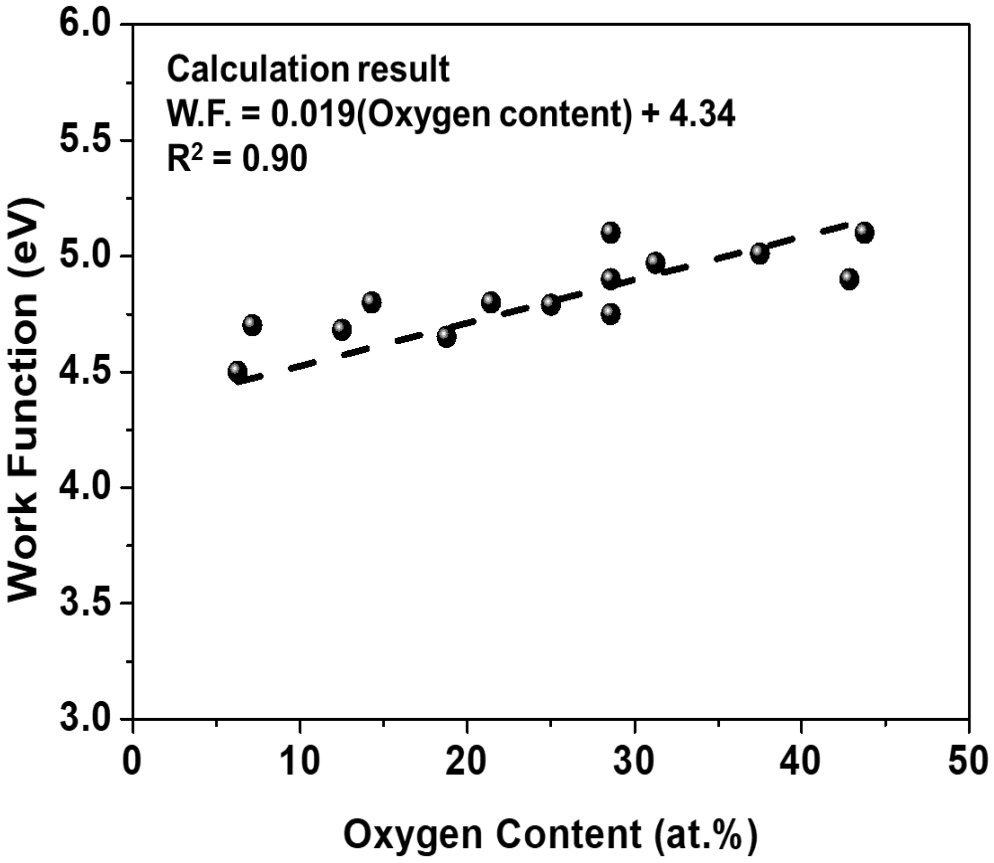

Figure 2.8. Replotted calculated work function of graphene from previous studies [25, 26] replotted by oxygen content

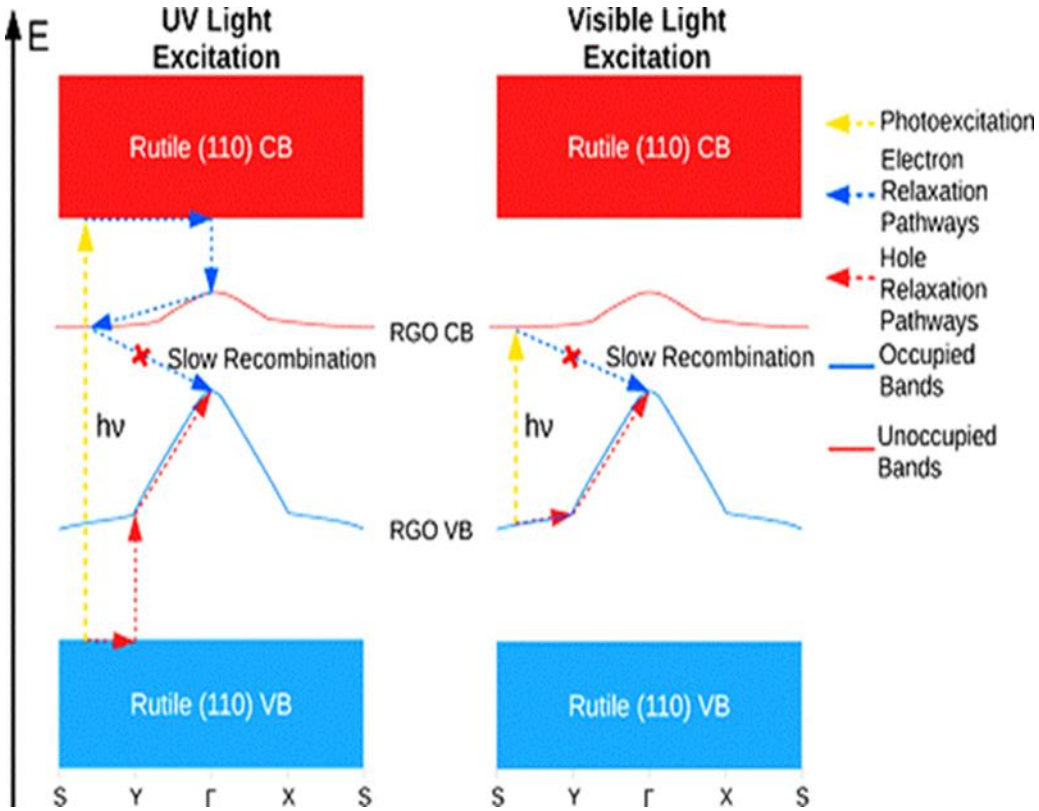

Figure 2.9. Suggested band diagram of rutile TiO_2/graphene from previous study that consider band gap and work function of embedded graphene. [27]

2.5 Conclusion

Band gap of GO based graphene can be controlled by effective mass and electron scattering based on the simple consideration about theory of modern physics. The key material parameters that can control the band gap of GO based graphene, non sp^2 carbon ratio and I_D/I_G ratio, are defined that controls each terms that decide band gap of graphene and defined it from the colligate previous calculation results. In contrary to the exiting point of view based on the oxygen atom, which not fully reflect the electron transport on graphene, this new model can show the effect of hindered electron transport to the band gap directly.

In addition, from the calculation result that showed band structure of graphene does not changed by environment materials, band diagram of GO based graphene composite is directly affected by the work function and band gap of graphene itself and estimated the relationship of work function and amount of dangled oxygen in the point of induced charge.

Despite the attempts to get insight into the band gap of GO based graphene and its composite, actual GO based graphene has more variable parameters in this study, and other parameters not dealt with here should be considered in order to estimate the specific calculation of band gap of GO based graphene more accurately.

2.6 Reference

[1] A.I. Aria, A.W. Gani, M. Gharib, Effect of dry oxidation on the energy gap and chemical composition of CVD graphene on nickel, Applied Surface Science 293 (2014) 1-11.

[2] S.D. Dabhi, P.K. Jha, Tuning the electronic band gap of graphene by oxidation, AIP Conference Proceedings 1665(1) (2015) 090013.

[3] L. Guo, R.-Q. Shao, Y.-L. Zhang, H.-B. Jiang, X.-B. Li, S.-Y. Xie, B.-B. Xu, Q.-D. Chen, J.-F. Song, H.-B. Sun, Bandgap Tailoring and Synchronous Microdevices Patterning of Graphene Oxides, The Journal of Physical Chemistry C 116(5) (2012) 3594-3599.

[4] H. Huang, Z. Li, J. She, W. Wang, Oxygen density dependent band gap of reduced graphene oxide, Journal of Applied Physics 111(5) (2012) 054317.

[5] R.J.W.E. Lahaye, H.K. Jeong, C.Y. Park, Y.H. Lee, Density functional theory study of graphite oxide for different oxidation levels, Physical Review B 79(12) (2009) 125435.

[6] M. Lundie, Ž. Šljivančanin, S. Tomić, Electronic and optical properties of reduced graphene oxide, Journal of Materials Chemistry C 3(29) (2015) 7632-7641.

[7] A. Mathkar, D. Tozier, P. Cox, P. Ong, C. Galande, K. Balakrishnan, A. Leela Mohana Reddy, P.M. Ajayan, Controlled, Stepwise Reduction and Band Gap Manipulation of Graphene Oxide, The Journal of Physical Chemistry Letters 3(8) (2012) 986-991.

[8] F. Nasehnia, S. Mohammadpour Lima, M. Seifi, E. Mehran, First principles study on optical response of graphene oxides: From reduced graphene oxide to the fully oxidized surface, Computational Materials Science 114 (2016) 112-120.

[9] A. Nourbakhsh, M. Cantoro, A.V. Klekachev, G. Pourtois, J. Hofkens, M.H. van der Veen, M.M. Heyns, S. De Gendt, B.F. Sels, Single Layer vs Bilayer

Graphene: A Comparative Study of the Effects of Oxygen Plasma Treatment on Their Electronic and Optical Properties, The Journal of Physical Chemistry C 115(33) (2011) 16619-16624.
[10] A. Nourbakhsh, M. Cantoro, T. Vosch, G. Pourtois, F. Clemente, M.H. van der Veen, J. Hofkens, M.M. Heyns, S. De Gendt, B.F. Sels, Bandgap opening in oxygen plasma-treated graphene, Nanotechnology 21(43) (2010) 435203.
[11] Y. Shen, S. Yang, P. Zhou, Q. Sun, P. Wang, L. Wan, J. Li, L. Chen, X. Wang, S. Ding, D.W. Zhang, Evolution of the band-gap and optical properties of graphene oxide with controllable reduction level, Carbon 62 (2013) 157-164.
[12] M.A. Velasco-Soto, S.A. Pérez-García, J. Alvarez-Quintana, Y. Cao, L. Nyborg, L. Licea-Jiménez, Selective band gap manipulation of graphene oxide by its reduction with mild reagents, Carbon 93 (2015) 967-973.
[13] J. Wang, R. Zhao, Z. Liu, Z. Liu, Widely Tunable Carrier Mobility of Boron Nitride-Embedded Graphene, 9(8) (2013) 1373-1378.
[14] J. Wang, R. Zhao, M. Yang, Z. Liu, Z. Liu, Inverse relationship between carrier mobility and bandgap in graphene, The Journal of Chemical Physics 138(8) (2013) 084701.
[15] Q. Zhang, Y. Lu, C.A. Richter, D. Jena, A. Seabaugh, Optimum Bandgap and Supply Voltage in Tunnel FETs, IEEE Transactions on Electron Devices 61(8) (2014) 2719-2724.
[16] P. YU, M. Cardona, Fundamentals of Semiconductors: Physics and Materials Properties, Springer Berlin Heidelberg2010.
[17] R. Ishikawa, S.D. Findlay, T. Seki, G. Sánchez-Santolino, Y. Kohno, Y. Ikuhara, N. Shibata, Direct electric field imaging of graphene defects, Nature Communications 9(1) (2018) 3878.
[18] M.A. Pimenta, G. Dresselhaus, M.S. Dresselhaus, L.G. Cançado, A. Jorio, R. Saito, Studying disorder in graphite-based systems by Raman spectroscopy, Physical Chemistry Chemical Physics 9(11) (2007) 1276-1290.

[19] V.B. Mohan, K.-t. Lau, D. Hui, D. Bhattacharyya, Graphene-based materials and their composites: A review on production, applications and product limitations, Composites Part B: Engineering 142 (2018) 200-220.
[20] X. Li, L. Zhi, Graphene hybridization for energy storage applications, Chemical Society Reviews 47(9) (2018) 3189-3216.
[21] Z. Li, B. Du, C. Han, H. Xu, Trap Modulated Charge Carrier Transport in Polyethylene/Graphene Nanocomposites, Scientific Reports 7(1) (2017) 4015.
[22] Y. Masuda, G. Giorgi, K. Yamashita, DFT study of anatase-derived TiO2 nanosheets/graphene hybrid materials, physica status solidi (b) 251(8) (2014) 1471-1479.
[23] W. Geng, X. Zhao, W. Zan, H. Liu, X. Yao, Effects of the electric field on the properties of ZnO–graphene composites: a density functional theory study, Physical Chemistry Chemical Physics 16(8) (2014) 3542-3548.
[24] H. Pinto, A. Markevich, Electronic and electrochemical doping of graphene by surface adsorbates, Beilstein Journal of Nanotechnology 5 (2014) 1842-1848.
[25] X. Peng, F. Tang, A. Copple, Engineering the work function of armchair graphene nanoribbons using strain and functional species: a first principles study, Journal of Physics: Condensed Matter 24(7) (2012) 075501.
[26] N. Yang, D. Yang, L. Chen, D. Liu, M. Cai, X. Fan, Design and adjustment of the graphene work function via size, modification, defects, and doping: a first-principle theory study, Nanoscale Research Letters 12(1) (2017) 642.
[27] P.N.O. Gillespie, N. Martsinovich, Origin of Charge Trapping in TiO2/Reduced Graphene Oxide Photocatalytic Composites: Insights from Theory, ACS Applied Materials & Interfaces 11(35) (2019) 31909-31922.

Chapter 3 Development of easy experimental ways to tailor fitted band gap of graphene to various applications.

3.1 Band gap tuning of graphene by oxidation

3.1.1 Introduction

Graphene has been considered as great materials because of its astounding performance than other transitional materials. [1-3] Therefore, many application fields tried to use its great performance, but failed to succeed to achieve because of failed to preparing tailor fitted band gap engineered graphene with large scale. In order to achieve this requirement for preparing band gap engineered graphene for manufacturing, graphene oxide (GO) based graphene taken attention because of its superior price competitiveness than any other graphene from other preparation route [2] and possibility of easy band gap engineering with controlling surface characteristics as shown in the study of **Chapter 2**. Considering preparation route of GO based graphene, [4, 5] band gap engineering of GO by surface characteristics of itself should be defined.

There are various preparation method of GO, but method developed by Hummers is usually used because of its yield by highest oxidation degree that other method. [6-8] This method has two step oxidation and both step strongly affect to the surface characteristics of GO with different oxidation mechanism. [4, 5] Plus, by the simple modification of acidic washing process followed by oxidation process, surface characteristics of GO also can be altered. [9] Because of the ease alternation of characteristics of GO by modification of preparation method, band gap of GO also can be changed with ease.

Thus, in this research of this chapter, band gap of GO which are prepared by verified modification route of graphene was measured and its correlation with (non sp^2 carbon ratio) and (I_D/I_G ratio) which was defined in **Chapter 2** was tested that the relationship can be applied in real experiment results.

3.1.2 Experimental

3.1.2.1 Materials

Potassium persulfate ($K_2S_2O_8$, 98%), phosphorus pentoxide (P_4O_{10}, 98%), potassium permanganate ($KMnO_4$, 98%), and natural flake graphite (Lot #: 17425HO, +100 mesh) were purchased from Sigma-Aldrich. Sulfuric acid (H_2SO_4, 98%), hydrogen peroxide (H_2O_2, 30%), and hydrochloric acid (HCl, 35–37%) were purchased from Daejung Chemicals & Metals. All chemicals were used as received.

3.1.2.2 Preparation of graphene oxide

Graphene oxide (GO) were prepared through the conventional Hummers method. [4, 5, 7, 10] First, natural flake graphite was pretreated with $K_2S_2O_8$ and P_4O_{10} for the ease of exfoliation to single layer. 10.0 g of $K_2S_2O_8$ and 10.0 g of P_4O_{10} were fully dissolved in 50 mL of 98% H_2SO_4 while vigorously stirring at 80°C. 5.0 g of graphite was slowly added to the mixture. The mixture was continuously stirred for 24 hours at the same temperature, and poured into 2 L of deionized water. The pretreated graphite was washed with excess water using repeated vacuum filtrations until pH of graphite became neutral, then dried in a vacuum oven under room temperature. 3.0 g of this pretreated graphite was dispersed into 138 mL of H_2SO_4 that had been cooled to 0°C 18.0 g of $KMnO_4$ added very carefully added so as to prevent the temperature from rising above 50°C. The reaction transferred to a 35°C and stirred in 300 rpm.

After 2 hours, 1/3 of the mixture was poured in water/ H_2O_2 mixture for direct finishing of oxidation without second oxidation step. This GO was named for GO 2A000. At the same time, 2/3 of the miture was mixed with 200 ml of water slowly so as to prevent the temperature from rising above 50°C and stirred in 45°C. For controlling time of second oxidation step, 10 ml of H_2O_2 was added

after 2 and 8 hours. These GO were named for GO 2A452 and GO 458.

After first and second oxidation steps, this mixture is ultra-centrifuged at 13000 rpm with 3.4 % HCl 3 times. The precipitant was repeatedly washed with and completely neutralized by exchanging the solvent with water in repeated ultra-centrifugations at 13000 rpm 5 times. For eliminating un-exfoliated graphite, the precipitant was centrifuged at 4000 rpm and the supernatant was gained.

3.1.2.3 Preparation of edge selectively oxidized graphene

3.0 g of pretreated graphite was dispersed into 138 ml of H_2SO_4 that had been cooled to 0°C in advance while 18.0 g of $KMnO_4$ was stirred in 200 ml of deionized (DI) water. 50 ml of DI water was very carefully added to prevent the temperature from rising above 70°C, and aqueous $KMnO_4$ was poured, followed by 50 ml of DI water. The reaction was transferred to a 70°C bath and mechanically stirred for 12 and 24 hours. The nomenclature of the EOG samples of this work represents the step II oxidation condition for each EOG experienced during the synthesis. For example, the EOG sample produced from the procedure, including step II oxidation for 12 h at 70°C, was named E70012. Another sample E7024, were prepared and named in this manner. After this stirring process, 10 ml of H_2O_2 was added to complete oxidation. This mixture was ultra-centrifuged three times at 13,000 rpm with 3.4% HCl. The precipitant was repeatedly washed with and completely neutralized five times by exchanging the solvent with DI water in repeated ultra-centrifugations at 4000 rpm. The product was finally obtained by vacuum filtration and dried in an 80°C oven.

Before bath sonication, EOG was mixed in 5 mg/ml with 0.1 M NaOH and stirred overnight. The solvent was sonicated by bath sonication for 6h and left overnight. The suspension was centrifuged in 4000 rpm and supernatant was obtained. This process was repeated for three times in order to eliminate unexfoliated graphene.

The graphene suspension was dialyzed with DI water until neutralized and we named the suspension as LPEOG. 1ml of LEPOG was dried and weighted for measuring the concentrations. The nomenclature of the LPEOG samples of this work represents the exfoliated EOG samples. For example, the LPEOG sample produced from E7012 was named LE7012. Another sample, LE7024, were prepared and named in this manner.

3.1.2.4 Preparation of GO with modified HCl washing process

3.0 g of the pretreated graphite was dispersed into 138 mL of H_2SO_4 that had been cooled to 0°C. 18.0 g of $KMnO_4$ was added very carefully to prevent the temperature from rising above 50°C. The reaction was finally transferred and stirred for 300 rpm at 35°C. After 2 hours, the mixture was poured in a water/H_2O_2 mixture to finish oxidation without the second oxidation step. The mixture was then washed with 1M HCl two times using centrifuge at 13000rpm. Then, we divided the precipitate into three groups and different washing processes were carried out. 1/3 of the mixture was directly centrifuged in 1M HCl at 13000rpm at room temperature. Another 1/3 of the precipitate were stirred in 1M HCl at 70°C for 16 hours and centrifuged at 13000rpm. The other 1/3 of the precipitate were stirred in 1M HCl at 70°C for 16 hours and centrifuged at 13000rpm. We named the GO from the first 1/3 precipitate as GO 2A000, the second 1/3 precipitate as HGO_1M, and the last 1/3 precipitate as HGO_5M. After the HCl washing steps, the precipitate was completely neutralized by exchanging the solvent with water over five times in repeated ultra-centrifugations at 13000 rpm. To eliminate un-exfoliated graphite and to produce supernatant, the precipitant was centrifuged at 4000 rpm. After purification, half of the GO was annealed in a 70°C oil bath and we named it AGO.

3.1.2.5 Characterization

To study the oxygen-containing functional groups of the samples, the functional groups were quantified by performing XPS with an AXIS-HSi spectrometer (Kratos). The obtained C1s spectra were fitted and deconvoluted using XPSPEAK41 software. FTIR spectra of the GO, AGO and HGO samples were recorded with a Thermo Scientific Nicolet TM iS10 spectrometer to obtain additional information about their functional groups. The scan range was 400–4,000 cm-1 in attenuated total reflection (ATR) mode. Thermogravimetric analysis (TGA) was carried out under nitrogen flow by using an SDTQ600 instrument (TA Instruments). Raman spectrum was obtained using a Raman plus confocal laser Raman microscope (Nanophoton) with a 532 nm Nd-YAG laser source. The optical absorbance data of the GO within the UV-visible region were obtained by using a UV-Vis-NIR Cary 5000 spectrometer (Varian) with a scan range of 400-700 nm. And from the previous studies, we measure band gap of graphene oxides using modified Tauc plot. [9, 11, 12]

3.1.3 Results and discussion

For comparing the populations of the functional groups, X-ray photoelectron spectroscopy (XPS), fourier transform infrared (FTIR) spectroscopy, thermogravimetric analysis (TGA) were used. Decrement of the amount of functional group and increment of sp^2 carbon of GO can be shown in the weight loss and improved thermal stability of the TGA results (**Figure 3.1**) because of the elimination of functional groups which disappeared at low temperature. [5, 13]

As shown in **Figure 3.2** of FT-IR spectrum normalized by the C=C double bond peak of aromatic carbon (1633 cm^{-1}) The absorption peaks of hydroxyl and epoxide groups (1105 cm^{-1}, 1248 cm^{-1}, and 3300 cm^{-1}) were smaller in the case of oxidation degree as shown in XPS result of **Figure 3.3** and **Figure 3.4** is decreased. In contrast, the peak of carboxyl (1410 cm^{-1}) and carbonyl (1730 cm^{-1}) groups of LE7024 showed large peak than any other GO because of enlarged functional groups of graphene edge by increased step II oxidation. [5, 9, 13, 14] This tendency of the functional group decrement and increment of sp^2 carbon, also showed in XPS result, result of binding ratio obtained by deconvoluted C1s spectra (**Figure 3.3** and **Figure 3.4**) and lots of C=O bonds of carboxyl and carbonyl also can be explained. [5, 9, 13, 14]

In order to verify that the degree of electron scattering by boundary carbon, atomistic defects of the graphite samples were characterized by Raman. Because the disorder in graphite induces D band in the Raman spectra and in-plane vibrational E2g phonon induces G band, the intensity ratio between D band and G band indicates structural disorder of the graphitic layer. [9, 15] As shown in **Figure 3.5** and **Figure 3.6** LPEOG has a low I_D/I_G ratio (up to 0.9) by edge selectively oxidation, which completely differs from other GO (~1.08).

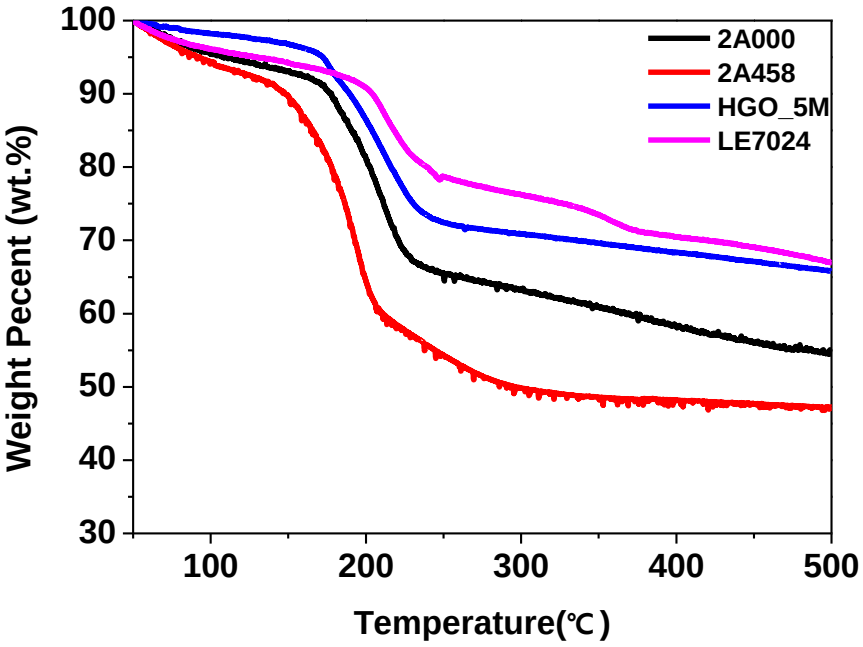

Figure 3.1 Thermogravimetric analysis (TGA) results of GO with modified Hummers method.

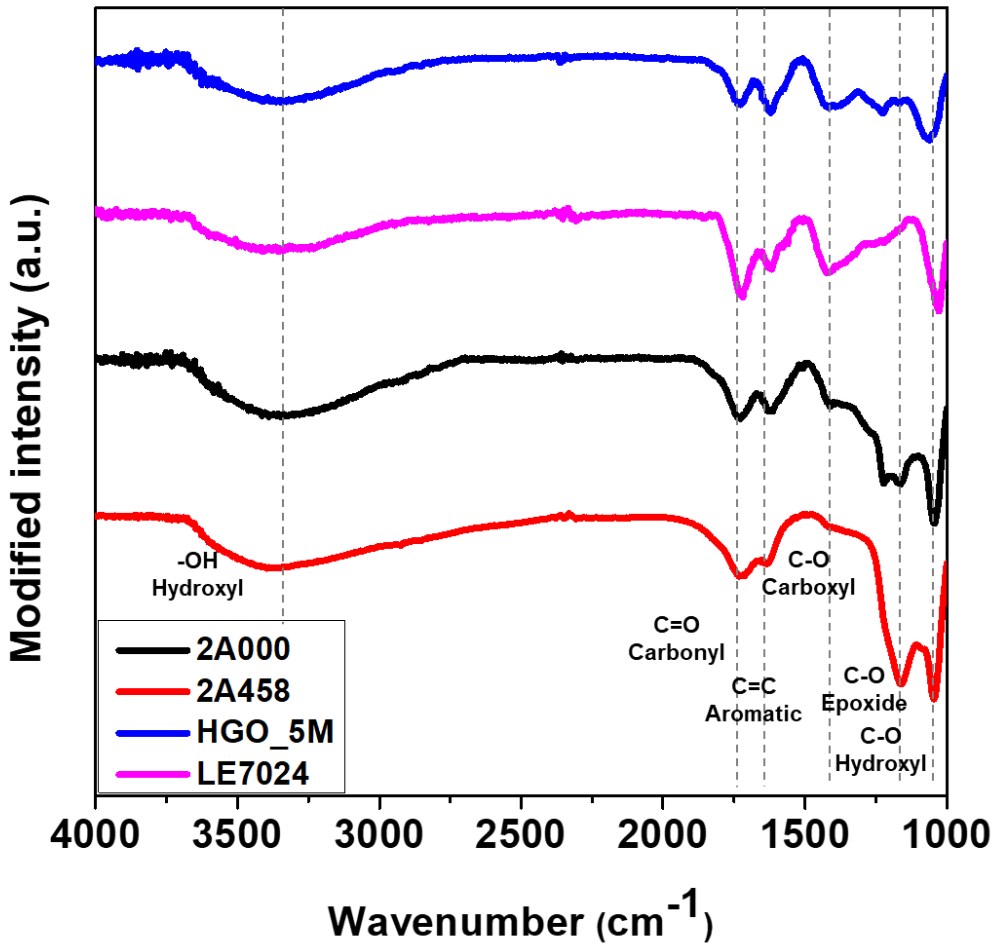

Figure 3.2 Fourier transform infrared (FT-IR) results of GO with modified Hummers method.

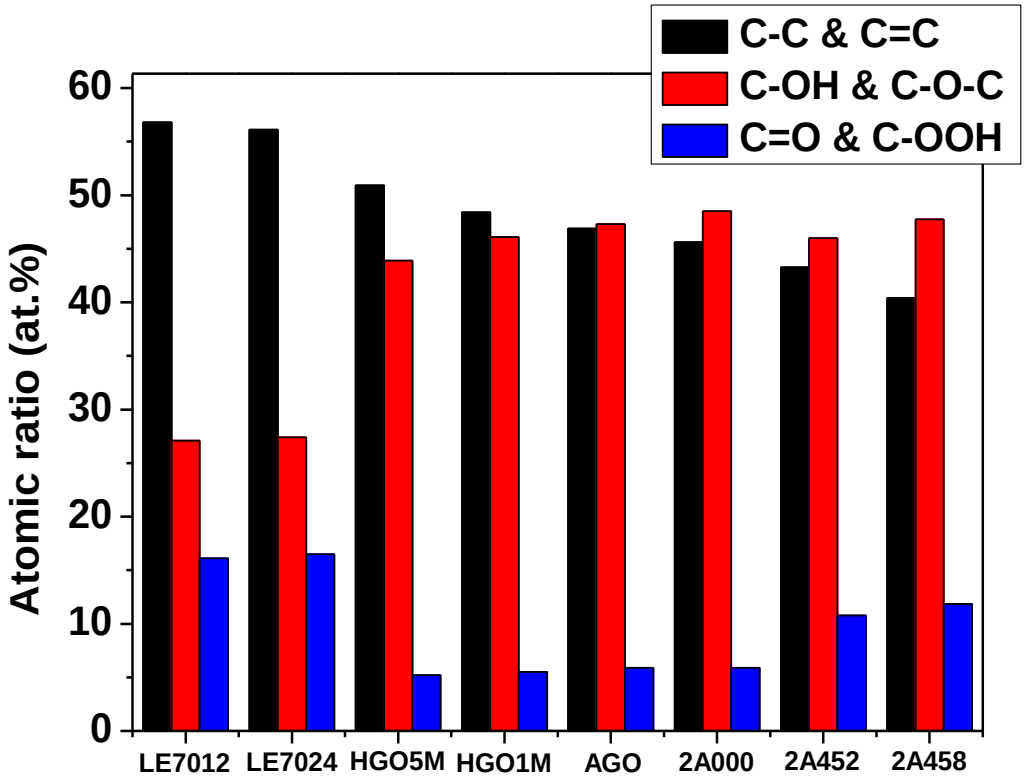

Figure 3.3 Binding ratio of carbon atoms measured by X-ray photoelectron spectroscopy (XPS) results of GO with modified Hummers method.

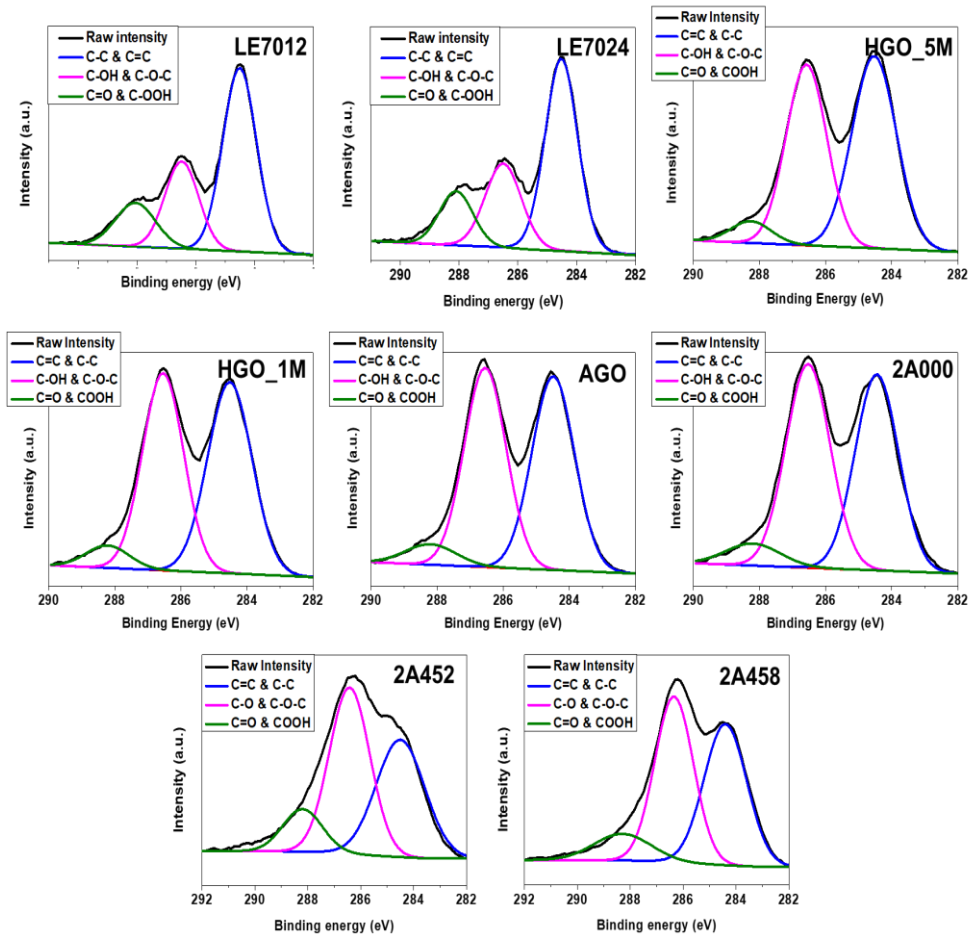

Figure 3.4 Deconvoluted C1s peak measured by X-ray photoelectron spectroscopy (XPS) results of GO with modified Hummers method.

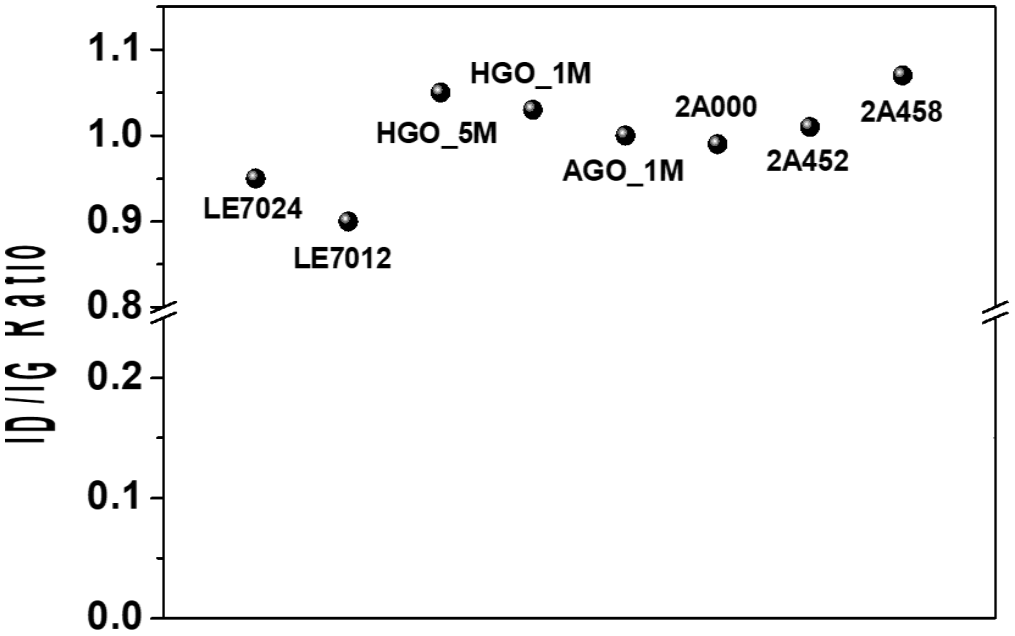

Figure 3.5 I_D/I_G ratio measured by Raman spectrum results of GO with modified Hummers method.

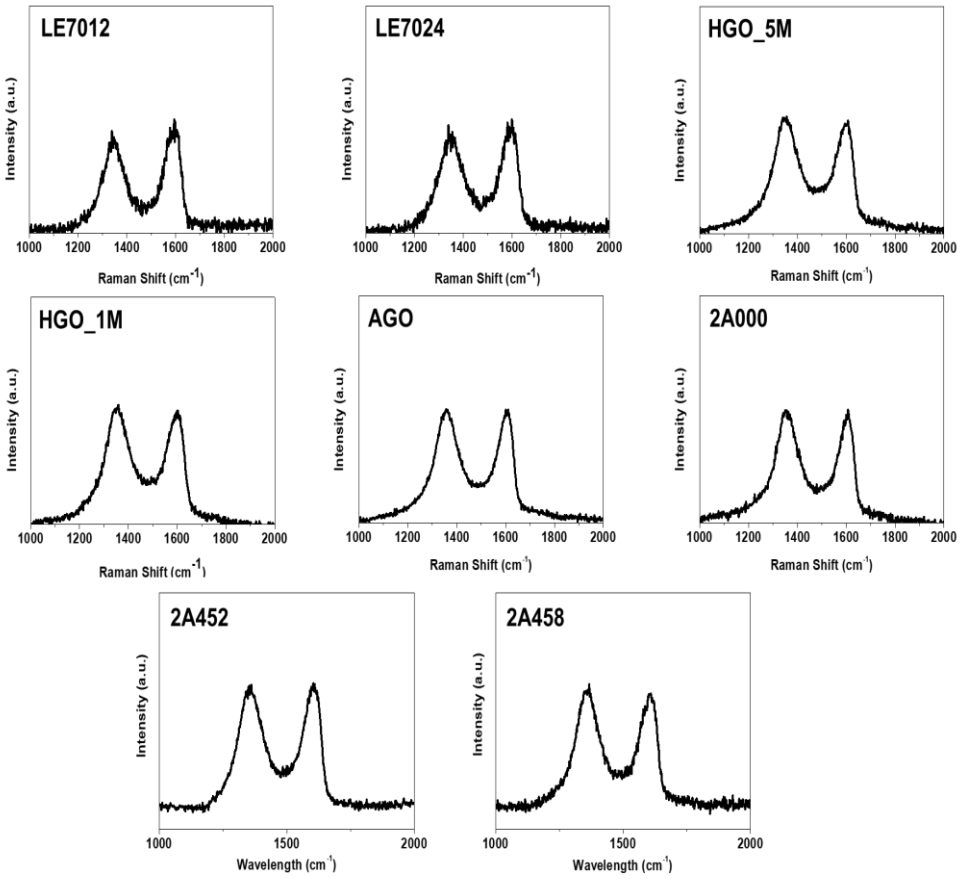

Figure 3.6 Raman spectra of GO with modified Hummers method.

A number of previous studies, showed that the band gap of materials, can be obtained by modified Tauc plot from the absorbance spectrum, [9, 11, 12] Therefore, we measured the absorbance of each GO from the ultraviolet to the visible range and we can obtain absorbance spectrums and Tauc plots of each sample successfully as shown in **Figure 3.7**. The band gap of GO showed narrower band gap by the decrement of oxidation degree from 1.45 to 2.5 eV. This implies that band gap of GO is strongly affected by its surface characteristics.

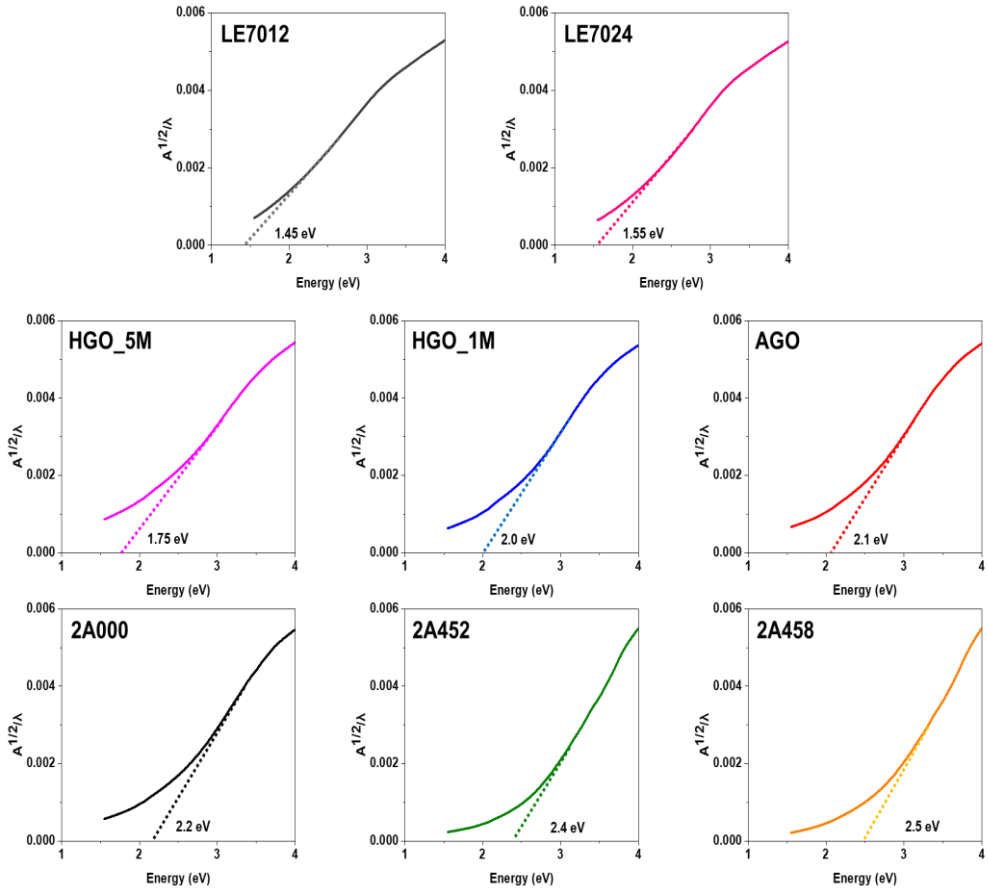

Figure 3.7 Modified Tauc plot of GO with modified Hummers method from the absorbance measured by UV-vis spectra.

In case of graphene oxide, functional groups is reduced from the low temperature because of existence of epoxide group, which shows low thermal stability and the band gap of GO based graphene, especially GO, shows unstable band gap. In order to apply GO based graphene in industrial field, the stability of band gap is also important for the accurate application of band gap to graphene based devices. Therefore, based on the result of thermogravimetric analysis result of chapter 5, the effect by elimination of epoxide group to the thermal stability of GO, we used Kissinger plot [16] to calculating activation energy for thermal reduction as shown in **Figure 3.8**. As a result, the thermal stability of graphene oxide increased by enlarged activation energy and epoxide eliminated graphene oxide (HGO) preserved its functional group until 32.8 h based on the XPS result of **Figure 3.9** of which the result after thermal treated of GO and HGO with 16h and 40h.

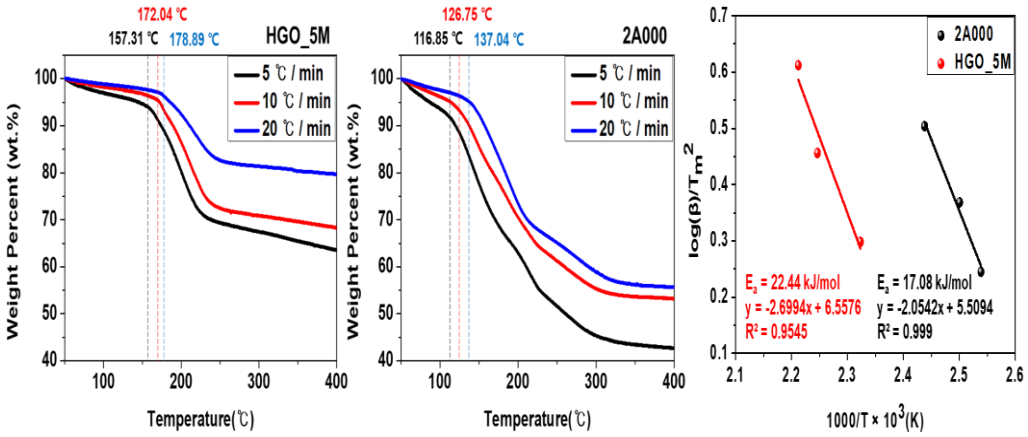

Figure 3.8 Thermogravimetric analysis (TGA) result of GO and HGO by differed heating ratio and those resultant Kissinger plot.

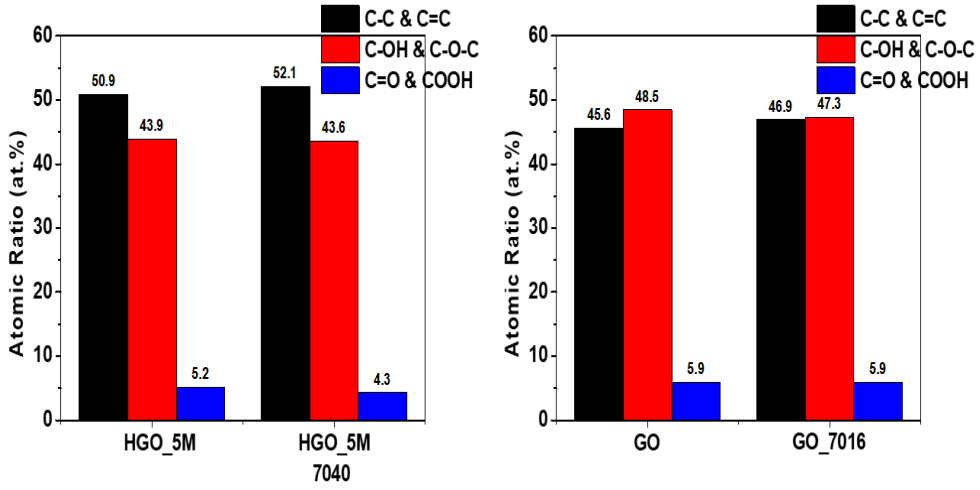

Figure 3.9 X-ray photoelectron spectroscopy (XPS) result of (left) HGO and 40 h annealed HGO and (right) GO and 16h annealed GO.

3.1.4 Conclusion

From measuring band gap of GO with differed surface characteristics, we made GO from three differed modification route of traditional Hummers method. After measurement of surface characteristics, especially oxidation degree and amount of boundary carbon, oxidation condition during preparation process strongly affect to the surface characteristics of resultant GO. These GO with surface characteristics showed band gap change with wide range by the exchange the ratio of sp^2 carbon and I_D/I_G ratio of itself. This implies that easy band gap engineering of GO is possible by simple modification of traditional Hummers method.

3.2 Band gap tuning of graphene by reduction

3.2.1 Introduction

For the use of GO for many application field, it should be reduced in for the generation of graphic sp^2 carbon. [17-22] Therefore, many researches tried produced reduced graphene oxide (RGO) by various route, but failed to succeed to realize graphene's great performance because of failed to preparing tailor fitted band gap engineering. In order to achieve this requirement for preparing band gap engineered RGO, many researches tried to fine the relationship between the surface characteristics and band gap of RGO, failed to appropriate relationship. However, RGO still shows the possibility of easy band gap engineering with controlling surface characteristics as shown in the study of **Chapter 2**.

There are various preparation method of RGO, but the methods can be divided into thermal reduction and chemical reduction route. [20, 22] The two ways showed different reduction mechanism and, even if chemical reduction, the reduction mechanism is different by the kind of reduction reagent. Thus, in this research of this chapter, band gap of RGO which are prepared by verified reduction route of graphene, especially thermally reduction and chemical reduction by hydrodic acid (HI) and sodium hydroxide (NaOH) was measured and its correlation with (non sp^2 carbon ratio) and (I_D/I_G ratio) which was defined in **Chapter 2** was tested that the relationship can be applied in real experiment results.

3.2.2 Experimental

3.2.2.1 Materials

Potassium persulfate ($K_2S_2O_8$, 98%), phosphorus pentoxide (P_4O_{10}, 98%), potassium permanganate ($KMnO_4$, 98%), natural flake graphite (Lot #: 17425HO, +100 mesh), and hydriodic acid (HI, 57% in water) were purchased from Sigma-Aldrich. Sulfuric acid (H_2SO_4, 98%), hydrogen peroxide (H_2O_2, 30%), and hydrochloric acid (HCl, 35–37%), and Sodium hydroxide (NaOH) were purchased from Daejung Chemicals & Metals. All chemicals were used as received.

3.2.2.2 Preparation of reduced graphene oxide

Graphene oxide (GO) were prepared through the conventional Hummers method. [4, 5, 7, 10] First, natural flake graphite was pretreated with $K_2S_2O_8$ and P_4O_{10} for the ease of exfoliation to single layer. 10.0 g of $K_2S_2O_8$ and 10.0 g of P_4O_{10} were fully dissolved in 50 mL of 98% H_2SO_4 while vigorously stirring at 80°C. 5.0 g of graphite was slowly added to the mixture. The mixture was continuously stirred for 24 hours at the same temperature, and poured into 2 L of deionized water. The pretreated graphite was washed with excess water using repeated vacuum filtrations until pH of graphite became neutral, then dried in a vacuum oven under room temperature. 3.0 g of this pretreated graphite was dispersed into 138 mL of H_2SO_4 that had been cooled to 0°C 18.0 g of $KMnO_4$ added very carefully added so as to prevent the temperature from rising above 50°C. The reaction transferred to a 35°C and stirred in 300 rpm.

After 2 hours, 1/3 of the mixture was poured in water/ H_2O_2 mixture for direct finishing of oxidation and this mixture is ultra-centrifuged at 13000 rpm with 3.4 % HCl 3 times. The precipitant was repeatedly washed with and completely neutralized by exchanging the solvent with water in repeated ultra-

centrifugations at 13000 rpm 5 times. For eliminating un-exfoliated graphite, the precipitant was centrifuged at 4000 rpm and the supernatant was gained.

For the reduction of GO, 20mg of aqueous GO dispersion was dried in Teflon dish for overnight and put it into horizontal furnace with inert air. The GO paper was thermally annealed to 300, 500, and 1100 °C with the heating rate of 5 °C min for the thermally reduction of GO. We named those RGO as RGO_300, RGO_500, and RGO_1100. Besides GO paper was immersed in HI and NaOH with the concentration of 0.1M, 0.01M and 0.001M for the different degree of chemical reduction. We named those RGO as RGO_HI_0.1M, RGO_HI_0.01M, RGO_HI_0.001M, RGO_SH_0.1M, RGO_SH_0.01M, and RGO_SH_0.001M.

3.2.2.3 Characterization

To study the oxygen-containing functional groups of the samples, the functional groups were quantified by performing XPS with an AXIS-HSi spectrometer (Kratos). The obtained C1s spectra were fitted and deconvoluted using XPSPEAK41 software. FTIR spectra of the GO, AGO and HGO samples were recorded with a Thermo Scientific Nicolet TM iS10 spectrometer to obtain additional information about their functional groups. The scan range was 400–4,000 cm-1 in attenuated total reflection (ATR) mode. Thermogravimetric analysis (TGA) was carried out under nitrogen flow with a heating rate of 10°C/min by using an SDTQ600 instrument (TA Instruments). Raman spectrum was obtained using a Raman plus confocal laser Raman microscope (Nanophoton) with a 532 nm Nd-YAG laser source. The optical absorbance data of the RGO within the UV-visible region were obtained by using a UV-Vis-NIR Cary 5000 spectrometer (Varian) with a scan range of 400-700 nm. And from the previous studies, we measure band gap of graphene oxides using modified Tauc plot. [9, 11, 12]

3.2.3 Results and discussion

From the previous researches, reduction of GO by HI, NaOH and heat was defined as shown in **Figure 3.10**. [9, 23-25] Based on this reaction formula, reduction by heat can reduce all kinds of functional groups, HI can reduce hydroxyl and epoxide, NaOH only reduce hydroxyl, it can be estimated that heat can reduce GO in highest degree and HI and NaOH is followed.

For comparing the populations of the functional groups, X-ray photoelectron spectroscopy (XPS), fourier transform infrared (FTIR) spectroscopy, thermogravimetric analysis (TGA) were used. Decrement of the amount of functional group and increment of sp^2 carbon of RGO can be shown in the weight loss of the TGA result **Figure 3.11** as like in **Chapter 3.1**. Each RGO showed improved thermal stability because of the dramatically decreased functional group and increased sp^2 carbon of itself. [5, 13]

As shown in **Figure 3.12** of FTIR spectrum normalized by the C=C double bond peak of aromatic carbon (1633 cm^{-1}) The absorption peaks of hydroxyl and epoxide groups (1105 cm^{-1}, 1248 cm^{-1}, and 3300 cm^{-1}) [5, 9, 13, 14] were smaller in the case of increment of reduction degree as shown in XPS result of increment of sp^2 carbon ratio as shown in **Figure 3.13** and **Figure 3.14**. [5, 9, 13, 14] Especially, the peak of epoxide showed highest intensity in NaOH reduced graphene because of epoxide group of GO does not reacted with NaOH as shown in reaction formula of **Figure 3.10**. Colligate the result of cauterization of surface characteristics of RGO, thermally reduction shows the highest reduction degree and the estimation of reduction degree based on the reaction formula of **Figure 3.10** is appropriate.

In order to verify that the degree of electron scattering by boundary carbon, were characterized by Raman. [9, 15] As shown in **Figure 3.15** and **Figure 3.16** rGO SH showed has a low I_D/I_G ratio (up to 1.0) by edge selectively oxidation, which

completely differs from other other RGO (~1.28). In the case of RGO_HI, showed higher I_D/I_G ratio than thermally reduced RGO in spite of the lower reduction degree comes from generated boundary carbon by remained hydroxyl group after reduction as shown in the reduction formula as shown in **Figure 3.10.**

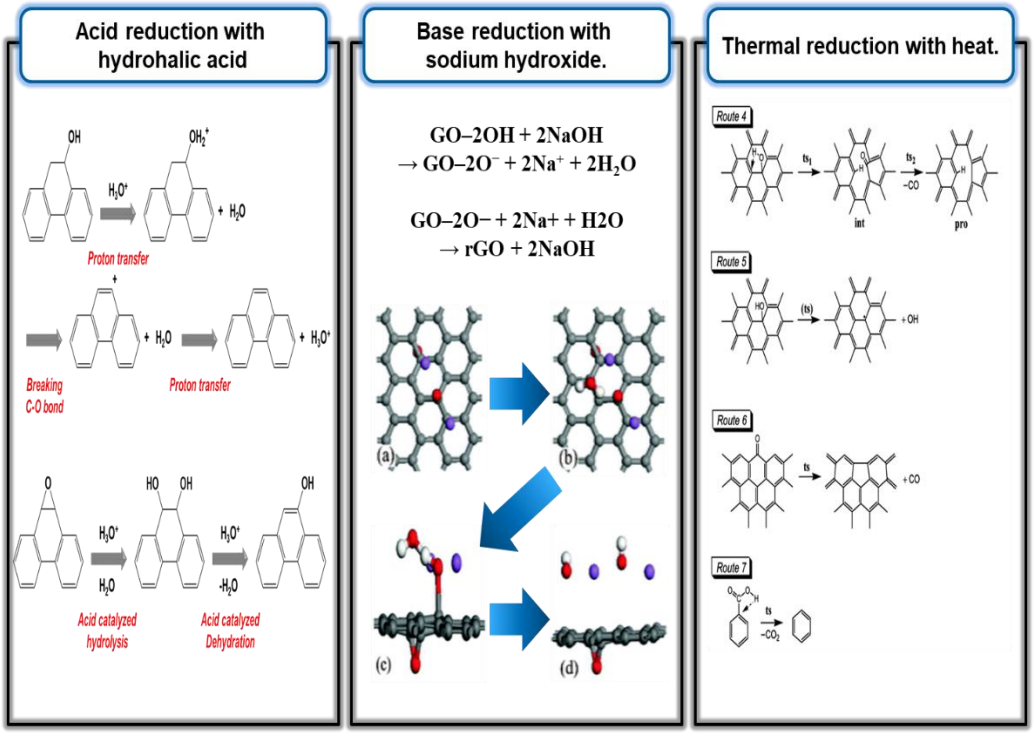

Figure 3.10 GO reduction mechanism by (left) hydriodic acid (HI) (middle) sodium hydroxide (NaOH) (right) Heat proposed in previous study. [9, 23-25]

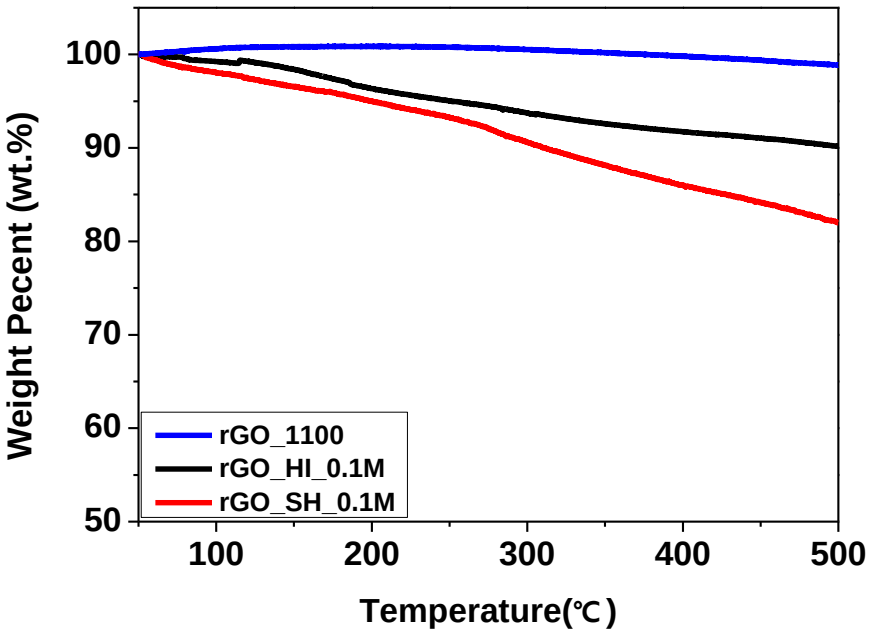

Figure 3.11 Thermogravimetric analysis (TGA) results of RGO reduced by heat, HI, and NaOH

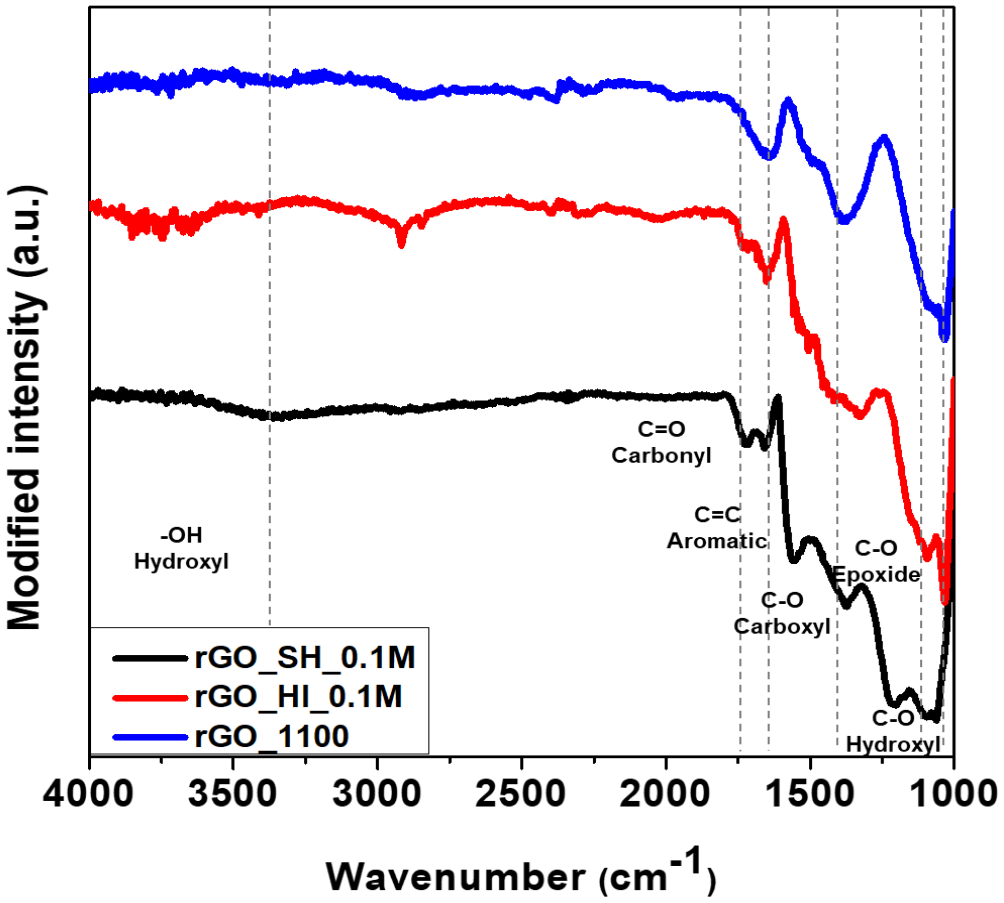

Figure 3.12 Fourier transform infrared (FT-IR) results of RGO reduced by heat, HI, and NaOH.

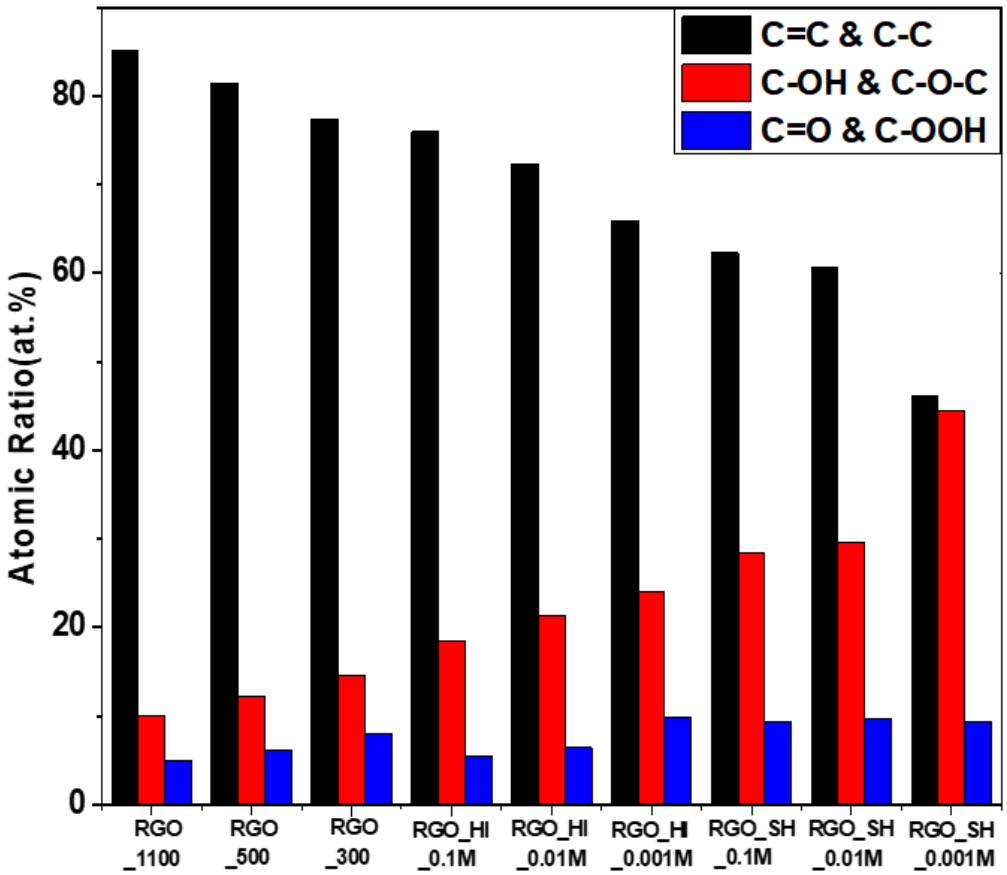

Figure 3.13 Binding ratio of carbon atoms measured by X-ray photoelectron spectroscopy (XPS) results of reduced by heat, HI, and NaOH.

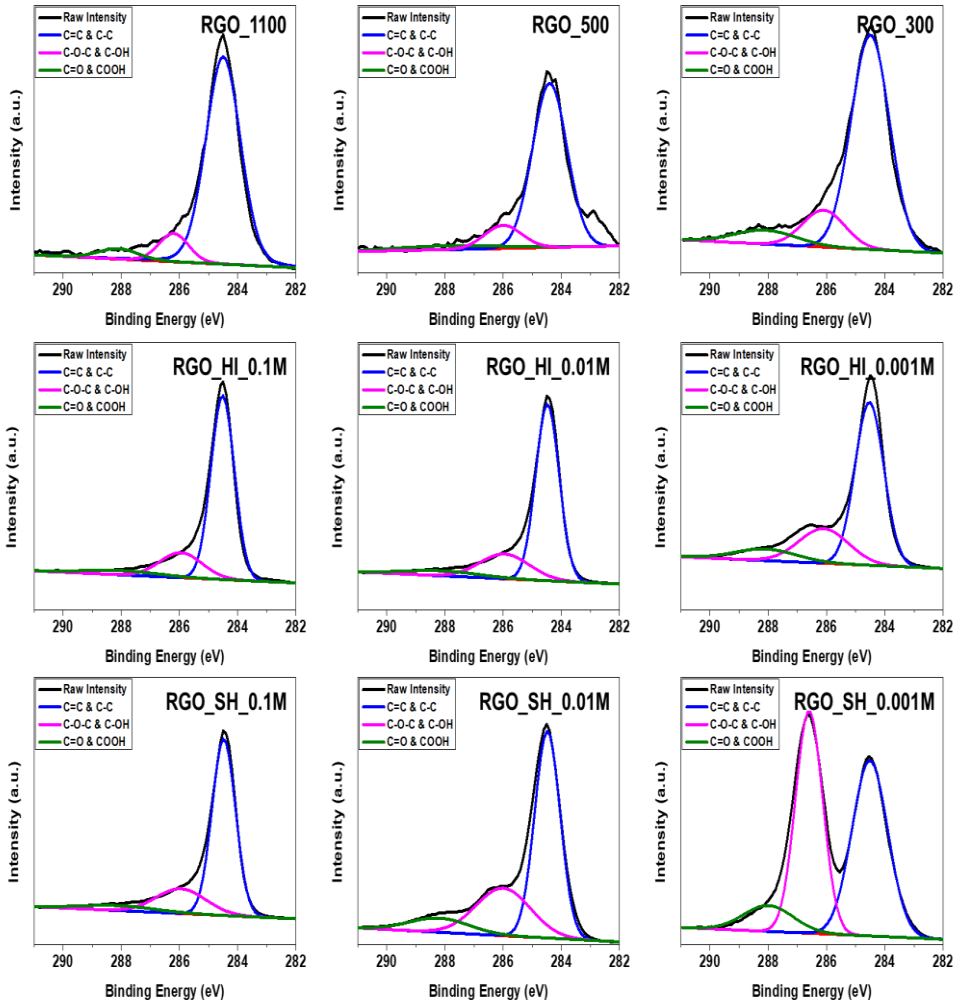

Figure 3.14 Deconvoluted C1s peak measured by X-ray photoelectron spectroscopy (XPS) results of reduced by heat, HI, and NaOH.

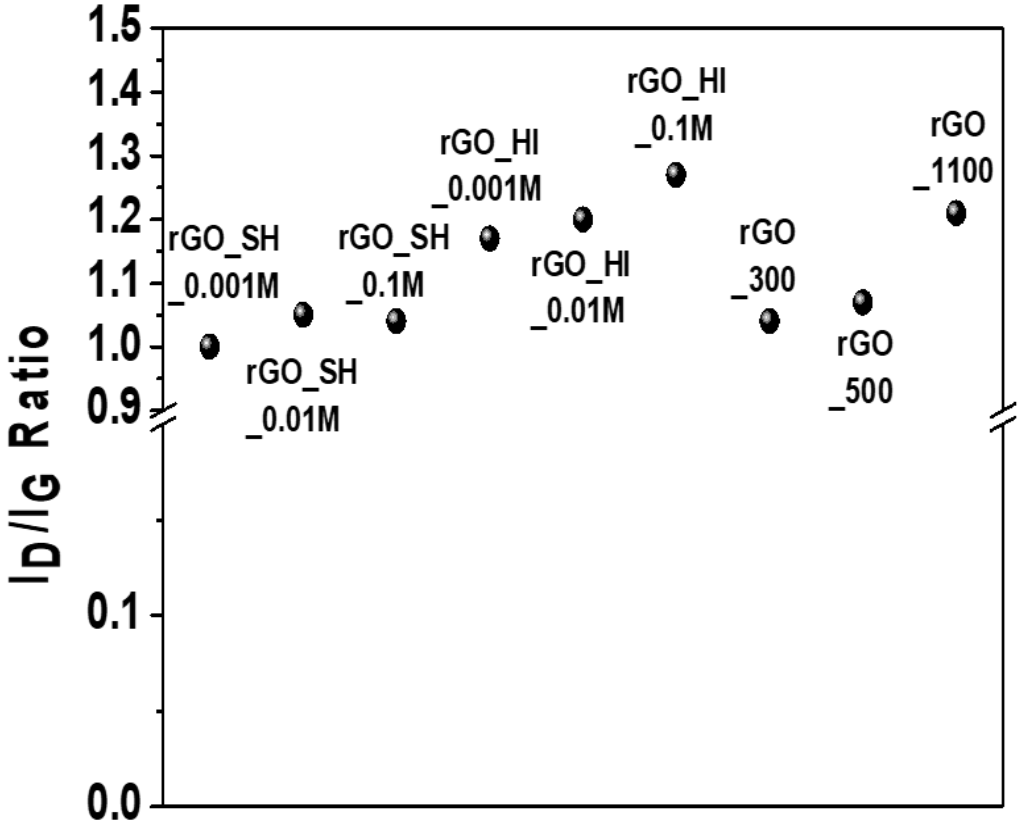

Figure 3.15 I_D/I_G ratio measured by Raman spectrum results of reduced by heat, HI, and NaOH.

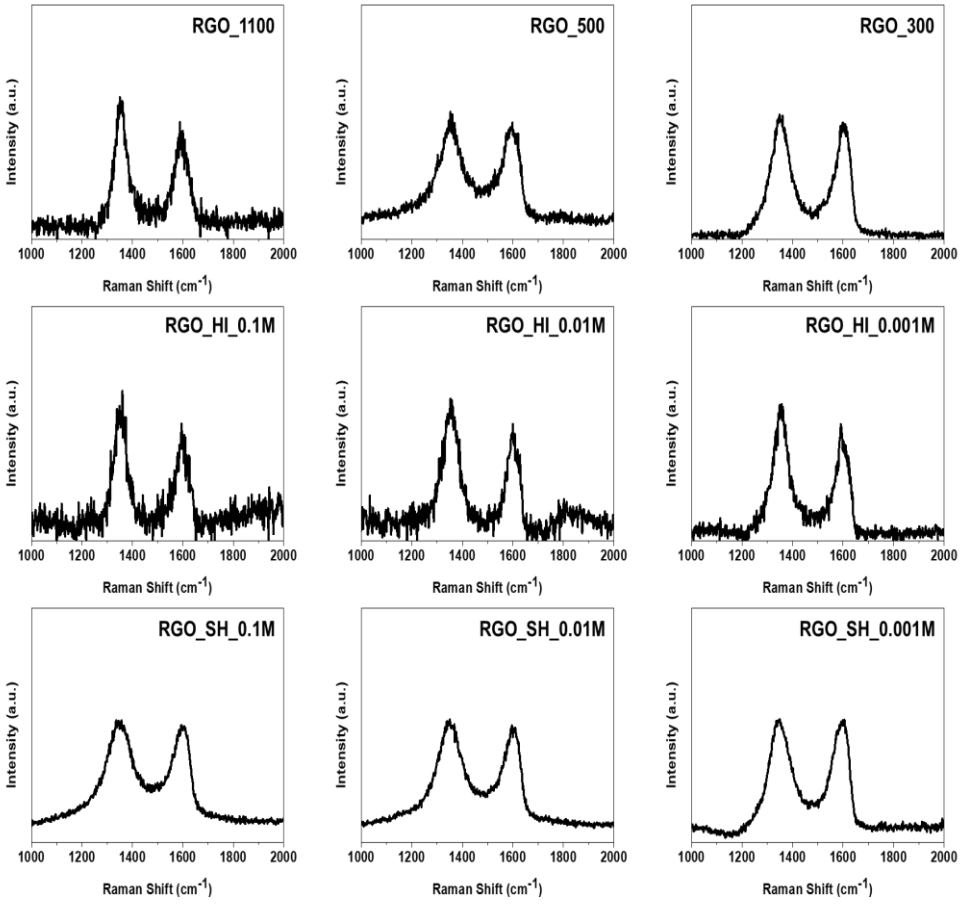

Figure 3.16 Raman spectra of reduced by heat, HI, and NaOH.

As shown in the case of GO of **Chapter 3.1**, band gap of RGO can be obtained by modified Tauc plot from the absorbance spectrum, [9, 11, 12] Therefore, we measured the absorbance of each RGO film which deposited on glass from the ultraviolet to the visible range and we can obtain absorbance spectrums and Tauc plots of each sample successfully as shown in **Figure 3.17**. The band gap of RGO showed narrower band gap by the increment of reduction degree from 0.4 to 2.1 eV. This implies that band gap of RGO is also strongly affected by its surface characteristics.

Based on the result of **Chapter 3.1** and **Chapter 3.2**, we colligate the band gap, ratio of non sp^2 carbon ratio, and I_D/I_G ratio in order to verifying the established relationship of **Chapter 2** from the theoretical view. [26-33] After the linear plot as shown in **Figure 3.18**, the calculation and experimental results shows great coincidence and it can be told that band gap of GO based graphene are linearly increased by the multiple of ratio of non sp^2 carbon ratio and I_D/I_G ratio.

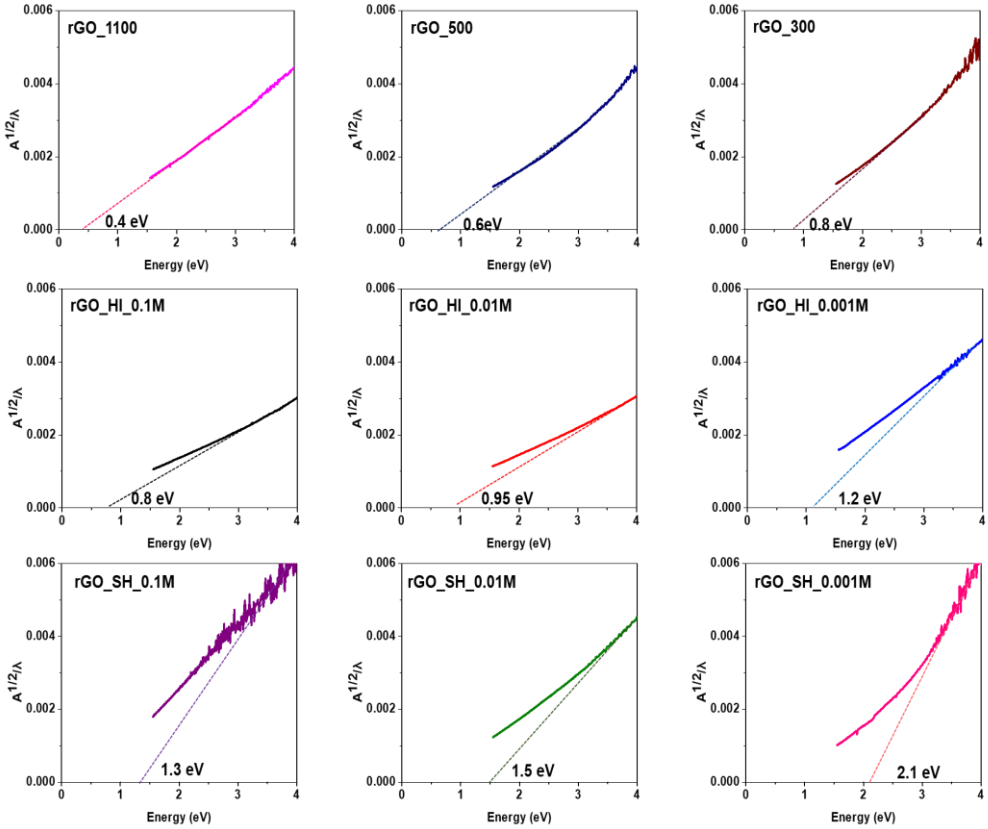

Figure 3.17 Modified Tauc plot of reduced by heat, HI, and NaOH from the absorbance measured by UV-vis spectra.

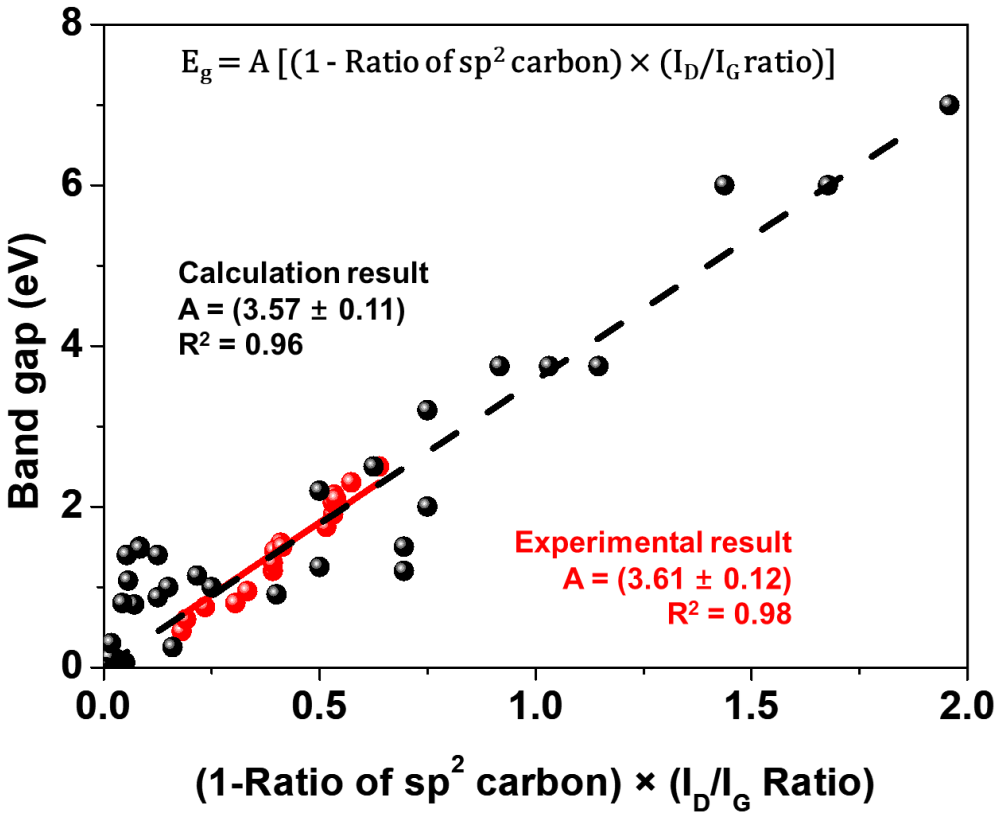

Figure 3.18 Linear plot of band gap of GO based graphene plotted by the multiple of (non sp^2 carbon ratio) and (I_D/I_G ratio).

3.2.4 Conclusion

From measuring band gap of RGO with differed surface characteristics, we prepared RGO from three differed reduction route including thermal and chemical method. After measurement of surface characteristics, especially reduction degree and amount of boundary carbon, reduction method strongly affect to the surface characteristics of resultant RGO. These RGO with surface characteristics showed band gap change with wide range by the exchange the ratio of sp^2 carbon and I_D/I_G ratio of itself. After linear plotting combined with the result of GO, the trend showed great coincidence with the calculation result and this implies that easy band gap engineering of GO based graphene is possible by simple modification of oxidation and reduction method.

3.3 Band gap tuning of graphene by hybridization.

3.2.1 Introduction

GO based graphene has been typically used in hybridized from with other materials for the enhancement of the performance of itself by application of the great performance of graphene. [34, 35] However when GO based graphene is simply mixed with other materials, the whole system showed different band gap but any studies found any reasons of alternating whole band gap by adding GO based graphene.

Therefore, in **Chapter 2.4**, the way of estimating band gap of GO based graphene based composite was proposed from the previous theoretically calculated results. As a result, band gap and work function of GO based graphene act as important parameters that determine the band gap of hybridized system. [36-38] However, the experimental evidence are not studied well and experimentally calculated band gap of GO based graphene composite with typically used materials like metal oxides should be presented.

Thus, we tried to find the experimental researches tried to defined the accurate band gap of GO based composite materials and in the case RGO with some traditional materials like zinc oxide (ZnO) and titanium oxide (TiO_2) showed similar results with the band gap which calculated based on **Chapter 2.4**. Plus, the case of indium-gallium-zinc oxide (IGZO), which are typically used to produce transistor device, is composited with RGO and band gap of IGZO/RGO composite are calculated and measured in this chapter.

3.3.2 Experimental

3.3.2.1 Materials

Potassium persulfate ($K_2S_2O_8$, 98%), phosphorus pentoxide (P_4O_{10}, 98%), potassium permanganate ($KMnO_4$, 98%), natural flake graphite (Lot #: 17425HO, +100 mesh), were purchased from Sigma-Aldrich. Sulfuric acid (H_2SO_4, 98%), hydrogen peroxide (H_2O_2, 30%), hydrochloric acid (HCl, 35–37%), and ethyl alcohol (anhydrous) were purchased from Daejung Chemicals & Metals. Soluble indium-gallium-zinc oxide (IGZO, iXsenic) was purchased from Evonik. All chemicals were used as received.

3.3.2.2 Preparation of IGZO/reduced graphene oxide hybrid.

Graphene oxide (GO) were prepared through the conventional Hummers method. [4, 5, 7, 10] First, natural flake graphite was pretreated with $K_2S_2O_8$ and P_4O_{10} for the ease of exfoliation to single layer. 10.0 g of $K_2S_2O_8$ and 10.0 g of P_4O_{10} were fully dissolved in 50 mL of 98% H_2SO_4 while vigorously stirring at 80°C. 5.0 g of graphite was slowly added to the mixture. The mixture was continuously stirred for 24 hours at the same temperature, and poured into 2 L of deionized water. The pretreated graphite was washed with excess water using repeated vacuum filtrations until pH of graphite became neutral, then dried in a vacuum oven under room temperature. 3.0 g of this pretreated graphite was dispersed into 138 mL of H_2SO_4 that had been cooled to 0°C 18.0 g of $KMnO_4$ added very carefully added so as to prevent the temperature from rising above 50°C. The reaction transferred to a 35°C and stirred in 300 rpm.

After 2 hours, the mixture was poured in water/ H_2O_2 mixture for direct finishing of oxidation and this mixture is ultra-centrifuged at 13000 rpm with 3.4 % HCl 3 times. The precipitant was repeatedly washed with and completely neutralized by exchanging the solvent with water in repeated ultra-centrifugations at 13000

rpm 5 times. For eliminating un-exfoliated graphite, the precipitant was centrifuged at 4000 rpm and the supernatant was gained. The solvent of gained GO was exchanged to ethanol and mixed with soluble IGZO in various concentration of 0.05, 0.1 0.5, 1.0 and 4.0 wt.% and fabricated this composite in glass substrate. After fabrication, the IGZO/GO composite were annealed at 500°C in inert atmosphere. The IGZO/RGO was named as IGZO/RGO_0.05, IGZO/RGO_0.1, IGZO/RGO_0.5, IGZO/RGO_1, and IGZO/RGO_4 by the altered concentration of RGO.

3.3.2.3 Characterization

To study the oxygen-containing functional groups of the samples, the functional groups were quantified by performing XPS with an AXIS-HSi spectrometer (Kratos). The obtained C1s spectra were fitted and deconvoluted using XPSPEAK41 software. Raman spectrum was obtained using a Raman plus confocal laser Raman microscope (Nanophoton) with a 532 nm Nd-YAG laser source. UPS spectrum was obtained using UPS of PHI 5800 ESCA System with a monochromatized Al Kα radiation source (h = 1486.6 eV); the angle between the excitation and detection radiation was 90°, while the takeoff angle was 45°

The optical absorbance data of the RGO within the UV-visible region were obtained by using a UV-Vis-NIR Cary 5000 spectrometer (Varian) with a scan range of 400-700 nm. And from the previous studies, we measure band gap of graphene oxides using modified Tauc plot. [9, 11, 12]

.

3.3.3 Results and discussion

In order to estimate the band gap of RGO based composite, band gap and work function has to be decided as shown in **Chapter 2.4**. Band gap of RGO is plotted as shown in Chapter 3.1, band gap of RGO can be calculated, and therefore, band diagram of RGO can be estimated when work function of graphene is decided. Thus, work function of RGO of previous researches [39-44] is plotted linearly by the dangle oxygen atom with the point of view suggested in **Chapter 2.4** and found that high coincidence with calculation data. (**Figure 3.19**) This indicates that work function of RGO can be easily known when oxygen content of itself is experimentally obtained.

Based on this data and band diagram of some metal oxides like ZnO and TiO_2 as studied from the previous work as shown in **Figure 3.20**, [45] band gap them composited with RGO can be calculated considering metal oxide and graphene are mixed ideal with the structure of periodically repeated 1:1 unit cell.

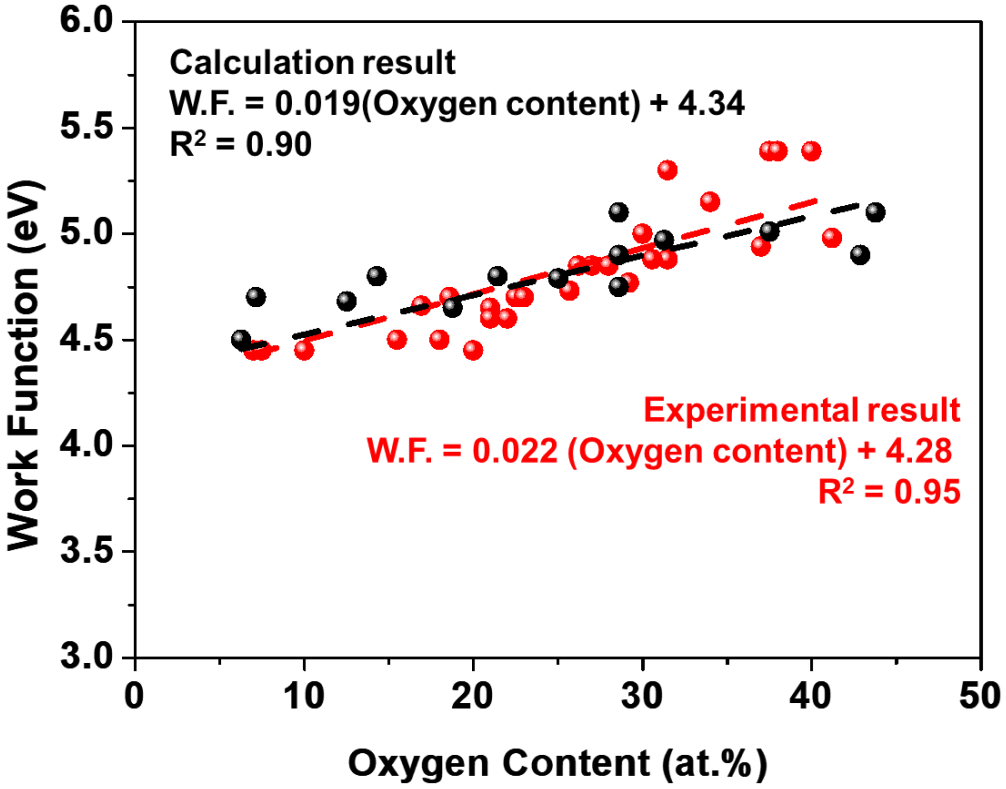

Figure 3.19 Linear plot of work function of GO based graphene plotted by the oxygen content. [39-44]

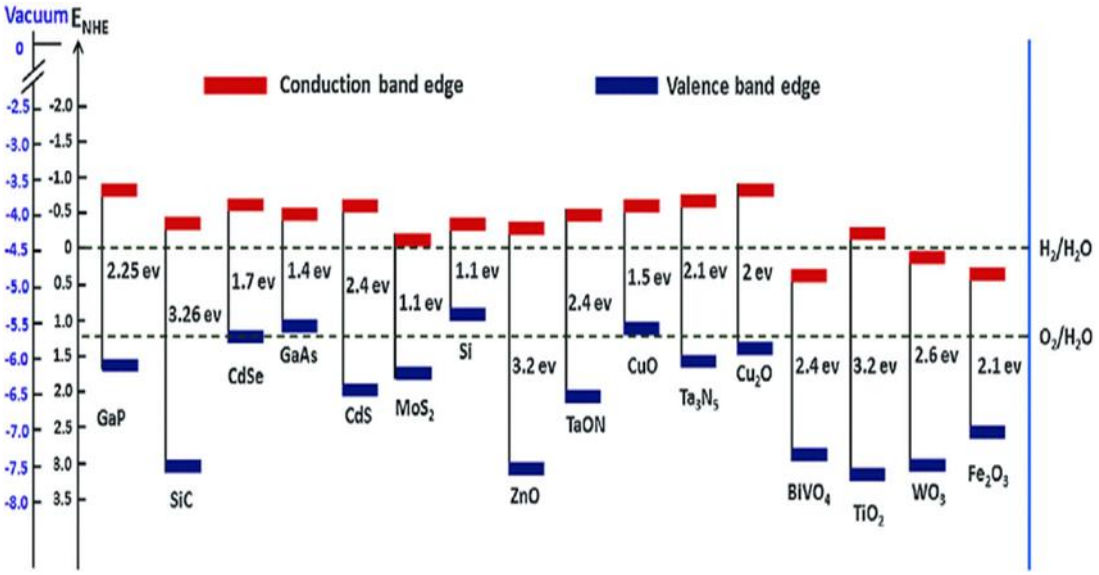

Figure 3.20 Band diagram of typical metal oxides proposed in previous studies. [45]

In the case of ZnO/RGO after annealed in 450°C for thermal reduction of GO, [46, 47] band gap and work function of graphene can be decided to 0.6eV and 4.6 eV, therefore, band gap of ZnO/RGO can be calculated to 2.5 eV when the weight percent of RGO is 40.4 wt.% in case of ideal mixture. Therefore, when measuring band gap with tauc plot, band gap of ZnO/RGO is decreased to 2.8 eV when weigh percent of RGO is increased. (**Figure 3.21**)

This phenomena is also can be found in the case of TiO_2/RGO annealed to 180°C for reduction of GO. [48] Band gap and work function of graphene can be decided to 0.8eV and 5.0 eV, therefore, band gap of TiO_2/RGO can be calculated to 2.3 eV when the weight percent of RGO is 19.4 wt.% in case of ideal mixture. Therefore, when measuring band gap with tauc plot, band gap of TiO_2/RGO is decreased to 2.7 eV when weigh percent of RGO is increased. (**Figure 3.22**)

In order to see directly the case of IGZO/RGO annealed to 500 °C for reduction of GO, we mixed IGZO with RGO in the weight percent of 0.05, 0.1, 0.5, 1 and 4 weight percent. After measuring percent of sp2 carbon, I_D/I_G ratio, and band gap as shown in **Figure 3.23**, RGO annealed in 500°C shows the band gap of 0.6 eV. When measuring work function using ultraviolet photoelectron spectroscopy (UPS), work function of RGO is calculated to 4.6 eV. Therefore, considering band gap diagram of IGZO, band gap of IGZO/RGO can be calculated to 2.4 eV considering when the weight percent of RGO is 4.5 wt.% in case of ideal mixture. Band gap of IGZO/RGO calculated by tauc plot is converged to 2.4 eV by the increment of weight percent of RGO increased to 4 wt.% and it is perfectly matches with the calculated result. (**Figure 3.24**) This indicates that band gap estimation with the point of view from **Chapter 2.4** is appropriate in RGO based composite.

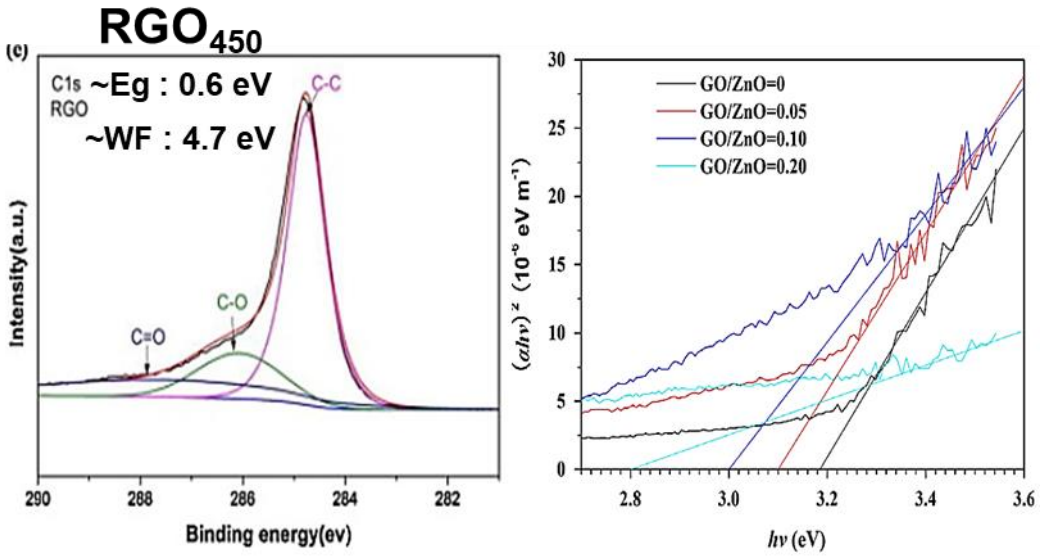

Figure 3.21 (left) Deconvoluted C1s peak measured by X-ray photoelectron spectroscopy (XPS) results of RGO reduced at 450°C (right) Tauc plot of ZnO/RGO from the absorbance measured by UV-vis spectra. [46, 47]

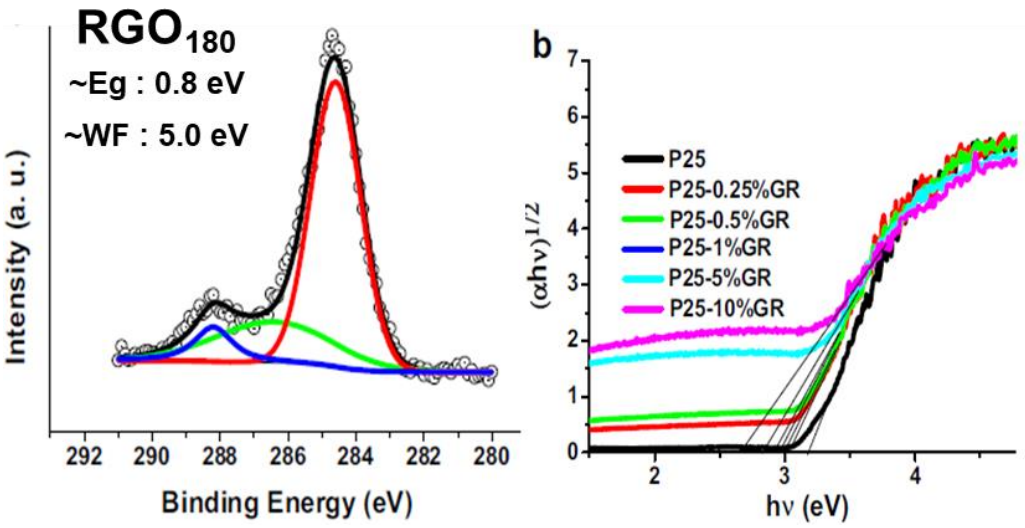

Figure 3.22 (left) Deconvoluted C1s peak measured by X-ray photoelectron spectroscopy (XPS) results of RGO reduced at 180°C (right) Tauc plot of TiO_2/RGO from the absorbance measured by UV-vis spectra. [48]

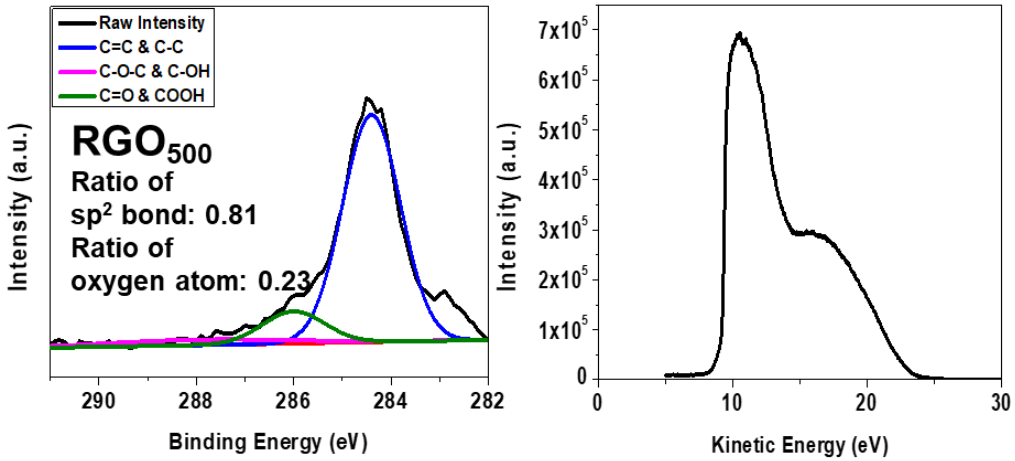

Figure 3.23 (left) Deconvoluted C1s peak measured by X-ray photoelectron spectroscopy (XPS) results (right) Secondary electron spectra measured by UPS RGO reduced at 500°C.

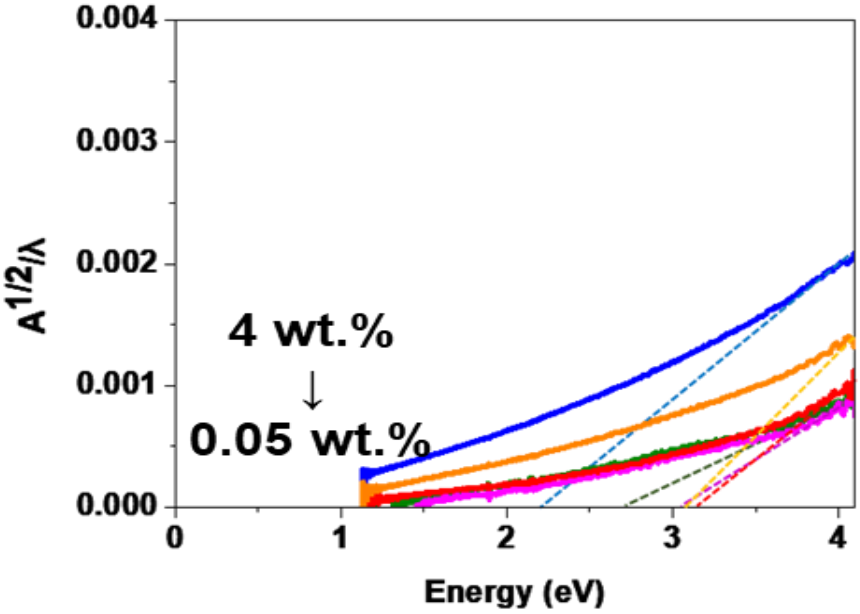

Figure 3.24 Modified Tauc plot of IGZO/RGO that weight percent of 0.05 wt.% ~ 0.4 wt.% from the absorbance measured by UV-vis spectra.

3.3.4 Conclusion

In order to define the insight that deciding band gap of GO based graphene composite materials that suggested in **Chapter 2.4**, some experimental case study are required for supporting this theoretical view.

From the case study that calculating band gap of RGO based composite with differed metal oxides, ZnO, TiO_2 and IGZO, we calculated band gap and work function of RGO from the proven relationship between surface characteristics, band gap and work function of RGO and the experimental band gap controlled by weight percent of RGO is shown as experimental data matches with the theatrically calculated result. In spite of the small amount of case study, This shows that band gap of composite materials based on graphene from GO can be controlled by the surface characteristics and weight percent of GO based graphene itself.

3.4 **Conclusion**

Based on the theoretical background suggest in **Chapter 2**, experimental support is proposed in this chapter. By the oxidation, reduction and hybridization, band gap of GO based graphene and its composite materials showed the trend of band gap that matches with the theoretical considerations of **Chapter 2**. This indicates that the fine band gap tuning of GO based graphene and its hybrid materials can be considered as an easy work by the controlled preparation method that affects the surface nature of GO based graphene.

Plus, the result from the work of **chapter 2** and **Chapter 3** shows the way of easy band gap engineering of GO based graphene for various applications of conductive and semiconductive devices and it is also should be defined in followed chapter.

3.5 **Reference**

[1] J. Kim, L.J. Cote, J. Huang, Two Dimensional Soft Material: New Faces of Graphene Oxide, Accounts of Chemical Research 45(8) (2012) 1356-1364.

[2] K.S. Novoselov, V.I. Falko, L. Colombo, P.R. Gellert, M.G. Schwab, K. Kim, A roadmap for graphene, Nature 490(7419) (2012) 192-200.

[3] C. Soldano, A. Mahmood, E. Dujardin, Production, properties and potential of graphene, Carbon 48(8) (2010) 2127-2150.

[4] M.S. Chang, Y.S. Kim, J.H. Kang, J. Park, S.J. Sung, S.H. So, K.T. Park, S.J. Yang, T. Kim, C.R. Park, Guidelines for Tailored Chemical Functionalization of Graphene, Chemistry of Materials 29(1) (2017) 307-318.

[5] J.H. Kang, T. Kim, J. Choi, J. Park, Y.S. Kim, M.S. Chang, H. Jung, K.T. Park, S.J. Yang, C.R. Park, Hidden Second Oxidation Step of Hummers Method, Chemistry of Materials 28(3) (2016) 756-764.

[6] B.C. Brodie, On the Atomic Weight of Graphite, Philosophical Transactions of the Royal Society of London 149 (1859) 249-259.

[7] W.S. Hummers, R.E. Offeman, Preparation of Graphitic Oxide, Journal of the American Chemical Society 80(6) (1958) 1339-1339.

[8] L. Staudenmaier, Verfahren zur Darstellung der Graphitsäure, Berichte der deutschen chemischen Gesellschaft 31(2) (1898) 1481-1487.

[9] J. Park, Y. Kim, S.Y. Park, S.J. Sung, H.W. Jang, C.R. Park, Band gap engineering of graphene oxide for ultrasensitive NO2 gas sensing, Carbon 159 (2020) 175-184.

[10] N.I. Kovtyukhova, P.J. Ollivier, B.R. Martin, T.E. Mallouk, S.A. Chizhik, E.V. Buzaneva, A.D. Gorchinskiy, Layer-by-Layer Assembly of Ultrathin Composite Films from Micron-Sized Graphite Oxide Sheets and Polycations, Chemistry of Materials 11(3) (1999) 771-778.

[11] A. Mathkar, D. Tozier, P. Cox, P. Ong, C. Galande, K. Balakrishnan, A. Leela

Mohana Reddy, P.M. Ajayan, Controlled, Stepwise Reduction and Band Gap Manipulation of Graphene Oxide, The Journal of Physical Chemistry Letters 3(8) (2012) 986-991.
[12] S. Wang, I.S. Cole, Q. Li, Quantum-confined bandgap narrowing of TiO2 nanoparticles by graphene quantum dots for visible-light-driven applications, Chemical Communications 52(59) (2016) 9208-9211.
[13] M. Acik, G. Lee, C. Mattevi, A. Pirkle, R.M. Wallace, M. Chhowalla, K. Cho, Y. Chabal, The Role of Oxygen during Thermal Reduction of Graphene Oxide Studied by Infrared Absorption Spectroscopy, The Journal of Physical Chemistry C 115(40) (2011) 19761-19781.
[14] J. Park, Y.S. Kim, S.J. Sung, T. Kim, C.R. Park, Highly dispersible edge-selectively oxidized graphene with improved electrical performance, Nanoscale 9(4) (2017) 1699-1708.
[15] M.A. Pimenta, G. Dresselhaus, M.S. Dresselhaus, L.G. Cançado, A. Jorio, R. Saito, Studying disorder in graphite-based systems by Raman spectroscopy, Physical Chemistry Chemical Physics 9(11) (2007) 1276-1290.
[16] W.-Y. Jung, J.-I. Weon, Characterization of Thermal Degradation of Polymide 66 Composite: Relationship between Lifetime Prediction and Activation Energy, Polymer Korea 36 (2012).
[17] H. Jung, S.J. Yang, T. Kim, J.H. Kang, C.R. Park, Ultrafast room-temperature reduction of graphene oxide to graphene with excellent dispersibility by lithium naphthalenide, Carbon 63 (2013) 165-174.
[18] D. Kim, S.J. Yang, Y.S. Kim, H. Jung, C.R. Park, Simple and cost-effective reduction of graphite oxide by sulfuric acid, Carbon 50(9) (2012) 3229-3232.
[19] S. Mao, H. Pu, J. Chen, Graphene oxide and its reduction: modeling and experimental progress, RSC Advances 2(7) (2012) 2643-2662.
[20] S. Pei, H.-M. Cheng, The reduction of graphene oxide, Carbon 50(9) (2012) 3210-3228.

[21] S.J. Yang, T. Kim, H. Jung, C.R. Park, The effect of heating rate on porosity production during the low temperature reduction of graphite oxide, Carbon 53 (2013) 73-80.
[22] J. Park, Y.S. Cho, S.J. Sung, M. Byeon, S.J. Yang, C.R. Park, Characteristics tuning of graphene-oxide-based-graphene to various end-uses, Energy Storage Materials 14 (2018) 8-21.
[23] C. Chen, W. Kong, H.-M. Duan, J. Zhang, Theoretical simulation of reduction mechanism of graphene oxide in sodium hydroxide solution, Physical Chemistry Chemical Physics 16(25) (2014) 12858-12864.
[24] S. Pei, J. Zhao, J. Du, W. Ren, H.-M. Cheng, Direct reduction of graphene oxide films into highly conductive and flexible graphene films by hydrohalic acids, Carbon 48(15) (2010) 4466-4474.
[25] X. Gao, J. Jang, S. Nagase, Hydrazine and Thermal Reduction of Graphene Oxide: Reaction Mechanisms, Product Structures, and Reaction Design, The Journal of Physical Chemistry C 114(2) (2010) 832-842.
[26] S.D. Dabhi, P.K. Jha, Tuning the electronic band gap of graphene by oxidation, AIP Conference Proceedings 1665(1) (2015) 090013.
[27] L. Guo, R.-Q. Shao, Y.-L. Zhang, H.-B. Jiang, X.-B. Li, S.-Y. Xie, B.-B. Xu, Q.-D. Chen, J.-F. Song, H.-B. Sun, Bandgap Tailoring and Synchronous Microdevices Patterning of Graphene Oxides, The Journal of Physical Chemistry C 116(5) (2012) 3594-3599.
[28] H. Huang, Z. Li, J. She, W. Wang, Oxygen density dependent band gap of reduced graphene oxide, Journal of Applied Physics 111(5) (2012) 054317.
[29] R.J.W.E. Lahaye, H.K. Jeong, C.Y. Park, Y.H. Lee, Density functional theory study of graphite oxide for different oxidation levels, Physical Review B 79(12) (2009) 125435.
[30] M. Lundie, Ž. Šljivančanin, S. Tomić, Electronic and optical properties of reduced graphene oxide, Journal of Materials Chemistry C 3(29) (2015) 7632-

7641.
[31] F. Nasehnia, S. Mohammadpour Lima, M. Seifi, E. Mehran, First principles study on optical response of graphene oxides: From reduced graphene oxide to the fully oxidized surface, Computational Materials Science 114 (2016) 112-120.
[32] A. Nourbakhsh, M. Cantoro, A.V. Klekachev, G. Pourtois, J. Hofkens, M.H. van der Veen, M.M. Heyns, S. De Gendt, B.F. Sels, Single Layer vs Bilayer Graphene: A Comparative Study of the Effects of Oxygen Plasma Treatment on Their Electronic and Optical Properties, The Journal of Physical Chemistry C 115(33) (2011) 16619-16624.
[33] A. Nourbakhsh, M. Cantoro, T. Vosch, G. Pourtois, F. Clemente, M.H. van der Veen, J. Hofkens, M.M. Heyns, S. De Gendt, B.F. Sels, Bandgap opening in oxygen plasma-treated graphene, Nanotechnology 21(43) (2010) 435203.
[34] X. Li, L. Zhi, Graphene hybridization for energy storage applications, Chemical Society Reviews 47(9) (2018) 3189-3216.
[35] V.B. Mohan, K.-t. Lau, D. Hui, D. Bhattacharyya, Graphene-based materials and their composites: A review on production, applications and product limitations, Composites Part B: Engineering 142 (2018) 200-220.
[36] Y. Masuda, G. Giorgi, K. Yamashita, DFT study of anatase-derived TiO2 nanosheets/graphene hybrid materials, physica status solidi (b) 251(8) (2014) 1471-1479.
[37] W. Geng, X. Zhao, W. Zan, H. Liu, X. Yao, Effects of the electric field on the properties of ZnO–graphene composites: a density functional theory study, Physical Chemistry Chemical Physics 16(8) (2014) 3542-3548.
[38] P.N.O. Gillespie, N. Martsinovich, Origin of Charge Trapping in TiO2/Reduced Graphene Oxide Photocatalytic Composites: Insights from Theory, ACS Applied Materials & Interfaces 11(35) (2019) 31909-31922.
[39] X. Peng, F. Tang, A. Copple, Engineering the work function of armchair graphene nanoribbons using strain and functional species: a first principles study,

Journal of Physics: Condensed Matter 24(7) (2012) 075501.
[40] N. Yang, D. Yang, L. Chen, D. Liu, M. Cai, X. Fan, Design and adjustment of the graphene work function via size, modification, defects, and doping: a first-principle theory study, Nanoscale Research Letters 12(1) (2017) 642.
[41] H.-H. Huang, K.K.H. De Silva, G.R.A. Kumara, M. Yoshimura, Structural Evolution of Hydrothermally Derived Reduced Graphene Oxide, Scientific Reports 8(1) (2018) 6849.
[42] L. Sygellou, G. Paterakis, C. Galiotis, D. Tasis, Work Function Tuning of Reduced Graphene Oxide Thin Films, The Journal of Physical Chemistry C 120(1) (2016) 281-290.
[43] A. Misra, H. Kalita, A. Kottantharayil, Work Function Modulation and Thermal Stability of Reduced Graphene Oxide Gate Electrodes in MOS Devices, ACS Applied Materials & Interfaces 6(2) (2014) 786-794.
[44] J. Zhang, H. Song, D. Zeng, H. Wang, Z. Qin, K. Xu, A. Pang, C. Xie, Facile synthesis of diverse graphene nanomeshes based on simultaneous regulation of pore size and surface structure, Scientific Reports 6(1) (2016) 32310.
[45] A.G. Tamirat, J. Rick, A.A. Dubale, W.-N. Su, B.-J. Hwang, Using hematite for photoelectrochemical water splitting: a review of current progress and challenges, Nanoscale Horizons 1(4) (2016) 243-267.
[46] H.Y. He, Photoinduced superhydrophilicity and high photocatalytic activity of ZnO–reduced graphene oxide nanocomposite films for self-cleaning applications, Materials Science in Semiconductor Processing 31 (2015) 200-208.
[47] F. Zhao, B. Dong, R. Gao, G. Su, W. Liu, L. Shi, C. Xia, L. Cao, A three-dimensional graphene-TiO2 nanotube nanocomposite with exceptional photocatalytic activity for dye degradation, Applied Surface Science 351 (2015) 303-308.
[48] P. Cheng, Z. Yang, H. Wang, W. Cheng, M. Chen, W. Shangguan, G. Ding, TiO2–graphene nanocomposites for photocatalytic hydrogen production from

splitting water, International Journal of Hydrogen Energy 37(3) (2012) 2224-2230.

Part III.
Performance of a few representative devices based on graphene with fine-tuned band gap

Chapter 4. Electrode performance of a band gap tuned graphene

4.1 Introduction

Graphene oxide (GO), a highly dispersible two-dimensional (2D) carbon monolayer with oxygen functional groups, has been broadly researched because solution-processable graphene film can be prepared from GO colloidal suspension.[1-3] Numerous applications including transparent conducting film,[4-7] gas barrier film,[8] sensor,[9, 10], and supercapacitors[11-13] have been fabricated based on the GO colloidal suspension. While oxygen functional groups enhance the dispersibility of GO in solvents, they lead to relatively low performance of reduced GO (rGO) based applications. During the oxidation of graphite through Hummers method, π-conjugation of the graphene layer is inevitably destroyed to produce oxygen functional groups on the basal plane of the graphene layer.[14-16]

To avoid the intrinsic limitation of GO, preparation methods of graphene by physical exfoliation in liquid media have been studied [17, 18] such as exfoliation in appropriate solvents,[19-21] with the aid of surfactants,[22, 23] and in ionic liquid added solutions.[24, 25] The physical exfoliation method is expected to enable mass production of defect-free graphene for various applications. However, low concentration of the solution and insufficient single layered graphene are not suitable for the preparation of graphene ink. While ionic liquids are effective for increasing the concentration of graphene suspension, issues on synthesis condition and cost still remain for mass production. To improve the yield of single layer and the concentration of graphene suspension obtained by physical exfoliation, a number of studies on the pretreatment of graphite have been performed. Formation of graphite intercalate compounds by intercalating alkali metal,[26] halogen element,[27] metallic salts,[28-30] and other

intercalants[31-33] into graphite is a common pretreatment method. The intercalants increase the interlayer distance of graphite and decrease the van der Waals force between graphene layers, leading to the straightforward exfoliation of graphene. Edge-selective oxidation of graphite is another pretreatment method to enhance dispersion stability after exfoliation.[34-38] It is known that carboxyl groups are mainly generated on the edge of graphene oxide, and hydroxyl and epoxide groups are mainly generated on the basal plane of graphene oxide.[39] Therefore, by introducing carboxyl groups on the edge of graphite and using its higher edge reactivity than that of the basal plane, dispersion stability can be improved with less destruction of the conjugation state. Indeed, stable graphene suspension could be obtained through ball milling with weak acid[34, 35] or exchanging conditions of the established Hummers method.[36-38] Nevertheless, a low concentration of the graphene suspension (<0.7 mg/ml) prepared by these methods is a remaining issue to be used for solution processable graphene. For example, most of the transparent conducting films based on graphene suspension have been fabricated by a vacuum filtration method due to the low concentration of the graphene suspension, which decreases the availability of graphene suspension. Moreover, these modifications still have the possibilities of oxidation of the basal plane. In this research, we proposed a new method to prepare edge-selectively oxidized graphite and graphene for preparation of graphene ink with a high concentration.

In our previous report, we revealed that Hummers method is composed of two step oxidation[40] and the second oxidation step(named as step II oxidation) induced further oxidation of the exfoliated GO. However, step II oxidation does not influence the yield of graphene oxide, which is distinguished from the first oxidation step (named as step I oxidation). The result suggests that step II oxidation does not produce additional graphite oxide from raw graphite because the unexposed inner layer of graphite does not oxidize during the step. This

phenomena occurs because of change of the oxidant from dimaganese heptoxide (Mn_2O_7) to permanganate ion (MnO_4^-) and solvent medium from H_2SO_4 to H_3O^+ and H_2O. This change of the oxidation environment of weaker acidity and de-intercalation of H_2SO_4[41-43] makes oxidation occur from the edge of the graphite, which has more reactivity than the basal plane.[44-46] The scientific observation gave rise to our strategy of omitting step I oxidation that promotes the full oxidation of graphite from the modified Hummers method to prevent oxidation of the inner part of graphite. We hypothesized and demonstrated that edge selectively oxidized graphite (EOG) and liquid phase exfoliated EOG (LPEOG) were successfully synthesized through step II oxidation. Concentrations of LPEOG suspension could be increased up to 14.7 mg/ml and 70% of the LPEOG sheets were single-layered. We drew electric circuits using the LPEOG ink for making conductive graphene circuit by simple brush painting, which showed higher conductivity (~5,440 S/m) than rGO (~3,470 S/m). Transparent conducting film prepared by spin-coating the LPEOG ink exhibited low surface resistance (~2.97 kΩ/sq.) and high transmittance (> 83.0 %.T).

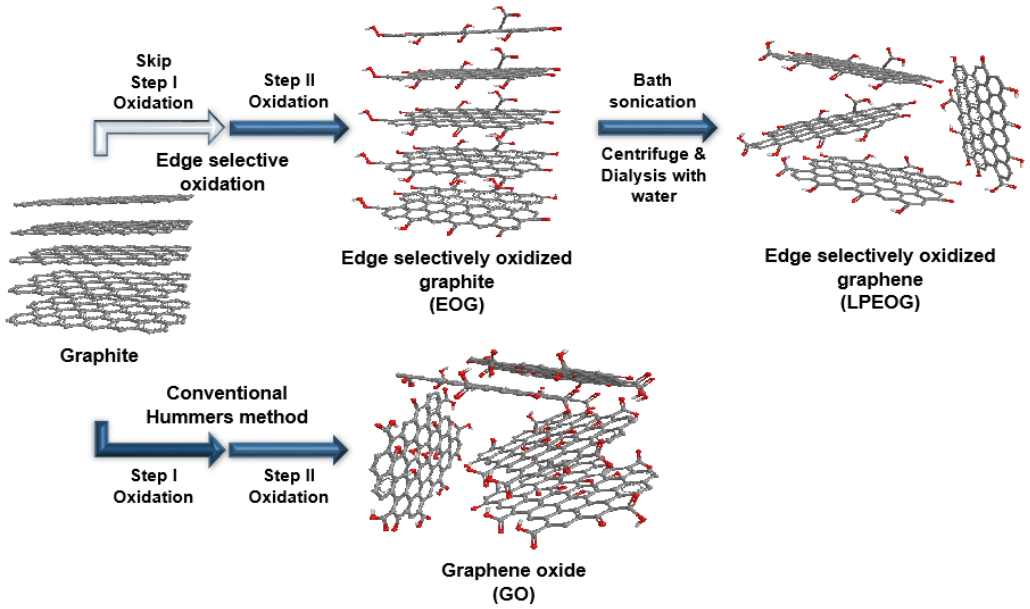

Figure 4.1 Experimental scheme for producing LPEOG suspension.

4.2 Experimental

4.2.1 Materials

Natural flake graphite (Lot #: 17425HO, +100 mesh), Potassium persulfate ($K_2S_2O_8$, 98%), phosphorus pentoxide (P_4O_{10}, 98%), potassium permanganate ($KMnO_4$, 98%), gold (III) chloride ($AuCl_3$, 99.0%), and dichloromethane (99.5%) were purchased from Sigma-Aldrich. Sulfuric acid (H_2SO_4, 98%), hydrogen peroxide (H_2O_2, 30%), hydrochloric acid (HCl, 35–37%), sodium hydroxide (NaOH, 97 %), o-dichlorobenzene (o-DCB, 99%), N-methyl-2-pyrrolidone (NMP, 99.5%), acetone, N,N'-dimethylformamide (DMF, 99.5%), tetrahydrofuran (THF, 99%), methyl alcohol (99.5%), n-hexane (95%), and toluene (99.5%) were purchased from Daejung Chemicals & Metals. All chemicals were used as received.

4.2.2 Syntheses of the EOG, FOG, and GO Samples

In this study, the EOG were prepared thorough simple modification of Hummers method for step II oxidation, which was reported in our group's previous work.[40] 3.0 g of graphite was dispersed into 138 ml of H_2SO_4 that had been cooled to 0°C in advance while 18.0 g of $KMnO_4$ was stirred in 200 ml of deionized (DI) water. 50 ml of DI water was very carefully added to prevent the temperature from rising above 70°C, and aqueous $KMnO_4$ was poured, followed by 50 ml of DI water. The reaction was transferred to a 70°C bath and mechanically stirred for 6, 12 and 24 hours. The nomenclature of the EOG samples of this work represents the step II oxidation condition for each EOG experienced during the synthesis. For example, the EOG sample produced from the procedure, including step II oxidation for 6 h at 70°C, was named E7006. The other two samples, E7012 and E7024, were prepared and named in this manner. After this stirring process, 10 ml of H_2O_2 was added to complete oxidation. This

mixture was ultra-centrifuged three times at 13,000 rpm with 3.4% HCl. The precipitant was repeatedly washed with and completely neutralized five times by exchanging the solvent with DI water in repeated ultra-centrifugations at 4000 rpm. The product was finally obtained by vacuum filtration and dried in an 80°C oven.

The synthesis of GO was prepared through the conventional Hummers method.[47] First, graphite was pretreated with $K_2S_2O_8$ and P_4O_{10} for the ease of exfoliation to a single layer. 10.0 g of $K_2S_2O_8$ and 10.0 g of P_4O_{10} were fully dissolved in 50 ml of 98% H_2SO_4 while vigorously stirring at 80°C. 10.0 g of graphite was gradually added to the mixture. This pretreated step was continued for 24 hours at the same temperature, and then the mixture was poured into 2 L of DI water. The pretreated graphite was washed with excess DI water via repeated vacuum filtrations until pH of the graphite became neutral, and then dried in a vacuum oven at room temperature. 3.0 g of this pretreated graphite was dispersed into 138 ml of H_2SO_4 that had been cooled to 0°C. 18.0 g of $KMnO_4$ was very carefully added to prevent the temperature from rising above 50°C. The reaction was transferred to 35°C and was stirred in 300 rpm for 2 hours. 300 ml of ice made from DI water was mixed with 10 ml of H_2O_2 very carefully added. This mixture was ultra-centrifuged three times at 13000 rpm with 3.4 % HCl. The precipitant was repeatedly washed with and completely neutralized five times by exchanging the solvent with DI water in repeated ultra-centrifugations at 13000 rpm.

FOG samples were prepared through the same conventional Hummer's method without pretreatment to obtain unexfoliated oxidized graphite for comparing with EOG. After oxidation, FOG was obtained by vacuum filtration and dried in an oven at 80°C.

4.2.3 Liquid Phase Exfoliation of EOG and Graphite

Before bath sonication, EOG was mixed in 5 mg/ml with 0.1 M NaOH and stirred overnight. The solvent was sonicated by bath sonication for 6h and left overnight. The suspension was centrifuged in 4000 rpm and supernatant was obtained. This process was repeated for three times in order to eliminate unexfoliated graphene. The graphene suspension was dialyzed with DI water until neutralized and we named the suspension as LPEOG. 1ml of LEPOG was dried and weighted for measuring the concentrations. The nomenclature of the LPEOG samples of this work represents the exfoliated EOG samples. For example, the LPEOG sample produced from E7006 was named LE7006. The other two samples, LE7012 and LE7024, were prepared and named in this manner.

4.2.4 Fabrication of LPEOG and GO Thin Film and Gold Chloride Doping

In order to produce transparent conducting film, LE7024 and GO was fabricated on quartz glass. The quartz glass was washed with water, acetone, and isopropyl alcohol using bath sonication. After ozone treatment, LE7024 and GO suspension was spin coated at 2000 rpm under N_2 flow. LE7024 and GO was filtered thick film and was produced using vacuum filtration on AAO film.

The spin coated and filtered films were reduced by thermal treatment under 1:9 mixed H_2/Ar gas condition. In order to avoid damage by self-generated oxygen, the thin film was heated to 400°C for 3h, cooled down to room temperature, and annealed 1100°C for 1h.[7]

Reduced spin coated rLE7024 and rGO films were doped with gold chloride ($AuCl_3$) because the effect of $AuCl_3$ doping was constantly maintained.[48] $AuCl_3$ dissolved in nitromethane was spin coated on reduced film at 2500 rpm for 60 seconds. After spin coating, the $AuCl_3$ doped films were baked at 150°C for 10min.

4.2.5 Characterization

To study the oxygen-containing functional groups of the samples, the functional groups were quantified by performing XPS with an AXIS-HSi spectrometer (Kratos). The obtained C1s spectra were fitted and deconvoluted using XPSPEAK41 software. FT-IR spectra of the EOG samples were recorded with a Thermo Scientific Nicolet TM iS10 spectrometer to obtain additional information about their functional groups. The scan range was 400–4,000 cm^{-1} in ATR mode. Thermogravimetric analysis (TGA) was carried out under nitrogen flow with a heating rate of 10°C/min by using an SDTQ600 instrument (TA Instruments). Raman spectrum was obtained using a Raman plus confocal laser Raman microscope (Nanophoton) with a 532 nm Nd-YAG laser source. The wide angle X-ray diffraction profile was acquired by using a Bruker D8 Advance diffractometer equipped with nickel filtered Cu Kα radiation (λ = 0.154184 nm). The zeta-potential data were acquired with ELSZ 1000ZS size and zeta-potential analyzer, Otsuka. Non-contact mode AFM images and topographic profiles of the LPEOG samples were obtained using a Surface Imaging Systems NANO Station II instrument. LPEOG was deposited on the Si/SiO2 substrates by using spin-coating. Analytical TEM (JEOL, JEM-2100F) micrographs were obtained to examine the morphologies of the LPEOG samples and FOG samples. The optical transmittance data for the rLE7024and rGO thin film within the UV-visible region were obtained by using a UV-Vis-NIR Cary 5000 spectrometer (Varian) with a scan range of 400-700 nm. The electrical performance of rLE7024 and rGO films was obtained by M4P-205 4 point probe station (MSTECH). Thickness of reduced graphene films were acquired using field emission scanning electron microscopy. (FE-SEM; MERLIN Compact) A 12V battery was used for the circuit test.

4.3. Results and Discussion

4.3.1 Synthesis of EOG

In previous work,[40] we divided Hummers method into two sequential steps by using oxidation materials and liquid media in each step:

Step I oxidation

$2\ KMnO_4 + 2\ H_2SO_4 \rightarrow \underline{\mathbf{Mn_2O_7}} + H_2O + 2\ KHSO_4$

$Mn_2O_7 + 2\ H_2SO_4 \rightarrow 2\ \underline{[MnO_3]}^+[HSO_4]^- + H_2O$

Step II oxidation

$Mn_2O_7 + 3\ H_2O \rightarrow \underline{\mathbf{2\ MnO_4}}^- + 2\ H_3O^+$

$MnO_3^+ + 3\ H_2O \rightarrow \underline{\mathbf{MnO_4}}^- + 2\ H_3O^+$

Potassium permanganate ($KMnO_4$) in concentrated sulfuric acid transformed to manganese heptoxide (Mn_2O_7) and manganese trioxide ion (MnO_3^+). These two manganic acids oxidize the whole parts of graphite and produce GO during step I oxidation. After the addition of water, the oxidants in step I oxidation is removed and permanganate ion (MnO_4^-), a main oxidant of step II oxidation, is formed in an acidic aqueous medium. The difference of the oxidizing agent can be easily seen through the colour of the solvent as shown in **Figure 4.2**

We omitted the step I oxidation process of the modified Hummer method and applied only step II oxidation for several hours on raw graphite. The step II oxidation was performed at 70°C and named E7006, E7012, and E7024 for 6, 12, and 24 hour oxidized samples, respectively. The detail nomenclature of EOG is explained in the experimental section. Conventional Hummers method was also performed to obtain fully oxidized graphite (FOG). **Figure 4.1** shows the experimental scheme for this step II only oxidation and conventional Hummers method.

In order to verify that permanganate ion selectively oxidize edge of the graphite, atomistic defects of the graphite samples were characterized by Raman. Because

the disorder in graphite induces D band in the Raman spectra and in-plane vibrational E2g phonon induces G band, the intensity ratio between D band and G band indicates structural disorder of the graphene layer.[49] EOG has a low I_D/I_G ratio (up to 0.33) at the basal plane and a high I_D/I_G ratio (1.08) at the edge, which completely differs from that of FOG (~1.05 for whole area) and raw graphite (~0.05 for whole area) (**Figure 4. 3** (a)-(c), **Figure 4.5**). A 2D mapping image also showed that the I_D/I_G ratio of EOG samples was clearly different comparison to the images of graphite and FOG (**Figure 4.3** (d)-(f), **Figure 4.4**). The colours of basal plane and edge in the mapping images of EOG are obviously different, which is contrast to the mapping image of FOG. This implies that EOG is edge-selectively oxidized by step II oxidation.

The samples were characterized by powder X-ray diffraction (XRD) in order to examine whether the interlayer distance of the graphite changed due to the oxidation steps. EOG shows a strong (002) peak at 26.2˚, corresponding to an ideal layered structure of graphite with d-spacing of 0.34 nm. This indicates that the internal structure of the EOG is similar with the graphite, implying a low population of functional groups on a basal plane. The peak at 13˚ (~0.72 nm) is induced by intercalation of H_2SO_4,[31] which disappeared when EOG is oxidized over 12 hours because H_2SO_4 was de-intercalated during step II oxidation by increased Hammett acidity function when solvent medium changes to H_3O^+ and H_2O by added water. (**Figure 4.6**(a)).[41-43] In contrast, FOG shows a strong peak at 7.9˚ (~1.12 nm) by induced functional groups of the basal plane (**Figure 4.6**(b)).[50] This result indicates that oxidation mechanisms and chemical structure of EOG and FOG are entirely different, which is consistent with the Raman spectra.

Further evidence for the edge-selective oxidation comes from the measurement of functional groups EOG rarely has functional groups at the basal plane, which imply an amount of functional groups would be less than FOG. To compare the

populations of the functional groups, we quantitatively analyzed the results of X-ray photoelectron spectroscopy (XPS) measurements. **Figure 4.7**(a) shows bonding ratios of the samples calculated from the area of each peaks in deconvoluted C1s spectra in **Figure 4.8**. The three peaks of deconvoluted spectra correspond to C=C and C-C graphitic carbon (284.5 eV), hydroxyl/epoxide group (286.2 eV), and carbonyl/carboxyl group (288.1 eV), respectively. The hydroxyl/epoxide groups and carbonyl/carboxyl groups of the EOG samples were continuously increased as oxidation time prolonged. Nevertheless, the amount of the oxygen functional groups were less than those of FOG. Since we considered that the step II oxidation at 70˚C generates a large amount of functional groups,[40] the small amount of functional groups of EOG implies that the basal plane of EOG is not oxidized. This tendency is also found in the C/O atomic ratio of EOG (3 ~ 5.3), which is higher than that of FOG (2.1) (**Figure 4.7**(b)).

We performed Fourier transform infrared (FT-IR) spectroscopic measurement in ATR absorbance mode to see the difference between chemical bonding of the EOG and FOG. The FT-IR spectra were normalized upon the absorbance of the C=C double bond (~1625 cm^{-1}) to compare the relative intensity of the peaks induced by the hydroxyl, epoxide, and carbonyl groups. The absorption peaks of EOG located at 1248 cm^{-1}, 1105 cm^{-1}, and 3300cm^{-1} (assigned to the hydroxyl and epoxide groups)[51] were smaller than those of FOG. In contrast, E7024 and FOG showed similar intensity of the peak at 1659 cm^{-1} (assigned to the carbonyl group)[51] (**Figure 4.7**(c)). Because the carbonyl groups are mainly generated at the edge of the graphene layer,[39] this result again confirms that EOG is edge selectively oxidized and oxidation degree can be controlled by oxidation time.

The tendency of the degree of oxidation of the samples can also be observed by the thermal stability measured by thermogravimetric analysis (TGA) as shown in **Figure 4.7**(d). The amount of functional groups can be analyzed based on the

fact that most of the oxygenated functional groups of GO is eliminated at the temperature range of 100°C - 300°C. Weight loss of EOG (5.6 wt.%~13.7 wt.%) in the range of 100°C - 300°C was much smaller than that of FOG (41.8 wt.%), indicating that EOG is less oxidized than FOG. In particular, FOG was degraded in the range of 110°C - 170°C, which is not observed in EOG samples. Because the epoxide and hydroxyl groups are known to be degraded in this temperature range,[52] this result is another evidence for edge-selective oxidation of EOG samples.

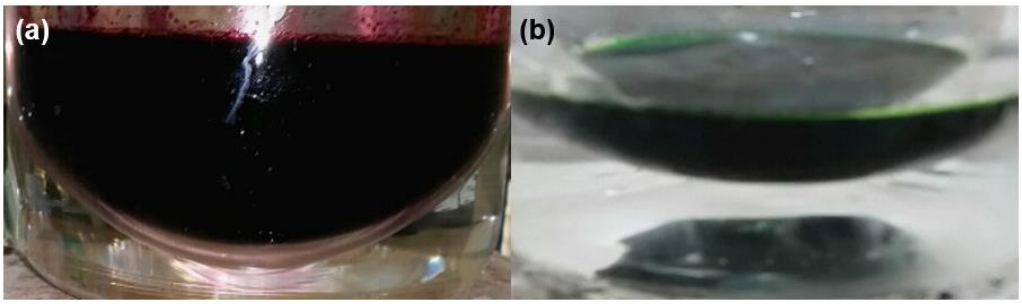

Figure. 4.2 (a) Solution of oxidant for step II oxidation and (b) step I oxidation.

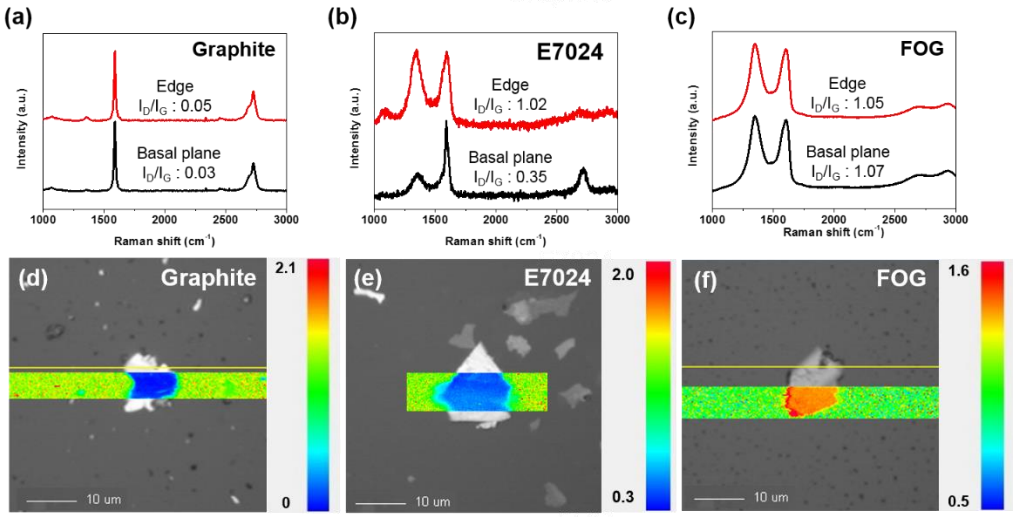

Figure 4.3 Raman spectra of (a) graphite, (b) E7024, and (c) FOG, and 2D mapping images (x100) for (d) graphite, (e) E7024, and (f) FOG.

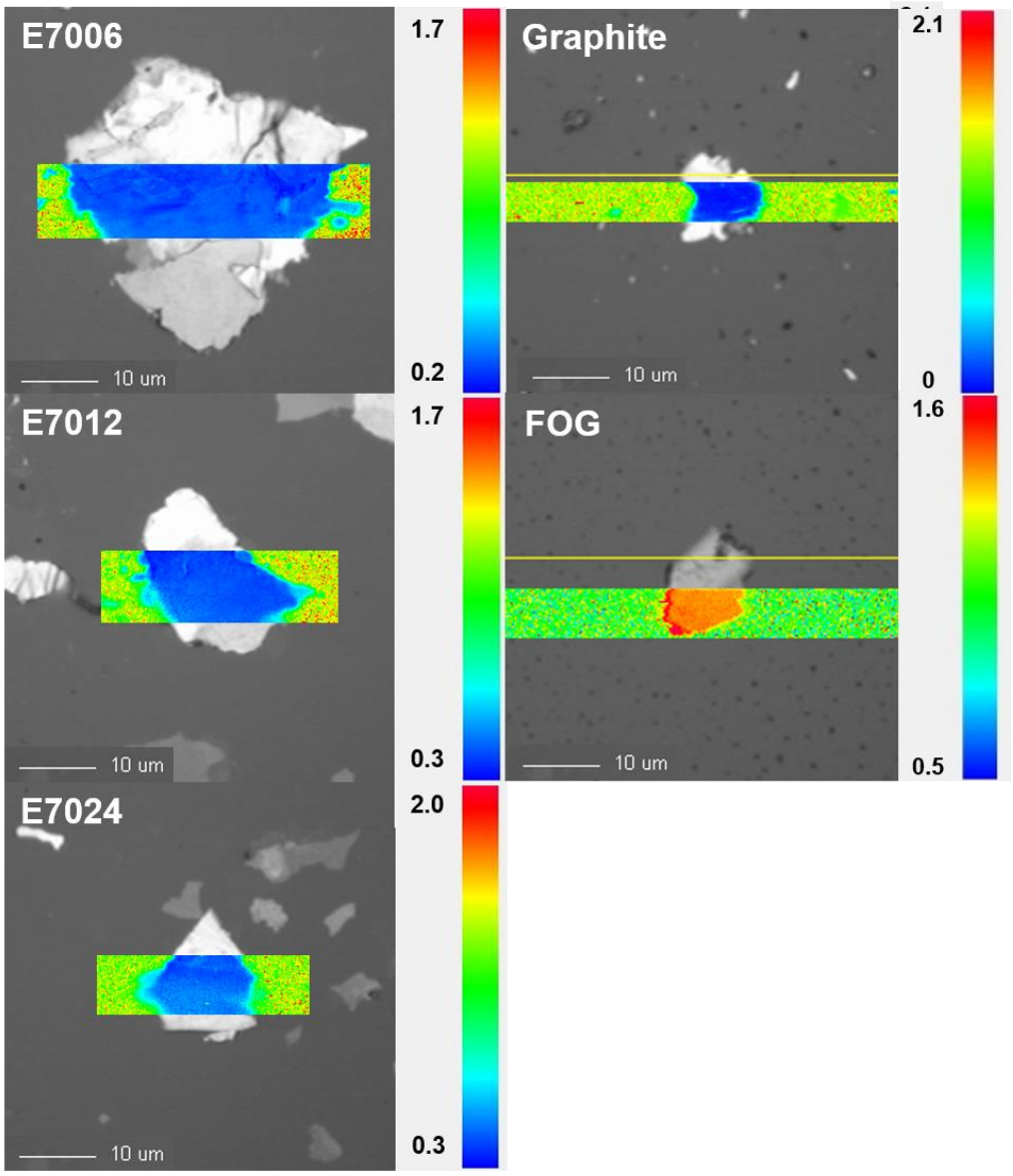

Figure. 4.4 Graphite, EOG and FOG's 2D mapping of I_D/I_G ratio

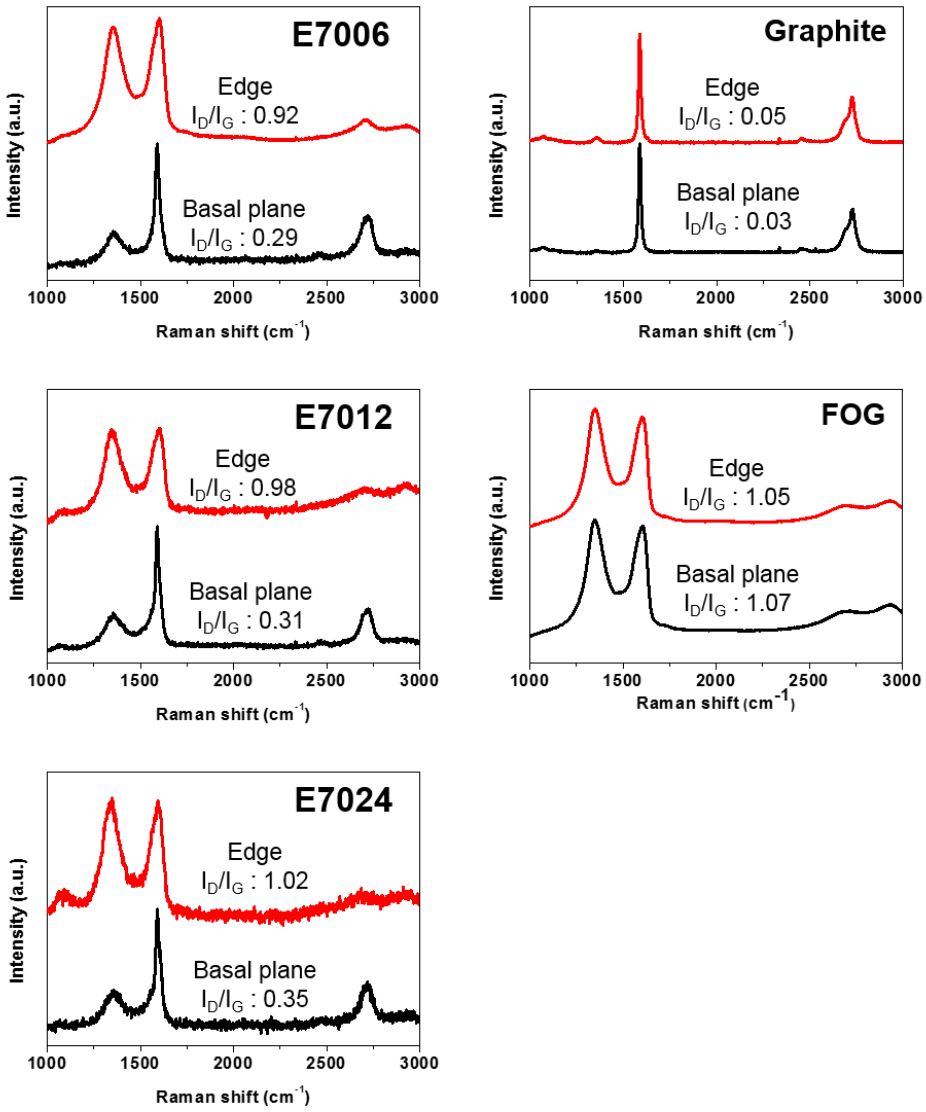

Figure. 4.5 Results of Raman spectroscopy and I_D/I_G ratio of graphite, EOG and FOG

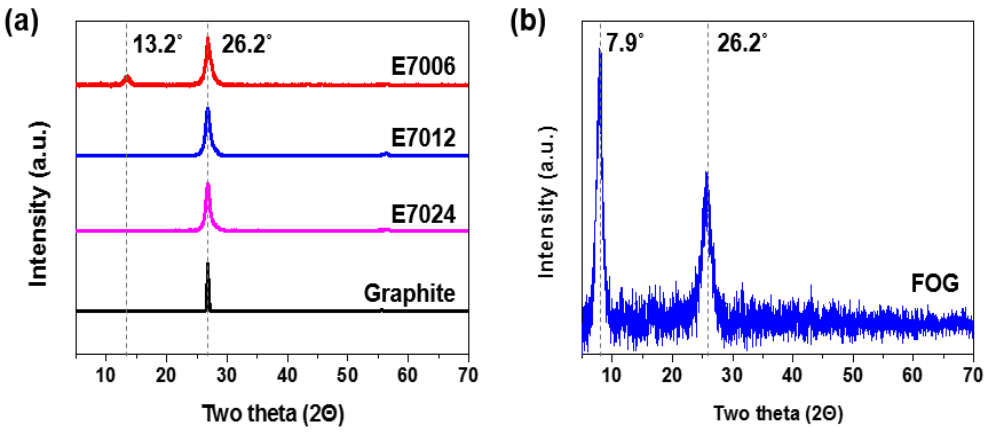

Figure 4.6 X-ray diffraction peaks of (a) graphite, EOG and (b) FOG normalized with the peak of 26.2˚.

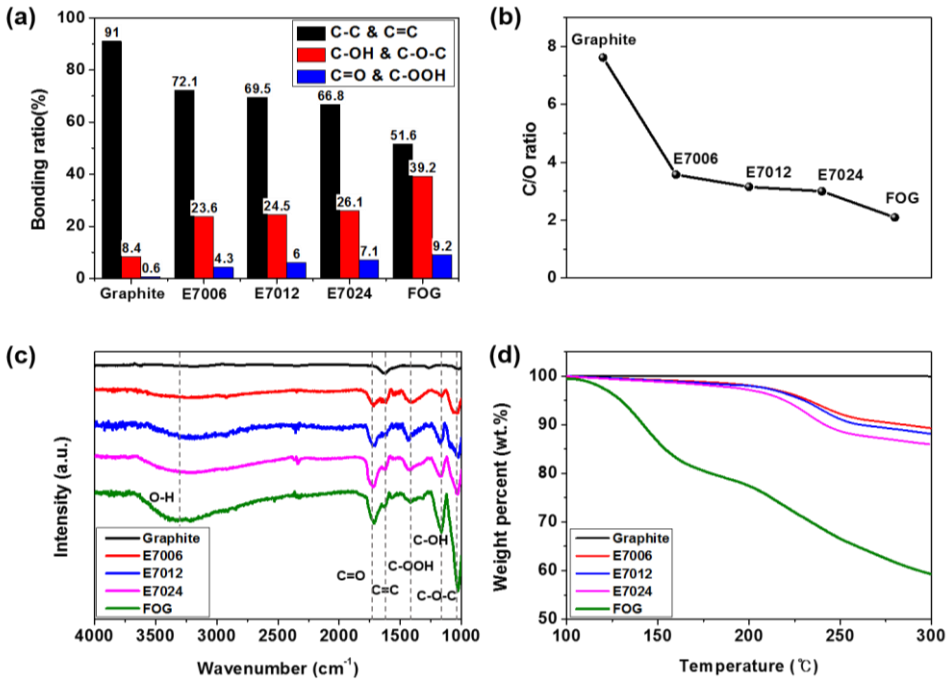

Figure 4.7 (a) Binding ratios and (b) C/O ratios examined by XPS. (c) FT-IR spectroscopy and (d) TGA data of graphite, EOG and FOG.

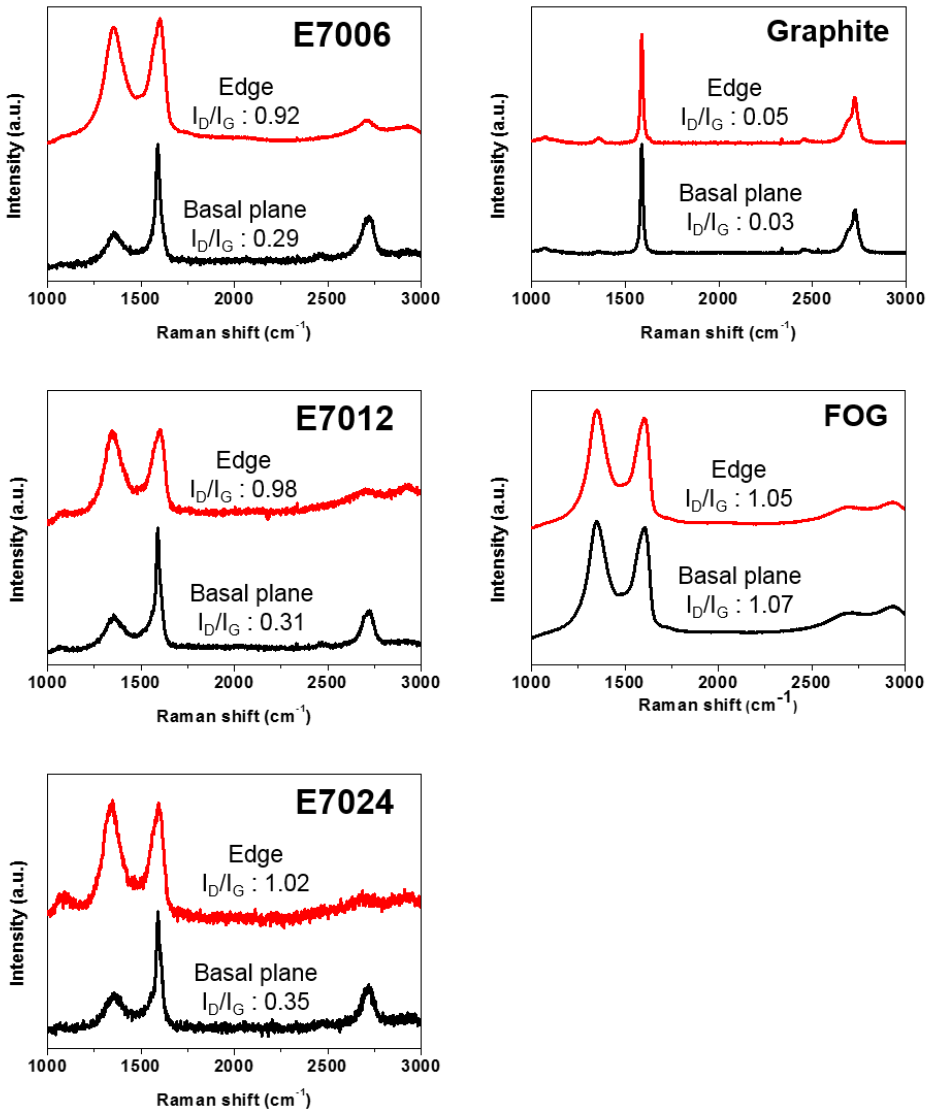

Figure 4.8 Results of Raman spectroscopy and I_D/I_G ratio of graphite, EOG and FOG

4.3.2 Liquid Phase Exfoliation of EOG

In order to obtain highly concentrated graphene suspension by liquid phase exfoliation of EOG, it is important to select an appropriate solvent for EOG dispersion. **Figure 4.9**(a) shows the dispersibility of EOG in various solvents after the sonication process. 0.1M NaOH solution showed the highest dispersibility because of repulsion between the carboxyl anion (COO-) generated by interaction of Na^+ cation and the carboxyl group of the EOG edge. [53] The highly stable dispersion state in NaOH 0.1M solution can stay for 9 months (**Figure 4.9**(b)). Based on this phenomenon, EOG was exfoliated in NaOH 0.1M solution by sonication and debris was removed by subsequent centrifuge. After dialysis in water, we can obtain exfoliated EOG without NaOH and we named them LPEOG (**Figure 4.10**(a)). The detail nomenclature of LPEOG is explained in the experimental section. As the oxidation time of EOG prolonged, we obtained a higher concentration of LPEOG due to the increased functional groups at the edge of the EOG facilitate dispersion (**Figure 4.10** (a)). The yield of the exfoliation reached about 20% in the case of LE7024. These LPEOG colloidal suspensions also exhibited high dispersion stability for 9 months. Moreover, the concentration of LPEOG increased up to 14.7 mg/ml (**Figure 4.11**) after high speed centrifuge and this concentration is considered to be applied to various kinds of solution based processes such as spin coating or brush painting.[54] The dispersibility and dispersion stability is closely related to surface charge of nanocarbon, which can be measured in the value of zeta potential. We evaluate the zeta potential of LPEOG and GO based on electrophoretic light scattering in order to find the origin of high dispersibility. All LPEOG samples show good dispersion stability and negative zeta potential increased with increased oxidation time (-45.9 mV ~ -47.9 mV), which is higher than GO (-45.9 mV) (**Figure 4.10** (b)). The negative zeta potential of nanocarbon is induced from the presence of ionizable functional groups such as the carboxyl group,[55] leading to

electrostatic repulsion between LPEOG. We conclude that the high zeta potential of LPEOG results in the high dispersibility and dispersion stability of LPEOG.

The population density of functional groups of LPEOG and GO was characterized by using XPS to identify the ionizable functional groups. Exfoliated raw graphite was also prepared through conventional sonication in bath to compare the effect of oxidation. **Figure 4.10** (c, d) showed the continuously increased functional groups and decreased C/O ratio of LPEOG as a prolonged step II oxidation time. The LPEOG demonstrated significantly less hydroxyl/epoxide groups and high C/O ratio in comparison to GO. This is consistent with the XPS data of EOG and FOG because LPEOG and EOG were less oxidized than GO and FOG. Nevertheless, the LPEOG showed stronger intensity of the peak assigned to the carbonyl/carboxyl groups than GO, implying selective edge oxidation induced a large amount of carbonyl/carboxyl groups at the edge of LPEOG. The high population density of the carbonyl/carboxyl group accounts for the origin of high absolute value of zeta potentials of LPEOG despite the high C/O ratio.

We performed atomic force microscopy (AFM) measurement in order to measure the lateral size and thickness of LPEOG. By measuring over 40 randomly selected sheets, we can attain distributions of lateral size and thickness of LPEOG (**Figure 4.13**(a, b), **Figure 4.14**). The lateral size of the LPEOG sheets were less than 2.5 μm and the average lateral size of the LPEOG sheet was decreased by increased oxidation time (**Figure 4.13** (c)) because step II oxidation occurred at the edge of graphene and the graphitic backbone is nibbled from the edge.[40] The thickness of the LPEOG sheets were less than ~2.00 nm (**Figure 4.15**), which were relevant to the bilayer considering thickness of the single layered LPEOG sheet are around 1.0 nm[34, 36] due to the functional groups at the edge. The ratio of single layer was increased from 52.1% to 70% with prolonged oxidation time (**Figure 4.13** (d)).

Transmission electron microscopy (TEM) and selective area electron diffraction (SAED) images of LPEOG and GO were obtained to examine the structural features. The edge of the LE7024 sheet in **Figure 4. 16**(b) showed that the LE7024 is single layered graphene, which is consistent with the AFM images. The LPEOG sheets exhibited strong sixfold SAED patterns in **Figure 4. 16** (c) and **Figure 4. 17**, implying that the crystal structure of the LPEOG's basal plane was successfully preserved during the oxidation process of graphite. In contrast, single layered GO exhibited timid crystalline patterns because the crystal structure of the basal plane was destroyed during step I oxidation (**Figure 4. 16** (f)). The higher crystallinity of LPEOG than GO would result in improved electrical performance of the LPEOG sheets.

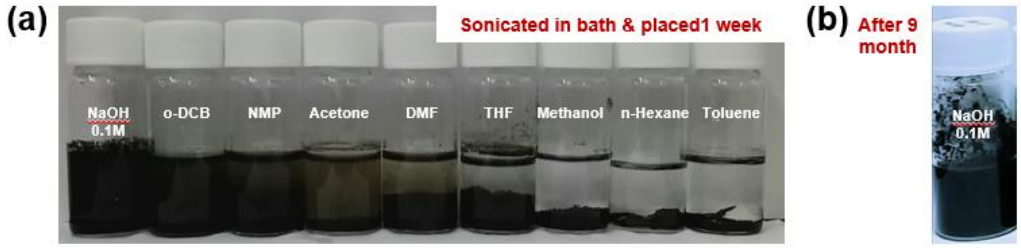

Figure. 4.9 EOG dispersions for various solvents and EOG, which was dispersed in NaOH 0.1M and settled for 9 months.

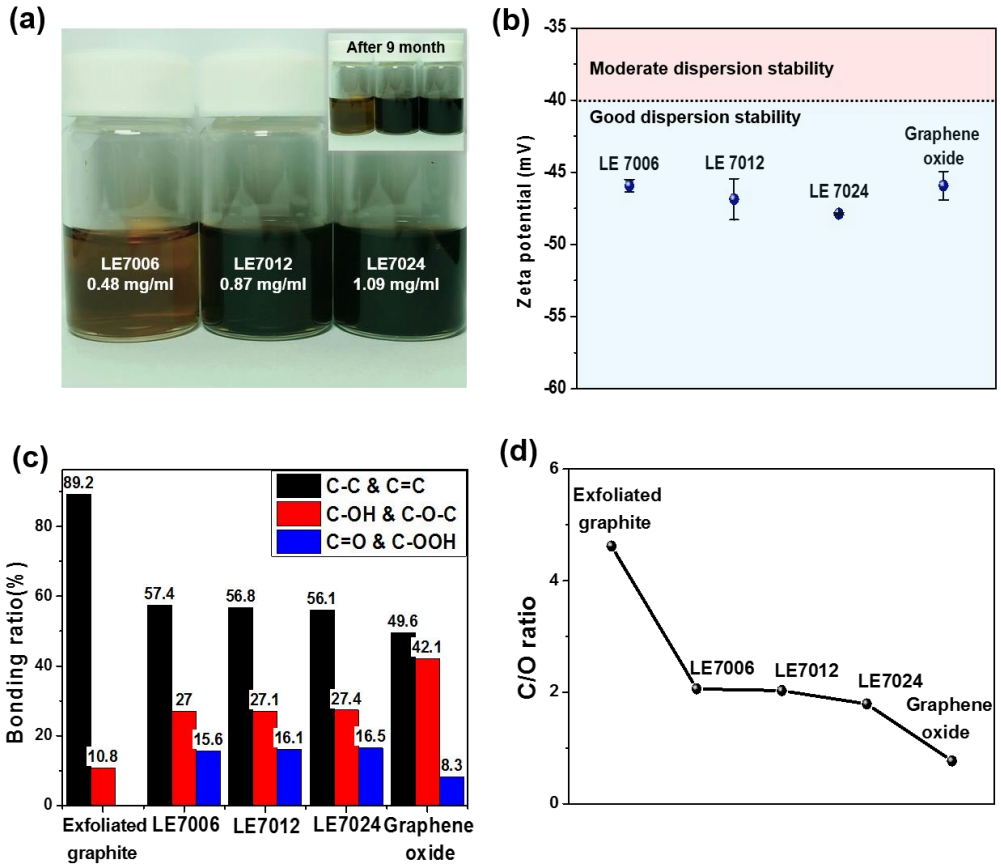

Figure 4.10 (a) Photograph and concentration of LPEOG suspension after dialysis. The inset shows images of LPEOG suspension 9 months after dispersion. (b) Zeta potentials of LPEOG and graphene oxide. (c) Bonding ratios and (d) C/O ratios obtained from the XPS results.

Figure 4.11 Concentrated LE7024 before and after drying. Concentration of concentrated LE7024 were measured by weighing.

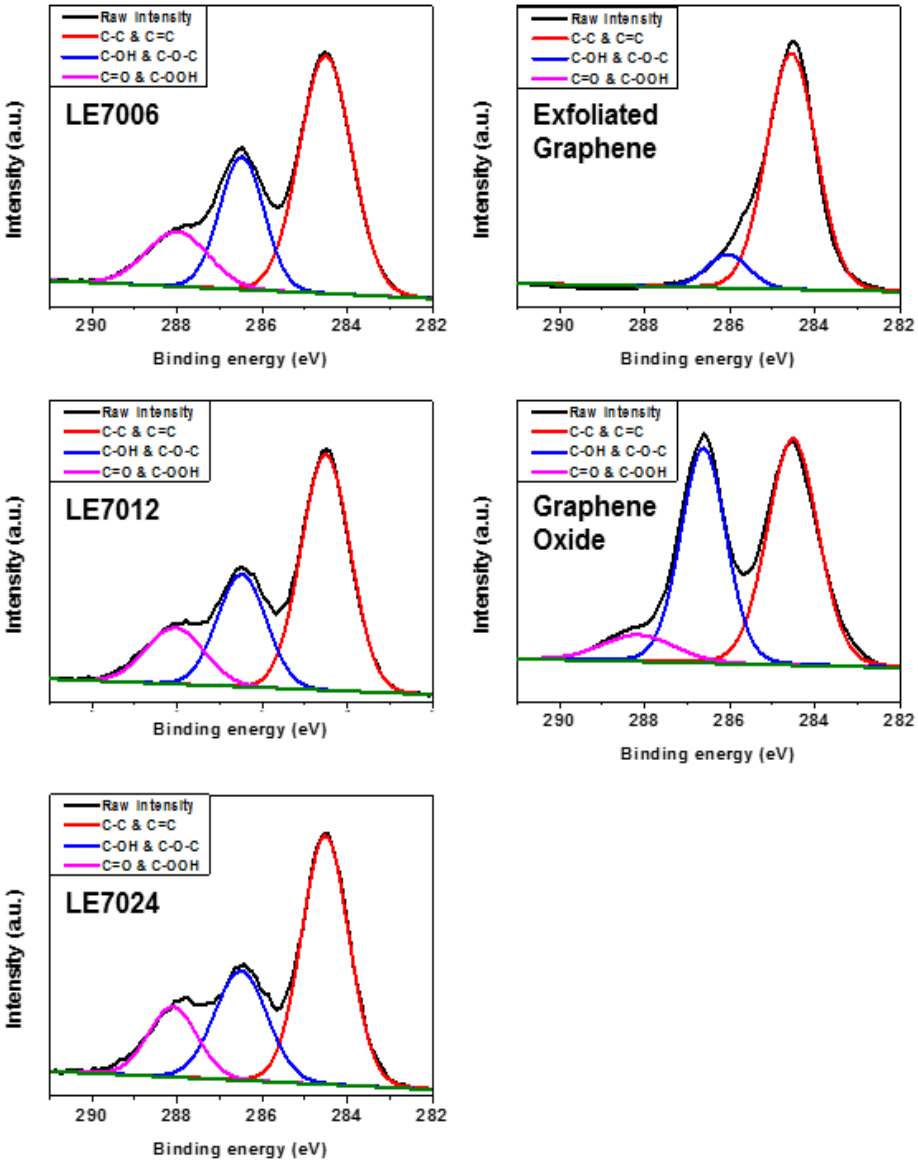

Figure 4.12 Deconvoluted Cls peak of exfoliated graphite, and LPEOG and graphene oxide measured by XPS.

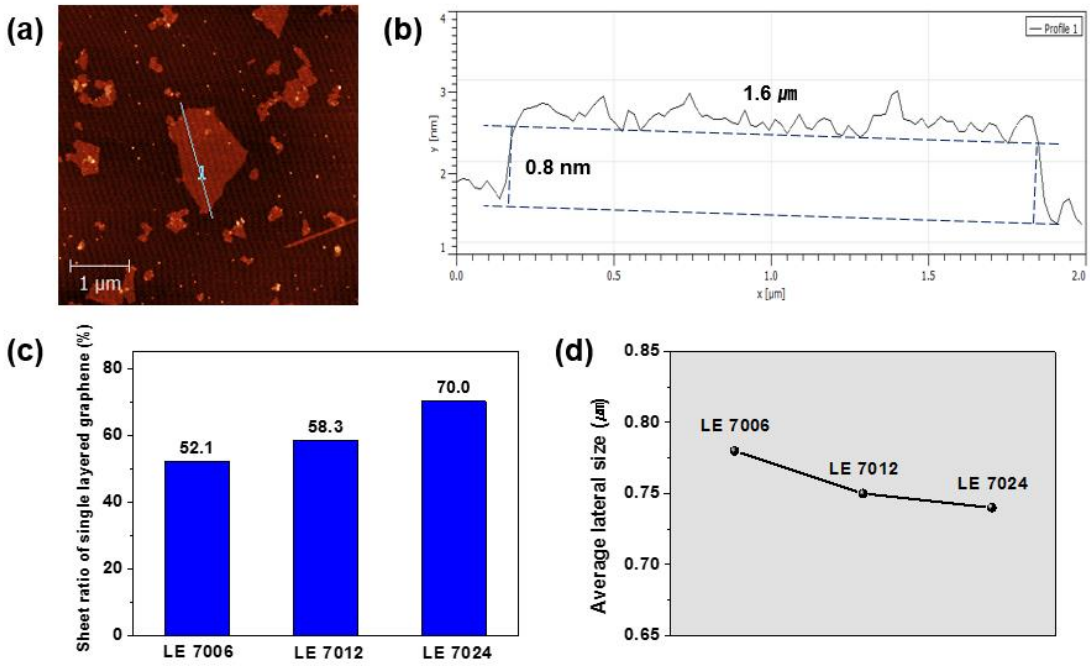

Figure 4.13 (a) Topography image and (b) profile of the LPEOG sheet, (c) ratio of single layered LPEOG sheets, and (d) average lateral size measured by AFM in aqueous solution

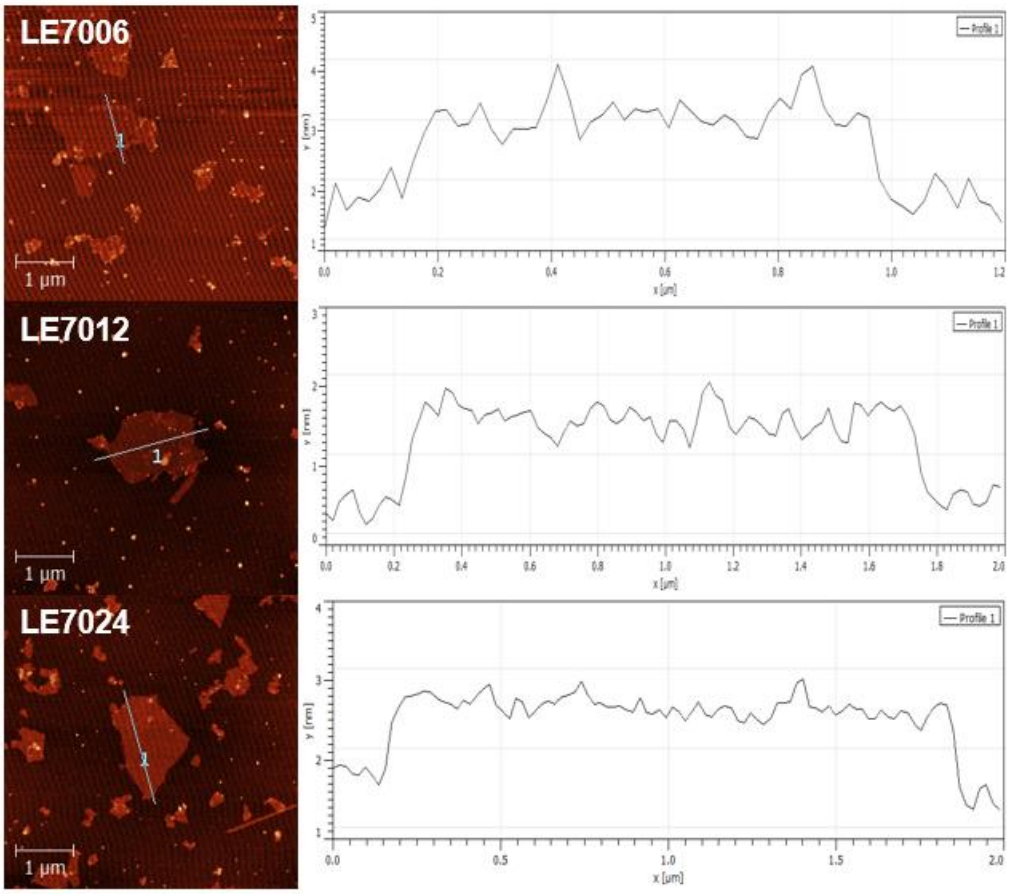

Figure. 4.14 Atomic Force Microscopy (AFM) topology image and profiles of the LPEOG sheets.

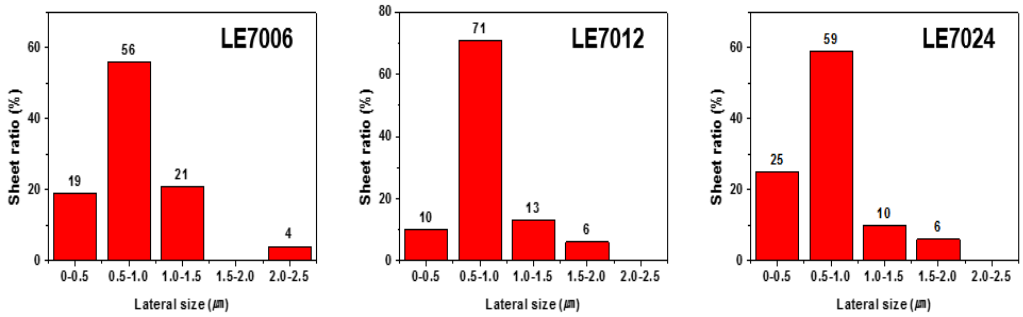

Figure 4.15 Lateral size distribution of the LPEOG sheets measured by AFM.

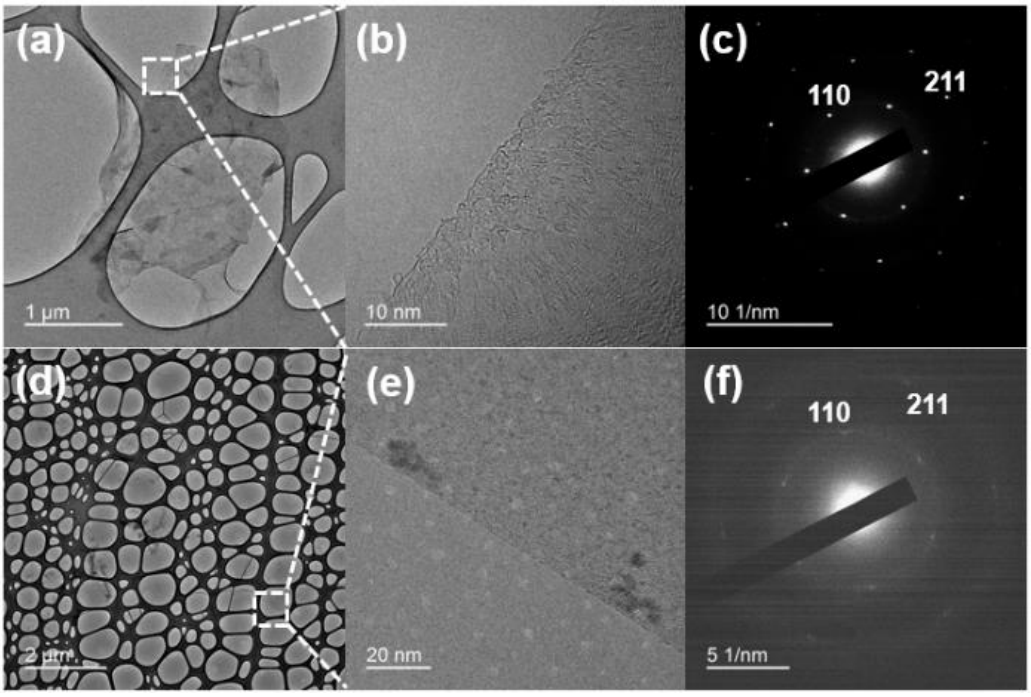

Figure 4.16 (a, d) Normal image, (b, e) high resolution image, and (c, f) SAED pattern of LE7024 and GO sheet.

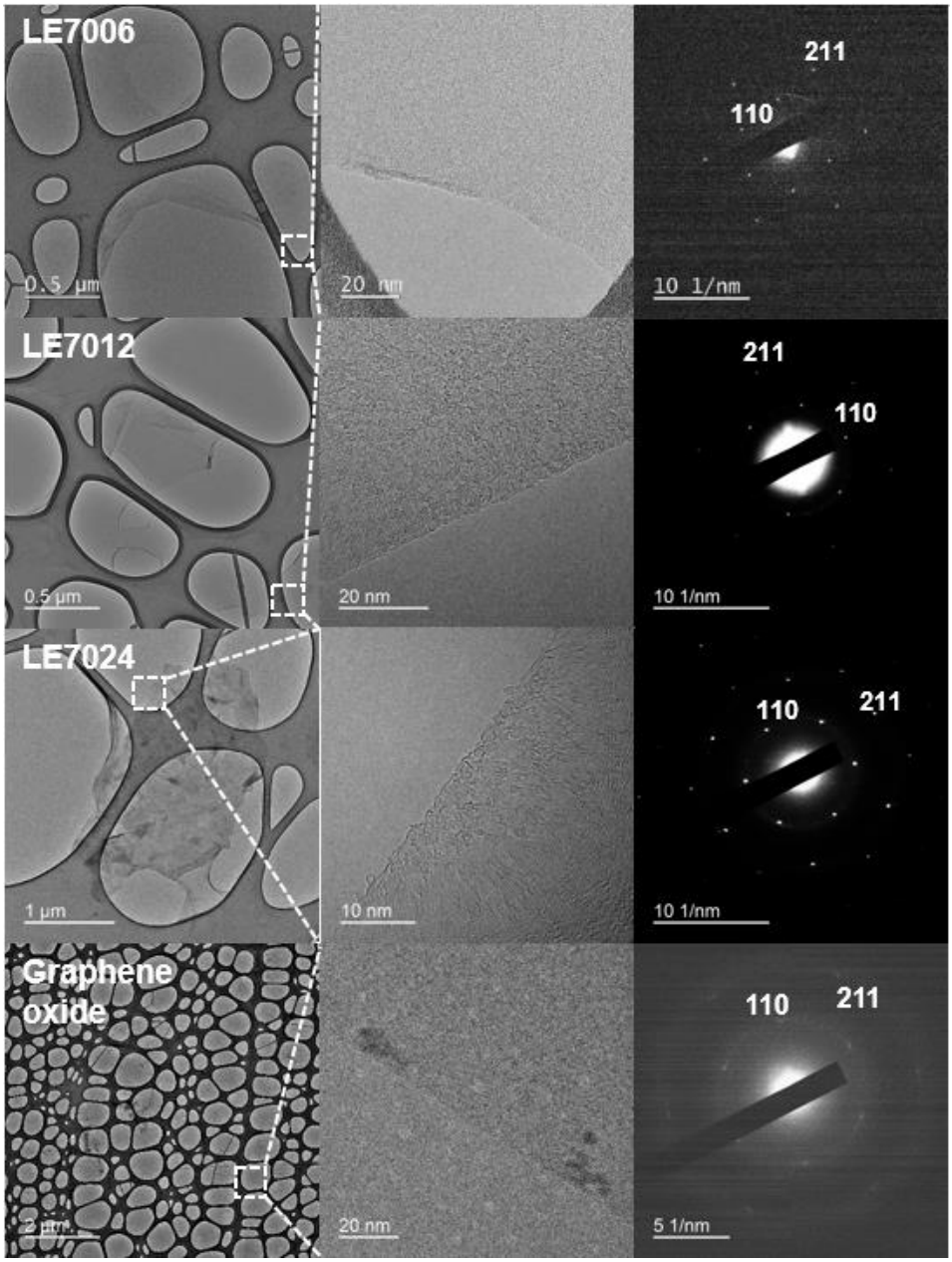

Figure 4.17 Transmission electron microscopy (TEM) normal images, high resolution images of the edge, and selective area electron diffraction (SAED) peaks of LPEOG and GO sheets.

4.3.3 Application of LPEOG as a conductive ink

We fabricated films to examine the performance of conductive ink by using highly concentrated LE7024 and GO ink, and subsequently annealed at 500°C in Ar to eliminate functional groups at the edge. After the annealing process, C/O ratio and electrical conductivity of the reduced LE7024 (rLE7024) are 3.30 and 5,440 S/m, respectively. The rLE7024 demonstrated a more reduced state and higher electrical conductivity than reduced GO (rGO, 3.08 for C/O ratio, 3,470 S/m for electrical conductivity), which is attributed to a less oxidized state of LE7024 in comparison to GO. The high concentrated LPEOG ink can be used to draw an electric circuit by brush painting as shown in **Figure 4.18**(a) and enough electrical performance for a conductive circuit (**Figure 4.18**(b)).

A higher electric property can be obtained by annealing the LPEOG at a high temperature. When rLE7024film was reduced at 1100°C in H_2/Ar mixed gas condition after preheating at 400°C to remove self-generated oxygen from LPEOG, a C/O ratio of 13.1 was achieved due to the elimination of residual functional groups. However, rGO showed a C/O ratio of 10.6. The high C/O ratio (**Figure 4.20**) and less damaged basal plane resulted in high electrical conductivity of the rLE7024 film (120,000 S/m), which is also quite larger than that of the rGO film (68,800 S/m). We applied high temperature annealing and subsequent doping with $AuCl_3$[48] on the rLE7024 thin films prepared by spin-casting of LE7024 ink in order to obtain transparent conducting films (**Figure 4.21, Figure 4.22**). The sheet resistance of the rLE7024 thin films after $AuCl_3$ doping was 2.97 kΩ/sq. at a transmittance of 83.4% (Figure of merit (FOM): 0.68) as shown in **Figure 4.18** (c). The rLE7024 based $AuCl_3$ doped transparent conducting film exhibited 30% improved performance than rGO based film (3.56 kΩ/sq. at 82.3%T, FOM: 0.52). It is noteworthy that the rLE7024 based transparent conducting film exhibited higher performance than rGO because the performance of transparent conducting film is significantly influenced by the size

of graphene.[5, 6] If we considering that the average lateral size of rGO (~ 10 um) is 13 times larger than that of rLE7024 (~ 0.74 μm), the result shows that preservation of π-conjugation of the basal plane is crucial for improvement of the electrical performance of graphene based film. Thus, we posit that increase of the average size of LPEOG by optimization of exfoliation and centrifugation of EOG would further improve the electrical performance of LPEOG.

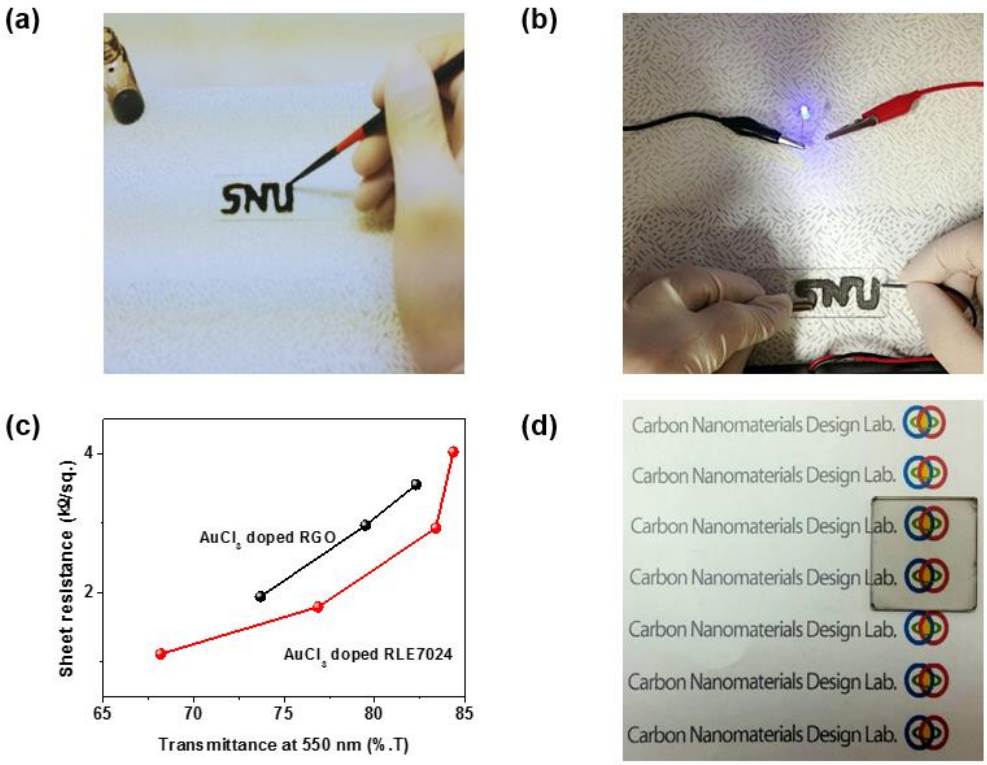

Figure 4.18 (a) Photograph of electric circuit drawn by LPEOG ink by brush printing on glass substrate, and (b) circuit test of rLE7024 film, which annealed at 500˚C. (c) Performance of $AuCl_3$ doped rLE7024 and rGO transparent conducting film measured by a 4-point probe and ultraviolet–visible spectroscopy, and (d) image of $AuCl_3$ doped rLE7024 based transparent conducting film.

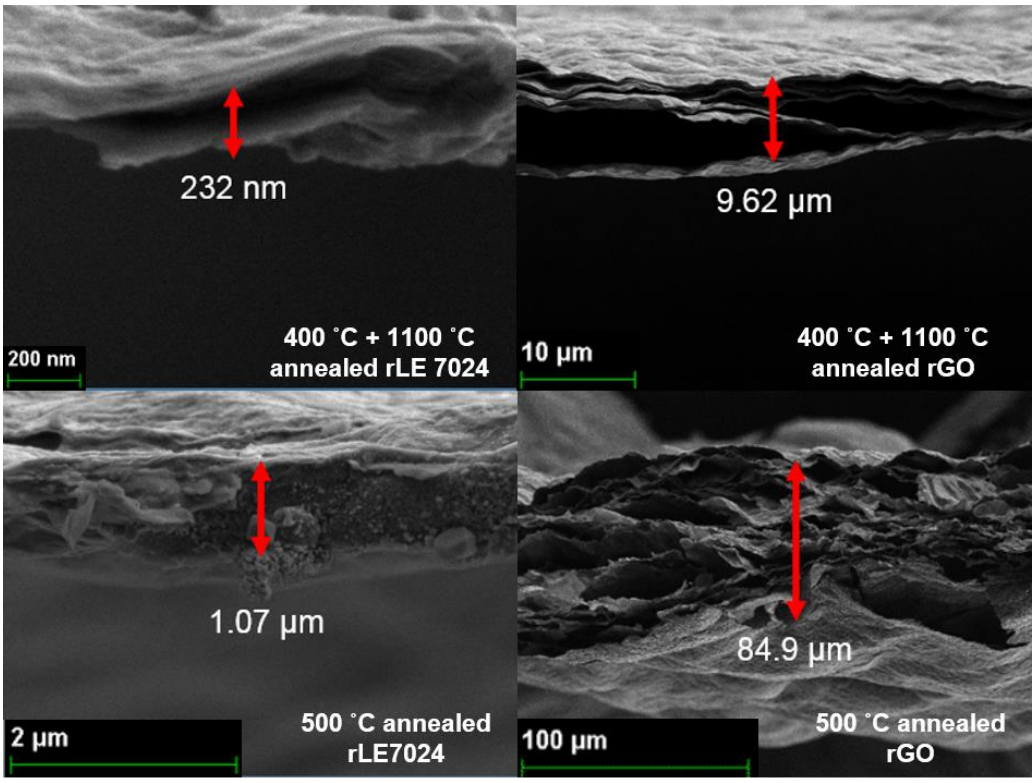

Figure 4.19 Thickness of rLE7024, rGO film for the measurement of electrical conductivity which were annealed under temperature condition of 400˚C + 1100˚C and 500˚C.

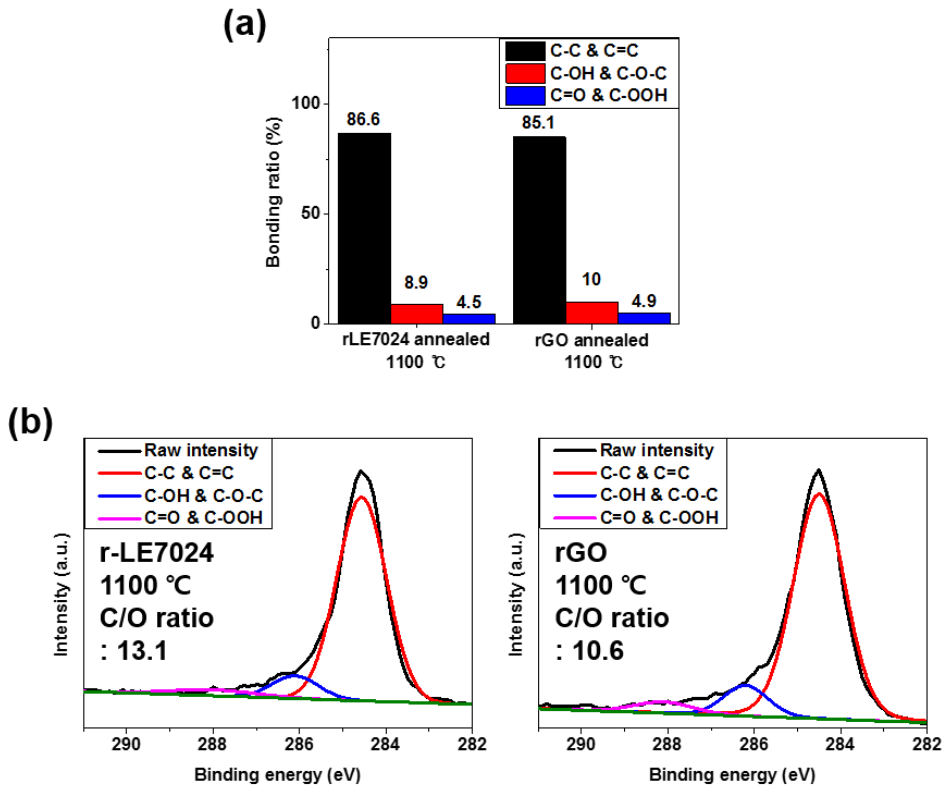

Figure 4.20 (a) Binding ratios and C/O ratios, and (b) deconvoluted C1s peak measured by (XPS)of 1100 ˚C annealed rLE7024 and rGO.

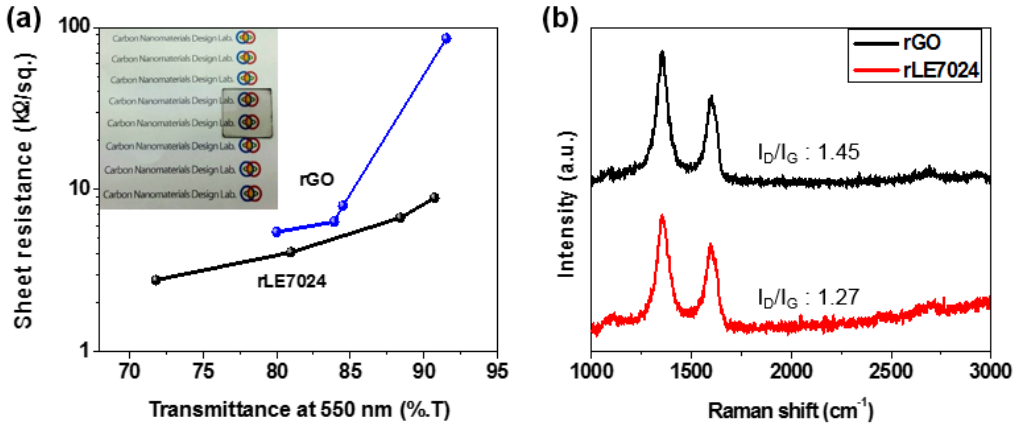

Figure 4.21 (a) Optoelectrical performance of rLE7024 and rGO transparent conductive film (TCF) measured by a 4-point probe and ultraviolet–visible (UV-vis) spectroscopy, and (b) results of Raman spectroscopy and I_D/I_G ratio of RLE7024 and RGO.

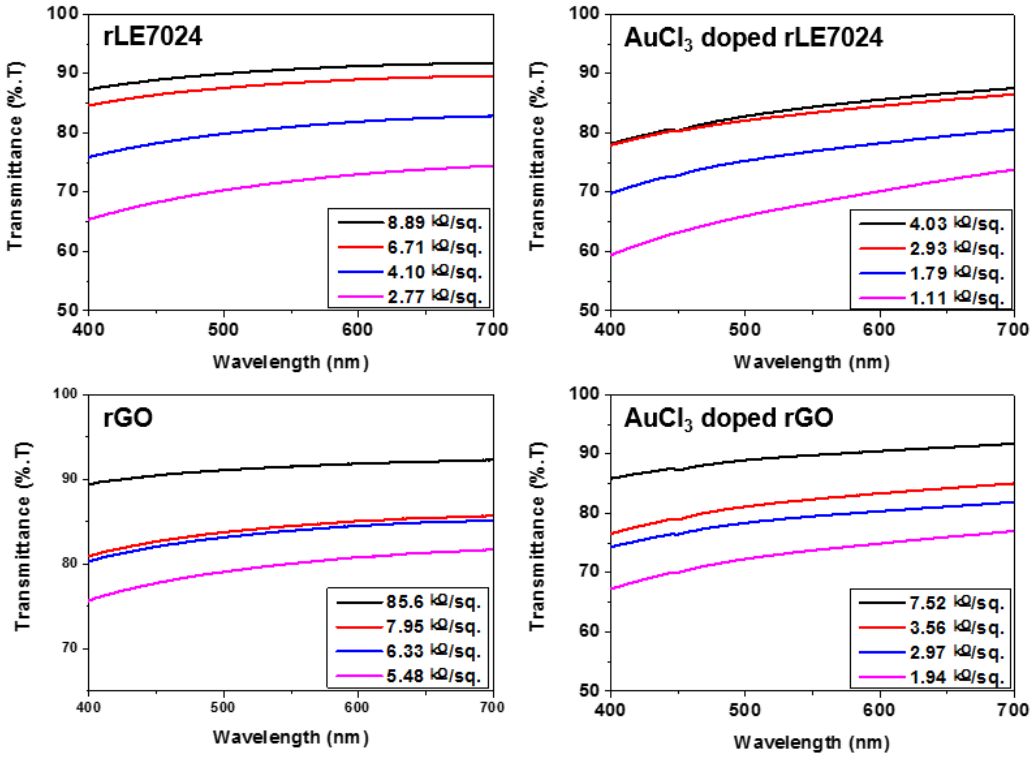

Figure 4.21 Transmittance at visible light range of rLE024, rGO, $AuCl_3$ doped rLE024, and $AuCl_3$ doped rGO transparent conductive film

4.4 Conclusion

We developed a new method of edge selective oxidation of graphene by skipping step I oxidation of the modified Hummers method in order to avoid oxidation of the basal plane. Selective use of step II oxidation generated oxygen functional groups at the edge of graphite as confirmed by Raman, XPS, FT-IR, XRD, Zeta potentiometric, and TEM. Single layered LPEOG was obtained by exfoliation of the EOG, which has high dispersibility and dispersion state in water. The high concentration of LPEOG solution enables this ink to be used in solution processing for graphene based devices. The rLE7024 prepared in this research showed outstanding electrical properties (conductivity: 120,000 S/m, FOM of TCF: 0.68) in comparison to conventional rGO (conductivity: 66,800 S/m, FOM of TCF: 0.52) counterparts due to the preserved π-conjugation of the basal plane. Thus, our method provides an efficient approach to obtain low-cost and high concentrated graphene ink that has better quality than GO based ink, and contributes to various applications of graphene through solution processing methods.

4.5. Reference

[1] A.K. Geim, K.S. Novoselov, The rise of graphene, Nat Mater 6(3) (2007) 183-191.

[2] Y. Zhu, S. Murali, W. Cai, X. Li, J.W. Suk, J.R. Potts, R.S. Ruoff, Graphene and graphene oxide: synthesis, properties, and applications, Adv Mater 22(35) (2010) 3906-24.

[3] O.C. Compton, S.T. Nguyen, Graphene oxide, highly reduced graphene oxide, and graphene: versatile building blocks for carbon-based materials, Small 6(6) (2010) 711-23.

[4] J. Du, S. Pei, L. Ma, H.M. Cheng, 25th anniversary article: carbon nanotube- and graphene-based transparent conductive films for optoelectronic devices, Adv Mater 26(13) (2014) 1958-91.

[5] Q. Zheng, W.H. Ip, X. Lin, N. Yousefi, K.K. Yeung, Z. Li, J.-K. Kim, Transparent Conductive Films Consisting of Ultralarge Graphene Sheets Produced by Langmuir–Blodgett Assembly, ACS Nano 5(7) (2011) 6039-6051.

[6] J. Zhao, S. Pei, W. Ren, L. Gao, H.-M. Cheng, Efficient Preparation of Large-Area Graphene Oxide Sheets for Transparent Conductive Films, ACS Nano 4(9) (2010) 5245-5252.

[7] J. Wu, H.c.A. Becerril, Z. Bao, Z. Liu, Y. Chen, P. Peumans, Organic solar cells with solution-processed graphene transparent electrodes, Applied Physics Letters 92(26) (2008) 263302.

[8] T. Kim, J.H. Kang, S.J. Yang, S.J. Sung, Y.S. Kim, C.R. Park, Facile preparation of reduced graphene oxide-based gas barrier films for organic photovoltaic devices, Energy Environ. Sci. 7(10) (2014) 3403-3411.

[9] S. Borini, R. White, D. Wei, M. Astley, S. Haque, E. Spigone, N. Harris, J. Kivioja, T. Ryhänen, Ultrafast Graphene Oxide Humidity Sensors, ACS Nano 7(12) (2013) 11166-11173.

[10] Y.R. Choi, Y.-G. Yoon, K.S. Choi, J.H. Kang, Y.-S. Shim, Y.H. Kim, H.J. Chang, J.-H. Lee, C.R. Park, S.Y. Kim, H.W. Jang, Role of oxygen functional groups in graphene oxide for reversible room-temperature NO2 sensing, Carbon 91 (2015) 178-187.

[11] B. Zhao, P. Liu, Y. Jiang, D. Pan, H. Tao, J. Song, T. Fang, W. Xu, Supercapacitor performances of thermally reduced graphene oxide, Journal of Power Sources 198 (2012) 423-427.

[12] J.H. Lee, N. Park, B.G. Kim, D.S. Jung, K. Im, J. Hur, J.W. Choi, Restacking-Inhibited 3D Reduced Graphene Oxide for High Performance Supercapacitor Electrodes, ACS Nano 7(10) (2013) 9366-9374.

[13] M.S. Chang, T. Kim, J.H. Kang, J. Park, C.R. Park, The effect of surface characteristics of reduced graphene oxide on the performance of a pseudocapacitor, 2D Materials 2(1) (2015) 014007.

[14] K. Erickson, R. Erni, Z. Lee, N. Alem, W. Gannett, A. Zettl, Determination of the local chemical structure of graphene oxide and reduced graphene oxide, Adv Mater 22(40) (2010) 4467-72.

[15] C. Gomez-Navarro, J.C. Meyer, R.S. Sundaram, A. Chuvilin, S. Kurasch, M. Burghard, K. Kern, U. Kaiser, Atomic structure of reduced graphene oxide, Nano Lett 10(4) (2010) 1144-8.

[16] X. Gao, J. Jang, S. Nagase, Hydrazine and Thermal Reduction of Graphene Oxide: Reaction Mechanisms, Product Structures, and Reaction Design, The Journal of Physical Chemistry C 114(2) (2010) 832-842.

[17] A. Ciesielski, P. Samori, Graphene via sonication assisted liquid-phase exfoliation, Chem Soc Rev 43(1) (2014) 381-98.

[18] M. Yi, Z. Shen, A review on mechanical exfoliation for the scalable production of graphene, J. Mater. Chem. A 3(22) (2015) 11700-11715.

[19] Y. Hernandez, V. Nicolosi, M. Lotya, F.M. Blighe, Z. Sun, S. De, I.T. McGovern, B. Holland, M. Byrne, Y.K. Gun'Ko, J.J. Boland, P. Niraj, G.

Duesberg, S. Krishnamurthy, R. Goodhue, J. Hutchison, V. Scardaci, A.C. Ferrari, J.N. Coleman, High-yield production of graphene by liquid-phase exfoliation of graphite, Nat Nanotechnol 3(9) (2008) 563-8.
[20] Y. Hernandez, M. Lotya, D. Rickard, S.D. Bergin, J.N. Coleman, Measurement of multicomponent solubility parameters for graphene facilitates solvent discovery, Langmuir 26(5) (2010) 3208-13.
[21] M. Yi, Z. Shen, S. Ma, X. Zhang, A mixed-solvent strategy for facile and green preparation of graphene by liquid-phase exfoliation of graphite, Journal of Nanoparticle Research 14(8) (2012).
[22] M. Lotya, P.J. King, U. Khan, S. De, J.N. Coleman, High-Concentration, Surfactant-Stabilized Graphene Dispersions, ACS Nano 4(6) (2010) 3155-3162.
[23] A. Ciesielski, S. Haar, M. El Gemayel, H. Yang, J. Clough, G. Melinte, M. Gobbi, E. Orgiu, M.V. Nardi, G. Ligorio, V. Palermo, N. Koch, O. Ersen, C. Casiraghi, P. Samori, Harnessing the liquid-phase exfoliation of graphene using aliphatic compounds: a supramolecular approach, Angew Chem Int Ed Engl 53(39) (2014) 10355-61.
[24] M. Matsumoto, Y. Saito, C. Park, T. Fukushima, T. Aida, Ultrahigh-throughput exfoliation of graphite into pristine 'single-layer' graphene using microwaves and molecularly engineered ionic liquids, Nat Chem 7(9) (2015) 730-6.
[25] S. Ravula, S.N. Baker, G. Kamath, G.A. Baker, Ionic liquid-assisted exfoliation and dispersion: stripping graphene and its two-dimensional layered inorganic counterparts of their inhibitions, Nanoscale 7(10) (2015) 4338-53.
[26] K.H. Park, D. Lee, J. Kim, J. Song, Y.M. Lee, H.T. Kim, J.K. Park, Defect-free, size-tunable graphene for high-performance lithium ion battery, Nano Lett 14(8) (2014) 4306-13.
[27] C.J. Shih, A. Vijayaraghavan, R. Krishnan, R. Sharma, J.H. Han, M.H. Ham, Z. Jin, S. Lin, G.L. Paulus, N.F. Reuel, Q.H. Wang, D. Blankschtein, M.S. Strano,

Bi- and trilayer graphene solutions, Nat Nanotechnol 6(7) (2011) 439-45.
[28] J. Kwon, S.H. Lee, K.H. Park, D.H. Seo, J. Lee, B.S. Kong, K. Kang, S. Jeon, Simple preparation of high-quality graphene flakes without oxidation using potassium salts, Small 7(7) (2011) 864-8.
[29] K.H. Park, B.H. Kim, S.H. Song, J. Kwon, B.S. Kong, K. Kang, S. Jeon, Exfoliation of non-oxidized graphene flakes for scalable conductive film, Nano Lett 12(6) (2012) 2871-6.
[30] S.H. Song, K.H. Park, B.H. Kim, Y.W. Choi, G.H. Jun, D.J. Lee, B.S. Kong, K.W. Paik, S. Jeon, Enhanced thermal conductivity of epoxy-graphene composites by using non-oxidized graphene flakes with non-covalent functionalization, Adv Mater 25(5) (2013) 732-7.
[31] N.I. Kovtyukhova, Y. Wang, A. Berkdemir, R. Cruz-Silva, M. Terrones, V.H. Crespi, T.E. Mallouk, Non-oxidative intercalation and exfoliation of graphite by Bronsted acids, Nat Chem 6(11) (2014) 957-63.
[32] S. Lin, L. Dong, J. Zhang, H. Lu, Room-Temperature Intercalation and ～1000-Fold Chemical Expansion for Scalable Preparation of High-Quality Graphene, Chemistry of Materials 28(7) (2016) 2138-2146.
[33] S. Eigler, Graphite sulphate - a precursor to graphene, Chem Commun (Camb) 51(15) (2015) 3162-5.
[34] I.Y. Jeon, Y.R. Shin, G.J. Sohn, H.J. Choi, S.Y. Bae, J. Mahmood, S.M. Jung, J.M. Seo, M.J. Kim, D. Wook Chang, L. Dai, J.B. Baek, Edge-carboxylated graphene nanosheets via ball milling, Proc Natl Acad Sci U S A 109(15) (2012) 5588-93.
[35] T. Lin, J. Chen, H. Bi, D. Wan, F. Huang, X. Xie, M. Jiang, Facile and economical exfoliation of graphite for mass production of high-quality graphene sheets, J. Mater. Chem. A 1(3) (2013) 500-504.
[36] L. Wei, F. Wu, D. Shi, C. Hu, X. Li, W. Yuan, J. Wang, J. Zhao, H. Geng, H. Wei, Y. Wang, N. Hu, Y. Zhang, Spontaneous intercalation of long-chain alkyl

ammonium into edge-selectively oxidized graphite to efficiently produce high-quality graphene, Sci Rep 3 (2013) 2636.
[37] M. Yang, S. Moriyama, M. Higuchi, Selective Edge Modification in Graphene and Graphite by Chemical Oxidation, Journal of Nanoscience and Nanotechnology 14(4) (2014) 2974-2978.
[38] G. Shi, A. Michelmore, J. Jin, L.H. Li, Y. Chen, L. Wang, H. Yu, G. Wallace, S. Gambhir, S. Zhu, P. Hojati-Talemi, J. Ma, Advancement in liquid exfoliation of graphite through simultaneously oxidizing and ultrasonicating, J. Mater. Chem. A 2(47) (2014) 20382-20392.
[39] D.R. Dreyer, S. Park, C.W. Bielawski, R.S. Ruoff, The chemistry of graphene oxide, Chem Soc Rev 39(1) (2010) 228-40.
[40] J.H. Kang, T. Kim, J. Choi, J. Park, Y.S. Kim, M.S. Chang, H. Jung, K.T. Park, S.J. Yang, C.R. Park, Hidden Second Oxidation Step of Hummers Method, Chemistry of Materials 28(3) (2016) 756-764.
[41] A.M. Dimiev, S.M. Bachilo, R. Saito, J.M. Tour, Reversible Formation of Ammonium Persulfate/Sulfuric Acid Graphite Intercalation Compounds and Their Peculiar Raman Spectra, ACS Nano 6(9) (2012) 7842-7849.
[42] A.M. Dimiev, G. Ceriotti, N. Behabtu, D. Zakhidov, M. Pasquali, R. Saito, J.M. Tour, Direct Real-Time Monitoring of Stage Transitions in Graphite Intercalation Compounds, ACS Nano 7(3) (2013) 2773-2780.
[43] N.E. Sorokina, O.N. Shornikova, V.V. Avdeev, Stability limits of graphite intercalation compounds in the systems graphite-HNO3(H2SO4)-H2O-KMnO4, Inorganic Materials 43(8) (2007) 822-826.
[44] P. Koskinen, S. Malola, H. Hakkinen, Self-passivating edge reconstructions of graphene, Phys Rev Lett 101(11) (2008) 115502.
[45] R. Sharma, J.H. Baik, C.J. Perera, M.S. Strano, Anomalously large reactivity of single graphene layers and edges toward electron transfer chemistries, Nano Lett 10(2) (2010) 398-405.

[46] K. He, G.D. Lee, A.W. Robertson, E. Yoon, J.H. Warner, Hydrogen-free graphene edges, Nat Commun 5 (2014) 3040.
[47] W.S. Hummers, R.E. Offeman, Preparation of Graphitic Oxide, Journal of the American Chemical Society 80(6) (1958) 1339-1339.
[48] M. Abdullah-Al-Galib, B. Hou, T. Shahriad, S. Zivanovic, A.D. Radadia, Stability of few layer graphene films doped with gold (III) chloride, Applied Surface Science 366 (2016) 78-84.
[49] K.N. Kudin, B. Ozbas, H.C. Schniepp, R.K. Prud'homme, I.A. Aksay, R. Car, Raman Spectra of Graphite Oxide and Functionalized Graphene Sheets, Nano Letters 8(1) (2008) 36-41.
[50] S.J. Yang, J.H. Kang, H. Jung, T. Kim, C.R. Park, Preparation of a freestanding, macroporous reduced graphene oxide film as an efficient and recyclable sorbent for oils and organic solvents, Journal of Materials Chemistry A 1(33) (2013) 9427.
[51] Y.S. Kim, J.H. Kang, T. Kim, Y. Jung, K. Lee, J.Y. Oh, J. Park, C.R. Park, Easy Preparation of Readily Self-Assembled High-Performance Graphene Oxide Fibers, Chemistry of Materials 26(19) (2014) 5549-5555.
[52] M. Acik, G. Lee, C. Mattevi, A. Pirkle, R.M. Wallace, M. Chhowalla, K. Cho, Y. Chabal, The Role of Oxygen during Thermal Reduction of Graphene Oxide Studied by Infrared Absorption Spectroscopy, The Journal of Physical Chemistry C 115(40) (2011) 19761-19781.
[53] K.B. Ricardo, A. Sendecki, H. Liu, Surfactant-free exfoliation of graphite in aqueous solutions, Chem Commun (Camb) 50(21) (2014) 2751-4.
[54] S. Gambhir, R. Jalili, D.L. Officer, G.G. Wallace, Chemically converted graphene: scalable chemistries to enable processing and fabrication, NPG Asia Materials 7(6) (2015) e186.
[55] D. Li, M.B. Muller, S. Gilje, R.B. Kaner, G.G. Wallace, Processable aqueous dispersions of graphene nanosheets, Nat Nanotechnol 3(2) (2008) 101-5.

Chapter 5. Gas sensing performance of band gap tuned graphene

5.1 Introduction

Nitrogen dioxide, (NO_2) one of the most common toxic air pollutant from combustion and automobile, causes the generation of ozone and acid rain.[1] Continuous exposure to NO_2 gas, even if low concentration of ppb level, causes chronic bronchitis, emphysema, and respiratory irritation.[2] Therefore, many countries tried to regulate the concentration of NO_2 in the air, U.S. (53 ppb), Europe (21 ppb), and WHO (21 ppb) have its own annual ambient air quality standards[3] and NO_2 gas sensing with low limit of detection (LOD) have become an important work for environmental protection and human health.

Traditionally, metal oxides were used for sensing NO_2 gas, but they showed a high limit of detection (LOD) because of its large band gap.[4-7] In the case of semiconductive 2D materials like molybdenum disulfide and phosphorene, low NO_2 adsorption energy and unstable nature itself remain as an obstacle.[8-13] On the other hand, graphene has been expected to be an appropriate gas sensing materials due to its excellent electrical property. However, the LOD of various kinds of graphene were not sufficient to be applied to device because of its low NO_2 adsorption energy.[14-18] Some studies tried to increase low NO_2 adsorption energy by hybridization of metal oxide and reduced graphene but failed to achieve low LOD.[19-22]

Considering the operation mechanism of the chemical sensor, adsorption of target gas and transfer of the generated charged carrier is the most important parameters.[23, 24] From the equation that used to calculate theoretical LOD,[25] sensitivity and root mean square (RMS) noise are considered as critical factor. Sensitivity, difference of resistance generated by adsorption of target gas, are the function of adsorption energy and mobility, and RMS noise are the function to

resistivity,[26] inverse of mobility. Therefore, it is necessary to secure high carrier mobility with a narrowed band gap and NO_2 adsorption energy. In case of graphene, foreign atoms can give higher NO_2 adsorption energy[18] as well as an enlarged band gap by a destructed sp^2 structure.[27, 28] Therefore, preparing graphene with high NO_2 adsorption energy, should have appropriate band gap of the semiconductor under 2 eV and the attachment of foreign atoms which shows high NO_2 adsorption energy. In the functionalization of graphene from the bottom up method, functional groups are efficiently generated and low LOD at a sub ppb level can be achieved.[29, 30] However, the preparation process is not suitable for manufacturing. In the case of the chemical exfoliation method, graphene is easily exfoliated with oxygenated functional groups,[31, 32] which show high NO_2 adsorption energy.[33, 34] However, excessively generated oxygenated functional groups enlarge band gap of graphene to insulative range. Therefore, establishing a method of controlling the amount of oxygenated functional groups suitable to NO_2 gas sensing is required.

Herein, in this research, we prepared graphene oxide (GO) with a narrowed band gap by controlling the amount of the functional groups with modification of acid washing process of Hummers method. As shown in our previous research, [35] the amount of the functional groups, especially epoxide groups which shows low NO_2 adsorption energy, was decreased. Therefore, the band gap of GO was narrowed to the semiconductive range with high NO_2 adsorption energy, and the GO based gas sensor showed outstanding NO_2 sensing performance of low LOD.

5.2 Experimental

5.2.1 Materials

Potassium persulfate ($K_2S_2O_8$, 98%), phosphorus pentoxide (P_4O_{10}, 98%), potassium permanganate ($KMnO_4$, 98%), and natural flake graphite (Lot #: 17425HO, +100 mesh) were purchased from Sigma-Aldrich. Sulfuric acid (H_2SO_4, 98%), hydrogen peroxide (H_2O_2, 30%), and hydrochloric acid (HCl, 35–37%) were purchased from Daejung Chemicals & Metals. All chemicals were used as received.

5.2.2 Syntheses of the GO, AGO, and HGO

In this study, GO, AGO, and HGO were prepared based on Hummers method. [31, 35-37] First, the natural flake graphite was pretreated with $K_2S_2O_8$ and P_4O_{10} to easily exfoliate to a single layer. 10.0 g of $K_2S_2O_8$ and 10.0 g of P_4O_{10} were fully dissolved in 50 mL of 98% H_2SO_4 while vigorously stirring at 80°C. Eventually, 5.0 g of graphite was slowly added to the mixture and continuously stirred for 24 hours at the same temperature before being poured into 2 L of deionized (DI) water. The pretreated graphite was washed with excess water using repeated vacuum filtrations until the graphite pH became neutral. It was then dried in a vacuum oven under room temperature. 3.0 g of the pretreated graphite was dispersed into 138 mL of H_2SO_4 that had been cooled to 0°C. 18.0 g of $KMnO_4$ was added very carefully to prevent the temperature from rising above 50°C. The reaction was finally transferred and stirred for 300 rpm at 35°C. After 2 hours, the mixture was poured in a water/H_2O_2 mixture to finish oxidation without the second oxidation step. The mixture was then washed with 1M HCl two times using centrifuge at 13000rpm. Then, we divided the precipitate into three groups and different washing processes were carried out. 1/3 of the mixture was directly centrifuged in 1M HCl at 13000rpm at room temperature. Another

1/3 of the precipitate were stirred in 1M HCl at 70°C for 16 hours and centrifuged at 13000rpm. The other 1/3 of the precipitate were stirred in 5M HCl at 70°C for 16 hours and centrifuged at 13000rpm. We named the GO from the first 1/3 precipitate as GO, the second 1/3 precipitate as HGO_1M, and the last 1/3 precipitate as HGO_5M. After the HCl washing steps, the precipitate was completely neutralized by exchanging the solvent with water over five times in repeated ultra-centrifugations at 13000 rpm. To eliminate un-exfoliated graphite and to produce supernatant, the precipitant was centrifuged at 4000 rpm. After purification, half of the GO was annealed in a 70°C oil bath and we named it AGO.

5.2.3 Sensor fabrication.

Interdigitated electrodes (IDEs) of 5 μm interspacing were fabricated on the SiO_2/Si substrate using photolithography followed by platinum (Pt) and titanium (Ti) deposition and a lift-off process for sensor application.[34] Before Pt deposition, 10-nm-thick Ti was deposited for the good adhesion of Pt to the substrate. 100-nm-thick Pt films were prepared on the SiO2/Si substrate using an electron beam evaporator at a base pressure of 2×10^{-6} mTorr. The active area for gas sensing was 1 mm x 1 mm consisting of 20 finger electrodes. A 2 μL drop of the 0.2 mg/mL GO, AGO, HGO_1M, and HGO_5M suspension was cast onto the Pt IDEs/SiO_2/Si substrate, and then dried 10 min at 100°C for removing the solvent.

5.2.4 NO_2 sensor measurement.

The gas sensing properties of the fabricated GO, AGO, HGO_1M, and HGO_5M were measured at a temperature of 150°C by monitoring the variation in sensor resistance by changing the flowing gas from dry air to a calibrated test gas (balanced with dry air, Shinyang Gases, Seoul). The sensor resistance was

measured under a DC bias voltage of 0.3 V using a source measurement unit (Keithley 236). The equivalent electric field for the measurement is 200 kV/m, which is lower than the breakdown voltage of graphene (7×10^7 kV/m).[34, 38] To eliminate any interfering effects, the sensor resistance was measured in quartz tube that is sealed from the outside and it can flow only injected gases to preserve the sensor from H_2O and external factor. A constant flow rate of 500 sccm was used for dry air (N2: 79%, O2: 21%, and humidity: 0%) and the test gases by controlling with mass flow controllers. All measurements were held on a computer by means of Lab VIEW over a general-purpose interface bus (GPIB). The response of the sensors was accurately determined by the ratio of the fully saturated resistances after exposure to the test gas to the base resistances in dry air. The device performance has been calculated using the following equation[30]

$$\Delta R\ (\%) = [|R_0 - R_G| / R_0] \times 100$$

$$Recovery\ (\%) = [|Ra - R_G| / |R_0 - R_G|] \times 100$$

where R_0 is the device resistance under dry gas, R_G is the device resistance under target gas, R_A is the device resistance exposed to dry air for a given recovery time. The response time has been estimated as the time required for the device resistance to change by a factor of 50% of $|R_A - R_G|$. The limit of detection (LOD) was calculated from the sensor noise, which is calculated from the variation in the relative resistance change in the baseline during 300 s before target gas injection, when gas sensor showed the stabilized resistance, using root-mean-square deviation (*rmsd*) form fifth order polynomial fitting and sensitivity from the slope of the linear fitting from the sensing response under different concentrations of NO_2 gas. [25, 39-42]

$$rmsd\ noise = [\ \Sigma\ (y - y_i)^2 / (N)\ ]^{0.5}$$

$$LOD = 3 \times rmsd\ noise / sensitivity$$

where y_i is the measured data point and y is the corresponding value calculated from the curve fitting equation. N is the number of data points used in the curve fitting.

5.2.5 Characterization

To study the oxygen-containing functional groups of the samples, the functional groups were quantified by performing XPS with an AXIS-HSi spectrometer (Kratos). The obtained C1s spectra were fitted and deconvoluted using XPSPEAK41 software. FTIR spectra of the GO, AGO and HGO samples were recorded with a Thermo Scientific Nicolet TM iS10 spectrometer to obtain additional information about their functional groups. The scan range was 400–4,000 cm^{-1} in attenuated total reflection (ATR) mode. Thermogravimetric analysis (TGA) was carried out under nitrogen flow with a heating rate of 10°C/min by using an SDTQ600 instrument (TA Instruments). Raman spectrum was obtained using a Raman plus confocal laser Raman microscope (Nanophoton) with a 532 nm Nd-YAG laser source. The wide angle X-ray diffraction profile was acquired by using a Bruker D8 Advance diffractometer equipped with nickel-filtered Cu Kα radiation (λ = 0.154184 nm). The zeta-potential data were acquired with ELSZ 1000ZS size and zeta-potential analyzer, Otsuka. Non-contact mode AFM images and topographic profiles of the GO, AGO and HGO samples were obtained using a Surface Imaging Systems NX-10 instrument (Park Systems). GO, AGO and HGO were deposited on the Si/SiO2 substrates by using spin-coating. Analytical TEM (JEOL, JEM-2100F) micrographs were obtained to examine the morphologies of the GO, AGO and HGO samples. The optical absorbance data of the aqueous GO, AGO, and HGO (0.2 mg/ml) within the UV-visible region were obtained by using a UV-Vis-NIR Cary 5000 spectrometer (Varian) with a scan range of 400-700 nm. The electrical resistance of GO, AGO,

and HGO deposited films on Au sputtered Si wafer was obtained by point probe station (MSTECH).

5.2.6 Computational method

Monte Carlo (MC) simulations of NO_2 adsorptions were performed to calculate the preferential adsorption site and the adsorption energy on HGO_5M and GO.[43] Prior to the MC simulations, each adsorbent structure was fully optimized by the Forcite module in a Materials Studio 7.0 platform. A universal forcefield (UFF) was applied in all of the calculations. The Ewald summation method with 10^{-5} kcal mol^{-1} accuracy for electrostatic interactions and an atom based summation method with 18.5 Å cut-off radius for van der Waals interactions were used. The lowest energy sites for the adsorbates were identified by the simulated annealing algorithm. In the MC simulation, the non-bond energies are only calculated, since both the adsorbate and the adsorbent are considered to be rigid bodies. Thus, lower interaction energy means a greater possibility of adsorption of NO_2 on the HGO_5M.

5.3 Result and Discussion

5.3.1 Band gap engineering of graphene oxide to semiconductor

In our previous study, we revealed that the hydrolysis of epoxide can occur under an acidic condition of diluted sulfuric acid (H_2SO_4) and is effective for reducing the epoxide groups.[35] Hydrochloric acid (HCl), typically used for the acidic washing process of Hummers method,[31, 35-37] is also a strong acid like H_2SO_4, HCl can reduce the functional group on the basal plane with the mechanisms of **Figure 5.1**. In order to define the effect of HCl during the washing process of Hummers method, we controlled the temperature at 70˚C and the concentration of HCl to 1M and 5M. GO produced by this process were named as HGO_1M and HGO_5M. Some of the GO, produced by Hummers method with typical washing process, is annealed at 70˚C in deionized water (DI water) and we named it AGO.

In order to verify the effect of HCl to the decrement of functional groups, the number of functional groups has to be measured. For comparing the populations of the functional groups, X-ray photoelectron spectroscopy (XPS), fourier transform infrared (FTIR) spectroscopy, zeta potential, thermogravimetric analysis (TGA) were used. As shown in **Figure 5.2**(a) of FTIR spectrum normalized by the C=C double bond peak of aromatic carbon (1633 cm^{-1}) The absorption peaks of hydroxyl and epoxide groups (1105 cm^{-1}, 1248 cm^{-1}, and 3300 cm^{-1}) were smaller in the case of HGO_1M and HGO_5M than those of AGO and GO. This indicates that a large amount of epoxide and a minor amount of hydroxyl groups were decreased by the hydrolysis and dehydration reaction by HCl. In contrast, the peak of carboxyl (1410 cm^{-1}) and carbonyl (1730 cm^{-1}) groups[35, 44, 45] of GO, AGO, HGO_1M, and HGO_5M showed an equal or slight decrease because HCl strongly reduced the functional groups on the basal plane contrary to the edge. This tendency of the functional group decrement, also

showed in XPS result, result of binding ratio obtained by deconvoluted C1s spectra. (**Figure 5. 2**(b) and **Figure 5.3**). This tendency was also found in the C/O atomic ratio of HGO_5M (2.08) and HGO_1M (1.91), which was higher than that of AGO (1.78) and GO (1.61). (**Figure 5. 2**(c)) Decrement of the epoxide and the hydroxyl group of HGO_1M and HGO_5M also can be shown in the weight loss and improved thermal stability of the TGA results because of the elimination of functional groups which disappeared at low temperature.[44] (**Figure 5. 4**(a)) The amount of carbonyl and carboxyl groups also remained and can be verified by the constant negative zeta potential of GO, AGO, HGO_1M, and HGO_5M (**Figure 5. 4**(b)), which is strongly affected by functional groups of the edge.[31, 35]

The number of functional groups on the basal plane can affect the morphology of the GO sheet.[35, 46-49] Therefore, we characterized thickness and crystallinity by powder X-ray diffraction (XRD), atomic force microscopy (AFM), transmittance electron microscopy (TEM) and Raman spectroscopy. As shown in **Figure 5. 6**(b) and **Figure 5.7** of XRD and AFM, which shows the thickness of GO sheets, HGO_5M, and HGO_1M shows lowered thickness than AGO and GO by the decrement of functional groups on the basal plane. These phenomena bring the improved sp^2 structure, and selected area electron diffraction (SAED) patterns measured by TEM (**Figure 5. 5**) of HGO 5M showed the strongest sixfold SAED patterns than other GO sheets. This can be verified with the increment intensity ratio of the D band (~1370 cm^{-1}) and G band (~1600 cm^{-1}) (I_D/I_G ratio) of HGO_1M and HGO_5M by elongated boundaries between the graphitic domain and the defective domain. (**Figure 5. 6**(a))

According to previous research, the improved sp^2 structure of GO by the decrement of functional groups on the basal plane resulted the narrowed band gap of GO. For verifying the effect of improved crystallinity of the basal plane to the electrical properties of graphene, we measured the band gap of GO, AGO,

HGO_1M, and HGO_5M using UV-vis spectroscopy. A number of previous studies, showed that the band gap of semiconductive materials, which can be dispersed in solvent, can be obtained by modified Tauc plot from the absorbance spectrum,[28, 50] Therefore, we measured the absorbance of each water-dispersed sample (0.2 mg/ml) (**Figure 5.8**(a), (b)) from the ultraviolet to the visible range. Each sample showed well dispersibility in water as shown in the negative zeta potential results, we can obtain absorbance spectrums and Tauc plots of each sample successfully as shown in **Figure 5.9**. The band gap of HGO_5M (1.75 eV) was narrower than HGO_1M (2.00 eV), AGO (2.1 eV), and GO (2.2eV). (**Figure 5. 10)** The diminished band gap by the decreased functional groups on the basal plane can be verified by the electrical transport of GO, AGO, HGO_1M, and HGO_5M because the electrical conductivity shows an inverse proportional to the band gap. After fabricating on the Au electrode sputtered Si wafer through spin coating, electrical conductivities of each sample were obtained by the I-V curve, which is obtained by a two-point-probe (**Figure 5.10**) [51] and the thickness of thin films measured by AFM (**Figure 5.11**). Considering the distance and width of the Au electrode (width: 450 μm, distance: 40 μm), the electrical conductivity of HGO_5M (3.23×10^{-3} S/cm) was higher than HGO_1M (9.55×10^{-4} S/cm), AGO (2.05×10^{-4} S/cm), and GO (6.48×10^{-5} S/cm). (**Figure 5.12**) Considering the lateral size of the samples are similar as shown in **Figure 5.13**, this result indicates that the recovered sp^2 carbon by the decrement of epoxide and hydroxyl groups strongly influence the improvement of the electrical performance of GO only,[52, 53] in spite of the small amount. Especially, in the case of HGO 5M, showing the highest electrical conductivity (3.23×10^{-3} S/cm) and band gap (1.75 eV) of semiconductors, has the possibility of a GO based NO_2 gas sensor with improved LOD.

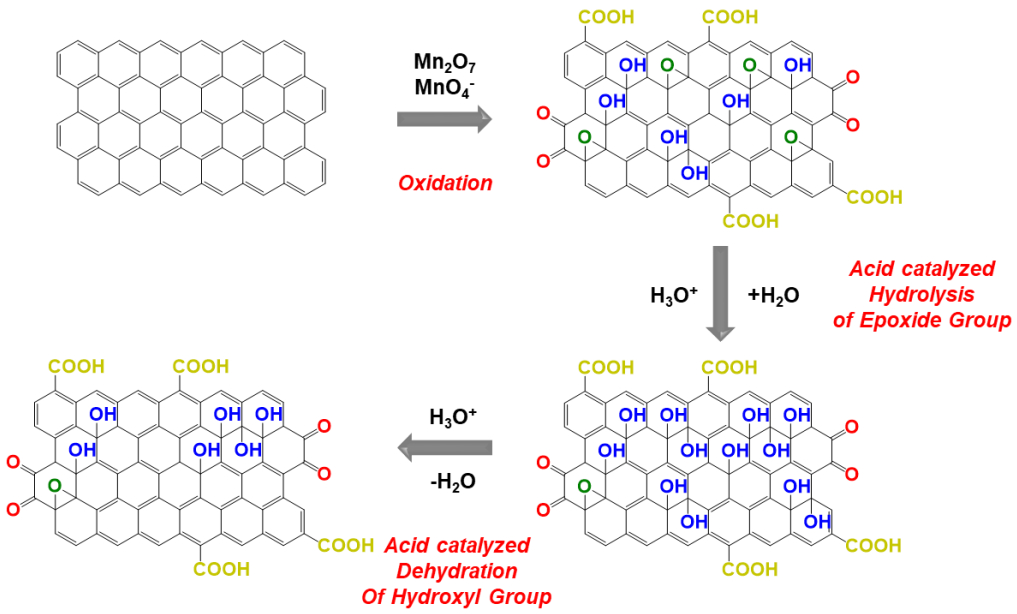

Figure 5.1 Schematic view of partially reduction of GO for synthesis of HGO_5M by hydrolysis and hydration reaction by HCl.

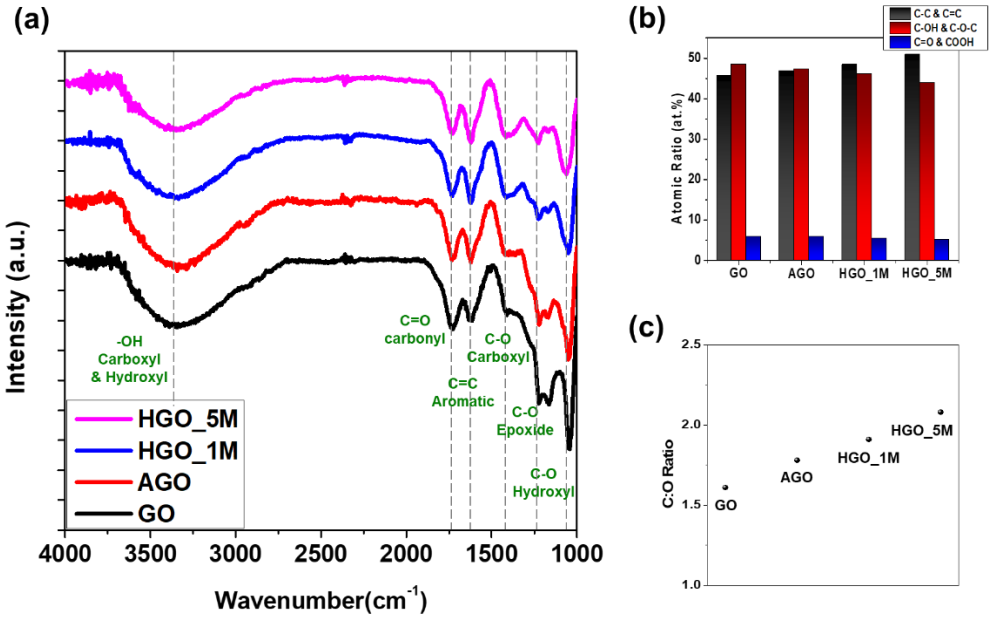

Figure 5.2 (a) Normalized FTIR spectrum normalized upon the absorbance of the C=C double bond from the graphitic domain, (b) Bonding configuration, and (c) C/O atomic ratio measured by XPS.

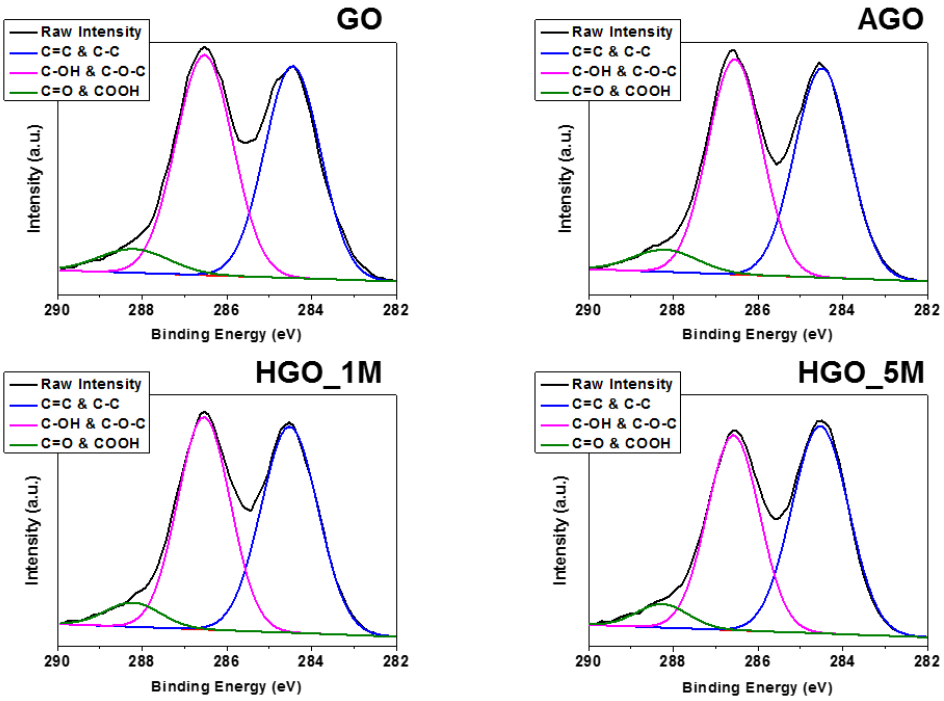

Figure 5.3 XPS C1s spectra of GO, AGO, HGO_1M and HGO_5M sheet.

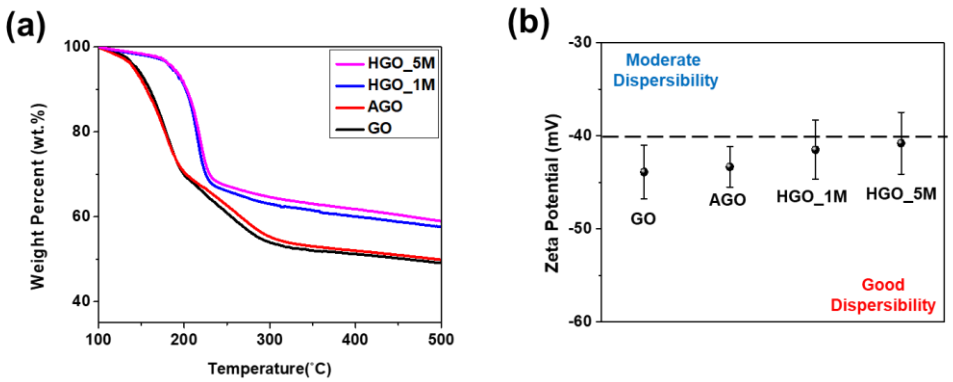

Figure 5.4. (a) Weihgt loss of GO, AGO, HGO_1M and HGO_5M from 100 ℃ ~ 500 ℃ measureed by TGA. (b) Negatice zeta potential of water dispered GO, AGO, HGO_1M and HGO_5M.

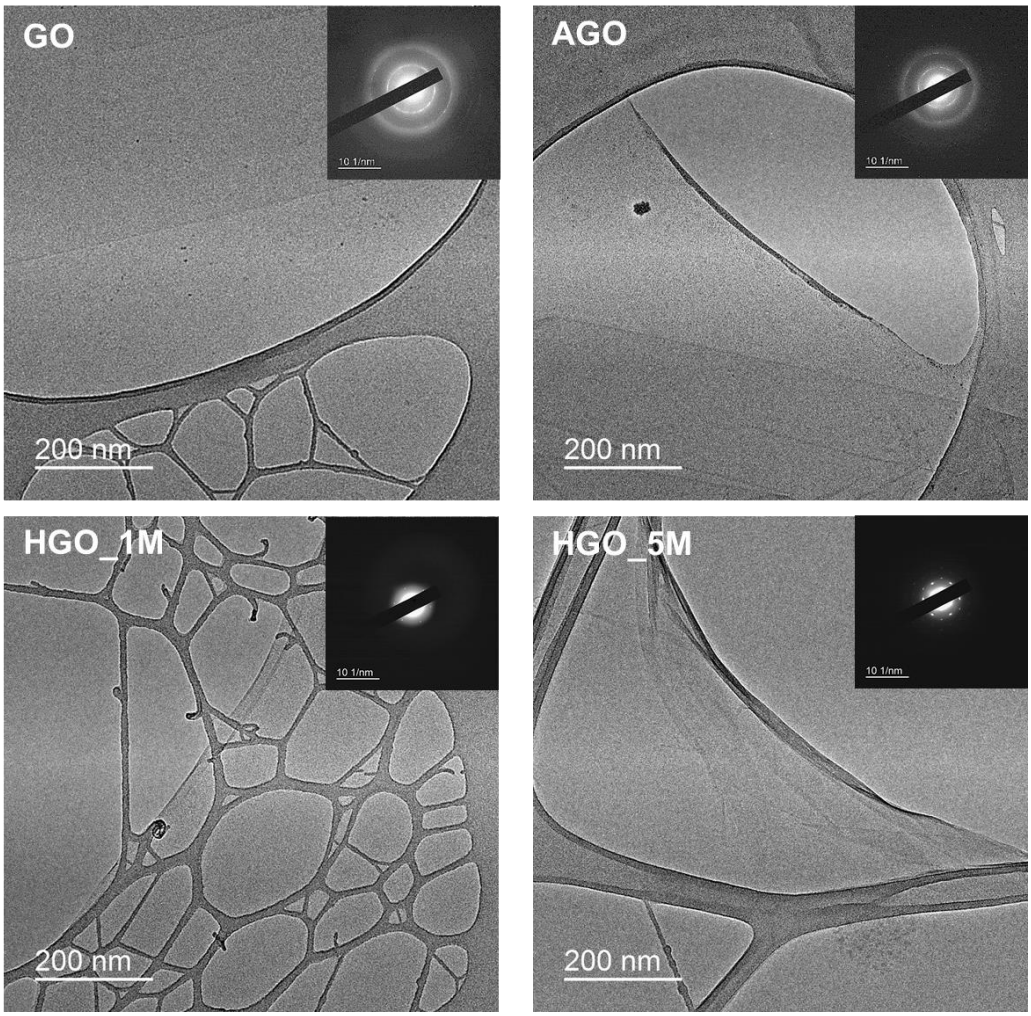

Figure 5.5 The TEM image of edge (x 25,000) and SAED pattern (inset) of GO, AGO, HGO_1M, and HGO_5M.

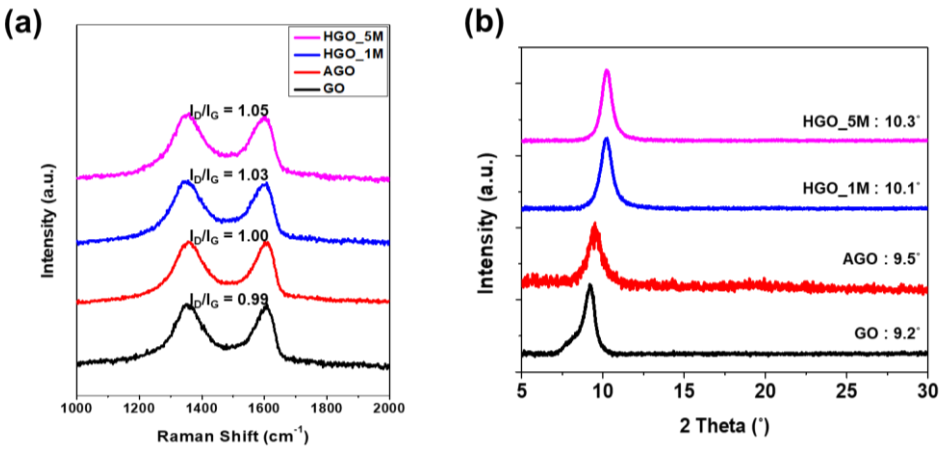

Figure 5.6 The (a) Raman and (b) XRD spectra of GO, AGO, HGO_1M, and HGO_5M

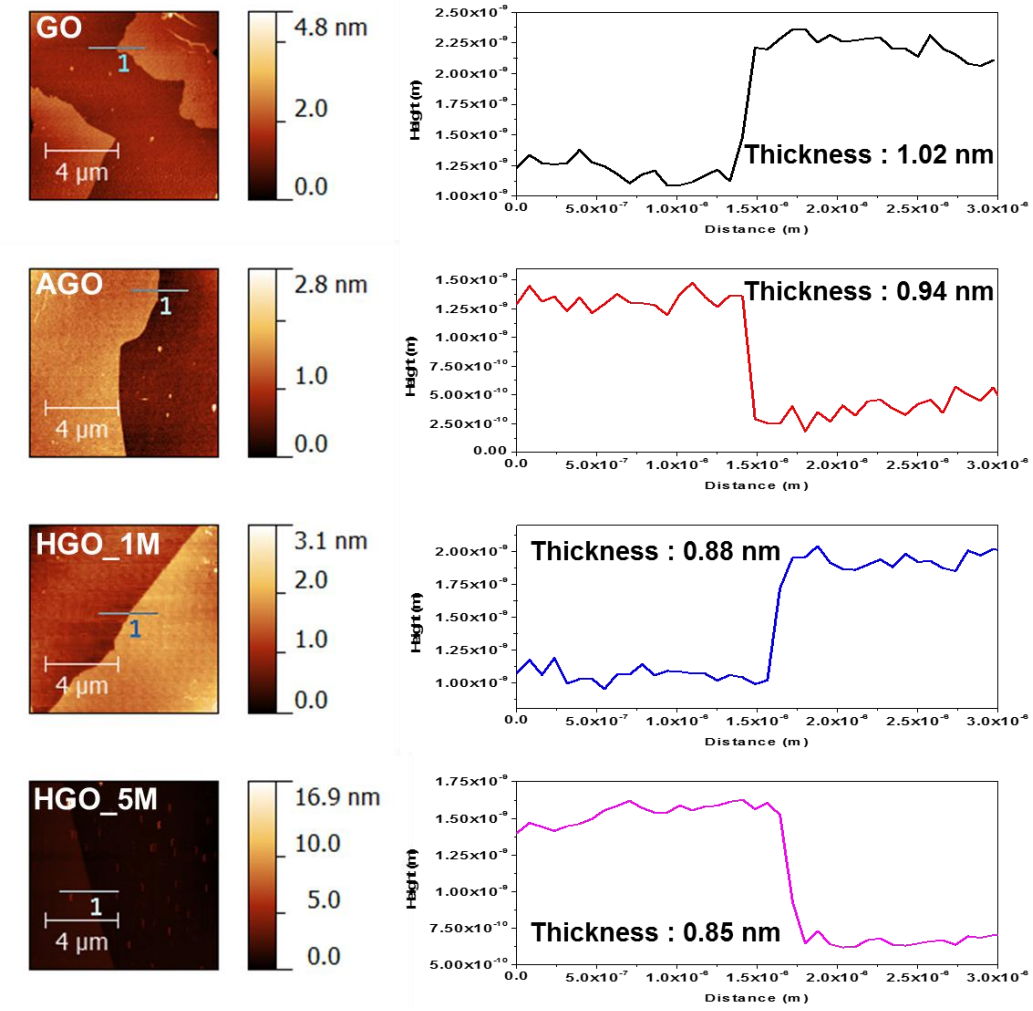

Figure 5.7 AFM topology image, profile of GO, AGO, HGO_1M and HGO_5M sheet.

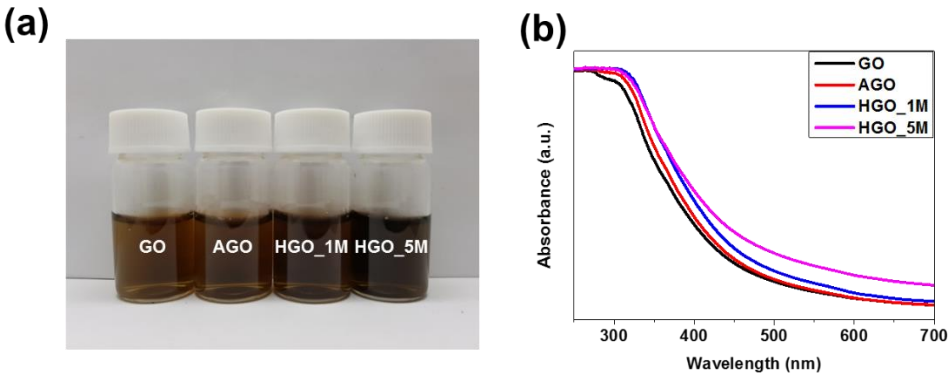

Figure 5.8 (a) Dispersed GO, AGO, HGO_1M and HGO_5M after neutralized by DI water. (b) UV-vis absorbance spectra of GO, AGO, HGO_1M and HGO_5M dispersed in water. (concentration: 0.2 mg/ml)

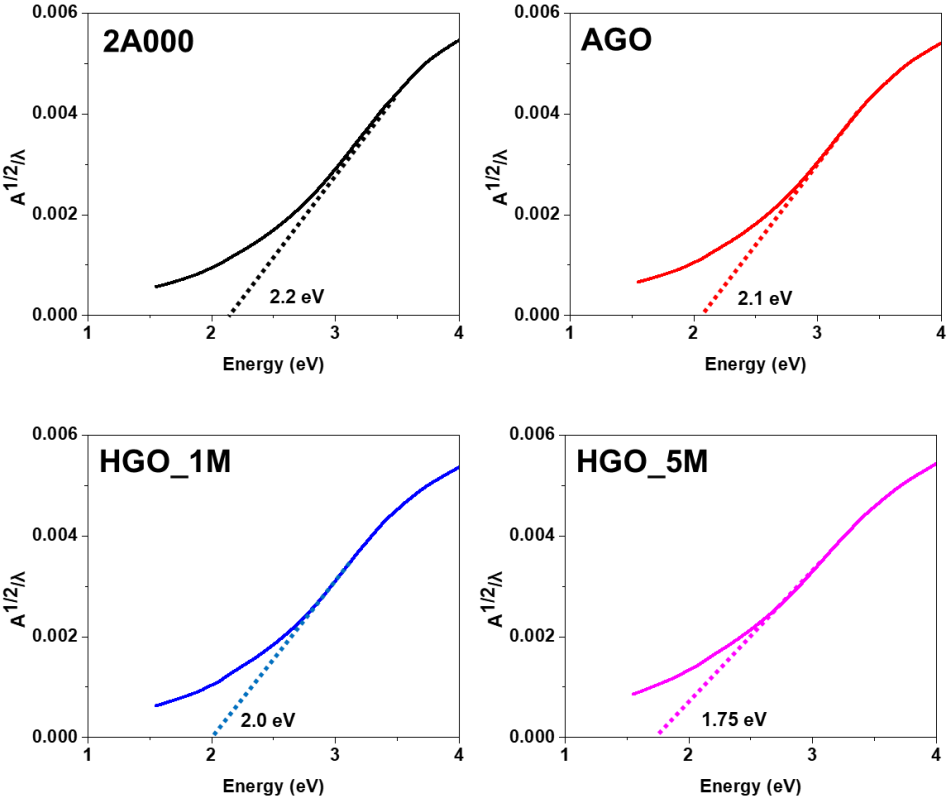

Figure 5.9 Modified Tauc plot of each GO, AGO, HGO_1M, and HGO_5M caculated from the UV-vis absorbance of **Figure 5.8**

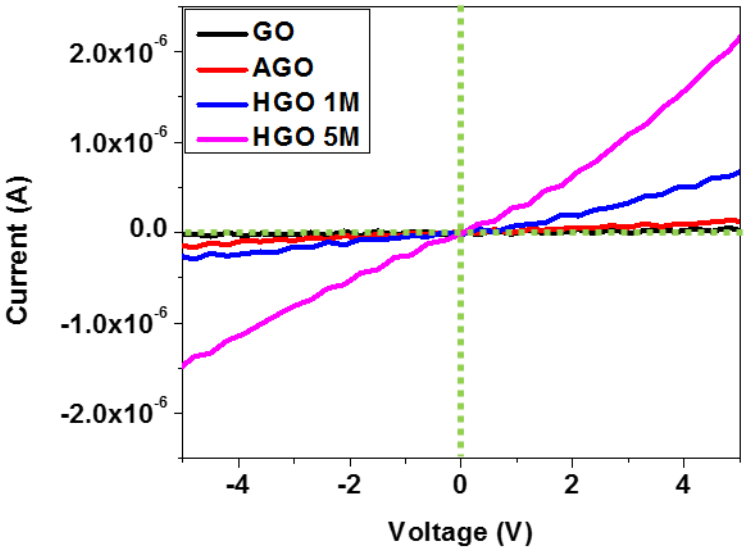

Figure 5.10 I-V curve of GO, AGO, HGO_1M and HGO_5M thin film deposited on Au electrode patterned Si subsrate obtained by 2-point-probe method.

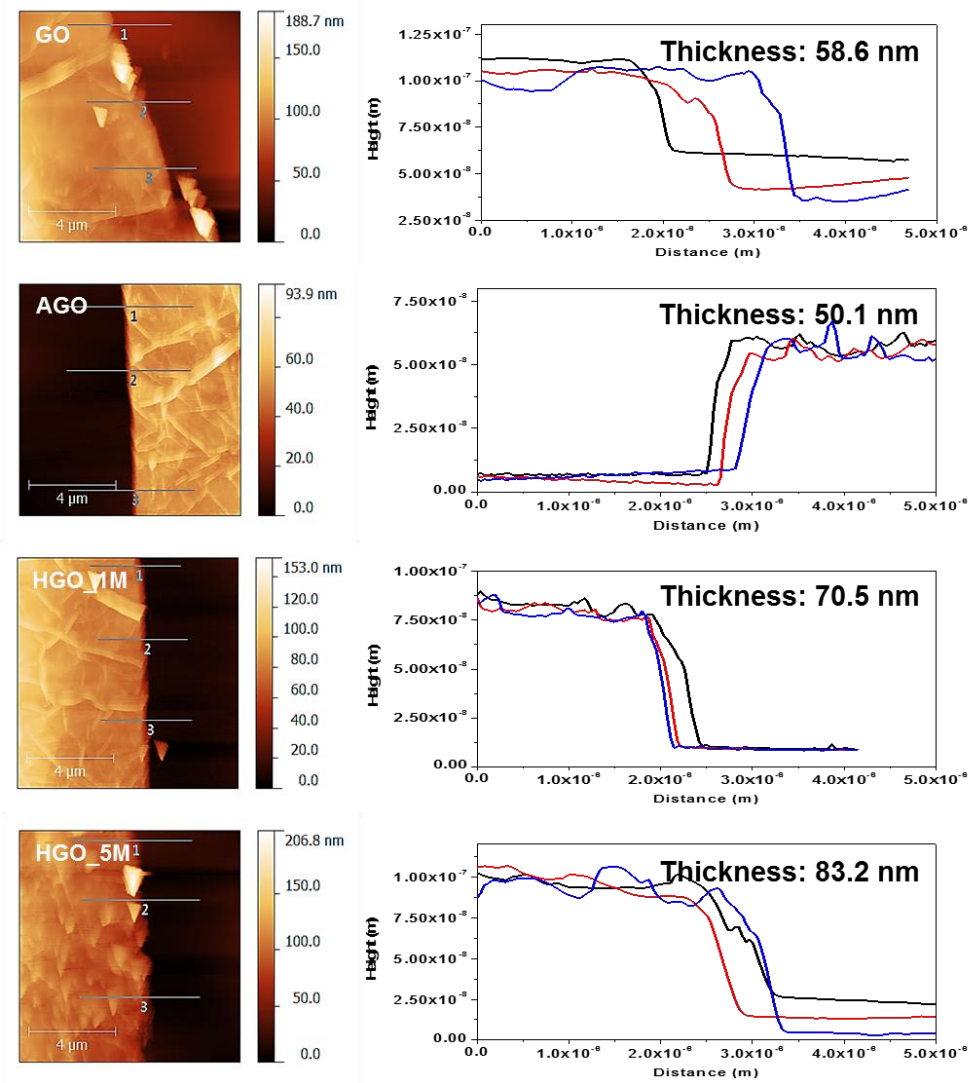

Figure 5.11 Thickness GO, AGO, HGO_1M and HGO_5M thin film obtained by AFM.

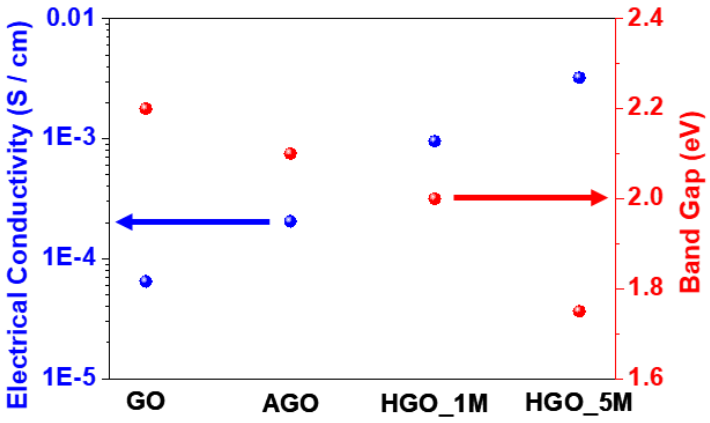

Figure 5.12 The band gap and eletctical conductivity of GO, AGO, HGO_1M, and HGO 5M changed by recovered of sp^2 structure of graphene.

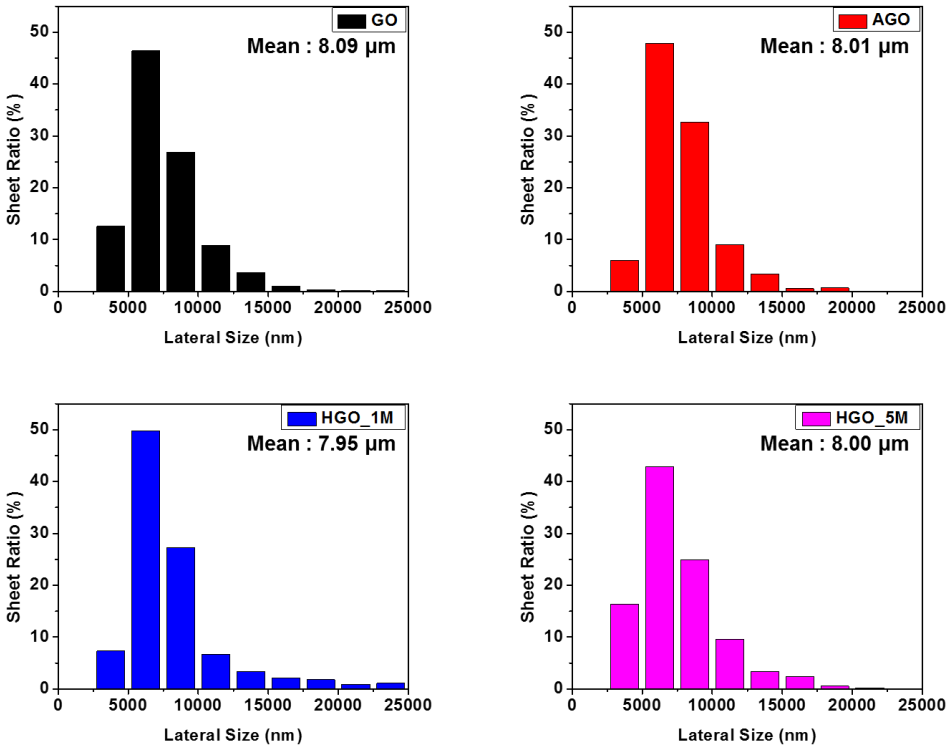

Figure 5.13, Distribution of lateral size of GO, AGO, HGO_1M and HGO_5M sheet obtained from the dynamic light scattering (DLS) result.

5.3.2 Performance of NO_2 gas sensor of band gap engineered GO.

In order to see the possibility of applying HGO to NO_2 gas sensing, we fabricated GO, AGO, 1HGO_1M, and HGO_5M gas sensors to single layered as shown in **Figure 5.14** and **Figure 5.15,** they showed the response characteristics of the GO, AGO, HGO_1M and HGO_5M sensors under 5 ppm NO_2 atmosphere at an applied voltage of 0.3V.(**Figure 5.16**) In order to avoid the slow response time under low temperature as shown in **Figure 5.17**, gas sensing properties of the sensors were measured at 150˚C with monitoring the variation in the sensor resistance with a change in the gas flow from dry air to the target gas. [14, 24] Because thermally reduction of GO is started when the temperature is over 160˚C as shown in **Figure 5. 4**(a), 150˚C are considered as an effective temperature for GO and HGO based NO_2 sensing with the fast response time. The target gas was injected into the chamber for 1000 s, and then the sensors were allowed to recover for 5000 s in dry ambient air. Because the majority carrier of the p-type chemiresistive sensor is a hole, which shows a resistance increase in the presence of traces of reducing gases, the resistance decreased by oxidizing gases such as NO and NO_2.[24, 33, 34]

After the sensors were exposed to the 5 ppm of the target gas, the HGO_5M sensors show reversible sensing behavior under exposures to NO_2. However, other GO, AGO and HGO_1M shows no reversible sensing behavior because of low conductivity from the insulative band gap from the excessive amount of functional groups. (**Figure 5.16**) Conversely, due to the band gap narrowed to the semiconductive range with controlled the amount of functional groups on the basal plane with the narrowed amount of epoxide groups, the HGO_5M sensor showed improved sensing response ($\Delta R/R_0$: ~32 %) in comparison to the HGO_1M ($\Delta R/R_0$: ~12.8%) and AGO ($\Delta R/R_0$: ~9.9%) sensors (**Figure 5.18**(a)) with the improved electrical transport as shown in shortened t_{50} response time (125 s) (**Figure 5.18**) than the HGO_1M (192 s) and AGO (263 s) sensor. This

result implies that improved carrier transport by narrowed band gap to the semiconductive range with high affinity to NO_2 gas is the key point to the enhancement of the gas sensing performance of the GO based NO_2 gas sensor.

The HGO_5M sensor also shows the greatest recovery (81.25 %) than the HGO_1M and AGO sensors as shown in **Figure 5.18**(a). (HGO_1M: 65.8 %, AGO: 41.0 %) in spite of the short restoration time of 5000s. We repeated the injection and subtraction of the target gas for six times in 35000s in order to verify the stability of the sensing properties. As shown in **Figure 5.18**(f), the gas sensing properties of HGO_5M sensor shows a stable performance under repeated injection and subtraction of target gas and showed similar gas sensing performance after 24 h (**Figure 5.19**) because of the improved stability of HGO_5M at 150 ˚C by reduction of the epoxide groups, the most unstable functional groups under the temperature over 100 ˚C, as shown in the TGA result. [35, 44] This improved stability also implies that the reduction of the epoxide group is also important to the enhancement of the gas sensing properties of the GO-based gas sensor. In spite of the the humid environment of RH 50%, the HGO_5M still showed high response of 23%, because of the reduced functional groups (**Figure 5.20**).

In order to see the selectivity of the HGO_5M sensor to NO_2 gas, we exposed 50 ppm of ammonia (NH_3), hydrogen (H_2) and carbon dioxide (CO), which GO can absorb on its surface, to the HGO_5M sensor. Even if there is ten times higher concentration (50 ppm) than NO_2 (5 ppm), the HGO_5M sensor exhibited a response of less than 10 %, which is four times lower than the NO_2 exposure. (**Figure 5.18**(c)) This result shows that the HGO_ 5M sensor has a high selectivity to NO_2 gas and the surface nature of HGO_ 5M was tailor fitted to NO_2 detection by the remaining hydroxyl groups on the basal plane, which shows the high affinity to NO_2 gas as shown in calculation result of **Figure 5.22**.

The high selectivity to NO_2 of HGO_5M implies that it is an appropriate materials to the extremely low concentration of NO_2 gas which can be applied to the sensing device that shows the LOD under the EU annual limit (~21 ppb). [14] Therefore, we exposed the HGO_5M sensor under various concentration of NO_2 gas (1, 2, 3, 4, 5, 7, and 9 ppm) to the HGO_5M sensor. (**Figure 5.18**(d)) The restorability of curves in Fig. 6d can be lowered because the base resistance is shifting with increasing the NO_2 concentration because the longer time is required for full recovery. [39] As the concentration of NO_2 target gas increased, the sensitivity of the HGO_5M sensor was increased precoitally when plotted linearly and the slope is calculated as 4.37 / ppm as shown in **Figure 5.18**(e). Because of the calculated root mean square (RMS) noise of 0.00031 % from fifth order polynomial plot of the base resistance measured during the 300 seconds before NO_2 gas exposure, (**Figure 5.21**) [25, 39-42] the LOD can be calculated as 0.21 ppb, which is extremely lower than other NO_2 sensors and EU annual limit. This result shows that the narrowed band gap energy with high NO_2 adsorption energy by the modified band gap of GO to the semiconductive range is important to preparing GO based NO_2 gas sensor.

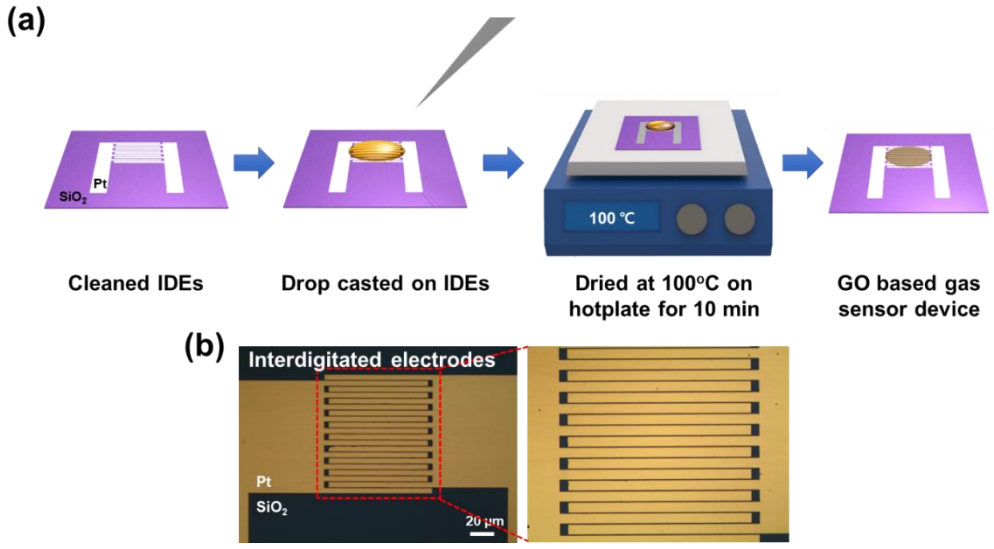

Figure 5.14 (a) Scheme of fabricating the GO, AGO, HGO_1M, and HGO_5M gas sensors and (b) optical microscope image of the HGO_5M gas sensor (left: x 5, right: x 10).

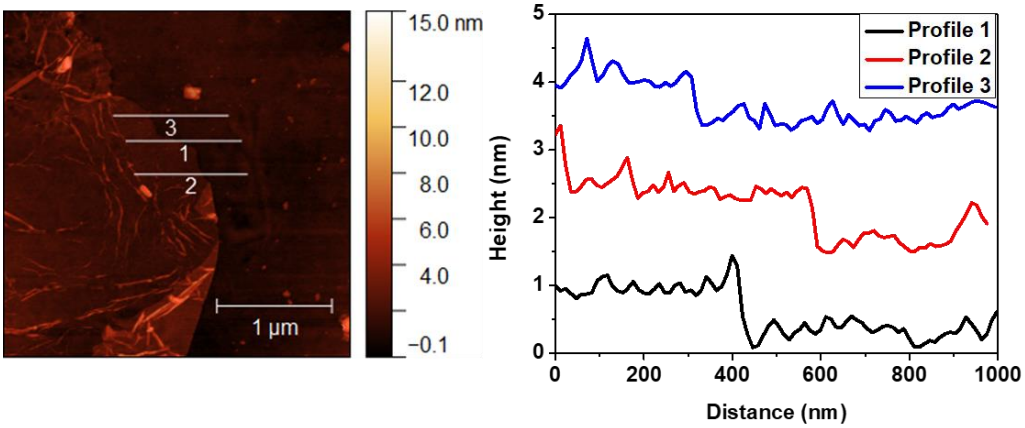

Figure 5.15 Thickness of fabricated HGO thin film measured by AFM (3 ㎛ × 3 ㎛)

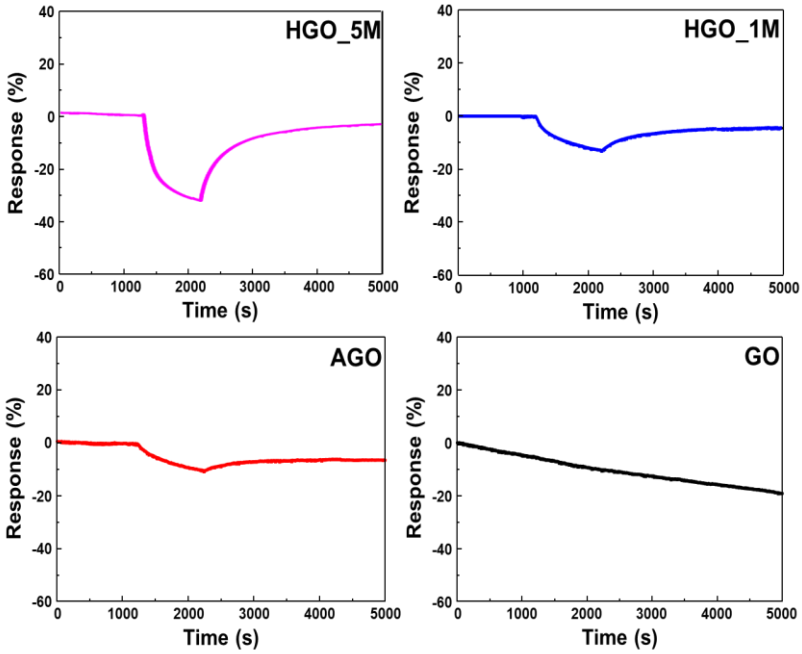

Figure 5.16 Response of GO, AGO, HGO_1M and HGO_5M gas sensor under 5ppm NO_2 injected once.

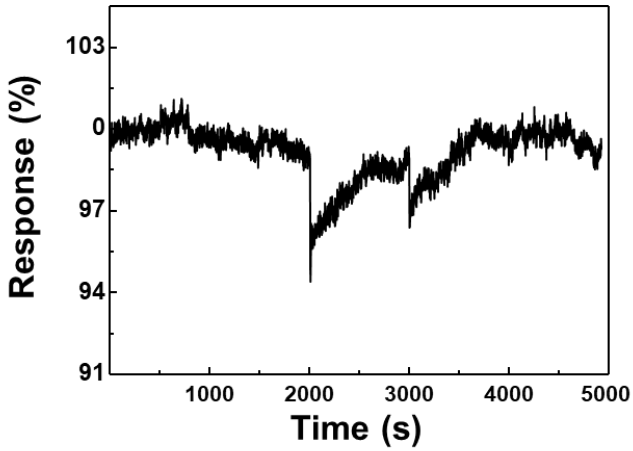

Figure 5.17 Response of HGO_5M sensor to NO_2 gas measured under room temperature.

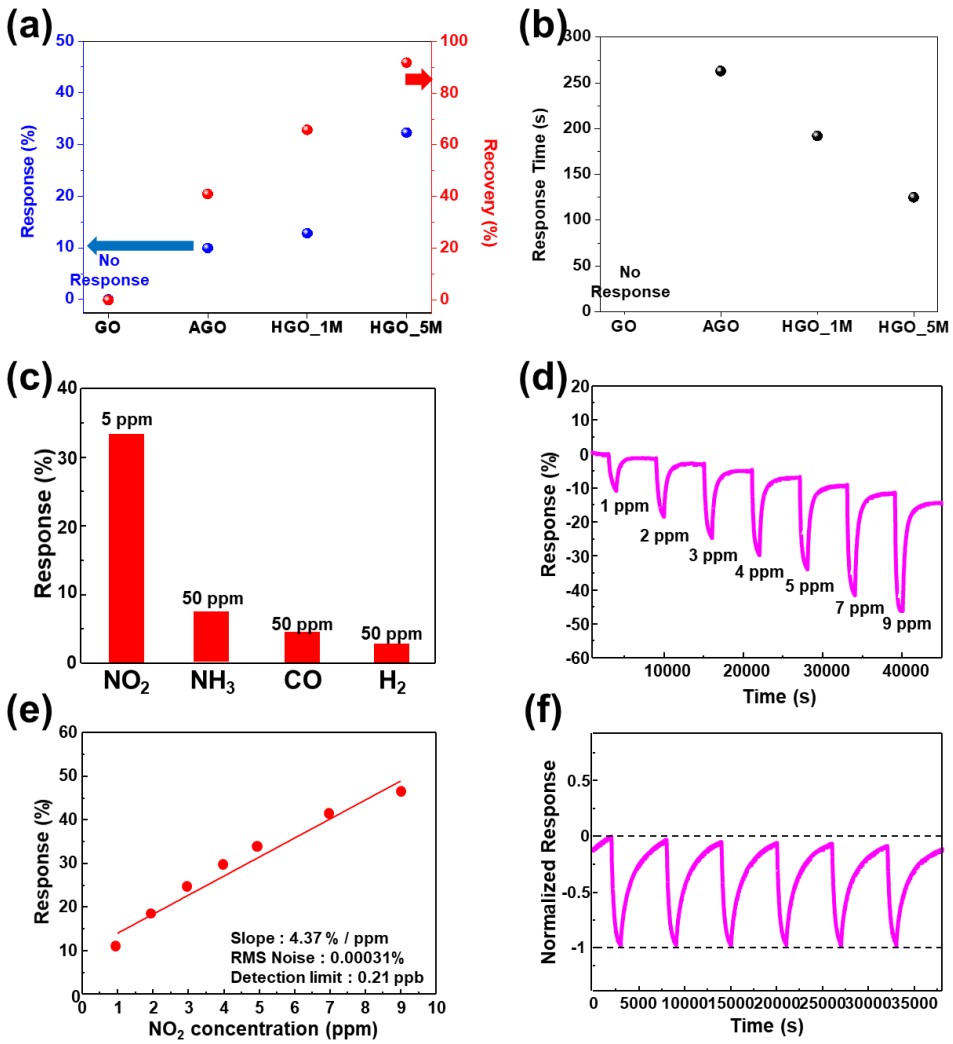

Fugure 5.18 (a) Response under 5ppm NO_2 gas, recovery under dry gas, and (b) response time of the GO, AGO, HGO_1M, and HGO_5M gas sensors calculated from the gas sensing curve. (c) Response of the HGO_5M gas sensor under NO_2 (5ppm), NH_3 (50ppm), CO (50ppm) and H_2(50ppm). (d), (e) Response of the HGO_5M sensor under injection NO_2 with different concentrations from 1ppm to 9ppm for calculating LOD. (f) Gas sensing curve of HGO_5M sensor under repeated injection and subtraction of 5ppm NO_2 gas.

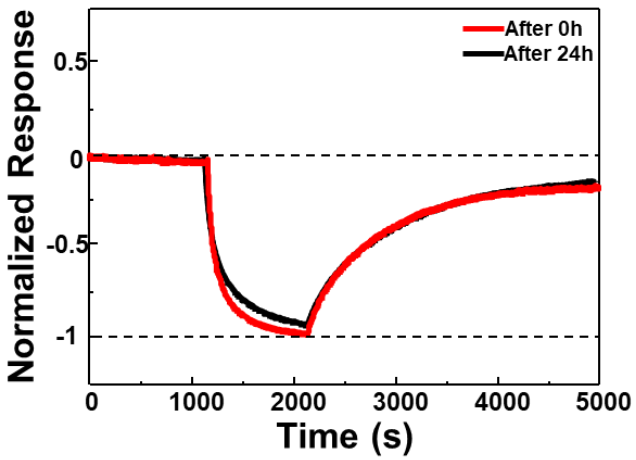

Figure 5.19 Response of HGO_5M sensor to 5 ppm NO_2 gas after 0 h and 24 h measurement normalized by the response after 0h.

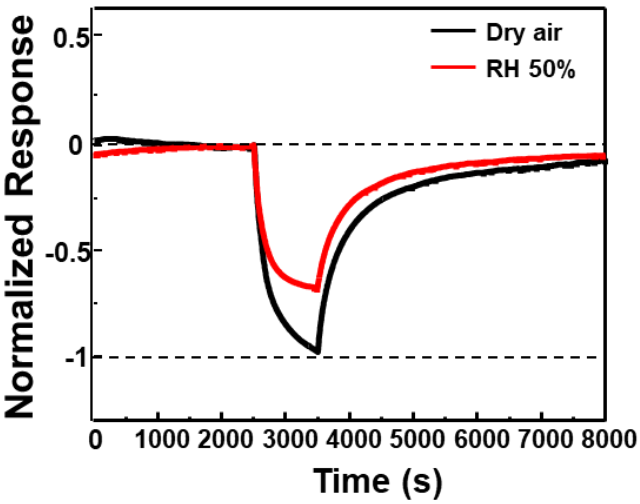

Figure 5.20 Response of HGO_5M sensor to NO_2 gas measured under dry air and RH 50% condition normalized by the response under dry air with 5ppm NO_2 gas.

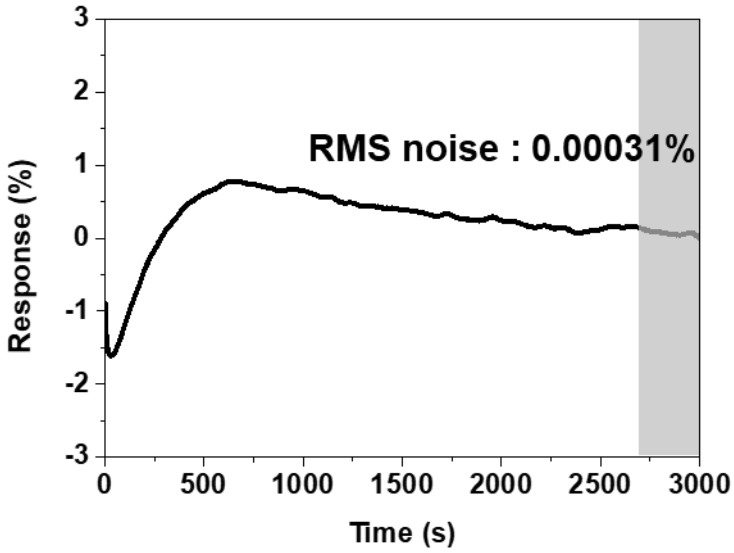

Figure 5.21 Base response of HGO_5M gas sensor under O_2 (21%) / N_2 (79%) dry air for the calculation of RMS noise.

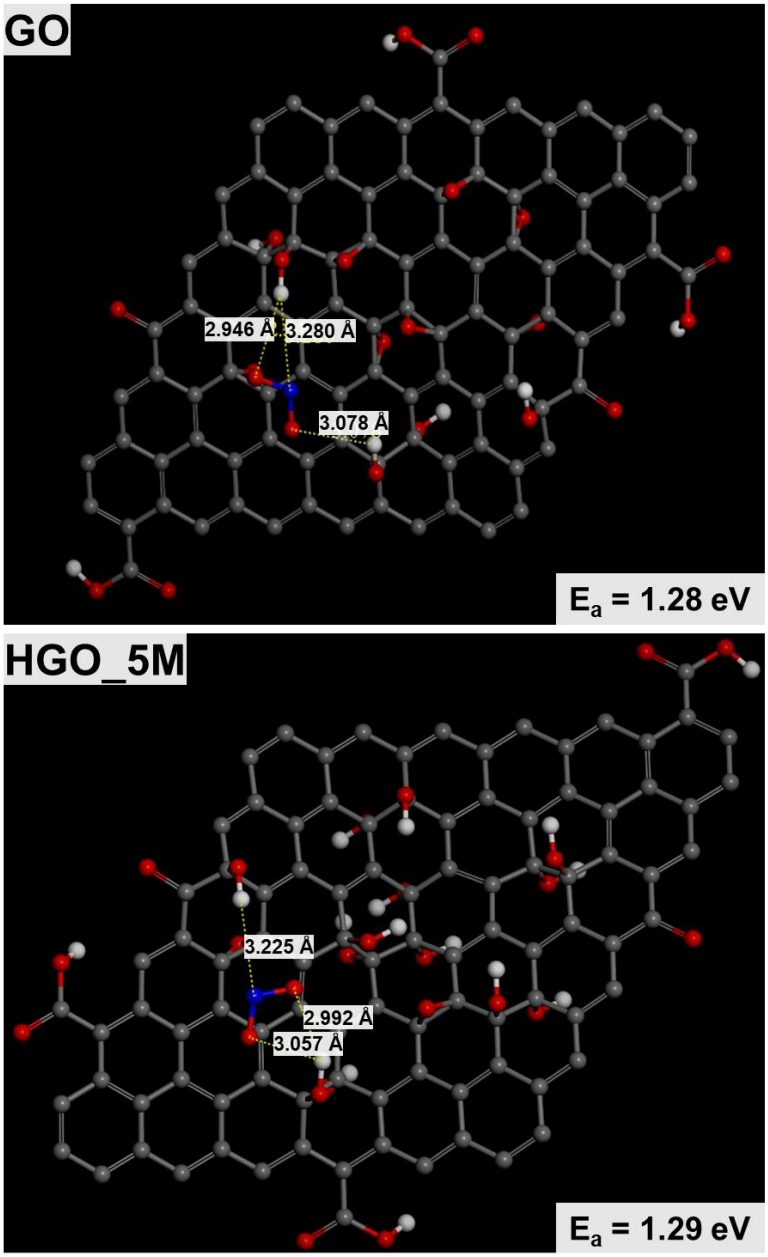

Figure 5.22, Stable molecular structure of NO_2 on GO and HGO_5M used to calculation of adsorption energy with distance between NO_2 molecule to adsorbable functional group of HGO_5M and resultant adsorption energy calculated by Monte Carlo simulation.

5.3.3 Theoretically consideration about the requirement of narrowing band gap of GO for high gas sensing performance.

Considering that the response of the gas sensor comes from the changed conductivity of sensing materials, the electrical conductivity of materials can be described as **Equation 5.1** below.

$$\Delta\sigma = \Delta ne\mu \quad \text{---------- (1)}$$

(σ = *electrical conductivity, n = number of charge carriers,* μ = *electrical mobility*)

In the case of a gas sensor, the number of charge carriers changed by the number of adsorbable target gas molecule,[54, 55] can be described as an exponential function of adsorption energy and temperature from classical Arrhenius form as **Equation 5.2**.[10, 56]

$$\Delta n \propto exp^2(-\frac{E_{ad}}{k_b T}) \quad \text{---------- (2)}$$

(E_{ad} = *adsorption energy,* k_b = *Boltzmann constant, T = operating temperature*)

Considering the equation for calculating theoretical LOD, [25] and RMS noise are proportional to square of resistivity, [26] and the electrical mobility of materials is generally known as the inverse proportional to band gap (**Equation 3**),[57] sensing performance of the gas sensor, LOD can be described as **Equation 5.4, 5.5**.

$$\mu \propto \frac{1}{E_g} \quad \text{---------- (3)}$$

(E_g = *Band gap of sensing materials)*

$$LOD = \frac{RMS\ noise}{sensitivy} \propto \frac{\rho^2}{\Delta ne\mu} = \frac{1}{\Delta ne\mu \times (n_0 e\mu)^2} \quad \text{---------- (4)}$$

(n_0 = *carrier number of sensing materials before adsorption* , ρ = *resistivity of sensing materials)*

$$\therefore \frac{1}{LOD} \propto \frac{exp^2(^{-E_{ad}}/_{k_BT})}{E_g^3} \qquad \text{---------- (5)}$$

From this equation, we can estimate that low band gap and high adsorption energy are required to achieve gas sensing materials with low LOD. However, in the case of graphene oxide, abundant functional groups high NO_2 adsorption energy but also widen the band gap to the insulative range. Therefore, in order to achieve high sensitive gas sensing graphene oxide, narrowing band gap of GO to semiconductive range with high adsorption energy are important. Espacially, epoxide group shows low adsorption energy to NO_2, and it should be minimized for narrowing band gap of GO effectively.[34] As shown in **Figure 5.22** GO and HGO_5M showed similar NO_2 adsorption energy in spite of the decreased epoxide groups.

In order to verify **Equation 5.5** that describes the LOD of NO_2 gas sensors, the function of the band gap and adsorption energy, we summarized the LOD of other materials based NO_2 sensors as shown in **Table 5.1**. With Monte Carlo simulation and with the molecular structure of **Figure 5.22**, HGO_5M showed high NO_2 adsorption energy because of abundant adjacent hydroxyl groups, which have higher NO_2 adsorption energy than any other oxygenated functional groups.[34] Therefore, as expected, the calculated parameter of [$Exp^2(-E_{ad}/k_BT) / E_g^3$)] shows a linear relationship with the inverse of LOD with high reliability ($R^2 \sim 0.94$) as shown in **Fig. 5.23**. This implies that high adsorption energy and low band gap are essential to a highly sensitive NO_2 gas sensor with low LOD. Especially, HGO shows the highest 1 / LOD because of its outstanding adsorption energy with a semiconductive band gap. This result showed that HGO has great potential to be used for NO2 gas sensing materials which can be prepared with a simple process.

Table 5.1. NO2 sensing parameters, band gap, and negative adsorption energy (eV) of representative sensing materials for finding the linear relationship between [$Exp^2(-E_{ad}/k_BT)/E_g^3$)] and 1 / LOD.

	Materials	Band gap (eV)	Negative adsorption energy (eV)	Reference	Operating temperature (ºC)	LOD (ppb)	Response (%) / Concentration (ppb)	Reference
1	NiO	3.6	0.36	[58]	160	160	43 / 1000	[4]
2	ZnO	3.3	0.6	[59]	210	30	1350 / 2100	[5]
3	WO3	2.75	1.12	[60]	150	1.6	26 / 16	[6]
4	SnO2/rGO	3.6	0.52	[61]	60	15.7	8 / 100	[21]
5	SnO2/rGO	3.6	0.52	[61]	150	10	1100 / 100	[19]
6	ZnO/rGO	3.3	0.6	[59]	100	5	1100 / 50	[22]
7	ZnO/rGO	3.3	0.6	[59]	25	47	80 / 400	[20]
8	MoS2	1.8	0.51	[62]	200	28	22.5 / 5000	[13]
9	Phosphorene	0.3[10]	0.65	[10]	25	3.3	120 / 100	[12]
10	Phosphorene	0.3[10]	0.65	[10]	25	5	16 / 40	[11]
11	Phosphorene	0.3[10]	0.65	[10]	25	7	15 / 1000	[9]
12	Sulfur doped graphene	1.0[63]	0.83	[63]	25	0.5	1.8 / 1000	[29]
13	Ozone treated graphene	0.5[27]	0.8	[64]	25	1.3	4 /5000	[30]
14	Reduced Graphene Oxide	0.3[27]	0.27	[33]	400	50	65 / 1000	[18]
15	Reduced Graphene Oxide	0.3[27]	0.27	[33]	22	187	3 / 5000	[17]
16	**Graphene Oxide**	**1.75**	**1.29**	**This work**	**150**	**0.21**	**32 / 5000**	**This work**

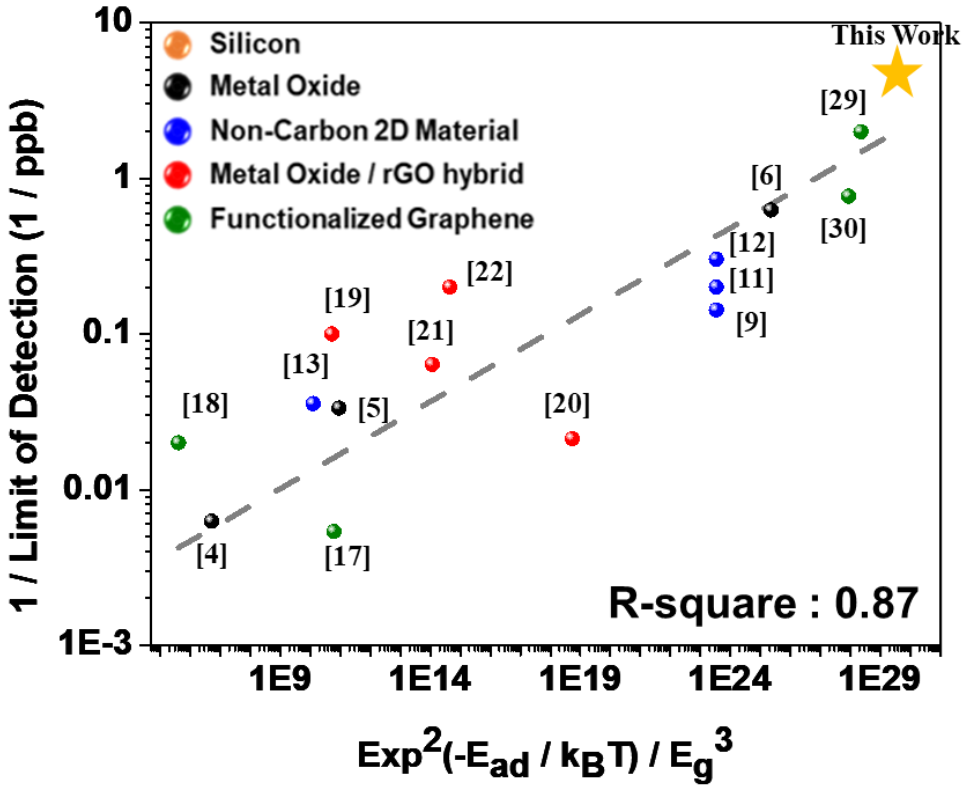

Figure 5.23. The linear relationship between [$Exp^2(-E_{ad}/k_BT) / E_g^3$)] and 1/ LOD shows the influence of band gap and adsorption energy to NO_2 gas sensing performance of materials.

5.4 Conclusion

We developed a new, cost effective method of preparing a semiconductive graphene based sensor with an extremely low NO_2 detection limit quite lower than quality standards of various countries. Through the simple consideration about the effect of the band gap and adsorption energy, eliminating functional groups such as epoxide groups, shows low adsorption energy, considered as an effective way. With a simple modification of the acid washing condition of traditional Hummers method, HCl successfully reduced the epoxide groups and the recovered sp^2 structure of HGO improved electronic performance in which a narrowed band gap of the semiconductor enables HGO_5M to be used in solution processable graphene-based NO_2 gas sensing devices. After sensor fabrication, HGO_5M based NO_2 gas sensor showed outstanding sensing performance with low LOD. This result implies that modification of the band gap of graphene, while considering adsorption energy, can provide an efficient approach to obtain a cost effective way to produce tailor fitted preparation of graphene for gas sensing applications.

5.5 Reference

[1] D. Zhang, Z. Liu, C. Li, T. Tang, X. Liu, S. Han, B. Lei, C. Zhou, Detection of NO2 down to ppb Levels Using Individual and Multiple In2O3 Nanowire Devices, Nano Letters 4(10) (2004) 1919-1924.

[2] H. Long, A. Harley-Trochimczyk, T. Pham, Z. Tang, T. Shi, A. Zettl, C. Carraro, M.A. Worsley, R. Maboudian, High Surface Area MoS2/Graphene Hybrid Aerogel for Ultrasensitive NO2 Detection, Advanced Functional Materials 26(28) (2016) 5158-5165.

[3] K. Kuklinska, L. Wolska, J. Namiesnik, Air quality policy in the U.S. and the EU – a review, Atmospheric Pollution Research 6(1) (2015) 129-137.

[4] I. Hotovy, V. Rehacek, P. Siciliano, S. Capone, L. Spiess, Sensing characteristics of NiO thin films as NO2 gas sensor, Thin Solid Films 418(1) (2002) 9-15.

[5] H.-U. Lee, K. Ahn, S.-J. Lee, J.-P. Kim, H.-G. Kim, S.-Y. Jeong, C.-R. Cho, ZnO nanobarbed fibers: Fabrication, sensing NO2 gas, and their sensing mechanism, Applied Physics Letters 98(19) (2011) 193114.

[6] C.S. Prajapati, N. Bhat, ppb level detection of NO2 using a WO3 thin film-based sensor: material optimization, device fabrication and packaging, RSC Advances 8(12) (2018) 6590-6599.

[7] X. Geng, D. Lahem, C. Zhang, C.-J. Li, M.-G. Olivier, M. Debliquy, Visible light enhanced black NiO sensors for ppb-level NO2 detection at room temperature, Ceramics International 45(4) (2019) 4253-4261.

[8] B. Liu, L. Chen, G. Liu, A.N. Abbas, M. Fathi, C. Zhou, High-Performance Chemical Sensing Using Schottky-Contacted Chemical Vapor Deposition Grown Monolayer MoS2 Transistors, ACS Nano 8(5) (2014) 5304-5314.

[9] M. Donarelli, L. Ottaviano, L. Giancaterini, G. Fioravanti, F. Perrozzi, C.

Cantalini, Exfoliated black phosphorus gas sensing properties at room temperature, 2D Materials 3(2) (2016) 025002.
[10] S. Cui, H. Pu, S.A. Wells, Z. Wen, S. Mao, J. Chang, M.C. Hersam, J. Chen, Ultrahigh sensitivity and layer-dependent sensing performance of phosphorene-based gas sensors, Nature Communications 6 (2015) 8632.
[11] A.N. Abbas, B. Liu, L. Chen, Y. Ma, S. Cong, N. Aroonyadet, M. Köpf, T. Nilges, C. Zhou, Black Phosphorus Gas Sensors, ACS Nano 9(5) (2015) 5618-5624.
[12] S. Shi, R. Hu, E. Wu, Q. Li, X. Chen, W. Guo, C. Sun, X. Hu, D. Zhang, J. Liu, Highly-sensitive gas sensor based on two-dimensional material field effect transistor, Nanotechnology 29(43) (2018) 435502.
[13] H. Long, L. Chan, A. Harley-Trochimczyk, L.E. Luna, Z. Tang, T. Shi, A. Zettl, C. Carraro, M.A. Worsley, R. Maboudian, 3D MoS2 Aerogel for Ultrasensitive NO2 Detection and Its Tunable Sensing Behavior, Advanced Materials Interfaces 4(16) (2017).
[14] C. Melios, V. Panchal, K. Edmonds, A. Lartsev, R. Yakimova, O. Kazakova, Detection of Ultralow Concentration NO2 in Complex Environment Using Epitaxial Graphene Sensors, ACS Sensors 3(9) (2018) 1666-1674.
[15] M.W.K. Nomani, R. Shishir, M. Qazi, D. Diwan, V.B. Shields, M.G. Spencer, G.S. Tompa, N.M. Sbrockey, G. Koley, Highly sensitive and selective detection of NO2 using epitaxial graphene on 6H-SiC, Sensors and Actuators B: Chemical 150(1) (2010) 301-307.
[16] J.T. Robinson, F.K. Perkins, E.S. Snow, Z. Wei, P.E. Sheehan, Reduced Graphene Oxide Molecular Sensors, Nano Letters 8(10) (2008) 3137-3140.
[17] J. Wu, K. Tao, J. Miao, L.K. Norford, Improved Selectivity and Sensitivity of Gas Sensing Using a 3D Reduced Graphene Oxide Hydrogel with an Integrated Microheater, ACS Applied Materials & Interfaces 7(49) (2015) 27502-27510.

[18] S. Cui, H. Pu, E.C. Mattson, Z. Wen, J. Chang, Y. Hou, C.J. Hirschmugl, J. Chen, Ultrasensitive Chemical Sensing through Facile Tuning Defects and Functional Groups in Reduced Graphene Oxide, Analytical Chemistry 86(15) (2014) 7516-7522.
[19] Y. Xiao, Q. Yang, Z. Wang, R. Zhang, Y. Gao, P. Sun, Y. Sun, G. Lu, Improvement of NO2 gas sensing performance based on discoid tin oxide modified by reduced graphene oxide, Sensors and Actuators B: Chemical 227 (2016) 419-426.
[20] Y. Xia, J. Wang, J.-L. Xu, X. Li, D. Xie, L. Xiang, S. Komarneni, Confined Formation of Ultrathin ZnO Nanorods/Reduced Graphene Oxide Mesoporous Nanocomposites for High-Performance Room-Temperature NO2 Sensors, ACS Applied Materials & Interfaces 8(51) (2016) 35454-35463.
[21] X. Zhu, Y. Guo, H. Ren, C. Gao, Y. Zhou, Enhancing the NO2 gas sensing properties of rGO/SnO2 nanocomposite films by using microporous substrates, Sensors and Actuators B: Chemical 248 (2017) 560-570.
[22] J. Liu, S. Li, B. Zhang, Y. Xiao, Y. Gao, Q. Yang, Y. Wang, G. Lu, Ultrasensitive and low detection limit of nitrogen dioxide gas sensor based on flower-like ZnO hierarchical nanostructure modified by reduced graphene oxide, Sensors and Actuators B: Chemical 249 (2017) 715-724.
[23] M. Donarelli, L. Ottaviano, 2D Materials for Gas Sensing Applications: A Review on Graphene Oxide, MoS(2), WS(2) and Phosphorene, Sensors (Basel) 18(11) (2018).
[24] S. Prezioso, F. Perrozzi, L. Giancaterini, C. Cantalini, E. Treossi, V. Palermo, M. Nardone, S. Santucci, L. Ottaviano, Graphene Oxide as a Practical Solution to High Sensitivity Gas Sensing, The Journal of Physical Chemistry C 117(20) (2013) 10683-10690.
[25] J. Li, Y. Lu, Q. Ye, M. Cinke, J. Han, M. Meyyappan, Carbon Nanotube Sensors for Gas and Organic Vapor Detection, Nano Letters 3(7) (2003) 929-933.

[26] M. Marzano, A. Cultrera, M. Ortolano, L. Callegaro, A correlation noise spectrometer for flicker noise measurement in graphene samples, Measurement Science and Technology 30(3) (2019) 035102.
[27] H. Huang, Z. Li, J. She, W. Wang, Oxygen density dependent band gap of reduced graphene oxide, Journal of Applied Physics 111(5) (2012) 054317.
[28] A. Mathkar, D. Tozier, P. Cox, P. Ong, C. Galande, K. Balakrishnan, A. Leela Mohana Reddy, P.M. Ajayan, Controlled, Stepwise Reduction and Band Gap Manipulation of Graphene Oxide, The Journal of Physical Chemistry Letters 3(8) (2012) 986-991.
[29] L. Guo, T. Li, Sub-ppb and ultra selective nitrogen dioxide sensor based on sulfur doped graphene, Sensors and Actuators B: Chemical 255 (2018) 2258-2263.
[30] M.G. Chung, D.H. Kim, H.M. Lee, T. Kim, J.H. Choi, D.k. Seo, J.-B. Yoo, S.-H. Hong, T.J. Kang, Y.H. Kim, Highly sensitive NO2 gas sensor based on ozone treated graphene, Sensors and Actuators B: Chemical 166-167 (2012) 172-176.
[31] M.S. Chang, Y.S. Kim, J.H. Kang, J. Park, S.J. Sung, S.H. So, K.T. Park, S.J. Yang, T. Kim, C.R. Park, Guidelines for Tailored Chemical Functionalization of Graphene, Chemistry of Materials 29(1) (2017) 307-318.
[32] J. Park, Y.S. Cho, S.J. Sung, M. Byeon, S.J. Yang, C.R. Park, Characteristics tuning of graphene-oxide-based-graphene to various end-uses, Energy Storage Materials 14 (2018) 8-21.
[33] Shaobin Tang, Z. Cao, Adsorption of nitrogen oxides on graphene and graphene oxides: Insights from density functional calculations, The Journal of Chemical Physics 134(4) (2011) 044710.
[34] Y.R. Choi, Y.-G. Yoon, K.S. Choi, J.H. Kang, Y.-S. Shim, Y.H. Kim, H.J. Chang, J.-H. Lee, C.R. Park, S.Y. Kim, H.W. Jang, Role of oxygen functional groups in graphene oxide for reversible room-temperature NO2 sensing, Carbon

91 (2015) 178-187.
[35] J.H. Kang, T. Kim, J. Choi, J. Park, Y.S. Kim, M.S. Chang, H. Jung, K.T. Park, S.J. Yang, C.R. Park, Hidden Second Oxidation Step of Hummers Method, Chemistry of Materials 28(3) (2016) 756-764.
[36] W.S. Hummers, R.E. Offeman, Preparation of Graphitic Oxide, Journal of the American Chemical Society 80(6) (1958) 1339-1339.
[37] N.I. Kovtyukhova, P.J. Ollivier, B.R. Martin, T.E. Mallouk, S.A. Chizhik, E.V. Buzaneva, A.D. Gorchinskiy, Layer-by-Layer Assembly of Ultrathin Composite Films from Micron-Sized Graphite Oxide Sheets and Polycations, Chemistry of Materials 11(3) (1999) 771-778.
[38] Y.H. Kim, J.S. Park, Y.-R. Choi, S.Y. Park, S.Y. Lee, W. Sohn, Y.-S. Shim, J.-H. Lee, C.R. Park, Y.S. Choi, B.H. Hong, J.H. Lee, W.H. Lee, D. Lee, H.W. Jang, Chemically fluorinated graphene oxide for room temperature ammonia detection at ppb levels, Journal of Materials Chemistry A 5(36) (2017) 19116-19125.
[39] Y.H. Kim, S.J. Kim, Y.-J. Kim, Y.-S. Shim, S.Y. Kim, B.H. Hong, H.W. Jang, Self-Activated Transparent All-Graphene Gas Sensor with Endurance to Humidity and Mechanical Bending, ACS Nano 9(10) (2015) 10453-10460.
[40] L.A. Currie, Nomenclature in evaluation of analytical methods including detection and quantification capabilities - International Union of Pure and Applied Chemistry (IUPAC Recommendations 1995), Pure Appl. Chem. 67 (1995) 1699-1723.
[41] S.J. Kim, H.-J. Koh, C.E. Ren, O. Kwon, K. Maleski, S.-Y. Cho, B. Anasori, C.-K. Kim, Y.-K. Choi, J. Kim, Y. Gogotsi, H.-T. Jung, Metallic Ti3C2Tx MXene Gas Sensors with Ultrahigh Signal-to-Noise Ratio, ACS Nano 12(2) (2018) 986-993.
[42] V. Dua, S.P. Surwade, S. Ammu, S.R. Agnihotra, S. Jain, K.E. Roberts, S. Park, R.S. Ruoff, S.K. Manohar, All-Organic Vapor Sensor Using Inkjet-Printed

Reduced Graphene Oxide, Angewandte Chemie International Edition 49(12) (2010) 2154-2157.
[43] Y.C. Jeong, K. Lee, T. Kim, J.H. Kim, J. Park, Y.S. Cho, S.J. Yang, C.R. Park, Partially unzipped carbon nanotubes for high-rate and stable lithium–sulfur batteries, Journal of Materials Chemistry A 4(3) (2016) 819-826.
[44] M. Acik, G. Lee, C. Mattevi, A. Pirkle, R.M. Wallace, M. Chhowalla, K. Cho, Y. Chabal, The Role of Oxygen during Thermal Reduction of Graphene Oxide Studied by Infrared Absorption Spectroscopy, The Journal of Physical Chemistry C 115(40) (2011) 19761-19781.
[45] O.J. Young, P. Jisoo, J.Y. Chan, K.J. Ho, Y.S. Jae, P.C. Rae, Secondary Interactions of Graphene Oxide on Liquid Crystal Formation and Stability, Particle & Particle Systems Characterization 34(9) (2017) 1600383.
[46] D.R. Dreyer, S. Park, C.W. Bielawski, R.S. Ruoff, The chemistry of graphene oxide, Chemical Society Reviews 39(1) (2010) 228-240.
[47] K. Krishnamoorthy, M. Veerapandian, K. Yun, S.J. Kim, The chemical and structural analysis of graphene oxide with different degrees of oxidation, Carbon 53 (2013) 38-49.
[48] I.K. Moon, J. Lee, R.S. Ruoff, H. Lee, Reduced graphene oxide by chemical graphitization, Nature Communications 1 (2010) 73.
[49] J. Park, Y.S. Kim, S.J. Sung, T. Kim, C.R. Park, Highly dispersible edge-selectively oxidized graphene with improved electrical performance, Nanoscale 9(4) (2017) 1699-1708.
[50] S. Wang, I.S. Cole, Q. Li, Quantum-confined bandgap narrowing of TiO2 nanoparticles by graphene quantum dots for visible-light-driven applications, Chemical Communications 52(59) (2016) 9208-9211.
[51] M. Savchak, N. Borodinov, R. Burtovyy, M. Anayee, K. Hu, R. Ma, A. Grant, H. Li, D.B. Cutshall, Y. Wen, G. Koley, W.R. Harrell, G. Chumanov, V. Tsukruk, I. Luzinov, Highly Conductive and Transparent Reduced Graphene Oxide

Nanoscale Films via Thermal Conversion of Polymer-Encapsulated Graphene Oxide Sheets, ACS Applied Materials & Interfaces 10(4) (2018) 3975-3985.
[52] J. Zhao, S. Pei, W. Ren, L. Gao, H.-M. Cheng, Efficient Preparation of Large-Area Graphene Oxide Sheets for Transparent Conductive Films, ACS Nano 4(9) (2010) 5245-5252.
[53] Q. Zheng, W.H. Ip, X. Lin, N. Yousefi, K.K. Yeung, Z. Li, J.-K. Kim, Transparent Conductive Films Consisting of Ultralarge Graphene Sheets Produced by Langmuir–Blodgett Assembly, ACS Nano 5(7) (2011) 6039-6051.
[54] M. Donarelli, L. Ottaviano, 2D Materials for Gas Sensing Applications: A Review on Graphene Oxide, MoS2, WS2 and Phosphorene, Sensors 18(11) (2018) 3638.
[55] T. Wang, D. Huang, Z. Yang, S. Xu, G. He, X. Li, N. Hu, G. Yin, D. He, L. Zhang, A Review on Graphene-Based Gas/Vapor Sensors with Unique Properties and Potential Applications, Nano-Micro Letters 8(2) (2016) 95-119.
[56] H.H. Pu, S.H. Rhim, M. Gajdardziksa-Josifovska, C.J. Hirschmugl, M. Weinert, J.H. Chen, A statistical thermodynamics model for monolayer gas adsorption on graphene-based materials: implications for gas sensing applications, RSC Advances 4(88) (2014) 47481-47487.
[57] J. Wang, R. Zhao, M. Yang, Z. Liu, Z. Liu, Inverse relationship between carrier mobility and bandgap in graphene, The Journal of Chemical Physics 138(8) (2013) 084701.
[58] B. Wang, J. Nisar, R. Ahuja, Molecular Simulation for Gas Adsorption at NiO (100) Surface, ACS Applied Materials & Interfaces 4(10) (2012) 5691-5697.
[59] Nugraha, A.G. Saputro, M.K. Agusta, B. Yuliarto, H.K. Dipojono, R. Maezono, Density functional study of adsorptions of CO2, NO2and SO2molecules on Zn(0002) surfaces, Journal of Physics: Conference Series 739 (2016) 012080.
[60] L. Saadi, C. Lambert-Mauriat, V. Oison, H. Ouali, R. Hayn, Mechanism of

NOx sensing on WO3 surface: First principle calculations, Applied Surface Science 293 (2014) 76-79.
[61] J.D. Prades, A. Cirera, J.R. Morante, J.M. Pruneda, P. Ordejón, Ab initio study of NOx compounds adsorption on SnO2 surface, Sensors and Actuators B: Chemical 126(1) (2007) 62-67.
[62] G. Deokar, P. Vancsó, R. Arenal, F. Ravaux, J. Casanova-Cháfer, E. Llobet, A. Makarova, D. Vyalikh, C. Struzzi, P. Lambin, M. Jouiad, J.F. Colomer, MoS2–Carbon Nanotube Hybrid Material Growth and Gas Sensing, Advanced Materials Interfaces 4(24) (2017).
[63] J. Dai, J. Yuan, P. Giannozzi, Gas adsorption on graphene doped with B, N, Al, and S: A theoretical study, Applied Physics Letters 95(23) (2009) 232105.
[64] Y. You, J. Deng, X. Tan, N. Gorjizadeh, M. Yoshimura, S.C. Smith, V. Sahajwalla, R.K. Joshi, On the mechanism of gas adsorption for pristine, defective and functionalized graphene, Physical Chemistry Chemical Physics 19(8) (2017) 6051-6056.

Chapter 6 Thin film transistor performance of IGZO with band gap tuned graphene

6.1 Introduction

Graphene, which shows tremendous materials properties compared to other traditional materials and expected to be applied to next generation transistor with high mobility. [1-3] Therefore, there are many tries to make graphene based transistor with high mobility, but it is hard to be realized because of its low on/off ration from its zero band gap nature. [1-3] In order to overcome this barrier, many researches tried to enlarge band gap using specific graphene such as few layer graphene, [4-6] graphene nanoribbons, [7, 8] and chemically doped graphene, [9-11] but no method satisfied the requirement of industry field and new method of realizing the great potential of graphene to transistor.

Therefore, some researches tried to use graphene with other semiconductive materials in order to give on/off ratio to graphene based transistor and it showed better semiconductive performance. [5, 6, 12-27] In case of hybridized with zinc oxide (ZnO) or indium-gallium-zinc oxide (IGZO) showed great semiconductive performance compared to traditional Silicon (Si) based transistor. [28] However, those way of preparing graphene based composite is complicated and requires high cost.

In order to achieve low cost production of transistor with graphene based composite, ink based process is required. However, the properties of transistor with ink based process showed lowered performance than non-ink based process because of decrement of crystallinity of embedding materials itself. For example ink based IZGO showed mobility of ~2 cm^2/Vs [29] compared to prepared to sputtered IGZO of ~20 cm^2/Vs. [28, 30] Thus there are tries overcome this huddle by adding reduced graphene oxide (RGO) to IGZO by adding graphene oxide (GO) to IGZO ink before heat treatment, but failed to achieve high

semiconductive performance because of lack of deep insight of band gap of IGZO/RGO composite by increment weight percent of RGO.[31, 32]

Plus, during annealing process, there are possibility of break crystalline structure of embedding IGZO because of generated gas molecule from the reduced oxygenated functional groups as shown in previous researches that the reduction mechanism of thermal reduction of graphene oxide. [33, 34] Thus, preparing graphene oxide with lowered oxygenated functional group is requited. In addition, epoxide of graphene oxide generate largest amount of gas molecule with breaking carbon bond of basal plane, preparing GO with lowered epoxide is required for the preparing IGZO/RGO composite with high semiconductive performance.

Herein, in this manner, we prepared IGZO/RGO by using GO with lowered epoxide group prepared by modified acidic washing process as shown in previous research (HGO). [35] In order to preserve band gap of IGZO which can achieve high mobility and on/off ratio of itself, weight percent of RGO is controlled and this weight percent is applied to preparing IGZO/RGO with HGO (IGZO/RHGO). As a result, thin film transistor using band gap engineered IGZO/RHGO prepared from the simple spin coating and annealing process showed great performance with high mobility (~ 18 cm^2/Vs) and on/off ratio (~10^6) which can be applied to OLED and other electrical applications.

6.2 Experimental

6.2.1 Materials

Potassium persulfate ($K_2S_2O_8$, 98%), phosphorus pentoxide (P_4O_{10}, 98%), potassium permanganate ($KMnO_4$, 98%), natural flake graphite (Lot #: 17425HO, +100 mesh), were purchased from Sigma-Aldrich. Sulfuric acid (H_2SO_4, 98%), hydrogen peroxide (H_2O_2, 30%), hydrochloric acid (HCl, 35–37%), and ethyl alcohol (anhydrous) were purchased from Daejung Chemicals & Metals. Soluble indium-gallium-zinc oxide (IGZO, iXsenic) was purchased from Evonik. All chemicals were used as received.

6.2.2 Preparation of graphene oxide/IGZO composite

Graphene oxide (GO) were prepared through the conventional Hummers method. [35-39] First, natural flake graphite was pretreated with $K_2S_2O_8$ and P_4O_{10} for the ease of exfoliation to single layer. 10.0 g of $K_2S_2O_8$ and 10.0 g of P_4O_{10} were fully dissolved in 50 mL of 98% H_2SO_4 while vigorously stirring at 80°C. 5.0 g of graphite was slowly added to the mixture. The mixture was continuously stirred for 24 hours at the same temperature, and poured into 2 L of deionized water. The pretreated graphite was washed with excess water using repeated vacuum filtrations until pH of graphite became neutral, then dried in a vacuum oven under room temperature. 3.0 g of this pretreated graphite was dispersed into 138 mL of H_2SO_4 that had been cooled to 0°C 18.0 g of $KMnO_4$ added very carefully added so as to prevent the temperature from rising above 50°C. The reaction transferred to a 35°C and stirred in 300 rpm.

After 2 hours, the mixture was poured in water/ H_2O_2 mixture for direct finishing of oxidation and this mixture is ultra-centrifuged at 13000 rpm with 3.4 % HCl 3 times. Then, we divided the precipitate into two groups and different washing processes were carried out. 1/2 of the mixture was directly centrifuged in 1M HCl

at 13000rpm at room temperature. Another 1/2 of the precipitate were stirred in 5M HCl at 70°C for 16 hours and centrifuged at 13000rpm. We named the GO from the first 1/2 precipitate as GO, Another 1/2 of as HGO. After the HCl washing steps, the precipitate was completely neutralized by exchanging the solvent with water over five times in repeated ultra-centrifugations at 13000 rpm. To eliminate un-exfoliated graphite and to produce supernatant, the precipitant was centrifuged at 4000 rpm.

The solvent of gained GO and HGO was exchanged to ethanol and mixed with soluble IGZO in various concentration of 0.1 0.2, 0.4 and 0.8 wt.% and fabricated this composite in glass substrate. After fabrication, the IGZO/GO, and IGZO/HGO composite were annealed at 500°C in inert atmosphere. The IGZO/GO was named as IGZO/GO_0.05, IGZO/GO_0.1, IGZO/GO_0.5, IGZO/GO_1, and IGZO/GO_4 by the altered concentration of GO and IGZO/HGO was named with the same manner.

6.2.3 Fabrication of thin film transistor

The prepared 0.02 ml IGZO/GO and IGZO/HGO mixture were fabricated on Au patterned Si/SiO_2 substrate by spin coating at 3500 rpm and dried at 60 °C and the spin coated sample was annealed at 500°C with the heating rate of 2.5 °C / min for 4 hours inert atmosphere using tube furnace for the generation of IGZO/RGO and IGZO/RHGO.

6.2.4 Characterization

To study the oxygen-containing functional groups of the samples, the functional groups were quantified by performing XPS with an AXIS-HSi spectrometer (Kratos). The obtained C1s spectra were fitted and deconvoluted using XPSPEAK41 software. FTIR spectra of the GO, AGO and HGO samples were recorded with a Thermo Scientific Nicolet TM iS10 spectrometer to obtain

additional information about their functional groups. The scan range was 400–4,000 cm-1 in attenuated total reflection (ATR) mode and zeta-potential data were acquired with ELSZ 1000ZS size and zeta-potential analyzer, Otsuka. The optical absorbance data of the GO within the UV-visible region were obtained by using a UV-Vis-NIR Cary 5000 spectrometer (Varian) with a scan range of 400-700 nm. And from the previous studies, we measure band gap of graphene oxides using modified Tauc plot. [35, 40, 41] ultraviolet photoelectron spectroscopy (UPS) spectrum was obtained using UPS of PHI 5800 ESCA System with a monochromatized Al Kα radiation source (h = 1486.6 eV); the angle between the excitation and detection radiation was 90°, while the takeoff angle was 45° The nanostructure of measured by using field emission scanning electron microscopy (FE-SEM; SUPRA 55VP, Carl Zeiss) and atomic force microscope (AFM) with a surface imaging systems NX-10 instrument (Park Systems). The electrical conductivity of IGZO/RGO and IGZO/RHGO was obtained using M4P-205 4 point probe station (MSTECH) and semiconductive performance was tested using by point probe station MST 8000C (MSTECH).

6.3 Results and Discussion

6.3.1 Band gap modification of IGZO/RGO and IGZO/RHGO by concentration of graphene.

In order to calculate the band gap of IGZO/RGO and IGZO/RHGO composite, there should be the consideration about the band gap and work function of RGO and RHGO controlled by the surface characteristics themselves. Therefore, X-ray photoelectron spectroscopy (XPS) and Raman spectroscopy is used to measurement of surface characteristics of RGO and RHGO. In the case of RGO, after deconvolution of the C1s peak of the XPS result as the same manner as shown in previous study, [35, 38, 42, 43] the area ratio of the sp^2 carbon peak (284.5 eV) reaches to the 0.82 and the ratio of oxygen atom to 0.21 compared to the result of RHGO that show the ratio of sp^2 carbon peak is 0.81 and ratio of oxygen atom 0.23 as shown in the **Figure 6.1**. Combined with the I_D/I_G ratio measured by Raman spectroscopy of RGO (1.09) and RHGO (1.08), (**Figure 6.2**) [35, 44] the surface nature of RHGO and RGO is quite similar after reduction. Considering lots of epoxide, which is mainly reduced in this temperature range, is smaller in the case of HGO, it can be thought that HGO loses less functional groups than GO, results in has similar surface nature of RGO and RHGO. Because of this similar surface nature, RHGO and HGO showed similar band gap (0.6eV and 0.65eV) and work function (4.6 eV and 4.65eV) calculated from modified Tauc plot [35, 40, 41] using absorbance peak of UV-vis spectroscopy and secondary electron (SECO) spectrum using UPS measurement [45] as shown in the **Figure 6.3** and **Figure 6.4**. Therefore, the resultant band gap of IGZO/RGO and IGZO/RHGO shows similar band gap when RGO and RHGO are mixed in the same concentration.

In order to get band gap of IGZO/RGO and IGZO/RHGO, the dispersed IGZO/GO and IGZO/HGO solutions (**Figure 6.5**) are drop cased on the glass

substrate and annealed to 500 °C in inert atmosphere. After heat treatment, absorbance peak of UV to visible light range of the IGZO/RGO and IGZO/RHGO thin film are obtained using UV-vis spectroscopy and band gap of each sample can be obtained after calculation using modified Tauc plot as shown in previous research. (**Figure 6.6**) [35, 40, 41] The result shows that in the low concentration of RGO and RHGO, the band gap of IGZO/RGO and IGZO/RHGO showed similar band gap. Plus, they showed the decrement trend of band gap from around 3.2 eV to 2.8 eV the by the increased concentration of RGO and RHGO. This phenomena can be predicted by the band diagram of IGZO, RGO, and RHGO that considering volume ratio of IZGO and graphene is mixed with 1:1 unit cell. By this calculation, at 4.5 wt.% the band gap of IGZO/RGO and IGZO/RHGO converges to the 2.4 and 2.35 eV and this result can certify this prediction. Considering IGZO shows the highest semiconductive performance when it has the band gap of around 3.1eV, [46] it can be predicted that IGZO/RGO and IGZO/RHGO thin film with the concentration of RGO and RHGO are 0.1 wt.% and 0.2 wt.% can show the most improved semiconductive performance because of retained band gap from IGZO.

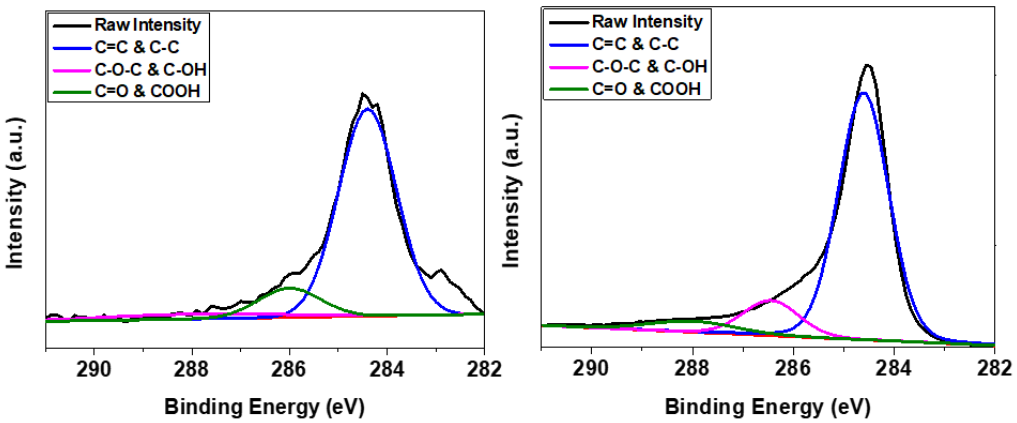

Figure 6.1 Deconvoluted XPS C1s peak of (left) GO and (right) HGO

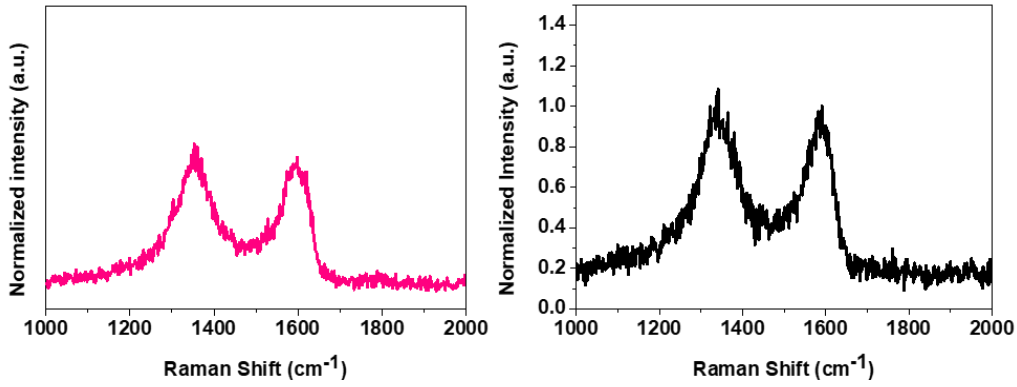

Figure 6.2 Raman spectra of (left) GO and (right) HGO

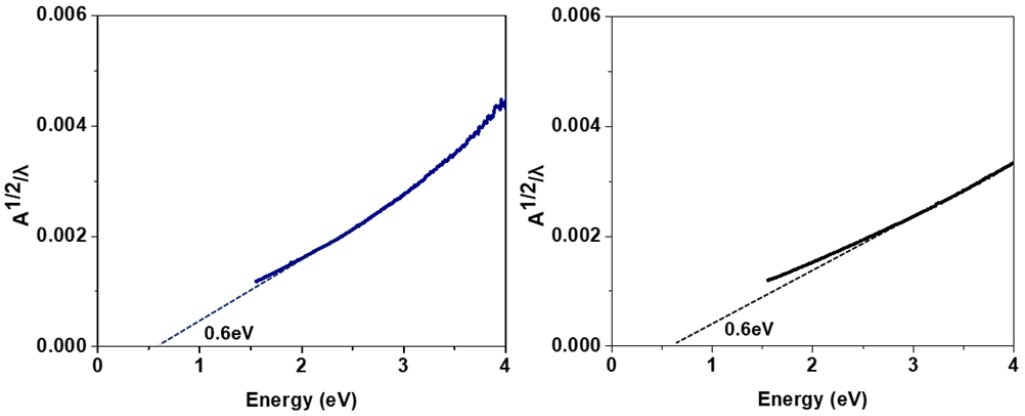

Figure 6.3 Band gap of (left) RGO and (right) RHGO reduced at 500 °C calculated by modified Tauc plot from the absorbance of UV-vis spectra.

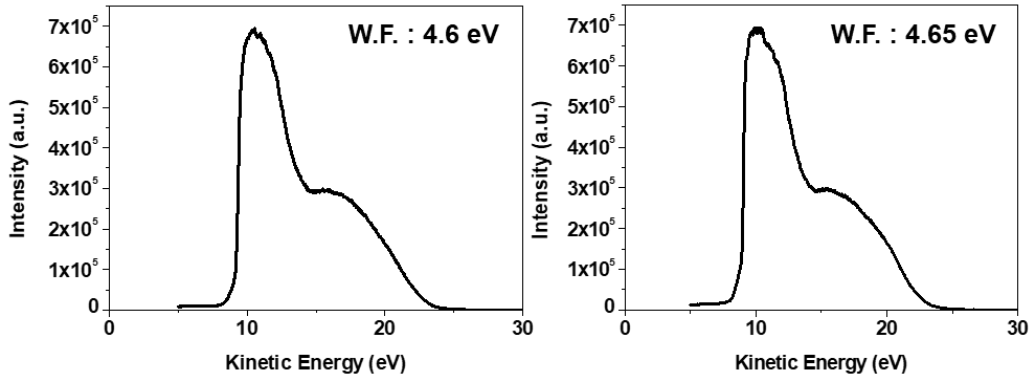

Figure 6.4 UPS secondary electron spectra of (left) RGO and (right) RHGO reduced at 500 °C calculated for the calculation of work function.

Figure 6.5 IGZO/GO solution that contains 0.1, 0.2, 0.4, and 0.8 wt.% of GO

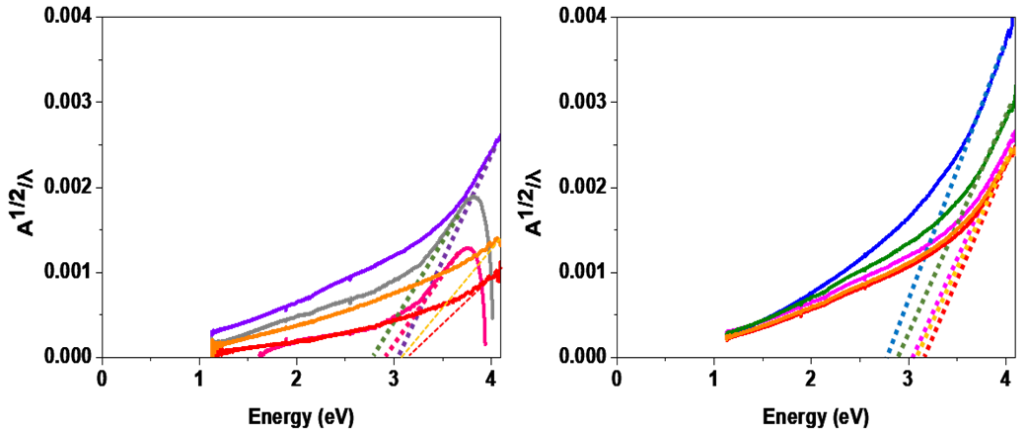

Figure 6.6 Band gap of (left) IGZO/RGO and (right) IGZO/RHGO reduced at 500 °C that contains 0.1, 0.2, 0.4, and 0.8 wt.% of reduced graphene, calculated by modified Tauc plot from the absorbance of UV-vis spectra.

6.3.2 Effect of gas generation by reduction of graphene to carrier transport of resultant IGZO/RGO composite.

During the thermal reduction process of GO, gas molecule like CO, CO_2, and H_2O can be generated by the elimination of functional group as studied in previous researches. The generation of gas molecule during thermal reduction process can generate gas channel considering the pore generation of RGO film by annealing as shown in previous research. [33, 34] Therefore, in the case of IGZO/RGO and IGZO/RHGO, the possibilities of generating gas channel by the ejection of gas molecule from functional group of GO as shown in **Figure 6.7**.

Especially, most of CO and CO_2 molecule generates from the epoxide group, the amount of this functional group should be compared with Fourier transformed infrared spectroscopy (FT-IR) The FT-IR absorbance spectra of each sample were normalized upon the absorbance of the C=C double bond (~1650 cm^{-1}) from graphitic domain to compare the relative intensity of the peaks induced by the hydroxyl, epoxide, carbonyl, and carboxyl groups. (**Figure 6.8**) The absorption peaks of HGO 5M located at 1105 cm^{-1}, 1248 cm^{-1}, and 3300cm^{-1} (assigned to the hydroxyl and epoxide groups) were smaller than those of GO. Especially, peak of epoxide group (1248 cm^{-1})[38, 42, 47] showed quietly decreased intensity compared to other functional groups. This indicates that lots of epoxide groups were decreased by hydrolysis reaction by HCl. [35] The peak intensity of hydroxyl group (1105 cm^{-1} and 3300 cm^{-1})[38, 42, 47] are slightly decreased because elimination reaction also occurred. [35] This result indicates that the gas generation during thermal reduction can be decreased by replacement of GO the HGO.

Thus, after annealing of IGZO/GO and IGZO/HGO, the surface roughness of IGZO/RGO and IGZO/RHGO with the same concentration reduced graphene (0.2 wt.%) are measured using atomic force microscope (AFM) with noncontact mode with the concept of which surface roughness can be increased by the crack

that generated by the ejection of the gas molecule generated from GO. As shown in **Figure 6.9**, IGZO/HGO surface showed lower RMS roughness (0.28 nm) than IGZO/GO surface (0.81 nm) after measuring 10μm × 10μm surface of the samples. This result implies that IGZO/RHGO has less defective structure than IGZO/HGO. In order to define the effect of crack by generation of gas molecule during thermal reduction process to the electrical transport, we measured electrical resistivity of IGZO/RGO and IGZO/RHGO with various graphene concentration from 0.1 wt.% to 0.8 wt.% via 4 point probe. As shown in **Figure 6.10**, IGZO/RGO and IGZO/RHGO showed resistivity of semiconductor and increased trend by the increased concentration of reduced graphene. Especially, in the same concentration of reduced graphene, IGZO/RHGO showed lowered resistivity than IGZO/RGO and this result showed that minimization of crack generated by thermal reduction of functional group of GO can be a key point that improving carrier transport of IGZO/RGO based semiconductor devices.

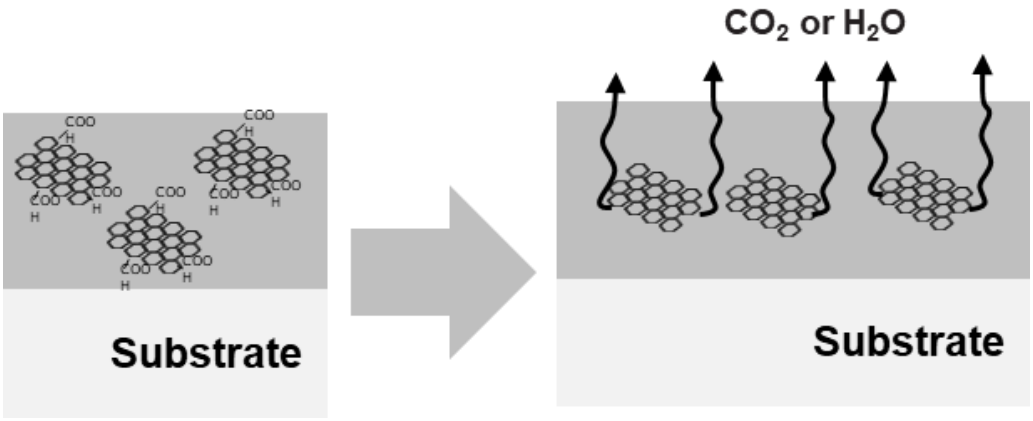

Figure 6.7 Scheme of gas generation during annealing of IGZO/GO.

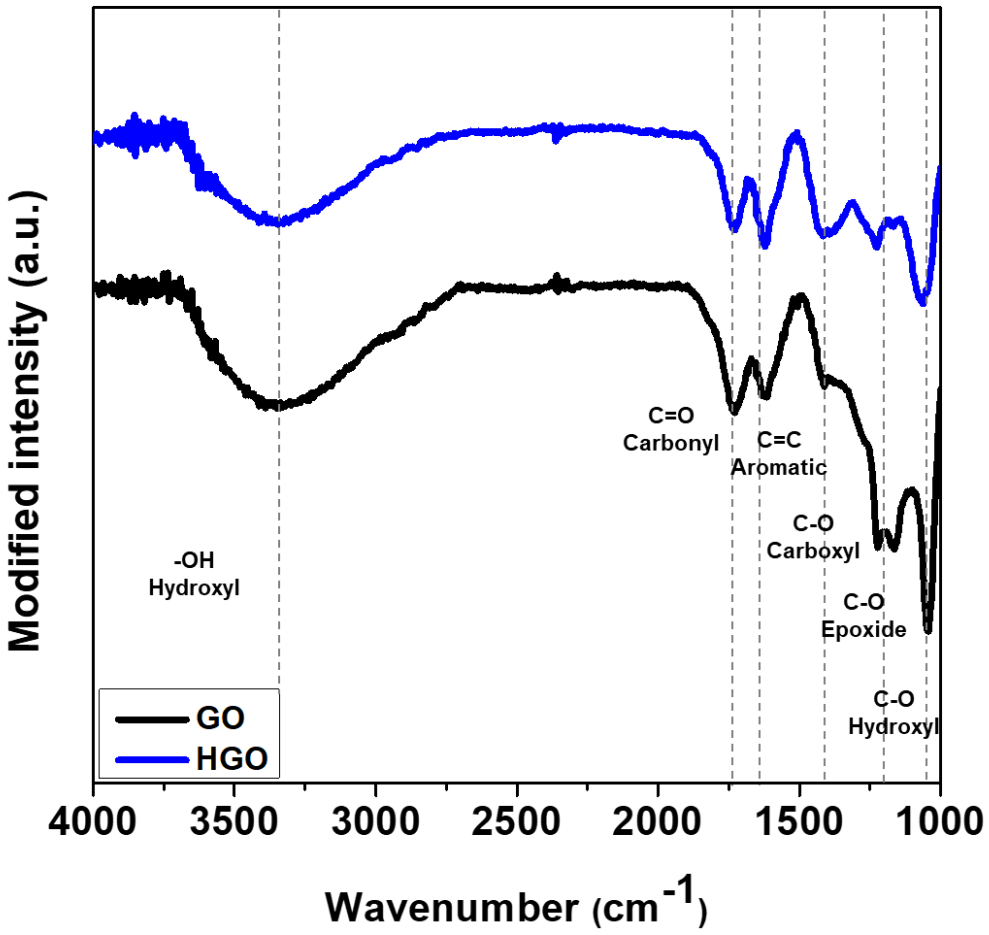

Figure 6.8 FT-IR spectra from ATR mode of GO and HGO

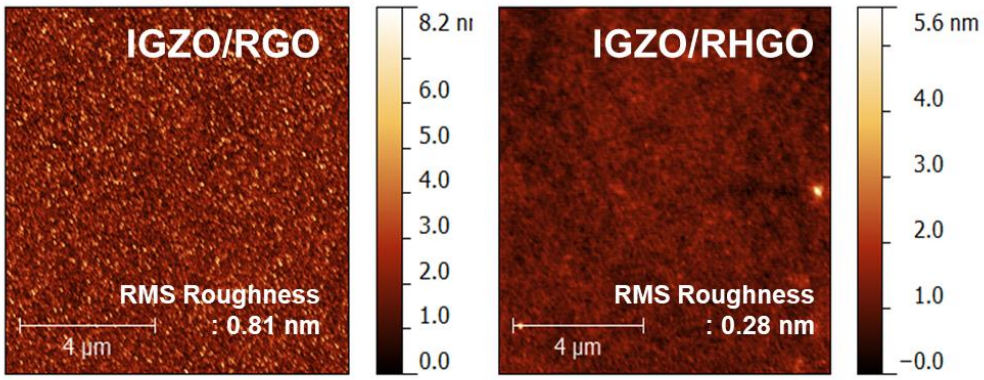

Figure 6.9 Surface roughness of (left) IGZO/RGO and (right) IGZO/RHGO reduced at 500 °C calculated from AFM topology image.

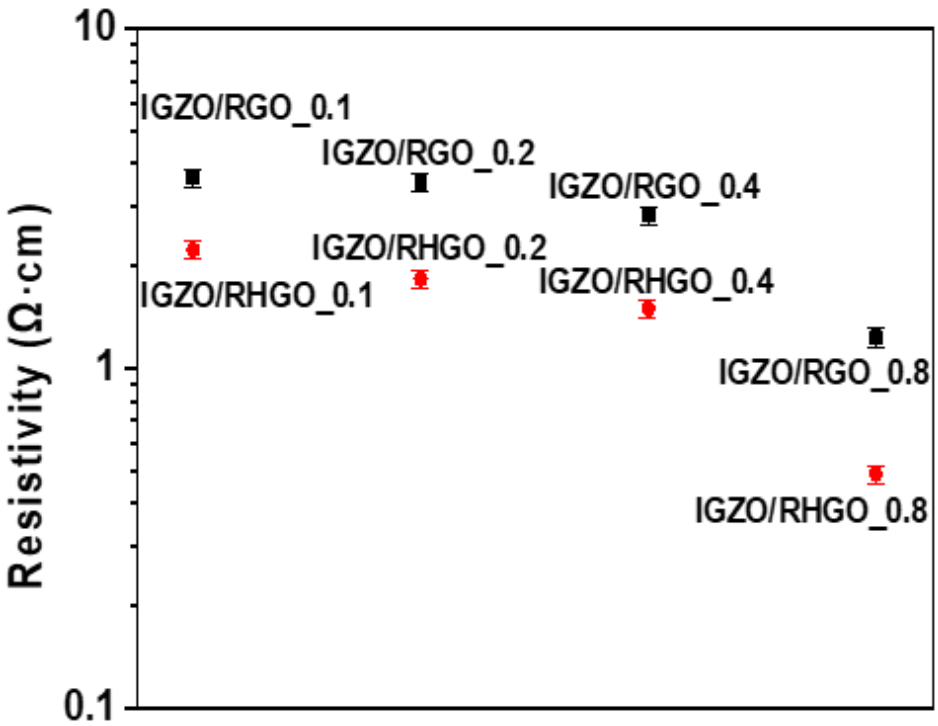

Figure 6.10 Electrical resistivity of (left) IGZO/RGO and (right) IGZO/RHGO reduced at 500 °C.

6.3.3 Effect of RGO arrangement to the performance of IGZO/RGO

In order to the effect of modified band gap and crack generation to the semiconductive performance of IGZO/RGO and IGZO/RHGO channel, thin film transistor (TFT) is fabricated. On the n type doped silicon / silicon (n^+Si / SiO_2) oxide substrate with patterned gold (Au) electrode with the width of 10μm and the length of 500 μm, IGZO/GO and IGZO/HGO solutions were fabricated with spin coating and the IGZO/RGO and IGZO/RHGO channel based TFT was prepared after annealed in inert atmosphere. (**Figure 6.11**) In order to test semiconductive performance of IGZO/RGO and IGZO/RHGO channel based TFT, we measured the source-drain current by the change of source-drain voltage from -40 V to +40V under gate voltage of 10.0V. And the carrier mobility of the TFT is calculated based on the equation as shown below; [27]

$$I_{DS} = \frac{W}{2L}\mu c_i(V_G - V_{th})^2 \qquad \text{..... (1)}$$

where V_{th} is the threshold voltage, W is the channel width, L is the channel length, and c_i is the dielectric capacitance per unit area. In the case of IGZO/RGO channel based TFT, the source-drain current increment from the threshold voltage around -15 V (0.1 wt.% of RGO) to -20 V (0.8 wt.% of RGO) because IGZO is n type semiconductor. As shown in **Figure 6.12**, The carrier mobility was highest (~7.5 cm^2/Vs) at 0.2 wt.% of RGO was mixed, then the concentration of RGO in increased, the carrier mobility dropped to 5.6 cm^2/Vs (0.4 wt.% of RGO) and 4.2 cm^2/Vs (0.8 wt.% of RGO). This level of carrier mobility is higher than pristine IGZO which reported from previous study, [29] but this performance is not appropriate to be applied to industrial field. [48]

For the finding the reason of mobility decrement by increment of RGO concentration, we obtained the microstructure of IGZO/RGO using scattering electron microscope (SEM) with 10000 magnification as shown in the Figure

(**6.13**) and we can find the aggregation of RGO occurred from the RGO concentration of 0.4 wt.%. Considering this aggregation of RGO cases the enlargement of depletion layer in IGZO/RGO channel and increment of metallic behavior [49] because RGO acts as p-type semiconductor because of remained oxygenated functional groups, [50, 51] this phenomena mainly results in the decrement of semiconductive behavior of IGZO/RGO. In addition increment of off current by increment of RGO concentration, the on/off ratio of IGZO/RGO TFT was also decreased followed by this manner. Therefore, it can be thought that IGZO/RGO based TFT showed best performance when the concentration of RGO is 0.2 wt.% when considering the required performance of TFT when applied to industry.

For the production of IGZO/RGO channel based TFT with the performance applicable to industrial field, we prepared IGZO/RHGO channel based TFT and the semiconductive performance was measured with the same process. As shown with the **Figure 6.14**, under the same reduced graphene concentration of 0.2 wt.%, IGZO/RHGO channel based TFT showed improved carrier mobility of 18.6 cm^2/Vs with the preserved on/off ratio compared to the IGZO/RGO channel based TFT in spite of the increased threshold voltage comparable to the required performance for industrial application compared to other researches as shown in **Figure 6.16**. It can be thought that improved carrier transport by lowered crack shows strong effect to the increment of carrier mobility and the preparation of IGZO/RHGO, which used the epoxide eliminated GO controlling band gap with the same level with IGZO/RGO is an effective way for the preparation of high performance IGZO/RGO channel based TFT.

In order to find the increased threshold voltage of IGZO/RHGO channel based TFT, we measured dispersion stability of GO and RHGO in ethanol solvent, which was used to preparing IGZO/GO and IGZO/HGO mixture and found that by the decrement of functional group, HGO showed similarly decreased

dispersion stability in ethanol than GO as shown in **Figure 6.15** because of the decrement of functional groups. [35, 52] This implies that in IGZO/RHGO, RHGO can be easily aggregated during fabrication and the depletion layer are enlarged. [49] This implies that for the production of ideal IGZO/RGO channel based TFT, GO with high dispersion stability with low amount function group is essential.

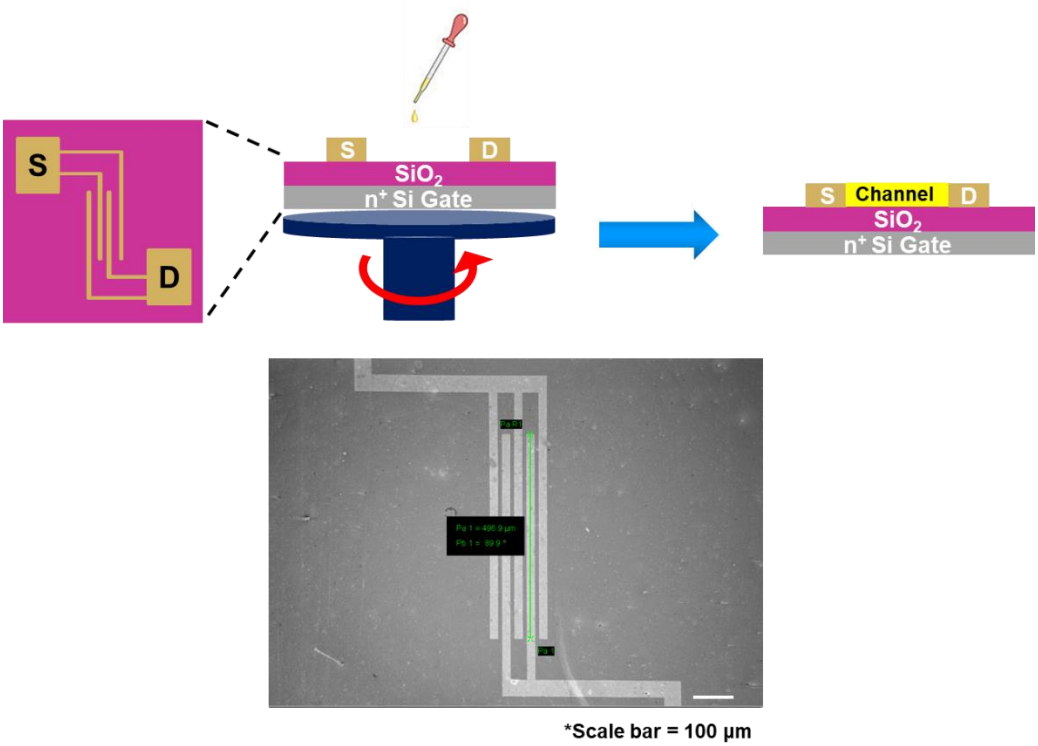

Figure 6.11 (upper) Schematic view of fabricating IGZO/RGO and IGZO/RHGO based TFT device (lower) SEM image of the patterned Au on n^{+}Si / SiO_2 substrate (magnification : x1000)

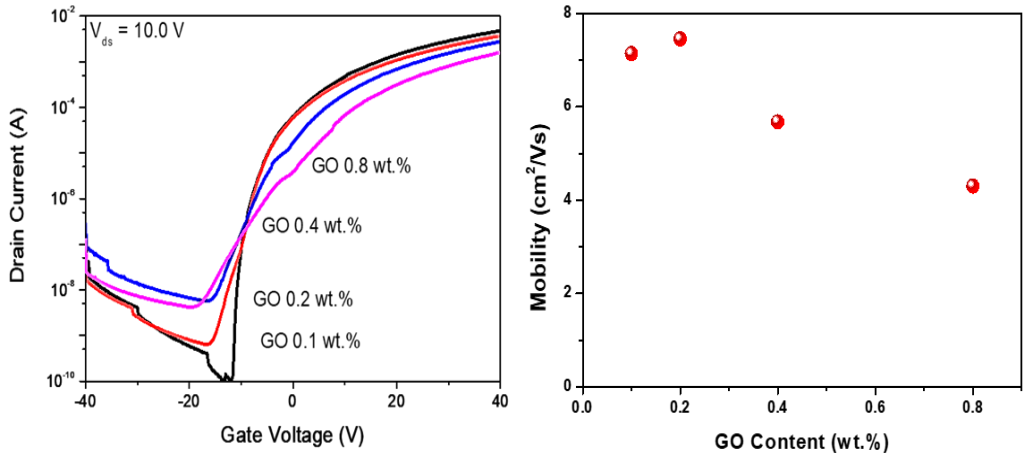

Figure 6.12 (left) Source drain current of IGZO/RGO TFT with various concentration of RGO by altered gate voltage (right) carrier mobility of IGZO/RGO TFT

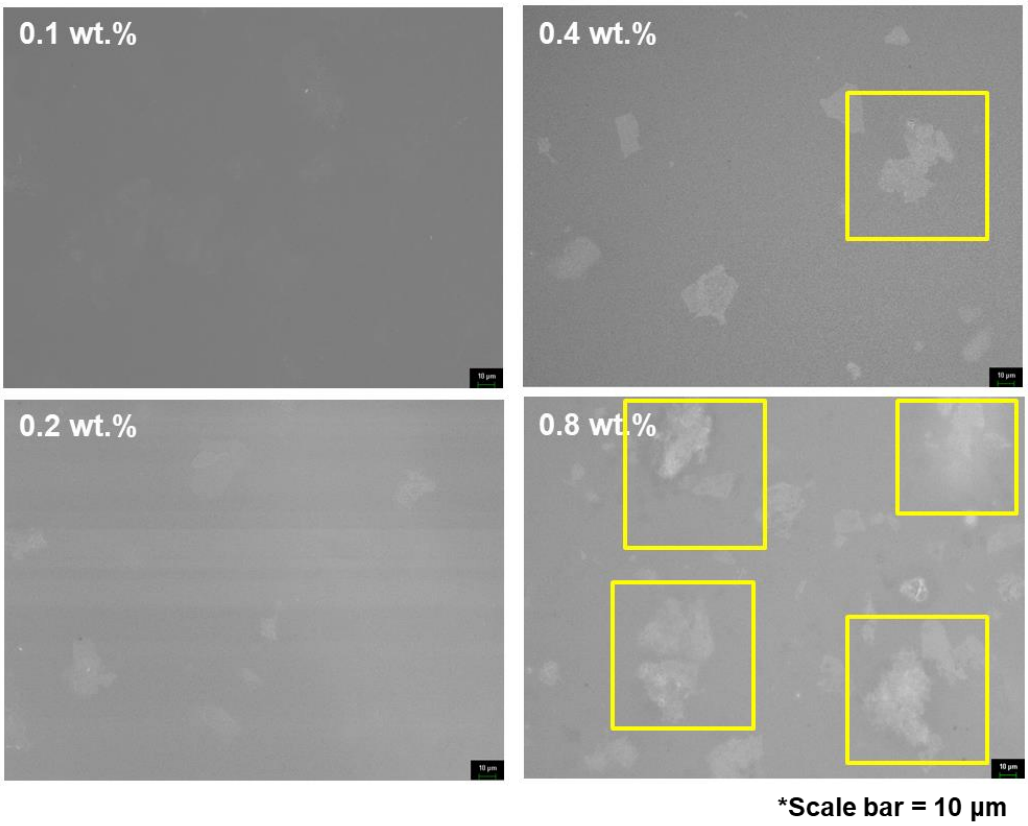

Figure 6.13 SEM image if IGZO/RGO on Si substrate with various concentration of RGO (magnification: x10000)

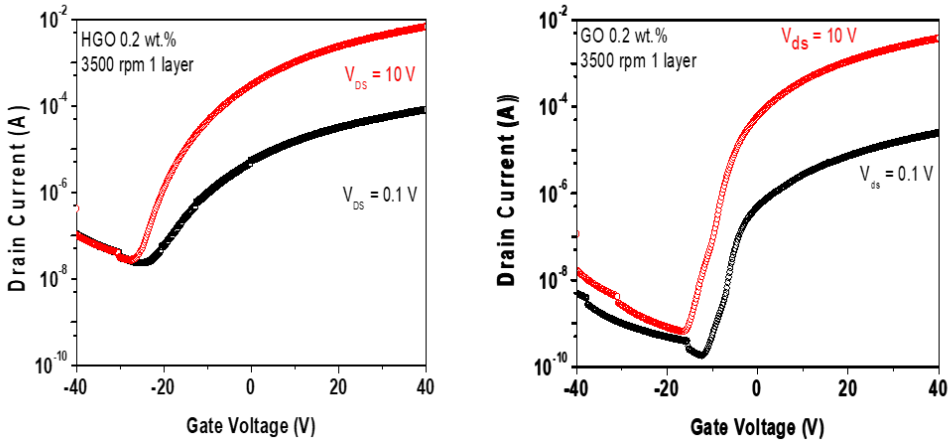

Figure 6.14 Source drain current of (left) IGZO/RHGO and (right) IGZO/RGO TFT with 0.2 wt.% concentration of graphene by altered gate voltage under source drain voltage of 0.1V and 10V

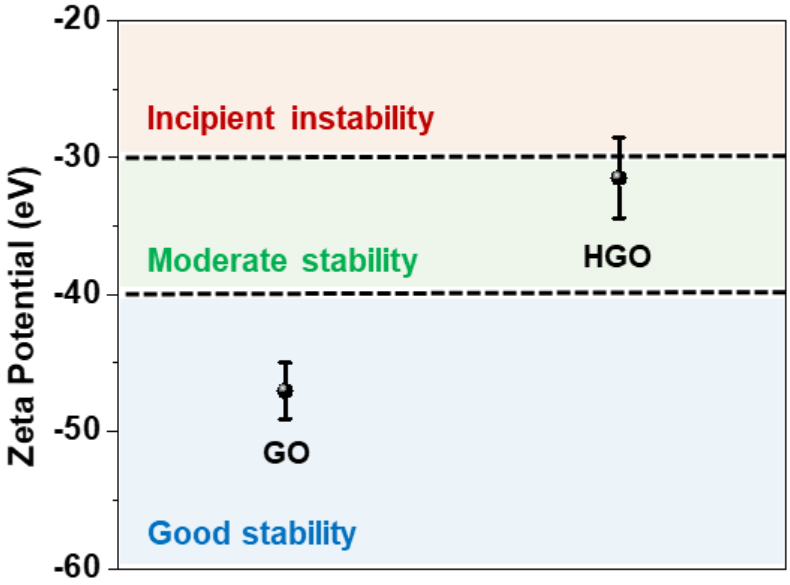

Figure 6.15 Zeta potential of GO and HGO dispersed in ethanol.

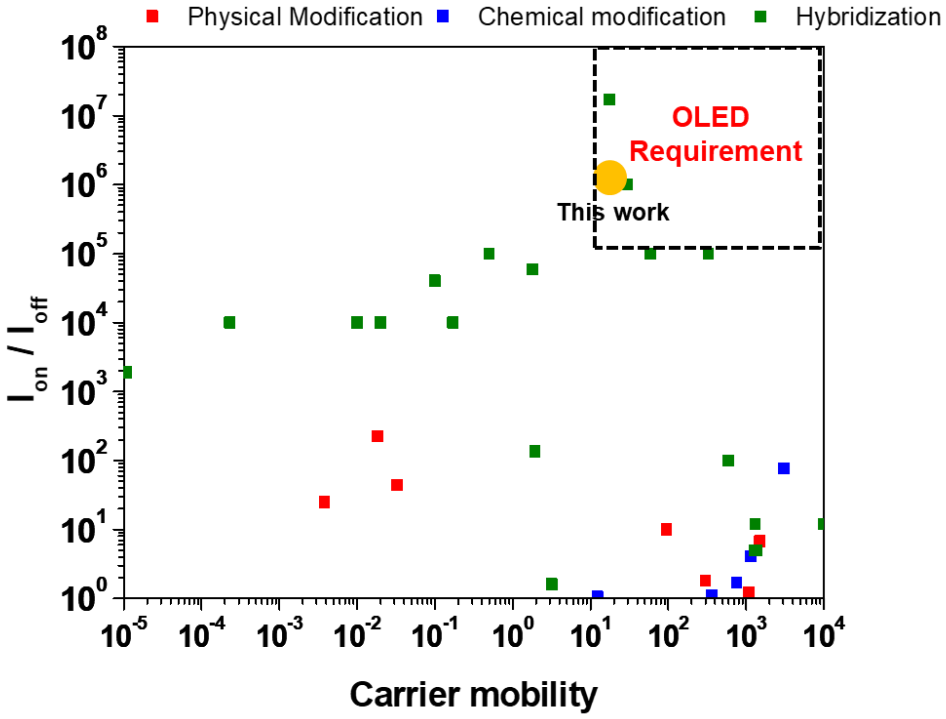

Figure 6.16 Carrier mobility and on/off ratio of various graphene based TFT for the compartment of the performance of IGZO/RHGO TFT with other graphene based TFT. [4-27]

6.4 Conclusion

In this research, we developed new insight for improving semiconductive performance reduced graphene based TFT via band gap engineering of RGO based composite. Through the fine band gap modification of IGZO/RGO based on the alternation of the concentration of RGO, the fittable band gap for TFT device was defined to 0.2 wt.% for the enhancement of the semiconductive performance. In addition, the followed control of crack generation during heat treatment by modification of graphene oxide by decreased amount of epoxide groups strongly effect on the improved carrier transport. As a result, the IGZO/RHGO with 0.2 wt.% of reduced graphene showed great TFT performance of the level that can be applicable to industrial field in spite of the high threshold voltage. This results show that the importance of band gap engineering of graphene based composite and modification of graphene oxide itself for improvement of the device performance.

6.5 Reference

[1] K.S. Novoselov, V.I. Falko, L. Colombo, P.R. Gellert, M.G. Schwab, K. Kim, A roadmap for graphene, Nature 490(7419) (2012) 192-200.

[2] F. Schwierz, Graphene transistors, Nature Nanotechnology 5(7) (2010) 487-496.

[3] A.K. Geim, Graphene: Status and Prospects, Science 324(5934) (2009) 1530.

[4] B.J. Kim, H. Jang, S.-K. Lee, B.H. Hong, J.-H. Ahn, J.H. Cho, High -Performance Flexible Graphene Field Effect Transistors with Ion Gel Gat e Dielectrics, Nano Letters 10(9) (2010) 3464-3466.

[5] W. Song, S.Y. Kwon, S. Myung, M.W. Jung, S.J. Kim, B.K. Min, M.-A. Kang, S.H. Kim, J. Lim, K.-S. An, High-mobility ambipolar ZnO-graphene hybrid thin film transistors, Scientific Reports 4(1) (2014) 4064.

[6] F. Torrisi, T. Hasan, W. Wu, Z. Sun, A. Lombardo, T.S. Kulmala, G. -W. Hsieh, S. Jung, F. Bonaccorso, P.J. Paul, D. Chu, A.C. Ferrari, Inkje t-Printed Graphene Electronics, ACS Nano 6(4) (2012) 2992-3006.

[7] K.T. Kim, J.W. Jung, W.H. Jo, Synthesis of graphene nanoribbons wi th various widths and its application to thin-film transistor, Carbon 63 (2 013) 202-209.

[8] Z. Chen, Y.-M. Lin, M.J. Rooks, P. Avouris, Graphene nano-ribbon e lectronics, Physica E: Low-dimensional Systems and Nanostructures 40(2) (2007) 228-232.

[9] S. Wang, P.K. Ang, Z. Wang, A.L.L. Tang, J.T.L. Thong, K.P. Loh, High Mobility, Printable, and Solution-Processed Graphene Electronics, Na no Letters 10(1) (2010) 92-98.

[10] D.W. Chang, E.K. Lee, E.Y. Park, H. Yu, H.-J. Choi, I.-Y. Jeon, G. -J. Sohn, D. Shin, N. Park, J.H. Oh, L. Dai, J.-B. Baek, Nitrogen-Doped

Graphene Nanoplatelets from Simple Solution Edge-Functionalization for n-Type Field-Effect Transistors, Journal of the American Chemical Society 135(24) (2013) 8981-8988.
[11] S.Y. Lee, D.L. Duong, Q.A. Vu, Y. Jin, P. Kim, Y.H. Lee, Chemically Modulated Band Gap in Bilayer Graphene Memory Transistors with High On/Off Ratio, ACS Nano 9(9) (2015) 9034-9042.
[12] T.-J. Ha, D. Akinwande, A. Dodabalapur, Hybrid graphene/organic semiconductor field-effect transistors, Applied Physics Letters 101(3) (2012) 033309.
[13] N. Petrone, T. Chari, I. Meric, L. Wang, K.L. Shepard, J. Hone, Flexible Graphene Field-Effect Transistors Encapsulated in Hexagonal Boron Nitride, ACS Nano 9(9) (2015) 8953-8959.
[14] S. Rathi, I. Lee, D. Lim, J. Wang, Y. Ochiai, N. Aoki, K. Watanabe, T. Taniguchi, G.-H. Lee, Y.-J. Yu, P. Kim, G.-H. Kim, Tunable Electrical and Optical Characteristics in Monolayer Graphene and Few-Layer MoS2 Heterostructure Devices, Nano Letters 15(8) (2015) 5017-5024.
[15] C.-J. Shih, Q.H. Wang, Y. Son, Z. Jin, D. Blankschtein, M.S. Strano, Tuning On–Off Current Ratio and Field-Effect Mobility in a MoS2–Graphene Heterostructure via Schottky Barrier Modulation, ACS Nano 8(6) (2014) 5790-5798.
[16] H. Tian, Z. Tan, C. Wu, X. Wang, M.A. Mohammad, D. Xie, Y. Yang, J. Wang, L.-J. Li, J. Xu, T.-L. Ren, Novel Field-Effect Schottky Barrier Transistors Based on Graphene-MoS2 Heterojunctions, Scientific Reports 4(1) (2014) 5951.
[17] T. Mosciatti, S. Haar, F. Liscio, A. Ciesielski, E. Orgiu, P. Samorì, A Multifunctional Polymer-Graphene Thin-Film Transistor with Tunable Transport Regimes, ACS Nano 9(3) (2015) 2357-2367.
[18] Y.-C. Lai, D.-Y. Wang, I.S. Huang, Y.-T. Chen, Y.-H. Hsu, T.-Y.

Lin, H.-F. Meng, T.-C. Chang, Y.-J. Yang, C.-C. Chen, F.-C. Hsu, Y.-F. Chen, Low operation voltage macromolecular composite memory assisted by graphene nanoflakes, Journal of Materials Chemistry C 1(3) (2013) 552-559.

[19] C.-B. Huang, S. Witomska, A. Aliprandi, M.-A. Stoeckel, M. Bonini, A. Ciesielski, P. Samorì, Molecule–Graphene Hybrid Materials with Tunable Mechanoresponse: Highly Sensitive Pressure Sensors for Health Monitoring, Advanced Materials 31(1) (2019) 1804600.

[20] J. Huang, D.R. Hines, B.J. Jung, M.S. Bronsgeest, A. Tunnell, V. Ballarotto, H.E. Katz, M.S. Fuhrer, E.D. Williams, J. Cumings, Polymeric semiconductor/graphene hybrid field-effect transistors, Organic Electronics 12(9) (2011) 1471-1476.

[21] H. Zhu, A. Liu, Y. Xu, F. Shan, A. Li, J. Wang, W. Yang, C. Barrow, J. Liu, Graphene quantum dots directly generated from graphite via magnetron sputtering and the application in thin-film transistors, Carbon 88 (2015) 225-232.

[22] L. Liao, J. Bai, Y.-C. Lin, Y. Qu, Y. Huang, X. Duan, High-Performance Top-Gated Graphene-Nanoribbon Transistors Using Zirconium Oxide Nanowires as High-Dielectric-Constant Gate Dielectrics, Advanced Materials 22(17) (2010) 1941-1945.

[23] S.M. Jilani, T.D. Gamot, P. Banerji, Thin-Film Transistors with a Graphene Oxide Nanocomposite Channel, Langmuir 28(48) (2012) 16485-16489.

[24] Z. Wang, S. Mohammadzadeh, T. Schmaltz, J. Kirschner, A. Khassanov, S. Eigler, U. Mundloch, C. Backes, H.-G. Steinrück, A. Magerl, F. Hauke, A. Hirsch, M. Halik, Region-Selective Self-Assembly of Functionalized Carbon Allotropes from Solution, ACS Nano 7(12) (2013) 11427-11434.

[25] A. Takahashi, C.-J. Lin, K. Ohshimizu, T. Higashihara, W.-C. Chen, M. Ueda, Synthesis and characterization of novel polythiophenes with gr aphene-like structures via intramolecular oxidative coupling, Polymer Che mistry 3(2) (2012) 479-485.
[26] C.-J. Lin, C.-L. Liu, W.-C. Chen, Poly(3-hexylthiophene)–graphene c omposite-based aligned nanofibers for high-performance field effect transis tors, Journal of Materials Chemistry C 3(17) (2015) 4290-4296.
[27] M.-K. Dai, J.-T. Lian, T.-Y. Lin, Y.-F. Chen, High-performance tran sparent and flexible inorganic thin film transistors: a facile integration of graphene nanosheets and amorphous InGaZnO, Journal of Materials Chem istry C 1(33) (2013) 5064-5071.
[28] A. Tixier-Mita, S. Ihida, B.-D. Ségard, G.A. Cathcart, T. Takahashi, H. Fujita, H. Toshiyoshi, Review on thin-film transistor technology, its a pplications, and possible new applications to biological cells, Japanese Jo urnal of Applied Physics 55(4S) (2016) 04EA08.
[29] J. Steiger, H. Thiem, A. Hoppe, D.V. Pham, A. Merkulov, R. Ansel mann, Development of low temperature solution-processed metal oxide TF T materials, IDW'10 - Proceedings of the 17th International Display Wor kshops 3 (2010) 1913-1914.
[30] L. Yan, M. Wang, L. Zhang, D. Wang, F. Liu, G. Yuan, G. Wang, 51.2: The Development of a High Mobility Zinc Oxynitride TFT for A MOLED, SID Symposium Digest of Technical Papers 46(1) (2015) 769-7 71.
[31] D.U. Lim, S. Choi, S. Kim, Y.J. Choi, S. Lee, M.S. Kang, Y.-H. K im, J.H. Cho, All-Inkjet-Printed Vertical Heterostructure for Wafer-Scale Electronics, ACS Nano 13(7) (2019) 8213-8221.
[32] S. Oh, T.H. Lee, M.-S. Chae, J.H. Park, T.G. Kim, Performance im provements of ZnO thin film transistors with reduced graphene oxide-emb

edded channel layers, Journal of Alloys and Compounds 777 (2019) 1367-1374.
[33] S.J. Yang, T. Kim, H. Jung, C.R. Park, The effect of heating rate on porosity production during the low temperature reduction of graphite oxide, Carbon 53 (2013) 73-80.
[34] L.-C. Lin, J.C. Grossman, Atomistic understandings of reduced graphene oxide as an ultrathin-film nanoporous membrane for separations, Nature Communications 6(1) (2015) 8335.
[35] J. Park, Y. Kim, S.Y. Park, S.J. Sung, H.W. Jang, C.R. Park, Band gap engineering of graphene oxide for ultrasensitive NO2 gas sensing, Carbon 159 (2020) 175-184.
[36] M.S. Chang, Y.S. Kim, J.H. Kang, J. Park, S.J. Sung, S.H. So, K.T. Park, S.J. Yang, T. Kim, C.R. Park, Guidelines for Tailored Chemical Functionalization of Graphene, Chemistry of Materials 29(1) (2017) 307-318.
[37] W.S. Hummers, R.E. Offeman, Preparation of Graphitic Oxide, Journal of the American Chemical Society 80(6) (1958) 1339-1339.
[38] J.H. Kang, T. Kim, J. Choi, J. Park, Y.S. Kim, M.S. Chang, H. Jung, K.T. Park, S.J. Yang, C.R. Park, Hidden Second Oxidation Step of Hummers Method, Chemistry of Materials 28(3) (2016) 756-764.
[39] N.I. Kovtyukhova, P.J. Ollivier, B.R. Martin, T.E. Mallouk, S.A. Chizhik, E.V. Buzaneva, A.D. Gorchinskiy, Layer-by-Layer Assembly of Ultrathin Composite Films from Micron-Sized Graphite Oxide Sheets and Polycations, Chemistry of Materials 11(3) (1999) 771-778.
[40] A. Mathkar, D. Tozier, P. Cox, P. Ong, C. Galande, K. Balakrishnan, A. Leela Mohana Reddy, P.M. Ajayan, Controlled, Stepwise Reduction and Band Gap Manipulation of Graphene Oxide, The Journal of Physical Chemistry Letters 3(8) (2012) 986-991.

[41] S. Wang, I.S. Cole, Q. Li, Quantum-confined bandgap narrowing of TiO2 nanoparticles by graphene quantum dots for visible-light-driven appl ications, Chemical Communications 52(59) (2016) 9208-9211.
[42] M. Acik, G. Lee, C. Mattevi, A. Pirkle, R.M. Wallace, M. Chhowal la, K. Cho, Y. Chabal, The Role of Oxygen during Thermal Reduction o f Graphene Oxide Studied by Infrared Absorption Spectroscopy, The Jour nal of Physical Chemistry C 115(40) (2011) 19761-19781.
[43] J. Park, Y.S. Kim, S.J. Sung, T. Kim, C.R. Park, Highly dispersible edge-selectively oxidized graphene with improved electrical performance, Nanoscale 9(4) (2017) 1699-1708.
[44] M.A. Pimenta, G. Dresselhaus, M.S. Dresselhaus, L.G. Cançado, A. Jorio, R. Saito, Studying disorder in graphite-based systems by Raman sp ectroscopy, Physical Chemistry Chemical Physics 9(11) (2007) 1276-1290.
[45] N.D.K. Tu, J. Choi, C.R. Park, H. Kim, Remarkable Conversion Bet ween n- and p-Type Reduced Graphene Oxide on Varying the Thermal Annealing Temperature, Chemistry of Materials 27(21) (2015) 7362-7369.
[46] T. Kamiya, K. Nomura, H. Hosono, Origins of High Mobility and Low Operation Voltage of Amorphous Oxide TFTs: Electronic Structure, Electron Transport, Defects and Doping*, Journal of Display Technology 5(12) (2009) 468-483.
[47] Y.H. Kim, J.S. Park, Y.-R. Choi, S.Y. Park, S.Y. Lee, W. Sohn, Y. -S. Shim, J.-H. Lee, C.R. Park, Y.S. Choi, B.H. Hong, J.H. Lee, W.H. L ee, D. Lee, H.W. Jang, Chemically fluorinated graphene oxide for room t emperature ammonia detection at ppb levels, Journal of Materials Chemist ry A 5(36) (2017) 19116-19125.
[48] T. Arai, T. Sasaoka, 49.1: Invited Paper: Emergent Oxide TFT Tech nologies for Next-Generation AM-OLED Displays, SID Symposium Diges t of Technical Papers 42(1) (2011) 710-713.

[49] W. Song, K.W. Kim, S.J. Kim, B.K. Min, Y.R. Lim, S. Myung, S. S. Lee, J. Lim, K.-S. An, Threshold voltage manipulation of ZnO-graphe ne oxide hybrid thin film transistors via Au nanoparticles doping, 2D Ma terials 2(4) (2015) 044007.
[50] A. Misra, H. Kalita, A. Kottantharayil, Work Function Modulation a nd Thermal Stability of Reduced Graphene Oxide Gate Electrodes in MO S Devices, ACS Applied Materials & Interfaces 6(2) (2014) 786-794.
[51] L. Sygellou, G. Paterakis, C. Galiotis, D. Tasis, Work Function Tuni ng of Reduced Graphene Oxide Thin Films, The Journal of Physical Che mistry C 120(1) (2016) 281-290.
[52] D. Li, M.B. Muller, S. Gilje, R.B. Kaner, G.G. Wallace, Processable aqueous dispersions of graphene nanosheets, Nat Nanotechnol 3(2) (2008) 101-5.

Part IV.

Concluding remarks

Chapter 7 Concluding remarks

7.1 General guidelines for band gap engineering of graphene oxide based graphene

Interest in graphene and graphene based materials is growing rapidly to achieve a high performance electronic devices. Over the about 20 years since the graphene is found by A. Geim and K. Novoselov, [1] graphene has been taken attention because its attractively great performance. [2-5] In addition, it is known that graphene can be easily obtained by the reduction of graphene oxide (GO) that the method, established from the past 70 years by Hummers, [6] the use of GO based graphene, called chemically prepared graphene (CCG) or reduced graphene oxide (RGO), is studied for the applying graphene's wonderful materials performances to the various electronic devices. [3, 5, 7] However, the required electrical performance those devices are different and application of RGO from the same method, without the deeper consideration of its tunable band gap by its differed surface nature remained as a huge barrier to the effective application of GO based graphene to electrical devices.

Herein, in this thesis, it is attempted to descried the practical band gap of GO based graphene itself to establish rational design guidelines for graphene based electronic devices. Through a comprehensive review of quantum electrical fundamentals, key parameters are studied to identify the difference of band gap by differed surface characteristic such as the ratio of non sp^2 carbon and I_D/I_G ratio. The multiple of these parameters showed linear relationship with the band gap of GO based graphene as shown below in chapter 2.

$$E_g = [ratio\ of\ non\ sp^2\ carbon] \times [\frac{I_D}{I_g}\ ratio]$$

Ratio of non sp^2 carbon can be predicted by the devolution of C1s peak measured by the x-ray photoelectron spectroscopy (XPS) and the I_D/I_G ratio can be

measured by Raman spectroscopy. Thus the relationship was verified from the calculation and experimental result as shown in the chapter 2 and 3.

In the case of GO based graphene composite the band gap of whole system can be altered by the band gap and work function of graphene itself, therefore, the we found that the work function of GO based graphene are showed linear relationship with dangle oxygen ratio as studied on chapter 2 and 3 and the band gap of GO based graphene composite with typical metal oxides are predicted accurately and the band gap can be narrowed by the increment of concentration of GO based graphene. This result implies that the band gap of GO based graphene itself and its composite system can be controlled easily.

Following this design guidelines the band gap of graphene based materials are controlled to metallic and semiconductive region for the appropriate propose the the effective control way of band gap engineering of GO based graphene in Part 3. As a result, the GO based graphene exhibited much improved performances that traditionally prepared GO that high electrical conductivity, gas sensing performance, carrier mobility and on/off ratio. Plus, the guidelines of band gap range of graphene based materials for the application can be proposed as shown in Figure 7.2 through the process are suggested in Figure 7.1.

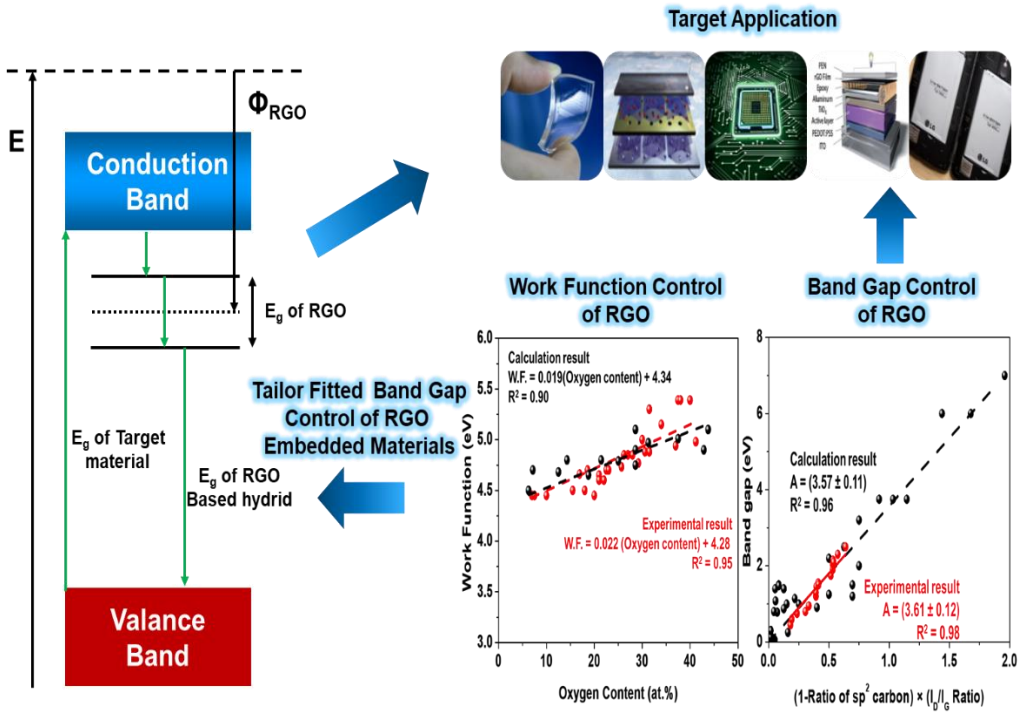

Figure 7.1 Schematic view of the process of band gap engineering of GO based graphene and its composite for target application.

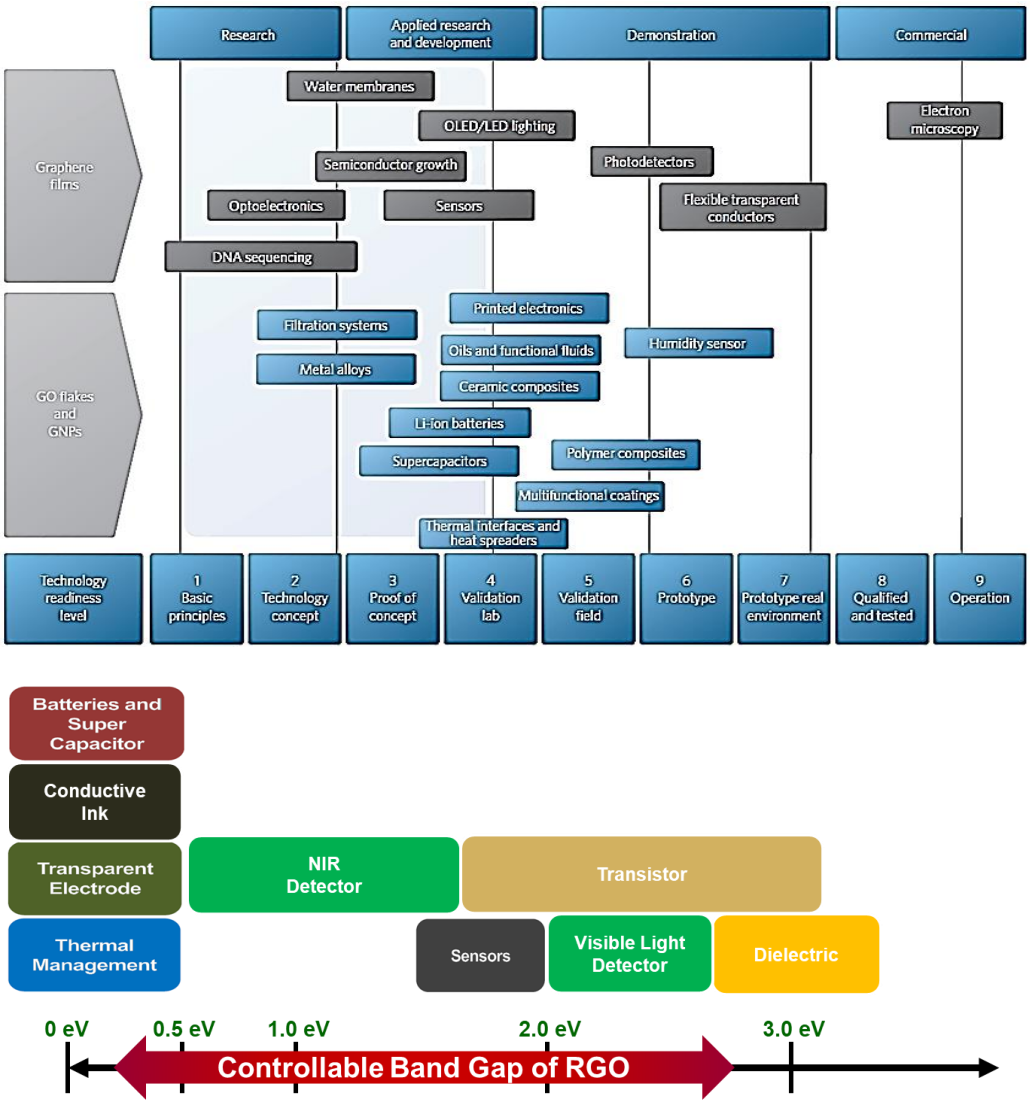

Figure 7.2 (upper) Expected application of GO based graphene [5] and (lower) predicted band gap range of GO based graphene and its composite for each application.

7.2 Further work

7.2.1 Band gap engineering of graphene with other foreign atoms.

In order to get mole stable functionalized graphene with enlarged band gap, graphene should be functionalized with other heteroatoms except oxygen. Therefore, there are many tries that functionalization of graphene with nitrogen, boron, fluorine, sulfur and that can show more thermal stability than graphene oxide.[8] Especially, graphene fluorination using graphene oxide and fluorine plasma shows high degree of functionalization and high potential of enlargement of band gap as shown in **Figure 7.3**. [9] However, in spite of many method that dangling other functional groups to graphene except oxygen, but there isn't any guidelines of band gap engineering and it should be established for more stable band gap engineering of GO based graphene.

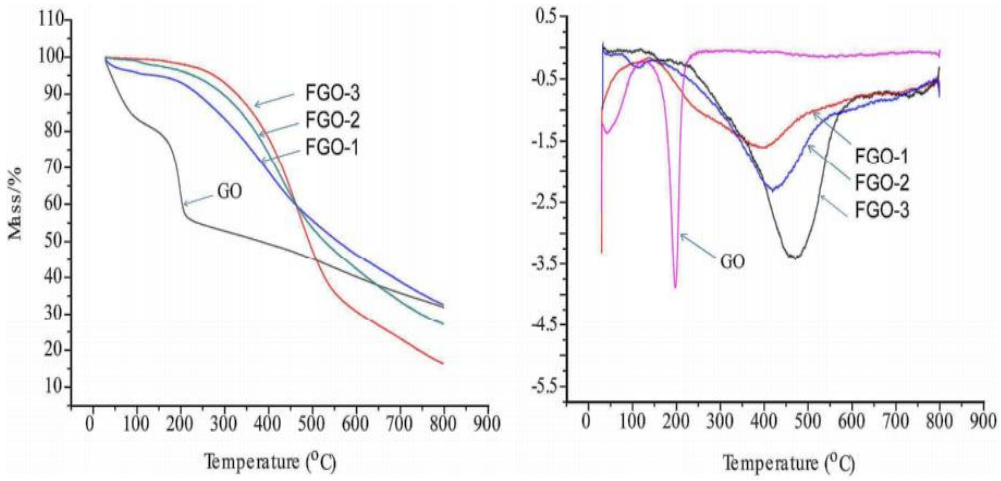

Figure 7.3 Improved thermal stability of GO by exchanging oxygenated functional groups to fluorinated functional groups with different degree measured by (left) TGA and (right) dynamic thermal analysis. (DTA) [9]

7.2.2 Requirement of guidelines for band gap engineering of graphene in various surrounding materials.

In the use of IGZO/RHGO for transistor, it showed high mobility than IGZO/RGO. However, for the next generation display devices over 8K display, faster transport of charge carrier over 20 cm^2/Vs is required. [10] In order to overcome this huddle, other surrounding materials that makes more synergetic performance with GO based graphene should be considered with the model that suggested in **Chapter 2** and **Chapter 3**. For example, Indium-gallium-tin oxide (IGTO), has similar structure and energy level of conduction band with IGZO, showed improved performance than IGZO with enlarged band gap of 3.9 eV and carrier mobility of 13 cm^2/Vs. (**Figure 7.4**) [11] Therefore IGTO can show similar effect with the case of IGZO/RHGO, that improves mobility 9 times than pristine ink based IGZO, it can be thought that IGTO/RHGO has high potential of ultra-fast carrier mobility.

In addition, for the right application of GO based graphene with improved charge carrier transport, the two problems should be solved. The one is minimize oxygenated functional group of graphene that makes depletion layer, another is make graphene with increased lateral size. From the previous study, ZnO/GO composite showed large threshold voltage by depletion layer by oxygen functional groups as shown in **Figure 7.5** [12] In addition, the use of large graphene produced by chemical vapor deposition (CVD) with non-oxidized structure, the ZnO/graphene showed carrier mobility of 290 cm^2/Vs and showed the effect of enlargement of graphene size and low threshold voltage. (**Figure 7.6**) [13] Therefore, the GO based graphene should be prepared with large lateral size and low oxidation degree makes IGZO/RGO transistor with improved carrier mobility over 20 cm^2/Vs.

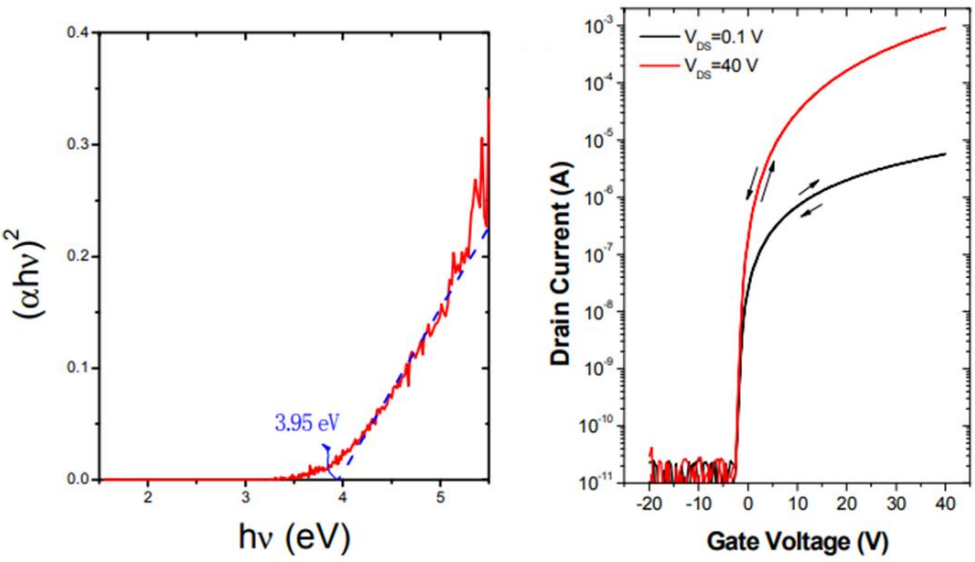

Figure 7.4 (left) Band gap calculated by Tauc plot and (right) transistor performance of ink based IGTO channel after annealing process. [11]

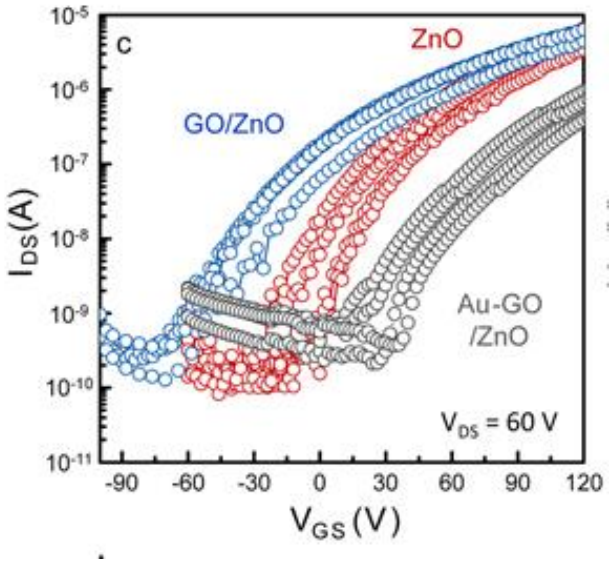

Figure 7.5 Improved carrier mobility of ZnO/GO transistor channel by elimination of depletion mode by adding gold doping of GO. [12]

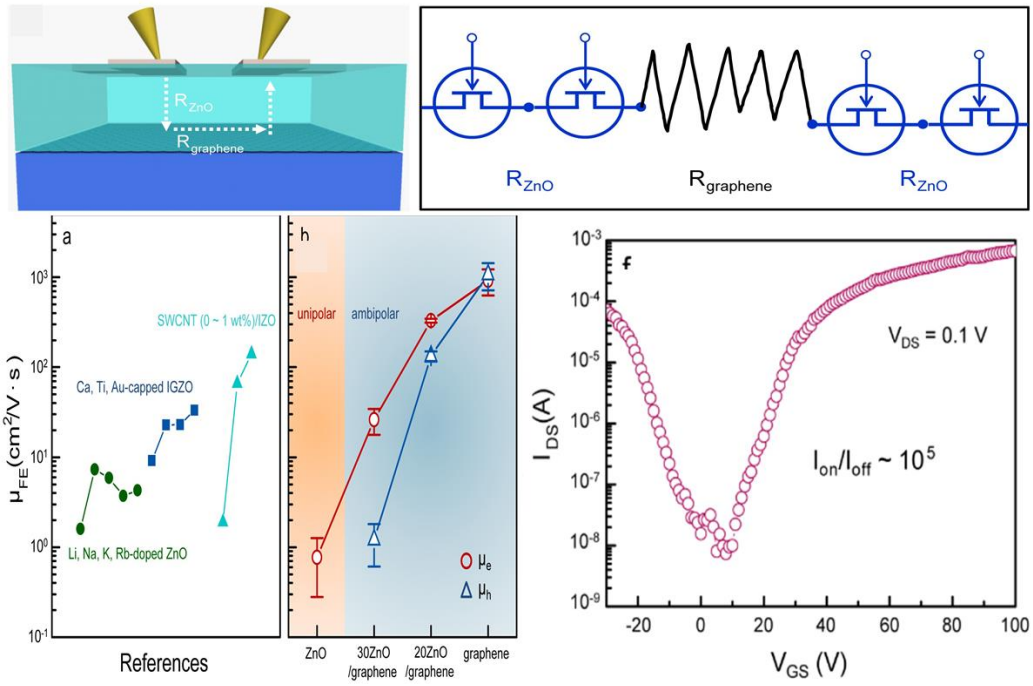

Figure 7.6 Improved carrier mobility of ZnO/graphene transistor channel by adding large sized graphene. [13]

7.3 Reference

[1] K.S. Novoselov, A.K. Geim, S.V. Morozov, D. Jiang, Y. Zhang, S.V. Dubonos, I.V. Grigorieva, A.A. Firsov, Electric Field Effect in Atomically Thin Carbon Films, Science 306(5696) (2004) 666.

[2] A.K. Geim, K.S. Novoselov, The rise of graphene, Nat Mater 6(3) (2007) 183-191.

[3] Y. Zhu, S. Murali, W. Cai, X. Li, J.W. Suk, J.R. Potts, R.S. Ruoff, Graphene and graphene oxide: synthesis, properties, and applications, Adv Mater 22(35) (2010) 3906-24.

[4] K.S. Novoselov, V.I. Fal′ko, L. Colombo, P.R. Gellert, M.G. Schwab, K. Kim, A roadmap for graphene, Nature 490(7419) (2012) 192-200.

[5] A. Zurutuza, C. Marinelli, Challenges and opportunities in graphene commercialization, Nature Nanotechnology 9(10) (2014) 730-734.

[6] W.S. Hummers, R.E. Offeman, Preparation of Graphitic Oxide, Journal of the American Chemical Society 80(6) (1958) 1339-1339.

[7] S. Mao, H. Pu, J. Chen, Graphene oxide and its reduction: modeling and experimental progress, RSC Advances 2(7) (2012) 2643-2662.

[8] X. Wang, G. Sun, P. Routh, D.-H. Kim, W. Huang, P. Chen, Heteroatom-doped graphene materials: syntheses, properties and applications, Chemical Society Reviews 43(20) (2014) 7067-7098.

[9] X. Wang, Y. Dai, J. Gao, J. Huang, B. Li, C. Fan, J. Yang, X. Liu, High-Yield Production of Highly Fluorinated Graphene by Direct Heating Fluorination of Graphene-oxide, ACS Applied Materials & Interfaces 5 (17) (2013) 8294-8299.

[10] T. Arai, T. Sasaoka, 49.1: Invited Paper: Emergent Oxide TFT Technologies for Next-Generation AM-OLED Displays, SID Symposium Digest of Technical Papers 42(1) (2011) 710-713.

[11] Y. Wang, Z. Wang, C. Liu, The Indium-Gallium-Tin-Oxide thin film transistor with better performance based on the solution procession, 2019 26th International Workshop on Active-Matrix Flatpanel Displays and De vices (AM-FPD), 2019, pp. 1-4.
[12] W. Song, K.W. Kim, S.J. Kim, B.K. Min, Y.R. Lim, S. Myung, S. S. Lee, J. Lim, K.-S. An, Threshold voltage manipulation of ZnO-graphe ne oxide hybrid thin film transistors via Au nanoparticles doping, 2D Ma terials 2(4) (2015) 044007.
[13] W. Song, S.Y. Kwon, S. Myung, M.W. Jung, S.J. Kim, B.K. Min, M.-A. Kang, S.H. Kim, J. Lim, K.-S. An, High-mobility ambipolar ZnO-graphene hybrid thin film transistors, Scientific Reports 4(1) (2014) 4064.

List of Publications

1. Yern Seung Kim, Jong Hun Kang, Taehoon Kim, Yeonsu Jung, Kunsil Lee, Jun Young Oh, **Jisoo Park**, Chong Rae Park, "Easy Preparation of Readily Self-Assembled High-Performance Graphene Oxide Fibers" **Chemistry of Materials**, 2014

2. Mi Se Chang, Taehoon Kim, Jong Hun Kang, **Jisoo Park**, Chong Rae Park, "The Effect of Surface Characteristics of Reduced Graphene Oxide on The Performance of a Pseudocapacitor" **2D Materials**, 2015

3. Yo Chan Jeong, Kunsil Lee, Taehoon Kim, Jae Ho Kim, **Jisoo Park**, Young Shik Cho, Seung Jae Yang, Chong Rae Park, "Partially Unzipped Carbon Nanotubes for High-Rate and Stable Lithium-Sulfur Batteries", **Journal of Materials Chemistry A**, 2016

4. Jong Hun Kang, Taehoon Kim, Jaeyoo Choi, **Jisoo Park**, Yern Seung Kim, Mi Se Chang, Haesol Jung, Kyung Tae Park, Seung Jae Yang, Chong Rae Park, "Hidden Second Oxidation Step of Hummers Method", **Chemistry of Materials**, 2016

5. Mi Se Chang†, Yern Seung Kim†, Jong Hun Kang, **Jisoo Park**, Sae Jin Sung, Soon Hyeong So, Kyung Tae Park, Seung Jae Yang, Taehoon Kim, Chong Rae Park, "Guidelines for Tailored Chemical Functionalization of Graphene" **Chemistry of Materials**, 2017 (†Contributed equally)

6. **Jisoo Park**, Yern Seung Kim, Sae Jin Sung, Taehoon Kim, Chong Rae Park, "Highly Dispersible Edge Selectively Oxidized Graphene with Improved Electrical Performance", **Nanoscale**, 2017

7. Yern Seung Kim†, Jun Young Oh†, Jae Ho Kim, Minho Shin, Yo Chan

Jeong, Sae Jin Sung, **Jisoo Park**, Seung Jae Yang, Chong Rae Park, "Crucial Role of Oxidation Debris of Carbon Nanotubes in Subsequent End-Use Applications of Carbon Nanotubes", **ACS Applied Materials & Interfaces**, 2017 (†Contributed equally)

8. Sae Jin Sung, Taehoon Kim, **Jisoo Park**, Soon Hyeong So, Jaeyoo Choi, Seung Jae Yang, Chong Rae Park, "Influence of Physicochemical Characteristics of Reduced Graphene Oxides on Gas Permeability of The Barrier Films for Organic Electronics", **Chemical Communications**, 2017

9. Jun Young Oh†, **Jisoo Park**†, Yo Chan Jeong, Jae Ho Kim, Seung Jae Yang, Chong Rae Park, "Secondary Interactions of Graphene Oxide on Liquid Crystal Formation and Stability", **Particle & Particle Systems Characterization**, 2017 (†Contributed equally)

10. Yeon Hoo Kim, **Jisoo Park**, You Rim Choi, Seo Yun Park, Seon Yong Lee, Woonbae Sohn, Young-Seok Shim, Jong-Heun Lee, Chong Rae Park, Yong Seok Choi, Byung Hee Hong, Jung Hun Lee, Wi Hyoung Lee, Donghwa Lee, Ho Won Jang, "Chemically Fluorinated Graphene Oxide for Room Temperature Ammonia Detection Capability at ppb Levels", **Journal of Materials Chemistry A**, 2017

11. Yo Chan Jeong, Jae Ho Kim, Sung Hyun Kwon, Jun Young Oh, **Jisoo Park**, Yeonsu Jung, Seung Geol Lee, Seung Jae Yang, Chong Rae Park, "Rational Design of Exfoliated 1T MoS_2 @ CNT-based Bifunctional Separator for Lithium Sulfur Batteries", **Journal of Materials Chemistry A**, 2017

12. **Jisoo Park**†, Young Shik Cho†, Sae Jin Sung, Minhoo Byeon, Seung Jae

Yang, Chong Rae Park, "Characteristics Tuning of Graphene-Oxide-Based-Graphene to Various End-Uses", **Energy Storage Materials**, 2018 (†Contributed equally)

13. Sae Jin Sung, **Jisoo Park**, Young Shik Cho, Se Hoon Gihm, Seung Jae Yang, Chong Rae Park, "Enhanced Gas Barrier Property of Stacking-Controlled Reduced Graphene Oxide Films for Encapsulation of Polymer Solar Cells", **Carbon**, 2019

14. Sae Jin Sung, Jae Ho Kim, Se Hoon Gihm, **Jisoo Park**, Young Shik Cho, Seung Jae Yang, Chong Rae Park, "Revisiting The Role of Graphene Quantum Dots in Ternary Organic Solar Cells: Insights into the Nanostructure Reconstruction and Effective Förster Resonance Energy Transfer", **ACS Applied Energy Materials**, 2019

15. **Jisoo Park**, Yeonhoo Kim, Seo Yeon Park, Sae Jin Sung, Ho Won Jang, Chong Rae Park, "Band Gap Engineering of Graphene Oxide for Ultrasensitive NO_2 Gas Sensing." **Carbon**, 2020

국 문 초 록

그래핀은 그 자체가 가지고 있는 기존 재료 대비 뛰어난 특성 때문에 그 동안 큰 주목을 받아왔다. 이에 따라, 다양한 응용 분야에서 그래핀을 사용하여 고성능 장치를 구현하고자 수 많은 연구들이 진행되어 왔다. 그러나, 그래핀 제조 공정에 의해 변경 될 수 있는 그래핀의 그 자체의 재료 특성에 대한 인지 부족으로 인해 실제 디바이스에 대한 적용 시 요구되는 다양한 범위의 그래핀을 만족시키지 못하여 그래핀이 가지고 있는 뛰어난 물성을 완전하게 구현하는데 실패하였다. 특히, 전자소자로의 응용의 경우, 전기적 특성을 결정하는 중요한 특성인 밴드갭은 그래핀의 경우 존재하지 않으며, 물리적 혹은 화학적 구조 변화에 의해서만 확보 될 수 있으므로, 그래핀 기반 장치의 성능의 비약적인 향상을 위해 그래핀의 밴드갭 확보 과정에 대한 분석이 필수적이라고 할 수 있다.

이를 위해 일부 연구자들은 밴드갭을 결정하는 그래핀 자체의 물질적 파라미터를 찾아내고자 하였으나, 그 밴드갭과 물질적 파라미터 간의 관계를 실질적으로 명확하게 밝혀내는 데에는 실패하였다. 이러한 그래핀 연구의 장애물을 극복하기 위해서는 기존 연구진이 시도해왔던 것과는 차별화하여, 그래핀이 가지고 있는 탄소원자를 기반으로 그래핀의 밴드갭을 제어하는 숨겨진 파라미터를 밝혀내는 것이 중요하다. 따라서, 이 연구는 기존의 관점에서 탈피하여 공액구조를 가지고 있는 탄소원자의 비율과 경계탄소의 비율, 그리고 그래핀의 밴드갭 사이의 관계 확립에 중점을 두어 명확한 선형관계가 성립함을 입증하였다. 또한, 대표적인 응용 분야들을 위해 실제 미세 조정된 밴드갭을 갖는 그래핀을 실험적으로 적용하여 그 효과를 실질적으로 증명하고자 하였다.

Part I 에서는 그래핀의 밴드갭 미세 조정에 대한 배경과 필요성을 정리하였다. 그래핀의 밴드갭 엔지니어링에 대한 현재 연구 동향을 면밀하게 검토하였으며, 이를 기반으로 그래핀의 이론적으로 예측된 성능과 실제 그래핀 기반 장치 사이의 격차를 극복하기 위한 이 연구의 목적을 확립하고자 하였다.

Part II에서는 이론적으로 그래핀의 밴드갭과 표면 파라미터 간의 관계를 예측하고, 이를 검증하기 위해 기본적인 이론을 확립하는데 중점을 두었으며, 공액구조를 가지는 탄소원자의 비율과 그 중 경계탄소의 비율을 기반으로 표면 특성에 따라

실제 밴드갭을 결정하는 주요 파라미터를 도출하고자 하였다. 주요 재료적 파라미터들은 기본 전자 공학 이론을 기반으로 검토 후 도출하였다. 이를 바탕으로 화학적인 방법으로 합성된 그래핀 옥사이드 기반 그래핀의 밴드갭을 예측하기 위해 공액구조를 가지는 탄소원자 및 공액구조 경계 탄소원자의 비율을 도입하였으며, 이들 파라미터들과 실제 그래핀 옥사이드 기반 그래핀의 관계에 대한 실험적인 검증을 통해 확립된 이론의 신뢰성을 확보하고자 하였다.

Part III은 Part II에서 제시된 그래핀 밴드갭과 그 자체의 물질적 파라미터 간의 관계를 따라 맞춤형 밴드갭을 갖는 그래핀의 설계 및 합성에 중점을 둔다. Chapter 3에서는 그래핀의 가장자리 선택적 산화에 의해 환원 후 그래핀 옥사이드 기반 그래핀의 밴드갭을 낮추는 것을 시도한다. 그 결과 그래핀 산화물의 환원공정 동안 발생하는 결함을이 기존 그래핀 옥사이드에 비해 크게 감소하였으며 그 결과 환원된 그래핀의 전기전도도를 크게 향상시키는데 성공하였다. Chapter 4 에서는 그래핀 옥사이드의 표면의 에폭사이드 작용기를 선택적으로 감소시킴으로써, 표적 가스 분자의 흡착 및 전하 운반체의 이동을 향상 시켜 타겟 물질에 대한 감도를 증가시키는데 성공하였다. Chapter 5에서는 인듐-갈륨-아연-산화물 (IGZO) 박막 트랜지스터의 채널 물질의 전기적 수송을 개선하기 위해 그래핀의 양에 따른 전체계의 밴드갭을 미세하게 조정하였고, 채널 물질의 열처리 동안 기공 발생을 최소화하기 위해 에폭사이드 작용기가 감소된 그래핀 옥사이드를 사용하여 밴드갭이 조정된 그래핀 / IGZO 복합체의 전하 수송을 효과적으로 증가시켰다.

이 연구는 그래핀 기반 장치의 성능과 관련된 변수에 대한 이론적 고려를 통해 그래핀의 밴드갭에 영향을 미치는 주요 재료 매개 변수를 도출하고 이를 실질적으로 검증한다는 점에서 그 의의를 찾을 수 있으며, 실제적으로 대표적인 적용 분야에서 성능 향상을 보인 만큼, 이 연구에서 제시된 그래핀 설계 지침은 이론적으로 예측된 그래핀의 성능과 실제 장치 성능 사이의 격차를 극복하고 차세대 그래핀 기반 재료로 연구를 발전시키는 것에 대한 통찰력을 제공 할 수 있을 것이라 사려된다.

핵심어: 그래핀, 그래핀 옥사이드, 밴드갭, 재료 설계, 용도 맞춤형 합성
학번: 2014-21442